Title
Data-driven approaches to resolving feedback processes driving the earth system over multi- spatial and temporal scales

Author
Ma, Hongxu

Publication Date
2019

Peer reviewed|Thesis/dissertation

Data-driven approaches to resolving feedback processes driving the earth system over multi- spatial and temporal scales

by

Hongxu Ma

A dissertation submitted in partial satisfaction of the
requirement for the degree of
Doctor of Philosophy
in
Geography
and the Designated Emphasis
in
Computational and Data Science and Engineering
in the
Graduate Division
of the
University of California, Berkeley

Committee in charge:

Professor Laurel G. Larsen, Chair
Professor John Chiang
Professor Bin Yu
Professor Jeffrey Chambers

Spring 2019

Abstract

Data-driven approaches to resolving feedback processes driving the earth system over multi- spatial and temporal scales

By

Hongxu Ma

Doctor of Philosophy in Geography

University of California, Berkeley

Professor Laurel G. Larsen, Chair

Data is one of the essential components in analyzing complex earth system problems. With high-quality data more feasible to the researchers, more details of the system could be revealed by those data-intensive computational and data-driven approaches. The measurement and data collection devices have been developing dramatically, especially those used for earth system science. The high sampling resolution in all spatial, temporal and spectral scale have enabled the analysis of earth system problems into a data-driven era. Meanwhile, the fast development of computational ability and resources allow the emergence of innovative data-driven methods (e.g., information theory, traditional statistical learning models, deep learning models). The data-driven approach is different from the physical-based (or knowledge-based) modeling. It emphasizes learning and generalizing the rules from large amounts of representative data. It tries to fit the probability distribution function, for any questions, with the support of large numbers of observations with little constraining conditions like those from the physical-based model. However, before relying on purely data-driven methods, it is essential to remember that Earth systems are characterized as nonlinear, complex and dynamic systems with couplings and feedback among components and subsystems.

Additionally, these coupled processes change depending on the status of the system and the spatial and temporal scale at which the system is analyzed. To understand the underlying mechanisms that drive complex systems, it is useful to conceptualize the system as a network of variables undergoing interactions and feedback. Traditional statistical analysis methods are ill-suited to capture the key attributes of this type of feedback processes due to the stochasticity of the variables, the nonlinearities of the couplings and the non-stationarity of the system. The limitation of the data (in terms of resolution and length in both spatial and temporal scale) and computational ability further narrow the effectiveness of those methods.

The various science communities are now facing a new challenging problem. On the one hand, you have 1) more and more data being collected, 2) the significantly-

improved ability to depict the status of a system and to describe the details of a relationship between the components within the system, and 3) the computational capacity and resources to be able to handle this large number of data, motivating the use of data-driven methods.

In this dissertation, I will examine the potential for integrating data-driven techniques into earth systems science to improve our understanding of earth-surface processes. Specifically, I focus on applying data-driven techniques for resolving causal interactions of the several complex earth systems over multispectral and temporal scales. Four complex earth system problems with different spatial and temporal scales are discussed. First, we implement the data-driven methods in regional and decadal issues, streamflow prediction, as a case study. Our findings suggest that while information-flow identifies dominant streamflow controls, the results should not be limited to only "critical hydrologic timescales;" instead they should guide a range of timescales over which inputs, stores, and losses are filtered into catchment discharge. Second, we analyzed a regional and yearly problem, the feedback process between vegetation and topography in a lake delta ecosystem. The transfer entropy analysis suggests that different vegetation communities play functionally different roles in landscape evolution that should be differentiated in ecogeomorphic models. Within such models, it would be most imperative to resolve detailed flow characteristics at lower to low-middle island elevations.

Furthermore, within elevation zones, it is likely essential to differentiate between the roles of multiple vegetation communities rather than treating the entire elevation zone as a single ecogeomorphic entity. Third, we analyzed global and millennium problems, the interaction among climatically variables over 42,000 years. We show that, during the past 420,000 years, orbital forcings trigger temperature and CO2 responses at short (5 kyr) time lags. Over longer timescales, internal feedback, mediated by interactions with dust, also plays a significant role in governing temperature and CO2 concentrations. The short-term influence of CO2 on temperature was stronger than dust's long-term impact, consistent with on radiative forcing. However, dust remained an essential driver of temperature over 50-kyr time lags, the amount of time between sequential glacial maxima and minima during the latter portion of the Pleistocene. Last, we analyzed a global and decadal problem, the interaction between ocean and precipitation on land. We quantitatively demonstrate that Sea Surface Temperature (SST) over the Gulf of Guinea controls moisture advection and transport to the West Sahel region; strong bidirectional interaction exists between local vegetation dynamics and rainfall patterns. The spatial distribution map of time lag with most significant transfer entropy also shows the apparent trend of each climate indices tested in this research. The Niño 3+4 and Niño 4 have a relatively short time lag with significant transfer entropy to the west coast and have insignificant information transferred to the middle US. The Niño 1+2 and Niño 3 have a relatively short time lag with significant information transferred to the middle region but insignificant information transferred to the west coast.

By testing the effectiveness and efficiency of the data-driven methods in complex earth system problems over multiple spatial and temporal scales, the results verified the ability of those methods in identifying and quantifying the strength, statistical

significance, directionality and critical time lags of feedback (as well as one-way forcing) among variables. With these data-driven methods, we could identify which components comprise the system, and which dominate changes within the system. With the input of that knowledge, we could further predict the behavior of an element of interest or the stationery of the whole system and simulate the future behavior of the system under different scenario after fully understanding the rules and the connections of a system.

Acknowledgements

This dissertation includes my previously published and co-authored materials. I have received full permissions to use them from all co-authors.

Chapter 3 includes the paper, Ma, H., Larsen, L. G., & Wagner, R. W. (2018). Ecogeomorphic Feedbacks that Grow Deltas. Journal of Geophysical Research: Earth Surface, 123(12), 3228-3250. Hongxu Ma is the primary author of this work.

Chapter 4 includes the work, Dust mediates CO2 - Temperature feedbacks over Pleistocene glacial - interglacial cycles. (in prep.). Hongxu Ma is one of the primary authors and contribute to the idea discussion, method design and result analysis. The materials of this work serve as a case study using data driven approaches to resolve the feedback proceses of system with global and milennium scale.

Chapter 5 includes the paper, Liu, B. Y., Zhu, Q., Riley, W. J., Zhao, L., Ma, H., Van Gordon, M., & Larsen, L. (2019). Using Information Theory to Evaluate Directional Precipitation Interactions Over the West Sahel Region in Observations and Models. Journal of Geophysical Research: Atmospheres, 124(3), 1463-1473. Hongxu Ma contribute to the idea discussion, method design and implement. The materials of this work serve as a case study using data driven approaches to resolve the feedback processes of system with global and decadal scale.

Appdenix includes the work, Identification of critical timescales of water storage and flux improves streamflow prediction. Christopher Tennant, Laurel Larsen, Dino Bellugi, Edom Moges, Hongxu Ma, and Liang Zhang (in prep.). Hongxu Ma contribute to the idea discussion, method design and implement and results discussion. The materials of this work serve as a case study using data driven approaches to resolve the feedback processes of system with regional and yearly scale.

I would like to dedicate this work to my wife Xinliu,

my son Ethan and my parents Hong Liang and Shaozhong Ma.

I would also like to dedicate this to my grandparents.

Chapter 1
Introduction

Data is one of the most important components in analyzing complex earth system problems. With high quality data more feasible to the researchers, more details of the system could be revealed by those data-intensive computational and data-driven approaches. The measurement and data collection devices have been developing dramatically, especially those used for earth system science. The high sampling resolution in all spatial, temporal and spectral scale have enable the analysis of earth system problems into a data-driven era. Measurements of features that were nearly impossible to take in the past are now becoming possible (e.g. large range ground water estimation from GRACE (Rodell et al. 2007)).

Take remote sensing techniques for example. Landsat-8 (launched in 2013 by USGS) provides high quality earth surface observation images with 30-meter spatial resolution, 16-day temporal resolution and 9-band spectral resolution. Sentinel-2A/B (launched in 2015 and 2017 by ESA) provides images that are up to 10 meters in spatial resolution, have a 5-day temporal resolution and 13 bands. These imagery data significantly contribute to the study and analysis of the questions in multiple areas in earth system science, including, but not limited to, agriculture, forestry, hydrology, ecology, glaciology, and urban and climate change studies. Furthermore, there are local scale developments with flux towers and other in-site devices that support the high-quality data measurements of various variables. These devices provide high frequency (up to 20 Hz) and highly accurate measurements of CO2, air moisture, wind speed and direction, dust and so on. The whole communities asked for a new way to use and cooperate with these high-quality datasets.

Meanwhile, the fast development of computational ability and resources enable the emergence of innovative data-driven methods (e.g. information theory, traditional statistical learning models, deep learning models) (Labrinidis and Jagadish, 2012). The data-driven method is different from the physical-based (or knowledge-based) modeling. It emphasizes learning and generalizing the rules from large amounts of representative data. It tries to fit the probability distribution function, for any questions, with the support of large numbers of observations with little constraining conditions like those from physical-based model.

Take traditional statistical learning models (often referred to as machine learning models) for example. They are an interdisciplinary method involving probability, statistics, algorithms, computer science and optimization. By mimicking the way that humans learn, statistical learning models reorganize the knowledge structure and improve the generalizing and predicting ability through an iterative approach. With little human-defined rules or knowledge, the model has a systematic way to learn from the data and their features based on statistical estimation. There are four major types of statistical learning models. 1) Supervised learning, which is the most common statistical learning method. Supervised learning models will learn from the dataset with labelled data (given the correct classification or value) and generate a model to classify the new observation or predict the outcomes. Within the dataset, there is a mapping from the features (X) to the result (y). The result could be a label (for classification models) or a value (for regressive models). The model uses the features (X) to estimate the prediction. And by

comparing the model predicted value to the known true results, the model is able to be optimize to the direction with better predicting ability. 2) Unsupervised learning, which directly learns from a dataset without labelled results. Unsupervised learning models are usually used for clustering purposes. 3) Semi-supervised learning, which is a combination of supervised and unsupervised models. Considering the labelled data is costly, the semi-supervised learning model could use its unsupervised part to find and generalize the features from the unlabeled dataset, then use its supervised part to estimate and validate the prediction of the labeled dataset. 4) Reinforcement learning, which emphasizes on optimizing the expected outcomes based on the current environment status or stationary system. The idea comes from behavioral psychology, describing an organism could generate a series of behavior habits that leading to maximize benefit from learning the rewards and punishments from the environment. These traditional statistical learning models have become the new paradigm in dealing with the emerging high-quality datasets.

However, before relying on purely data-driven methods, it is important to remember that Earth systems are characterized as nonlinear, complex and dynamic systems with couplings and feedback among components and subsystems. Additionally, these coupled processes change depending on the status of the system and the spatial and temporal scale at which the system is analyzed. To understand the underlying mechanisms that drive complex systems, it is useful to conceptualize the system as a network of variables undergoing interactions and feedback. Traditional statistical analysis methods are ill-suited to capture the key attributes of this type of feedback processes due to the stochasticity of the variables, the nonlinearities of the couplings and the non-stationarity of the system. The limitation of the data (in terms of resolution and length in both spatial and temporal scale) and computational ability further narrow the effectiveness of those methods.

The various science communities are now facing a new challenging problem. On one hand, you have 1) more and more data being collected, 2) the significantly-improved ability to depict the status of a system and to describe the details of a relationship between the components within the system, and 3) the computational ability and resources to be able to handle this large number of data (Chen and Zhang, 2014), motivating the use of data-driven methods. However, on the other hand, we still want to gain a deeper understanding of the underlying mechanisms, so how do we now create a relationship between pure data-driven methods and pure physical-based models?

Research in earth system science often concerns itself with the following questions:

- Which components comprise the system, and which dominate changes within the system?
- How to predict the behavior of a component of interest or the stationary of the whole system?
- How to simulate the future behavior of the system under different scenario after fully understanding the rules and the connections of a system?
- What are the temporal trends and seasonal variability of a component of interest?
- What are the causal relationships of a component of interest to the others within the system?
- How to help with management (e.g. wetland restoration strategies)?

Chapter 1: Introduction

In the study of earth system science, most of the data or information are recorded in the form of spatial data and time series data. For example, the scientists could analyze the time series data of precipitation, snow melting, wind speed and temperature to predict the streamflow at the outlet. We could also analyze the time series data of historical climate data, like CO2, temperature (estimated from O18), dust and CH4 for up to 420,000 years to find the relationships between those components and how these relationships are changed along with time.

Meanwhile, with the development of remote sensing technology and LiDAR (Light Detection And Ranging), more and more earth system science data can be measured and recorded in the form of spatial data. Thus, it is becoming possible to fuse the temporal data with the spatial data to answer more complex questions. For example, we could analyze the temporal and spatial pattern of the sea surface temperature anomaly and the sea surface pressure to predict the climate extreme in the United States, or to predict the precipitation in the Sahel. Furthermore, we could also try to modify the methods to analyze spatiotemporal dataset that are traditionally used for time series data. This modification could then be used to analyze how different types of vegetation act differently in the feedback between bio-volume and topography at the wetland delta.

In this dissertation, I will examine the potential for integrating data-driven techniques into earth systems science to improve our understanding of earth-surface processes. Specifically, I focus on applying data-driven techniques for resolving causal interactions between variables sensed remotely and identifying critical timescales over which one variable has a significant causal effect on another. In the next section, I introduce transfer entropy, a different statistical method that we hope to be the key in integrating data-driven models into physical-based modeling work flows.

Transfer entropy, a way to study complex earth system science from a perspective of information theory.

Our technology for data collection and new computational tools for analysis are now such that we are faced with an unprecedented opportunity to gain new understandings of earth surface processes. However, appropriate application of this new arsenal has been challenging, due to the noisy and nonlinear nature of many environmental systems. Traditional machine learning methods and deep learning methods are good at predicting the variables of interest. But it is hard for those methods to depict the relationships, i.e. mechanisms, among the components that constitute the system. It is also challenging for traditional statistical models to identify the strength, directionality and the time lag of the effect of one variable on another. We have to infer causal associations between variables, thereby improving mechanistic understanding and facilitating prediction.

Transfer entropy is an information-theoretical method that statistically identifies directionality of forcing and feedback by measuring information transfer among pairs of variables. Information is defined as the Shannon entropy, H, or total uncertainty present in a variable's distribution (Shannon 1949):

$$H = -\sum_i p(i) log_2 p(i). \qquad [1.1]$$

where $p(i)$ denotes the probability that i th event happened. H measures uncertainty in units of bits.

Mutual information is used to measure the reduction in one variable's uncertainty by knowing the other variable. It is calculated as

$$I(X_t, Y_t) = \sum_{x_t, y_t} p(x_t, y_t) log_2 \frac{p(x_t, y_t)}{p(x_t)p(y_t)}. \quad [1.2]$$

where x_t, y_t are values in time series X_t and Y_t.

Transfer entropy (TE) adds directionality to mutual information. It measures how much information is transferred between two variables, quantifiable as the reduction in uncertainty in the distribution of variable Y based on knowing the value of variable X at a time lag τ, conditioned on Y's own history. Typically, (Schreiber 2000, Ruddell and Kumar 2009), it is formulated from time-series X_t and Y_t as follows:

$$T(X_t \to Y_t, k, l, \omega, \tau) = \sum_{y_t, y_{t-\omega\Delta t}^{[k]}, x_t^{[l]}} p(y_t, y_{t-\omega\Delta t}^{[k]}, x_{t-\tau\Delta t}^{[l]}) \, log_2 \frac{p(y_t | (y_{t-\omega\Delta t}^{[k]}, x_{t-\tau\Delta t}^{[l]}))}{p(y_t | y_{t-\omega\Delta t}^{[k]})}. \quad [1.3]$$

Here $x_{t-\tau\Delta t}^{[l]}$ and $y_{t-\omega\Delta t}^{[k]}$ are the immediate history of $x_{t-\tau\Delta t}$ and $y_{t-\omega\Delta t}$ with block length of l and k respectively, where $x_{t-\tau\Delta t}$ and $y_{t-\omega\Delta t}$ are the values of x_t and y_t at τ and ω time steps earlier respectively. The assumption that setting $k = l = 1$ is conservatively biased as it neglects the information transferred to Y_t with block lengths $k > 1$ and $l > 1$ (Marschinski and Kantz 2002, Sabesan, Narayanan et al. 2003). However, it is commonly employed in practice to reduce the dimensionality of the probability distributions in equation 2 to three-dimensional distributions (as shown in Figure 1.1), to make them computationally tractable (Ruddell and Kumar 2009, Larsen and Harvey 2017).

In TE analyses, a "source" variable is causally related to a "sink" variable if knowledge of the source variable's value significantly reduces uncertainty in a future value of the sink variable. Using a modified version of the equation by Schreiber (2000) that is appropriate for seasonally fluctuating variables (Larsen & Harvey, 316 2017), TE can be used to calculate the reduction in uncertainty for time lag τ.

Timescales of causal interactions among variables are deduced by computing TE over a range of different time lags τ, assessing both the magnitude and significance of the reduction in uncertainty in Y due to knowledge of lagged variable $Xt-\tau$. The reduction in uncertainty is deemed significant when the TE value exceeds the 95th percentile of a distribution of transfer entropies computed from 500 randomly shuffled versions of the input data matrices (Ruddell & Kumar, 2009a). Here, "critical timescales" are defined as those time lags or ranges of time lags for which a source variable significantly reduces uncertainty in a sink variable. The superiority of the TE based approach in identifying interaction time lags (timescales) relative to approaches based on lagged correlations or lagged mutual information has been demonstrated by Murari et al. (2015; 2018), who compared the performance of these approaches in the study of different signals in physics. Meanwhile, Wibral et al. (2013) demonstrated TE's effectiveness in resolving interaction times among different neuron signals from the different regions of the brain.

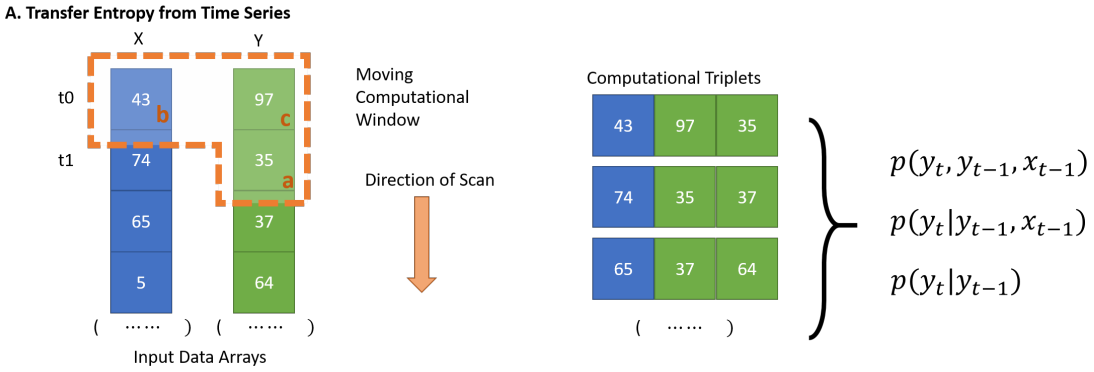

Figure 1.1 Transfer entropy is calculated from joint and conditional probability distributions based on triplets (a-c) of points: It measures the reduction of uncertainty in a dependent variable *Y* at a time t_1 (a) that is attributable to knowing the value of variable *X* at time t_0 (b), conditioned on the reduction of uncertainty attributable to knowing the value of *Y* at t_0 (c). In the traditional version of transfer entropy used to analyze time series, joint and conditional probability distributions based on these triplets are computed by scanning down the time-series (orange arrow) (Ma et al., 2018 Figure 4A).

TE has been broadly used in many scientific areas, such as financial markets, economics, social media, physiology, neuroscience, biochemical, chemistry, ecology, earth system science and so on (Vibral and Vicente, 2014; Barnett et al., 2009; Vicente et al., 2011). Schreiber (Schreiber, 2000) uses TE to analyze the relationship between heart and breath rates in the original transfer entropy paper. Ver Steeg and Galstyan (Ver Steeg and Galstyan 2013) analyze the TE of a Twitter social network formed by a group of users. Bauer (Bauer et al., 2007) uses TE identify the direction of disturbance propagation in a chemical process. Dimpfl and Peter (Dimpfl and Peter 2013) use TE to quantify the information flow between financial markets for pre-crisis, crisis and post-crisis periods and Baek et al use it to analyze the strength and the direction of information flows that are transferred within the US stock market and conclude that energy industries influence the whole market (Baek et al., 2005).

In earth system science, Ruddell and Kumar (Ruddel and Kumar, 2009a, 2009b) identify the feedback processes among ecohydrological variables at a flux tower by their directionality, relative strength, statistical significance. The process networks that formed from the results of the TE analysis are used to delineate the key couplings, critical time scales and the stationary of the system. Alicia Sendrowski and Paola Passalacqua (Sendrowski and Passalacqua, 2017) quantified process networks of water levels in different portions of a river delta and the extent to which those water levels were controlled by wind, tide, or measured river discharge. Mike Rinderer et al. (Rinderer et al., 2017) tested the ability of these techniques to map out flow paths in a highly instrumented watershed by evaluating the transfer of information between water level sensors. Goodwill et al. (Goodwill et al., 2018) characterize the relationship between joint connectivity and energy, water and carbon flux before, during, and after disturbances. Goodwill and Kumar (Goodwill and Kumar, 2017) introduced a framework for temporal information partitioning networks that enables us to interpret process connectivity and to inference of behavioral shifts in ecohydrological systems by measuring the lagged

multivariate mutual information. Transfer entropy is potentially more powerful to infer causal relationships between variables, especially within a complex system, than other tools like linear correlation. Transfer entropy is able to identify the driving or responding components in a system and to detect directional coupling of subsystem (Schreiber, 2008). The information theory measure is also able to detect the non-linear correlation and robust for noisy and chaotic system. And comparing with lagged mutual information, TE could further distinguish the information that is produced by shared history or input perturbations.

Strengths of TE that contributed to these applications are its ability to: 1) measure the strength of both linear and non-linear interactions between flux and state variables, 2) reveal the direction of these interactions in time/space, and 3) quantify the timescales of the interactions.

We now perform two tests to demonstrate the ability to identify the directionality and strength of the non-linear coupling in a complex system with noisy. More detailed tests and sample applications are done in the second chapter to illustrate the performance of TE analysis in identifying the strength, directionality and statistical significance of interactions.

Demonstration of transfer entropy to single coupled Lorenz system(s)

We used the Lorenz system (Figure 1.2), a simplified model of atmospheric convection to evaluate the effects of noise and coupling strength on information flow (i.e., transfer entropy (TE)). The Lorenz system is described by three differential equations:

$\frac{dx}{dt} = \sigma(y - x), \frac{dy}{dt} = x(\rho - z) - y, \frac{dz}{dt} = xy - \beta z$[4]

where x is the convective velocity, y is the vertical temperature gradient, and z is the heat flow, $\sigma$is the Prandtl number (dimensionless ratio of momentum diffusivity/thermal diffusivity), ρ is the Rayleigh number (dimensionless parameter that measures the fluid instability arising because of temperature and density stratification with change in depth), and β is the parameter describing the horizontal wave number of convective motions.

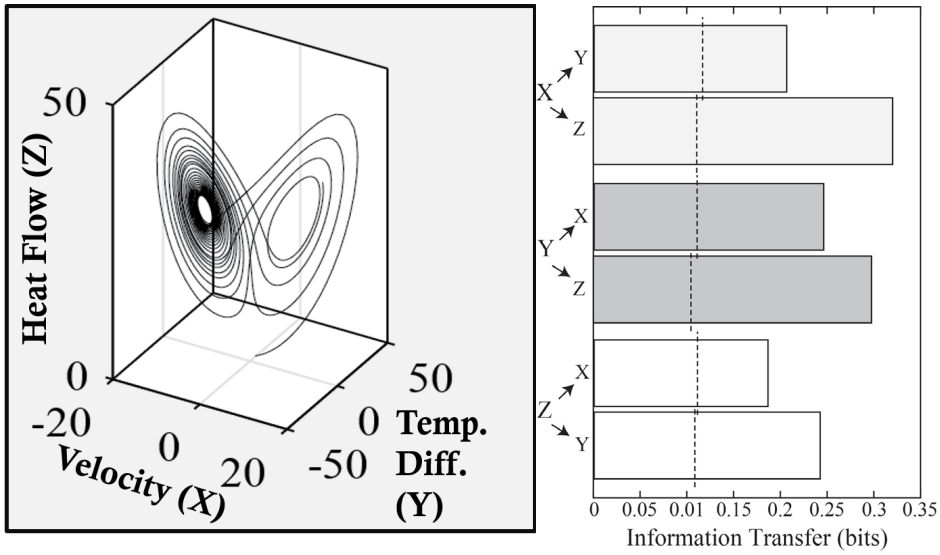

Figure 1.2: (A) The Lorenz system with σ =10, ρ = 8/3, and β = 28 and (B) pairwise information flow between X, Y, and Z with 98% statistical confidence levels (dashed lines).

TE for identifying the driving component and feedbacks

We initially computed information flow between all X, Y, and Z pairs (Figure 1.2) to demonstrate that TE was able to identify the driving component and feedbacks. By comparing the strength of directional information flow of each variable pairs. Y has stronger information flowing into X and Z than those receive from them. We see that TE correctly identifies y, the vertical temperature gradient, as the main system driver as it sets up the convective velocity (X) and subsequent heat flow (Z); this is evidenced by the fact that Y contributes the greatest amount of information among all the "system pairs".

TE for resolving causal relationships with increasing noise

We now test the ability of TE to resolve causal relationships as the noise within the system progressively increased. This can be formulated T as follows, Z_t = G(Z_{t-1} + $\in_{Oberservational+process}$), where G(Zt-1) is the noise-free map (Lorenz system) and is error-free in that no noise has been added and $\in_{Oberservational+process}$is the noise that is introduced both through observational (i.e., instrumental) error and process error. In this experiment, noise was progressively added to the system by adding white noise with an increasing standard deviation (described as relative noise in the figure below). We see that TE is quite sensitive to noise (Figure 1.3) where relatively low levels of noise affect its ability to resolve causal pairs. Because all of the results presented in our TE analysis (Figures 1.2 – 1.3) were highly significant we have high certainty in the technique for resolving causal interactions.

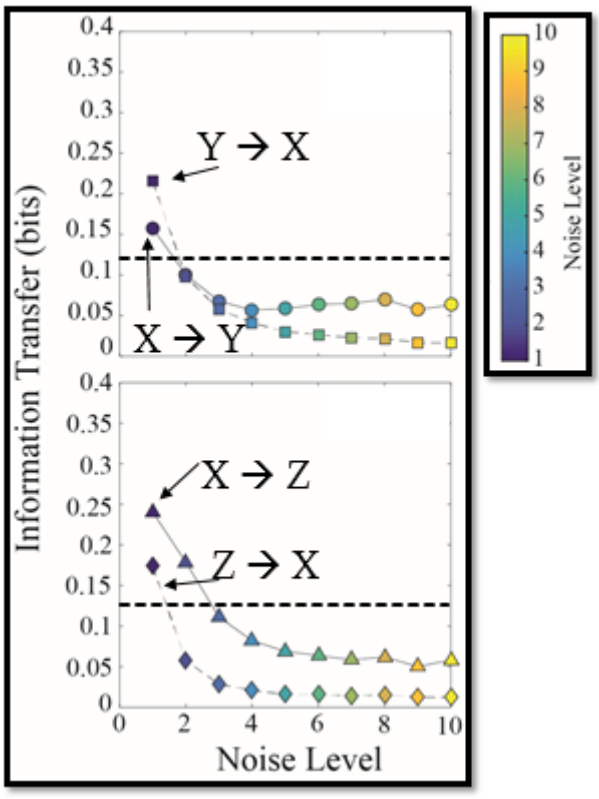

Figure 1.3: The influence of noise on information transfer between x and z in the Lorenz system. The dashed line shows 98% confidence level(s) and the noise level refers to the relative standard deviation of the white noise added as the Lorenz system was solved.

The application in earth system over multi-spatial and temporal scales

Function reconstruction using transfer entropy and statistical learning models (Chapter 2)

Transfer entropy (TE) can identify the critical time lags, information flow directions, relative strength among variables in a complex system. In this section, we discuss how to use the results from a TE analysis can help with function reconstruction. We explain how TE analyses identify the critical predictors, linearity, power of the non-linear terms and critical time lags. With this information, we use statistical learning models, like LASSO (Least Absolute Shrinkage and Selection Operator), random forest regression and support vector machine, to reconstruct the function by learning from the data. The R-square of test dataset in our analysis reaches 99%. We then implement this approach in a real earth system science problem, streamflow prediction, as a case study. Our findings suggest that while information-flow identifies dominant streamflow controls, the results should not be limited to only “critical hydrologic timescales;” rather they should guide a range of timescales over which inputs, stores, and losses are filtered into catchment discharge.

Regional and yearly scale problem (Chapter 3)

Coastal river deltas are complex and dynamic ecosystems where vegetation plays an essential role in influencing, as well as being influenced by, physical processes, creating ecogeomorphic feedbacks between vegetation species and topography. However, this feedback is poorly understood. This knowledge gap is due to difficulties in detecting and quantifying the interactions that define the feedback. Emerging technology and data analysis techniques like transfer entropy have made it possible to overcome former difficulties associated with sampling constraints and delineate bi-directional feedback within many vegetation classes at the delta scale. Here, the transfer entropy analysis was consistent with widespread understanding of marsh zonation, yet produced additional insight into which vegetation classes specifically had a dominant impact on topographic change. Ecogeomorphic feedback was resolvable only within native vegetation classes (Nelumbo and Polygonum) that occur over low to moderate elevations within the Wax Lake Delta. In contrast, nonnative vegetation classes (Colocasia and Eichhornia) are not as effective at accreting sediment as native classes. The transfer entropy analysis suggests that different vegetation communities play functionally different roles in landscape evolution that should be differentiated in ecogeomorphic models. Within such models, it would be most imperative to resolve detailed flow characteristics at lower to low-middle island elevations. Furthermore, within elevation zones, it is likely important to differentiate between the roles of multiple vegetation communities rather than treating the entire elevation zone as a single ecogeomorphic entity.

Global and millennium scale problem (Chapter 4)

Earth's climate system is controlled by multiple external forcings and internal dynamics, including orbital variations (Hays, Imbrie, and Shackleton 1976), greenhouse gases (Shakun et al. 2012; Petit et al. 1999), and atmospheric aerosols (Lambert et al. 2008). Because of the complexity and nonlinearity of the climate system, characterization of the relative contributions (causation) of each factor, and their interactions, to climate change is incomplete. Here, we quantify information exchange between orbital variations, greenhouse gases, atmospheric aerosols, and air temperature to attribute causal relationships and for the first time provide a network map showing the direction and strength of climate system feedbacks over a range of timescales. We show that, during the past 420,000 years, orbital forcings trigger temperature and CO2 responses at short (5 kyr) time lags. Over longer timescales, an internal feedback, mediated by interactions with dust, also plays a significant role in governing temperature and CO2 concentrations. The relative importance of the drivers engaged in this tripartite feedback shifts with timescale. At the shortest lags (5-25 kyr), CO2 drove temperature changes and dust abundance. However, at longer lags (26-55 kyr), dust assumed the role as a driver, mediating temperature and CO2 feedbacks. The short-term influence of CO2 on temperature was stronger than dust's long-term impact, consistent with on radiative forcing (Claquin et al. 2003; Takemura et al. 2009). However, dust remained an important driver of temperature over 50-kyr time lags, the amount of time between sequential glacial maxima and minima during the latter portion of the Pleistocene. We

hypothesize a mechanism whereby dust supplies essential micronutrients to enhance marine and terrestrial productivity (Martin 1990; Yu et al. 2015). Therefore, at longer timescales, temperature was controlled by dust via its strong effects on CO2. Challenging previous findings, we demonstrate that the relationship between dust and temperature was not synchronous (Lambert et al. 2008; Martínez-Garcia et al. 2011), but instead was highly dynamic: initially being weak, progressively strengthening, and finally dominating at long timescales.

Global and decadal scale problem (Chapter 5)

Climate teleconnection often interacts with local precipitation feedbacks and thus raise critical challenges in quantitatively partitioning the driving factors of regional precipitation variation. For example, for West Sahel precipitation, two interacting mechanisms are widely studied: 1) warming SSTs weaken the land-ocean temperature contrast and force deep convection towards the ocean (Giannini et al., 2003), leading to reduction in continental moisture convergence, with its impacts intensified by 2) variation in moisture-driven vegetation interactions induced by the interrupted recycling of moisture through precipitation and evapotranspiration (Zeng et al., 1999).

However, most of the previous work only test the correlation between remote/local climate factors and the precipitation over the region of interest; and map the spatial distribution of the correlation. Linear correlation theoretically failed due to two major reasons: (1) climate system is highly nonlinear; (2) The effect on precipitation from climate factors is not necessary happened immediately, it could have time lag before anomalies 'effect reach different location and cause the change in precipitation (Schepen et., al 2011). Meanwhile, transfer entropy method is ideal to analysis the time lagged correlation between climate factors and precipitation. It has been proofed effective and efficient in a broad range of research (Vicente et., al 2011; Rubinov and Sporms 2010; Verdes 2005; Kleeman 2007; Hannisdal and Peters 2011). The time lag could be easily introduced into this computation to detect the effect time lag in analyzing these correlations (Schreiber 2000; Ruddell and Kumar 2009).

We quantitatively demonstrate that (1) Sea Surface Temperature (SST) over the Gulf of Guinea controls moisture advection and transport to the West Sahel region; (2) strong bidirectional interaction exist between local vegetation dynamics and rainfall patterns. (3) We assess the directional interaction patterns from nine state-of-the-art Earth System Models (ESMs). We find that most of the ESMs are able to represent either the uni-directional control of SST on precipitation or the bi-directional interaction between vegetation and precipitation. (4) The climate indices in the Pacific Ocean have a relatively short time lag (0-3 months) with significant transfer entropy in west coast and have relatively intermediate ones (4-7 months) in the middle and long ones (more than 7 months) in east coast. (5) In Pacific Ocean, the time lag spatial distribution of transfer entropy from climate indices to precipitation has a strong correlation with the distance between the region that climate indices measured and U.S. mainland.

Chapter 2: Identifying critical lags τ using Transfer Entropy and application in reconstruction of non-linear function

Transfer entropy helps with identifying non-linear terms

Traditional time-series data analysis is the study in the time domain. For complex systems, time-series data should additionally be analyzed in phase space; the reconstruction of the phase space of the time-series data of a complex system (e.g., the climate system) is an essential step in understanding the system because of the establishment of the complex system models and the prediction of the future status are all performed in the phase space (Packard et al., 1980). Packard proposed a technique for reconstructing phase space pictures from observations of a single coordinate of any dissipative dynamical system (Packard et al., 1980). To reconstruct the space phase, two parameters, the dimensions d and the time lag of each dimensions τ, need to be identified. In this section, we will discuss how to identify time lag τ and then in the following section, discuss how to identify the dimension d.

In this section, we will compare the effectiveness of the transfer entropy (TE) and lagged correlation methods in identifying a critical time lag in a system where one variable affects the other variable. Additionally, we will compare the effectiveness of the TE method and autoregressive models in identifying critical time lags in a system where one variable affects itself in a longer time scale.

For the first comparison, we established three scenarios:

The variable X linearly affects variable Y in multi-temporal lags. X is randomly generated from $\mathcal{N}(0,1)$.

Scenario 1: $Y_t = 2X_{t-42\triangle t} + 7X_{t-33\triangle t} + \varepsilon$ [2.1]

The variable X affects variable Y in multi-temporal lags in both linear and non-linear ways

Scenario 2: $Y_t = 8X^{1.71}_{t-42\triangle t_t} + 7X_{t-33\triangle t} + \varepsilon$ [2.2]

The variable X non-linearly affects variable Y in multi-temporal lags.

Scenario 3: $Y_t = 1.5X^{0.67}_{t-42\triangle t_t} + 0.7X^{1.3}_{t-33\triangle t_t} + \varepsilon$ [2.3]

Where Y_t is the current value of time series data Y, $X_{t-42\triangle t}$, for example, is the historical value of time series data X in 42 unit-time ago, ε is the error term following $\varepsilon \sim \mathcal{N}(0,1)$.

The lagged correlation method is a method to calculate the correlation coefficients between the sink variable (Y) and the shifted source variable (X). It shifts the source variable by multi different time lag and calculates the correlation coefficients respectively.

The results are shown in the following figure.

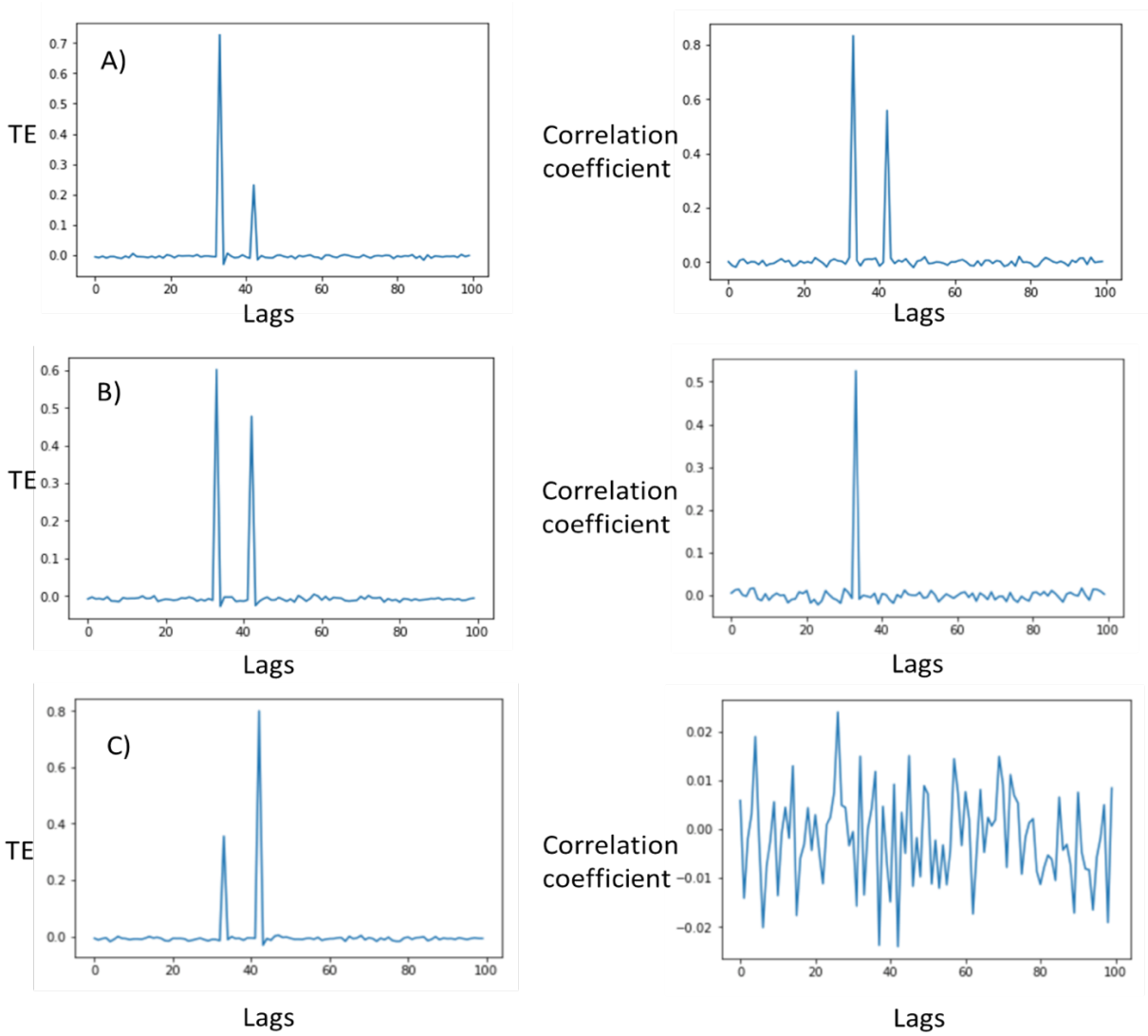

Figure 2.1. Results of transfer entropy analysis and lagged correlation analysis. A) both transfer entropy and lagged correlation could identify the critical time lag 42 and 33. B) transfer entropy could identify both the linear term lag 42 and the non-linear term lag 33. The lagged correlation method could only identify the linear term lag 42. C) transfer entropy could identify both the non-linear terms with lags 42 and 33. Lagged correlation is unable to identify any significant signals.

In scenario 1 (Figure 2.1 A), both transfer entropy and lagged correlation method are able to identify the critical time lag 42 and 33. In scenario 2 (Figure 2.1 B), transfer entropy identified both the linear term lag 42 and the non-linear term lag 33. The lagged correlation method could only identify the linear term lag 42. In scenario 3 (Figure 2.1 C), transfer entropy identified both the non-linear terms with lags 42 and 33. However, the lagged correlation method is unable to identify any significant signals.

Chapter 2: Identifying critical lags τ using Transfer Entropy and application in reconstruction of non-linear function

We have tested the effect from one source variable to the sink variable. We now explore how transfer entropy performs in an autocorrelated system. Here we use the time-series data X_t from the Lorenz system generated by the function 1.4.

The variable X will affect Y and Z, and meanwhile, Y and Z will also affect X. This constitutes a system with variables indirectly affecting themselves in the longer time scale.

The result of the transfer entropy analysis and autocorrelation is shown in figure 2.2.

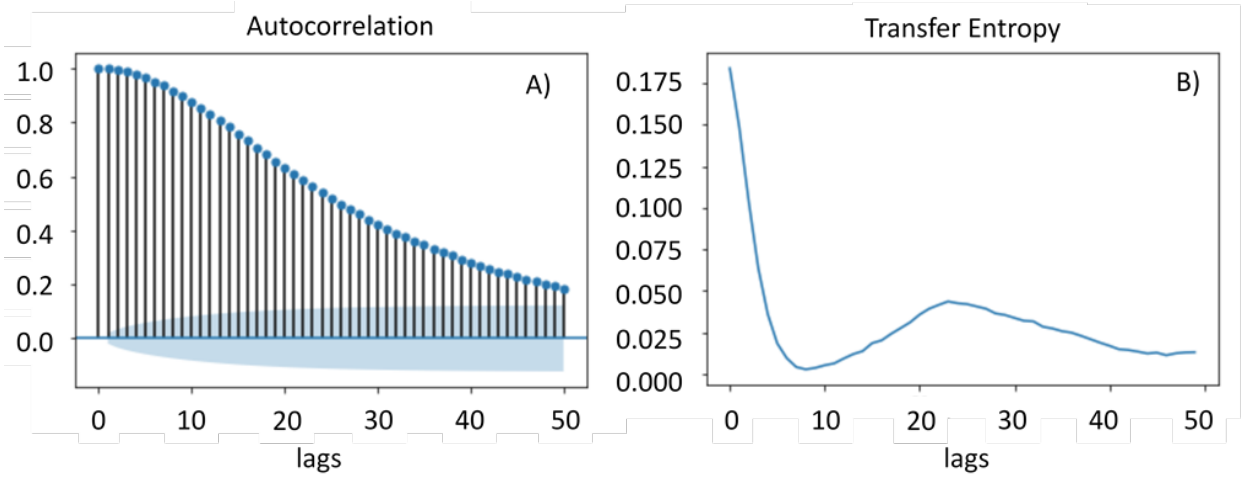

Figure 2.2. A) Results of autocorrelation analysis up to 50 units time lags. B) Transfer entropy analysis up to 50 units time lags.

In constructing a nonlinear time series system, appropriate delay time must be identified. However, traditionally used methods, like autocorrelation, cannot treat the nonlinearity appropriately and may yield incorrect values (Kim et al. 1999). The result of transfer entropy shows that the variable X has strong feedback to itself in a short time lag scale (less than 10 units time) which is supported by the autocorrelation analysis. However, in the longer time scale, there is a valley around 10-unit time lag and a peak around 20-30-unit time lag. This finding agrees with previous analysis using the correlation integral and first local minimum of the mutual information (Kim et al. 1999; Abarbanel et al., 1993), which is caused by loop effects among X, Y, and Z. However, the autocorrelation method is not able to identify these critical time lags.

Function Reconstruction with Transfer Entropy and LASSO

In the previous session, transfer entropy was used to identify the strength, directionality and the time lags of the information flow (or effect from one variable to another) in several examples of systems that are complex in different ways. To further study the system, our next step is to estimate the strength of each coupling and calculate the coefficients. In this session, LASSO (Least Absolute Shrinkage and Selection Operator) is implemented with the results from a transfer entropy analysis to calculate the coefficients in a complex system introduced by Rober Tibshirani (Tibshirani 1996). LASSO is an extension of ordinary least squares, which considers a penalty to the residual sum of squares equal to the sum of the absolute values of the non-intercept beta

coefficients. The penalty will be multiplied by parameter λ that slows or accelerates the process. As the λ increase, the coefficients of the least associated variables shrink to zero more quickly than the coefficients of the more strongly associated variables. Thus, LASSO has the ability to select the critical variables and help with identifying the dimension d.

To increase the abilities to predict and interpretation, LASSO is characterized as a regression with variable selection and regularization. It is originally formulated from least squares method with an L1 norm penalty.

$$\sum_{i=1}^{n}(y_i - \beta_0 - \sum_{j=1}^{p}\beta_j x_{ij})^2 + \lambda \sum_{j=1}^{p}|\beta_j| \quad [2.4]$$

The L1 penalty has the effect of forcing some of the coefficient estimates to be exactly equal to zero when the parameter λ is sufficiently large. Hence, models generated from the LASSO are much more interpretable than other traditional methods. LASSO usually perform better in a setting where a relatively small number of variables with substantial coefficients (James, Witten, et al., 2013). This setting matches the situation in most complex earth systems (Chatterjee, Steinhaeuser et al., 2012).

LASSO regression is extended by adding extra predictors, which are obtained by raising each of the original predictors to a power. Given the results from transfer entropy, we only add the extra predictors with significant entropy transferred to y.

Lastly, given the results from transfer entropy, we also add the predictors with the responding time lags shifted for taking lagged effect into consideration.

In our test case. Random variable X is generated from $\mathcal{N}(0,1)$ Y is calculated by the following equation:

$$y = 0.42x_{t-42\Delta t}^{3.3} + 1.12x_{t-33\Delta t} + 1.53x_{t-27\Delta t}^{0.86} + \varepsilon \quad [2.5]$$

We use transfer entropy, lagged correlation and LASSO to reconstruct the functions and their coefficients.

First, we randomly select 80% of the data as the training data, and then implement the transfer entropy on the time-series train data X and Y.

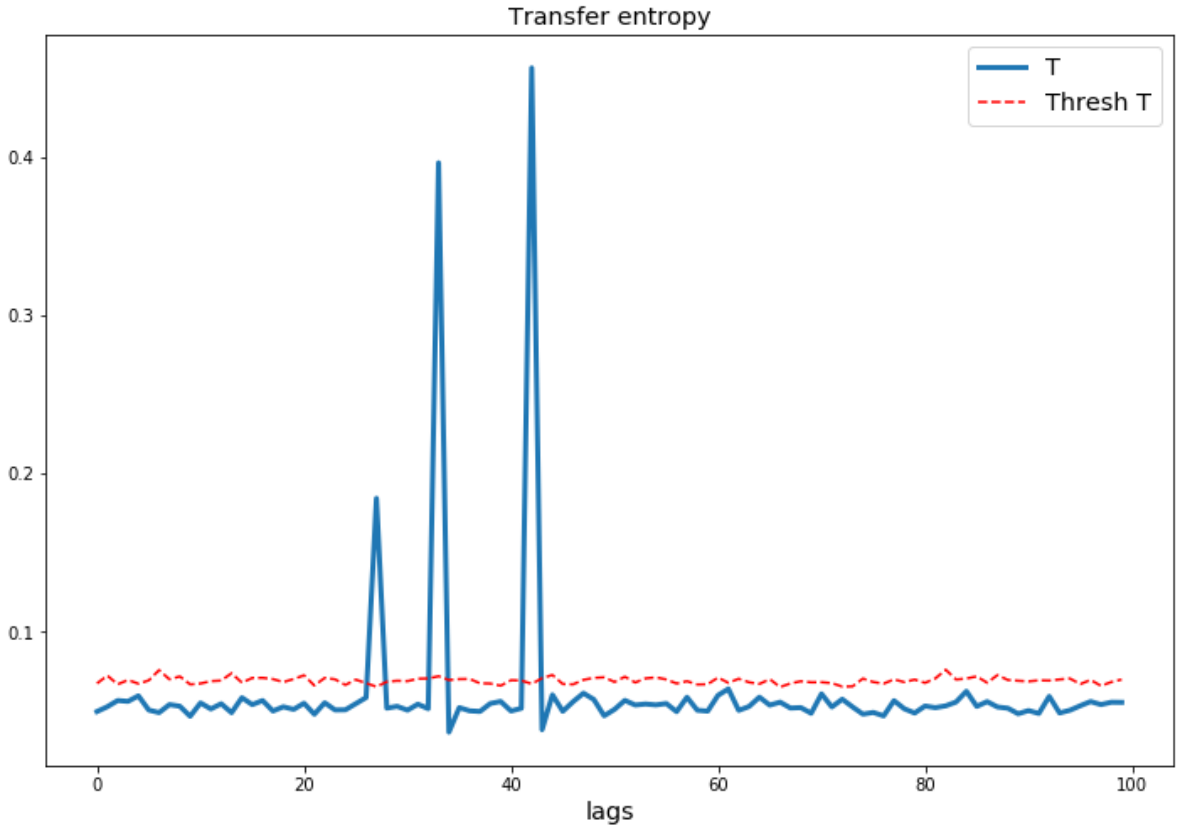

Figure 2.3. Results of transfer entropy analysis at lags from 0 unit time to 100 units time are shown in solid blue line. The thresholds with 95% confidence are shown in the red dash line.

The results show that there are three critical time lags. They are 27, 33 and 42, which is same in the target function.

Then we use the lagged correlation method to find any of the time lags are the linearly associated with y.

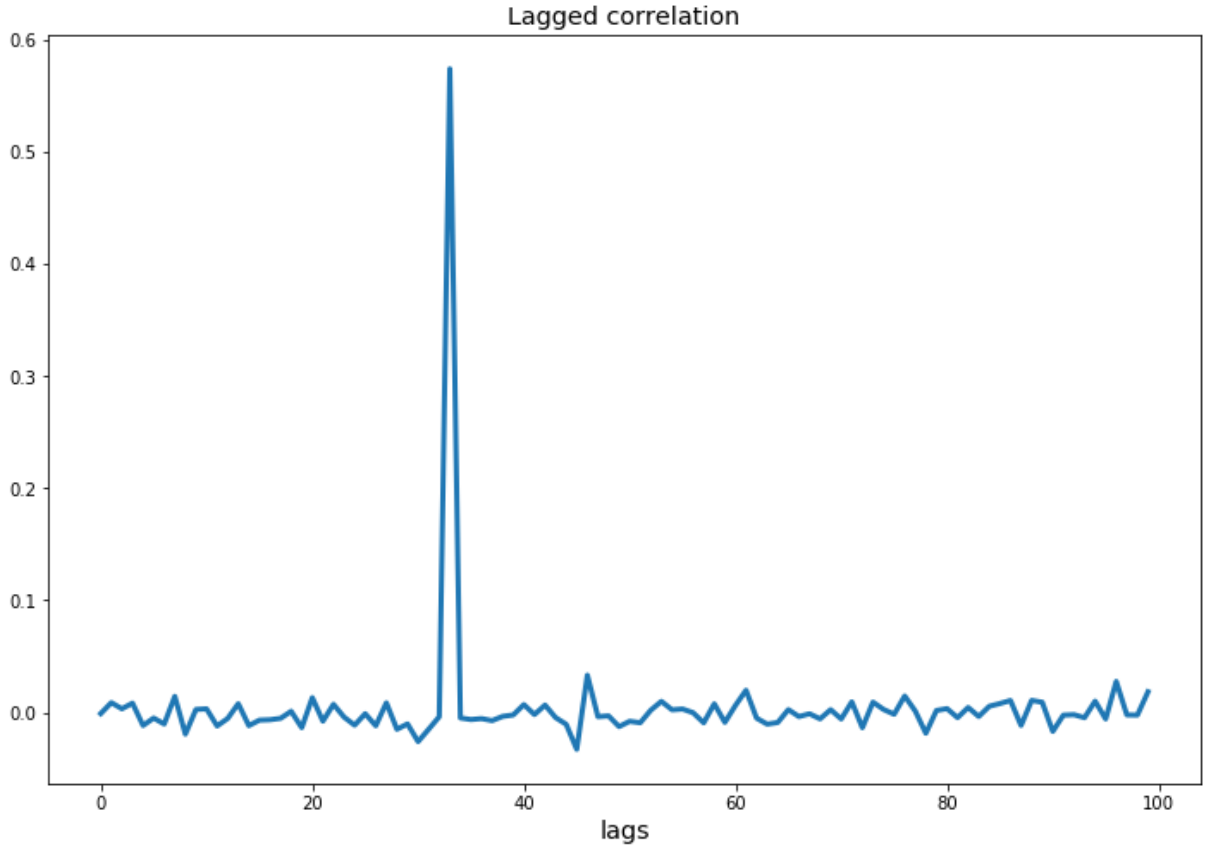

Figure 2.4. The result of lagged correlation analysis at lags from 0 unit time to 100 units time are shown in solid blue line.

In comparing the results of the lagged correlation analysis and transfer entropy analysis, we see both methods are able to detect lag 33, but lag 27 and lag 44 are only detected by transfer entropy. This is suggesting that lag 33 has a linear relationship with the target while lag 27 and lag 44 have a non-linear relationship.

To reconstruct the function, we use LASSO regression on modified predictors given the results from the previous analysis. We generate the possible representative non-linear terms of X with lag 27 and 42. Moreover, then lagged the predictors in temporal scale according to the results from transfer entropy analysis.

To identify the power of the nonlinear term, we calculate the mutual information between multiple potential representative non-linear terms and target variable Y. We begin with a rough search and only include the integer power for the potential representative non-linear terms, which is from -4 to 4 in this test case. Critical mutual information (threshold calculated at 95% confidence level subtracted from mutual information) for each power number are shown in the following figure 2.5.

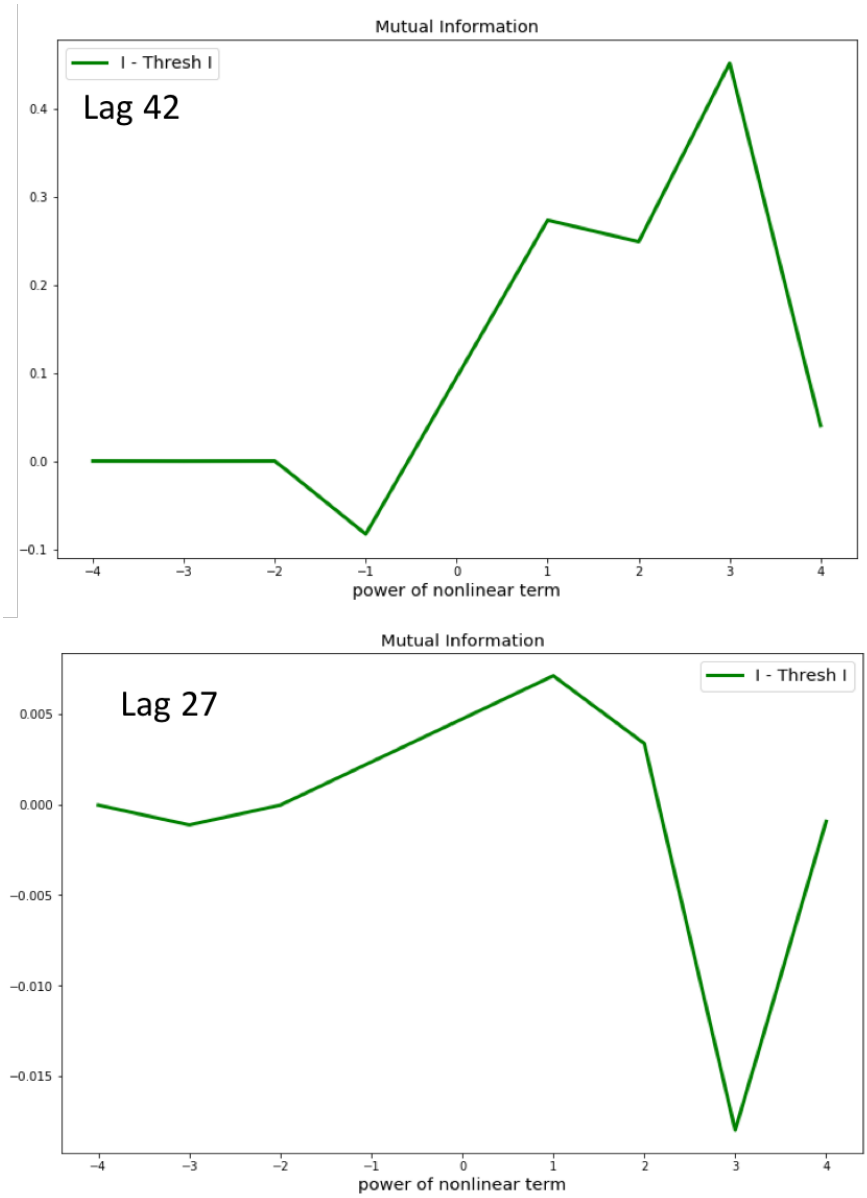

Figure 2.5. Critical mutual information (threshold calculated at 95% confidence level subtracted from mutual information) of each power number in rough search. For lag 42, the peak of critical mutual information is located around the power of 3. For lag 27, the peak of critical mutual information is located around the power of 1.

From the rough search, we find that for lag 42 and lag 27 the nonlinear terms have power around 3 and 1, respectively. Then we conduct the fine search around the peak power. Here we use linear space search with the step of 0.125. Critical mutual information of fine search is shown in the following figure.

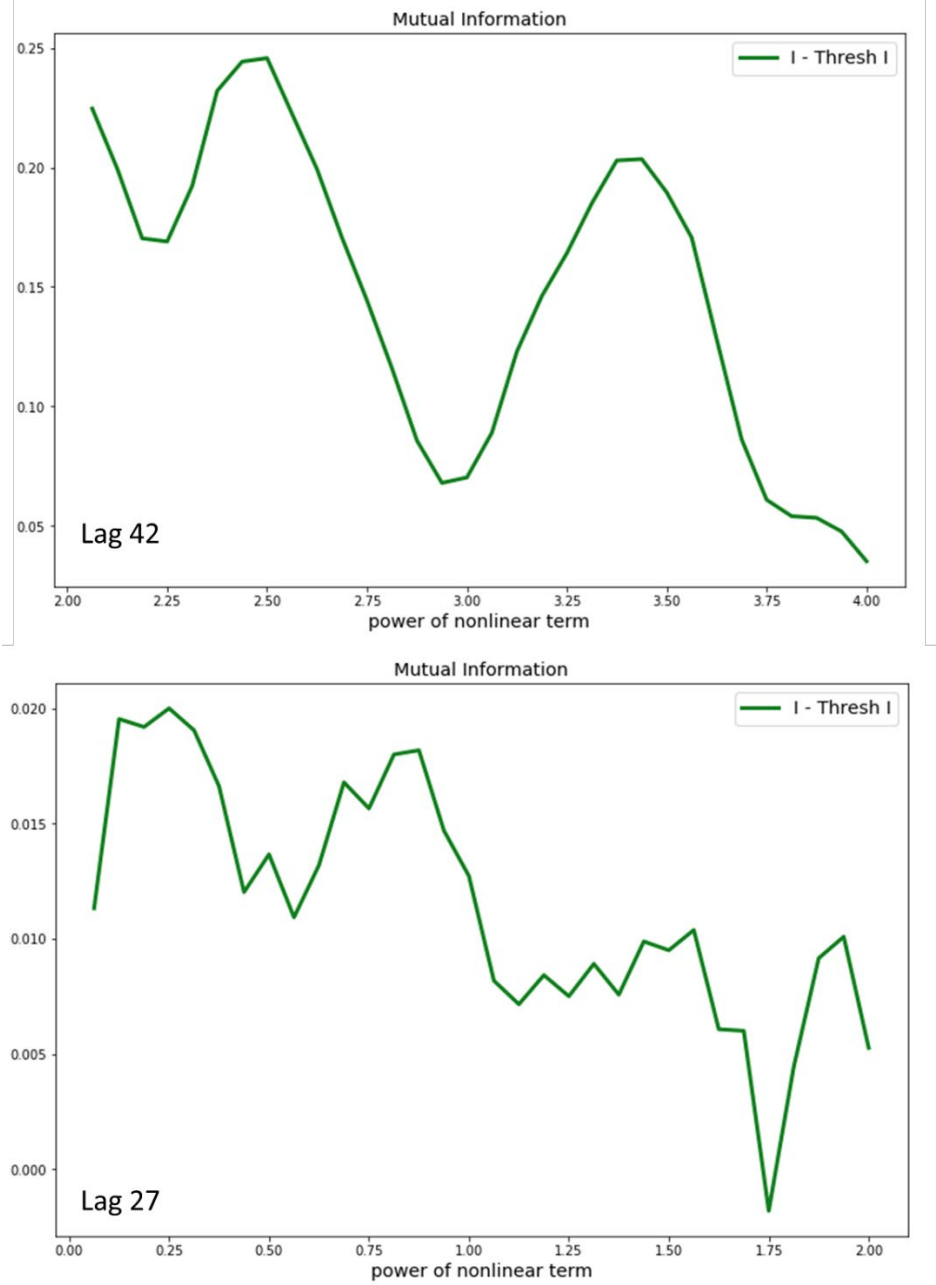

Figure 2.6. Critical mutual information (threshold I calculated at 95% confidence level is subtracted from mutual information) of each power number in fine search. For lag 42, the peak of critical mutual information is located around power 2, 2.5, and 3.4375. For lag 27, the peak of critical mutual information is located around the power of 0.125, 0.25, and 0.875.

From the fine search, we find three peaks around the power of 2, 2.5 and 3.4375 for lag 42. For lag 27, the results are much noisier than lag 42. This could be caused by the relatively high strength of noise comparing with lag 42. We select the top four peaks in lag 27 fine search, which is the power of 0.125, 0.25, and 0.875.

Chapter 2: Identifying critical lags τ using Transfer Entropy and application in reconstruction of non-linear function

Here we list several potential representative non-linear terms for each lag and combine them with the lagged linear term.

The predictor for LASSO will be:

$$X_{t-27\triangle t}, X_{t-33\triangle t}, X_{t-42\triangle t}, X_{t-27\triangle t}^{0.125}, X_{t-27\triangle t}^{0.25}, X_{t-27\triangle t}^{0.875}, X_{t-42\triangle t}^{2}, X_{t-42\triangle t}^{2.5}, X_{t-42\triangle t}^{3.4375}$$

The coefficients (after normalization) of each predictor in the LASSO regression, as λ decrease, are shown in the figure 2.7. The predictors that survive with higher λ usually represent higher importance in function reconstruction.

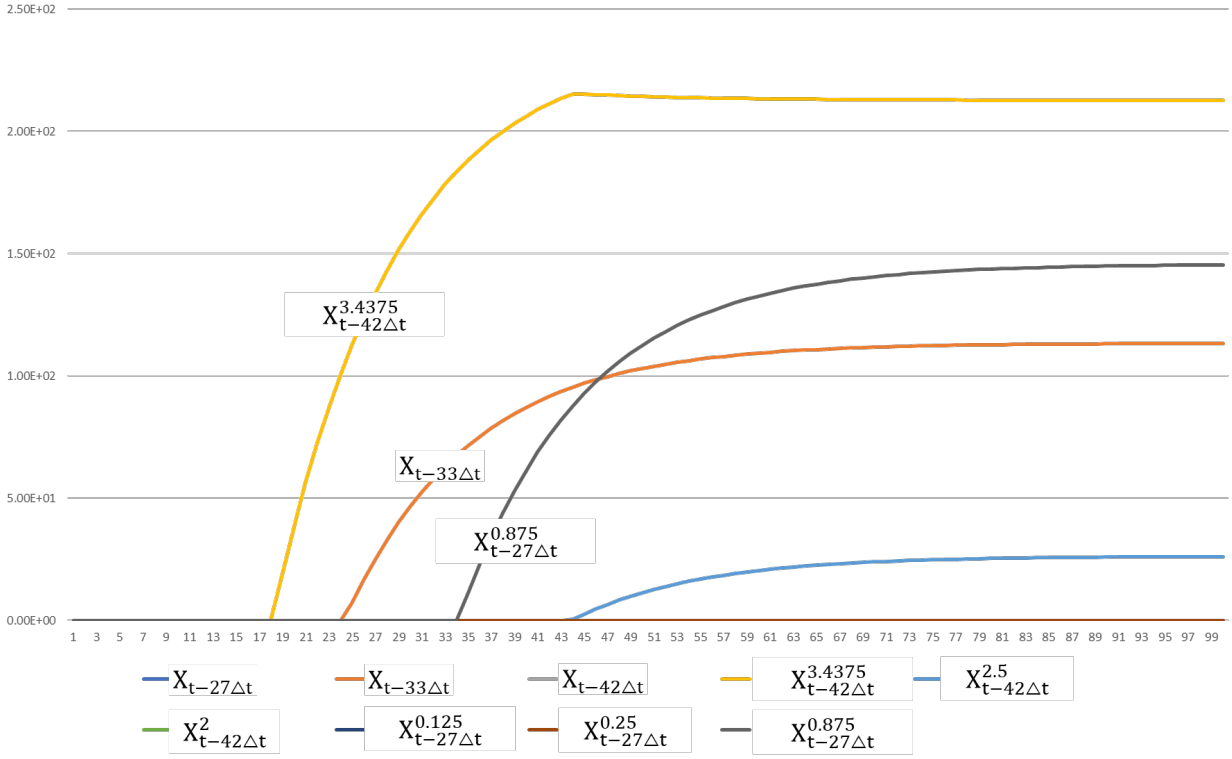

Figure 2.7. LASSO coefficients as a function of different level regularization.

The most significant terms of each time lag representation are $X_{t-42\triangle t}^{3.4375}, X_{t-33\triangle t}, and X_{t-27\triangle t}^{0.875}$.

Next, we use ordinary least square to predict y on these three predictors. The constructed values including lags, the power of each term and coefficients are shown in the following table.

Table 2.1. The comparison of construed coefficients and the true coefficients.

Variable	Constructed Value	True Value	Error rate
First lag	27	27	0.0%
Second lag	33	33	0.0%
Third lag	42	42	0.0%
Power of $X_{t-27\triangle t}$	0.875	0.86	1.7%
Power of $X_{t-33\triangle t}$	1	1	0.0%

Power of $X_{t-42\triangle t}$	3.43	3.3	3.9%
Coefficient of $X_{t-27\triangle t}$	1.51	1.53	1.3%
Coefficient of $X_{t-33\triangle t}$	1.12	1.12	0%
Coefficient of $X_{t-44\triangle t}$	0.38	0.42	9.5%

The constructed function is:

$y = 0.38x_{t-42\Delta t}^{3.43} + 1.12x_{t-33\Delta t} + 1.51x_{t-27\Delta t}^{0.875}$[2.6]

We use the 20% data that had intentionally been left out to compare the reconstructed value and the true value. The scatter plot and its R square value are shown in figure 2.8.

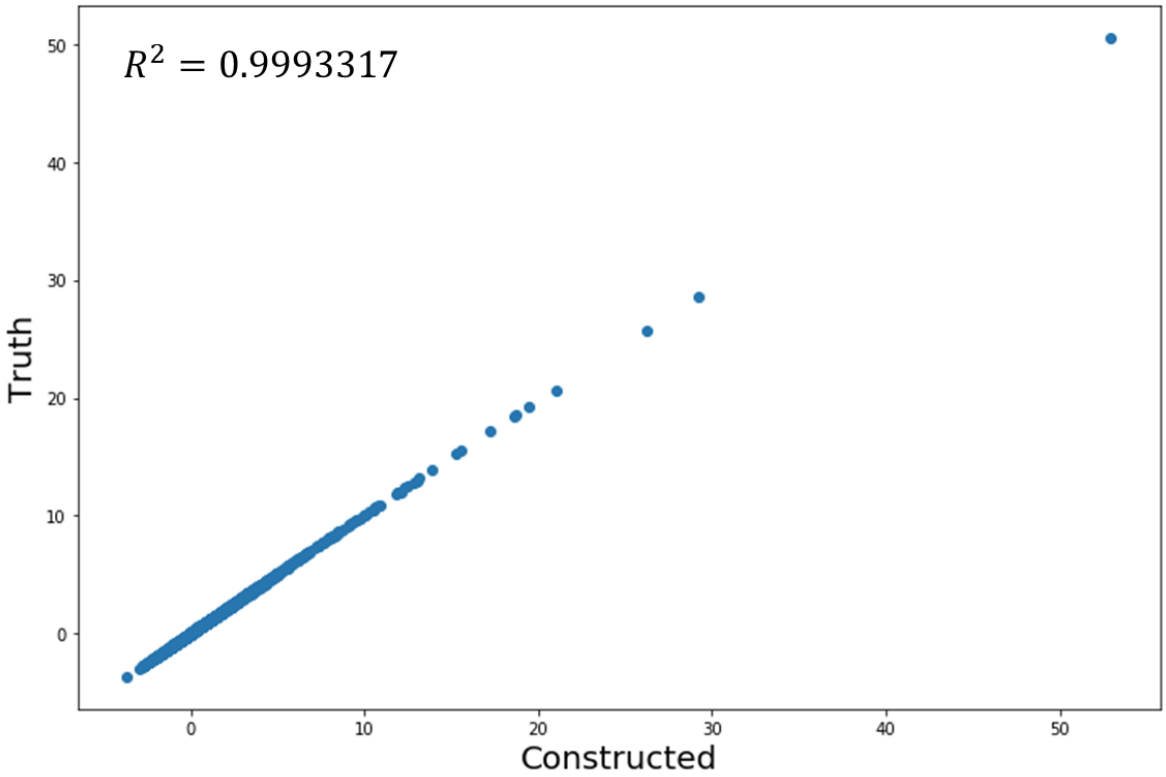

Figure 2.8. The scatter plot of constructed value and truth value, the R square value is 0.99.

We have shown that using transfer entropy and LASSO can help with function reconstruction. However, here we only considering the individual terms. In future work, the combination of multiple different terms should be taken into consideration.

In the appendix section, we test how transfer entropy helps with identifying critical time lags, non-linear terms and aggregation scales, and how it can be used with other machine learning models. This is done with a study case in prediction discharge using climatological and hydrological data.

Chapter 2: Identifying critical lags τ using Transfer Entropy and application in reconstruction of non-linear function

Formulating accurate streamflow forecasts is important for flood management, resource planning, and validation of hydrologic theory. However, forecasts often perform poorly because of improper representation of hydrologic response timescales in underlying models. Here, we test emerging tools from information theory to identify critical hydrologic response timescales using high-quality sensor data from the Dry Creek Experimental Watershed, ID, USA. We hypothesized that machine learning models informed by information-flow analyses could identify the dominant drivers of discharge and their timescales and outperform uninformed models developed through expert judgment or trial-and-error. Consistent with previous mechanistic studies, information-flow revealed that snowpack accumulation and partitioning into melt, recharge, and evaporative loss dominated discharge patterns. The informed models, driven by the time lags of predictor variables selected through information-flow, exhibited improved forecast skill relative to uniformed models that lacked lagged inputs, but only for the lowest 48 dimensionality models at short aggregation timescales (1 day-2 weeks). While the informed models captured the dominant process—seasonal snowmelt—they ultimately did not perform as well as the uniformed models, which disagree with our original hypothesis. We suggest that the uniformed models, not constrained by the lags of the dominant processes, more effectively represented variable interactions playing a critical role in translating rainfall or melt into streamflow across a range of time scales. Our findings suggest that while information-flow identifies dominant streamflow controls, the results should not be limited to only "critical hydrologic timescales;" rather they should guide a range of timescales over which inputs, stores, and losses are filtered into catchment discharge. (See Appendices)

Chapter 3: Ecogeomorphic Feedbacks that Grow Deltas*

* Ma, H., Larsen, L. G., & Wagner, R. W. (2018). Ecogeomorphic Feedbacks that Grow Deltas. Journal of Geophysical Research: Earth Surface, 123(12), 3228-3250.

1 Introduction

Vegetation is one of the primary geomorphic agents on the Earth surface, converting solar energy into geomorphic forces via photosynthesis(Phillips 2009). As an "ecosystem engineer," vegetation can exert control over geomorphic processes through biomechanical and biochemical impacts on sediment and soil (Butler 1995, Corenblit and Steiger 2009). Plant community composition and species distributions are affected by climate, physical processes such as seed transport (hydrochory) and scour, and geomorphology, particularly elevation relative to water level, which controls exposure to wave energy and root oxygen (Johnson, Sasser et al. 1985, Cahoon, White et al. 2011). Meanwhile, vegetation can influence geomorphology via sediment trapping through enhanced settling or direct interception, and stabilization of the substrate (Edmonds and Slingerland 2010, Cahoon, White et al. 2011, Paola, Twilley et al. 2011, Lorenzo-Trueba, Voller et al. 2012, Marani, Da Lio et al. 2013, Rosen and Xu 2013), though preferential routing of flow around vegetation patches can also induce scour (Temmerman, Bouma et al. 2007, Vandenbruwaene, Temmerman et al. 2011) and reduce net sedimentation (Nardin and Edmonds 2014).

The relative magnitude of biotic and abiotic forcing governs whether bidirectional ecogeomorphic feedback develops or whether vegetation simply responds to abiotic forcing, or vice-versa. On floodplains, the potential for ecogeomorphic feedback and vegetation to serve as an ecosystem engineer is generally maximized at intermediate elevations in close proximity to the channel, where flow is of sufficiently low energy or frequency to allow for colonization of vegetation, yet inundation is frequent enough that the vegetation interacts with fluvial processes (Gurnell, Bertoldi et al. 2012, Gurnell 2014). Likewise, in coastal deltaic and estuarine environments, marshes represent areas with large potential for ecogeomorphic feedback (van de Koppel, Bouma et al. 2012). In these environments, topography often acts as the primary factor impacting vegetation species distributions (White 1993, Cahoon, White et al. 2011). In turn, vegetation may play a critical role in promoting sedimentation and lateral expansion, even in areas experiencing regional subsidence (Reed 2002, Rosen and Xu 2013). Failing to account for the bidirectional nature of these feedbacks in planning restoration or management of these environments may have dire consequences. For example, recent work suggests that studies that do not account for the enhanced sediment trapping ability of macrophytes under high levels of inundation vastly overestimate future tidal marsh area loss to sea-level rise, but that to avoid inevitable loss, marshes may require accommodation space for inland transgression (Kirwan, Temmerman et al. 2016, Schuerch, Spencer et al. 2018). In contrast, pessimistic estimates of marsh loss based on an understanding of marshes passively responding to inundation may prevent implementation of relatively simple conservation or restoration measures (e.g. setting aside conservation zones landward of marshes, sediment augmentation) that could evade this outcome. Conversely, knowledge that vegetation is dominated by elevation-related forcing rather than engaging

in bidirectional feedback could emphasize the sensitivity of vegetation plantings to elevation gradients in a marsh restoration design.

Although ecogeomorphic feedback between vegetation and topography in general has been well studied in many ecosystems, such as rivers, coastal dunes and salt marshes (Stallins 2005, Corenblit, Tabacchi et al. 2007, Corenblit and Steiger 2009, Gurnell, Bertoldi et al. 2012, Balke, Herman et al. 2014, Vinent and Moore 2015, Eichel, Corenblit et al. 2016), understanding of distinct geomorphic roles of different species or communities remains limited. Physiological differences and diverse life-history strategies cause salient differences in how vegetation species respond to and modify abiotic forcing, referred to by Diehl et al. (2017) as biological-response traits and morphological-effect traits, respectively. For example, stem density is a morphological-effect trait that serves as a first-order control on local flow velocities and turbulence intensities and, together with flow velocities, determines patterns of erosion or deposition within or around the vegetation patch (Bouma, Friedrichs et al. 2009, Follett and Nepf 2012, Yager and Schmeeckle 2013, Diehl, Merritt et al. 2017). Although the morphologic arrangement of stems near the bed is particularly important as a control on bed shear stress, the configuration of stems higher in the water column (e.g., branching, upright) is secondary to stem density in its control on flow (Heuner, Silinski et al. 2015), though horizontal leaves can significantly enhance local sedimentation (Pluntke and Kozerski 2003). Further, vegetation that accumulates epiphytic biofilm may trap sediment more effectively than vegetation with bare stems (Coniglio and James 1985, Wharton, Cotton et al. 2006). Another important morphological-effect trait is stem flexibility (Luhar and Nepf 2013). Flexible submersed vegetation that bends over in high flow tends to impart less drag on the flow, produce more turbulent kinetic energy, and induce less sedimentation than rigid emergent vegetation (Heppell, Wharton et al. 2009, Ortiz, Ashton et al. 2013, Liu, Hu et al. 2017). Meanwhile, an ecological-response trait with geomorphic consequences is the ability to germinate and grow rapidly, which uniquely imbues pioneer species with the potential to occupy and stabilize flood-prone environments such as channel point bars or the marsh-mudflat interface (Perucca, Camporeale et al. 2006, Van der Wal, Wielemaker-Van den Dool et al. 2008, Gurnell, Bertoldi et al. 2012).

Increasingly, aquatic vegetation species and communities are categorized and catalogued by their biological-response and morphological-effect traits (Stallins 2006, Merritt, Scott et al. 2010, O'Hare, Mountford et al. 2015), but little has been done to quantify or catalogue the ecogeomorphic feedbacks or forcings into which these traits translate for specific species (though see the reviews of Folkard, 2011 and Curran and Hession, 2013, which focus on the geomorphic roles of vegetation in streams and floodplains). In part, this research gap is due to a dearth of robust, field-testable techniques to quantify the strength of feedbacks or forcings. In this paper, we exemplify a new method to detect feedback and forcing from remote sensing data and apply it to reveal relationships between vegetation and elevation change in a prograding river delta (Wax Lake Delta, Louisiana, USA). We perform these analyses within distinctive vegetation classes aligned along deltaic elevation and age gradients. This type of information will be broadly beneficial to the ongoing development of ecogeomorphic models designed to evaluate how coastal landscapes will respond to future sea-level rise, for which effective parameterization of vegetation creates large uncertainties (Zinke,

Olsen et al. 2011, Nardin, Larsen et al. 2018). It will also benefit restoration planners who need to understand how the choice of vegetation species will impact the future development of a landscape. Further, understanding the distinct ecogeomorphic roles of native versus widespread invasive species in coastal ecosystems will help resource managers determine how much funding and effort should be devoted to the eradication of invasive species (Fei, Phillips et al. 2014).

Sedimentation within marshes is typically studied using sediment elevation tables (SETs) or variants thereof (Boumans and Day 1993, Cahoon, Lynch et al. 2002), clay pads (DeLaune, Baumann et al. 1983), and/or Cs-137 dating (Roberts, DeLaune et al. 2015), but these techniques suffer from a few disadvantages. First, data acquired with these methods is relevant to small (<1 m2) scales, and rarely is spatial replication sufficient to extrapolate to larger scales. Second, they potentially resolve (i.e., detect and quantify) one-way interactions from vegetation to sedimentation but are unable to resolve bidirectional feedback. Further, it can be difficult to determine—without widespread spatial replication—whether observed sedimentation is attributable specifically to characteristics of the vegetation or local flow and sediment supply-related phenomena. SETs and clay pads are typically deployed only within a single vegetation community or a few communities along an elevation gradient, but replication within many communities of vegetation is rare. Similarly, biomass, the other component of ecogeomorphic feedback, is difficult to resolve over large spatial scales, given the time-consuming nature of field surveys and subsequent gravimetric analyses.

Recently, emerging technology and data analysis techniques have made it possible to overcome some of the challenges associated with small-scale sampling of sedimentation and/or vegetation characteristics to delineate bi-directional feedback within many vegetation communities at the delta scale, with substantial spatial replication. LiDAR (Light Detection And Ranging) imagery provides up to centimeter-scale resolution of vegetation canopy characteristics and topography. Further, emerging tools from information theory are increasingly being used in hydrology to quantify the strength and significance of directional interactions between pairs of variables (i.e., from a source variable to a sink variable) from time-series. Unlike lagged correlation statistics, transfer entropy, formulated within the probabilistic framework of uncertainty and uncertainty reduction, is robust in the detection of nonlinear interactions (Schreiber 2000). Popularized in studies of the brain's neural network and gene network patterns (Percha, Dzakpasu et al. 2005, Ma and Bohnert 2007), transfer entropy has been used in hydrology to infer land-atmosphere feedbacks from flux tower data (Ruddell and Kumar 2009, Goodwell and Kumar 2017, Goodwell and Kumar 2017), impacts of hydrologic and chemical disturbance on stream metabolism (Larsen and Harvey 2017) and surface-water connectivity within complex delta distributary networks (Sendrowski and Passalacqua 2017, Sendrowski, Sadid et al. 2018). Here we adapt this method to detect spatially consistent feedback processes from remote sensing datasets that are spatially dense but temporally sparse, effectively using a space-for-time substitution in the formulation of transfer entropy.

The main objectives of this study are 1) to identify and quantify feedbacks and forcing between vegetation canopy characteristics and elevation within the Wax Lake Delta, 2) to compare the distinct ecogeomorphic roles of different vegetation classes, and specificially, 3) to compare the ecogeomorphic roles of nonnative vegetation species and

the native species that they replace. Here we test the null hypotheses that nonnative (Eichhornia crassipes, Colocasia esculenta) and native (Nelumbo lutea, Polygonum spp.) vegetation species that occupy intermediate (subtidal to intertidal and supratidal) elevations on deltaic islands exhibit similar forcing or feedback between vegetation biovolume and elevation. In addressing objective 1, we establish a new precedent for analysis of causal interactions from commonly available remote sensing data, based on a simple modification of the transfer entropy formulation. Meanwhile, objectives 2 and 3 produce insight for coastal restoration and vegetation management in this deltaic ecosystem.

2 Site description and vegetation characteristics

Our study focuses on the Wax Lake Delta, located west of the Atchafalaya River Delta in Louisiana, USA, in the only actively prograding portion of the Louisiana coastline. The Wax Lake Outlet is an artificial flood control diversion of the Atchafalaya River constructed in 1941, which conveys one-third of the combined discharge of the Red River and the Mississippi River and an average of 20.5 tons of suspended sediment per year (Allison, Demas et al. 2012). The Wax Lake Delta (Figure 3.1) first became subaerial in 1973. Since 1997, about 51.1 km2 of new land has been built (Roberts, Walker et al. 1997). Since that time, the Wax Lake Delta has become one of the best-studied areas for coastal river-dominated delta dynamics. Currently, it is viewed as a model for engineered diversions of the Mississippi River planned to slow or mitigate coastal land loss. As projected land loss in the Mississippi River Delta plain is 5,700 km2 for the period 1950-2050 (Blum and Roberts 2009) this understanding is imperative.

Figure 3.1. Satellite image of the Wax Lake Delta region.

Land area in the Wax Lake Delta varies along gradients of chronosequence and elevation. Older islands and portions of islands tend to be found to the north (upstream), with more recently deposited strata in the south. Individual islands feature lateral and longitudinal elevation gradients. The highest elevations, occupied by trees (primarily Salix nigra), are found at the heads of islands. Natural levees, also colonized by Salix, form in a chevron-shaped fashion downstream of island heads. From the outer chevron, elevations decrease gradually downstream and into the island interiors. The most central,

lowest portions of the islands are often characterized by open water. Subtidal locations feature a mixture of submersed aquatic vegetation (SAV), which mixes with emergent floating-leaf vegetation such as Nelumbo lutea at higher elevations (Figure 3.2). Finally, intertidal to supratidal elevations, clonal emergents such as Phragmites australis, Colocasia esculenta, and Sagittaria spp. are abundant. Non-rooted floating vegetation such as Eichhornia crassipes (water hyacinth, an invasive species that tends to replace Nelumbo lutea and SAV) may occupy a range of elevations; its abundance at any single location may be transient, subject to wind patterns, tides, and/or major flow events. In this analysis, we distinguish between the seven major classes and species of vegetation outlined in Figure 3.2. These classes and species, based on the classification scheme of Carle et al. (2014) (see section 3.1.3), are the dominant groupings of vegetation by area on the Wax Lake Delta that are distinguishable from remote sensing imagery.

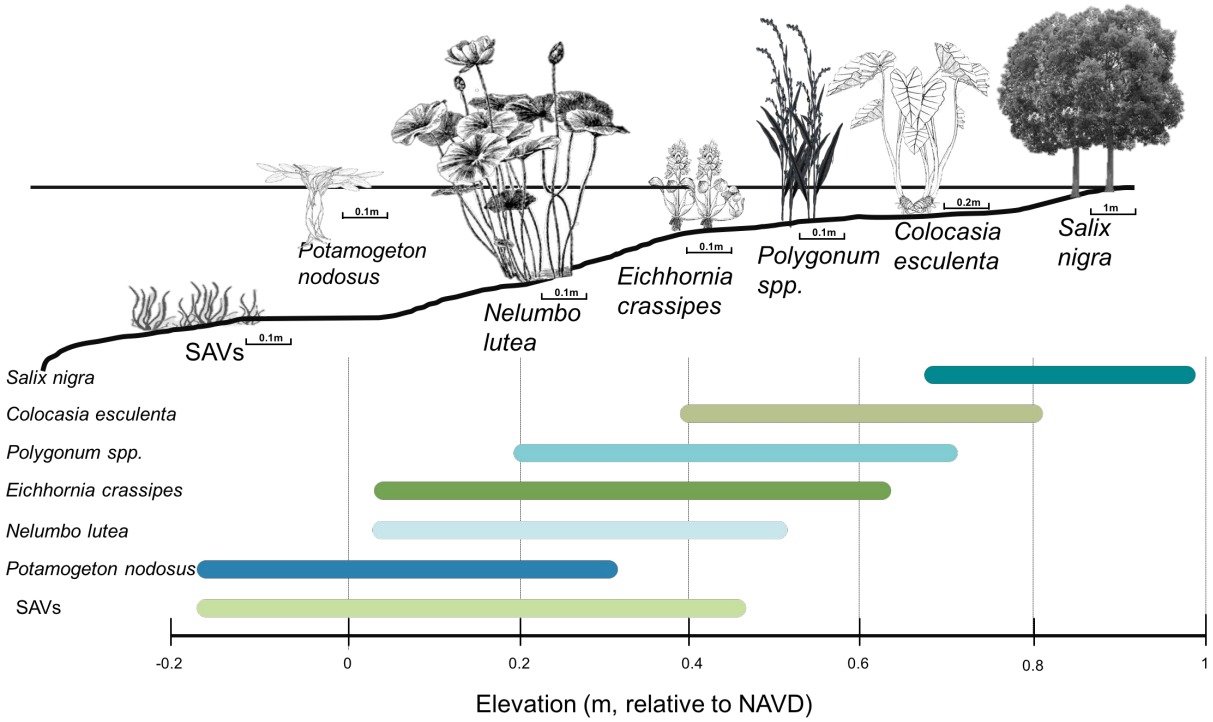

Figure 3.2. The elevation range and morphologic structure of each class of vegetation considered in this analysis.

The Wax Lake Delta experiences pronounced seasonality in flow and vegetation characteristics. Sediment is typically delivered to deltaic marshes through three mechanisms. Winter cold front events, which occur at a 4-7 day frequency between October and April (with the highest incidence in January-February) (Hardy and Henderson 2003), can deliver sediment resuspended from the coastal shelf to inland vegetation communities (Mossa and Roberts 1990, Feng and Li 2010, Li, Roberts et al. 2011, Roberts, DeLaune et al. 2015). River flooding originating from snowmelt within the headwaters of the Mississippi occurs in the spring (April through June) and is often associated with prolonged (i.e., multiple-week) inundation of lowland floodplains and deltaic marshes. In 2011 (central in time to the 2009-2013 duration of this study), the

Wax Lake Delta experienced record flooding, with a flood peak extending from early May to late and a total duration between March and August (Figure 2.3). This record flood exceeded the stage of other notable floods in 1927 and 1937, and the 1.1 million metric tons of sediment deposited during this event (Bevington, Twilley et al. 2017) caused the Wax Lake Delta areal extent to grow by approximately 6.5 km2 (at mean delta water level), an increase of 28% (Carle, Wang et al. 2014). Following the flood, 8.3 km2 (36% of the pre-flood delta's extent) experienced vegetation community transitions (Carle et al. 2015). Late-summer hurricanes and tropical storms represent the third mechanism of sediment delivery to coastal marshes.

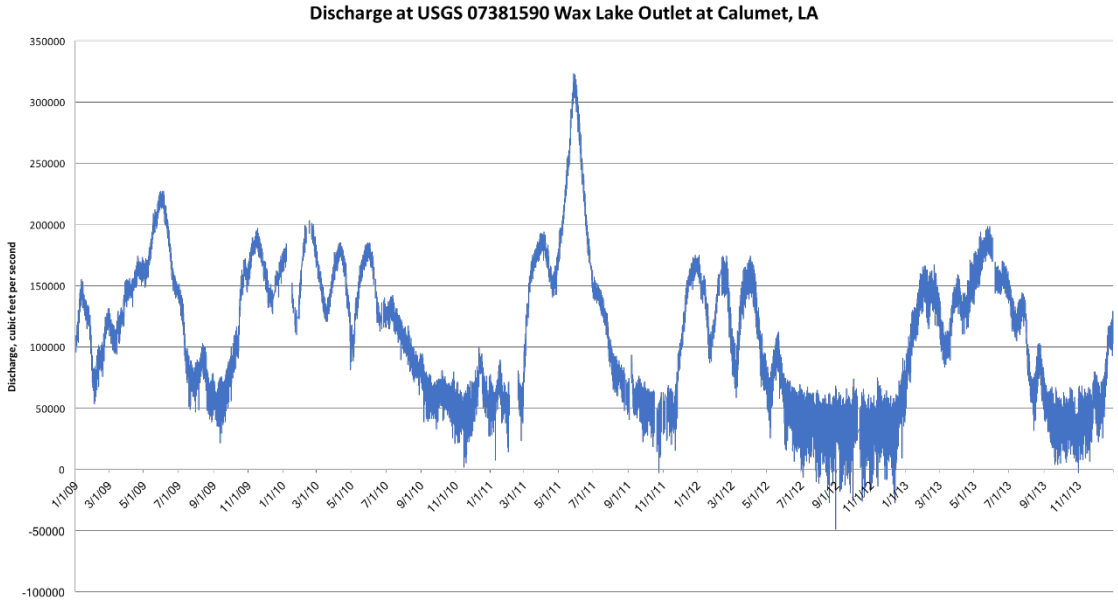

Figure 3.3. The hydrograph of the discharge at Wax Lake Delta Outlet from Jan 1st 2009 to Dec 31st 2013.

Although sediment characteristics vary by event, suspended sediment delivered to deltaic marshes typically has abundant clay-to-silt size fractions and is dominantly inorganic (Roberts, DeLaune et al. 2015). A D50 around 40 □m is common (L. Larsen, unpubl. data, 2017). Though the organic component measured in soil on islands of the Wax Lake Delta is low (5-16 g cm3; Roberts et al. 2015), others (Nyman, DeLaune et al. 1990, Reed 2002) have noted that organic accumulation can contribute significantly to sedimentation, particularly in older portions of the greater Mississippi River delta area. Further, models of long-term delta evolution suggest that when freshwater inputs to deltas decrease, the result is a rapid shoreline retreat attributable to the loss of organic matter accumulation (Lorenzo-Trueba, Voller et al. 2012).

Seasonality of vegetation characteristics is another important consideration in attempts to resolve ecogeomorphic feedbacks within the Wax Lake Delta. Vegetation within low-lying parts of deltaic islands senesces during the winter (November through April). Higher-elevation species (e.g., Colocasia esculenta) begin to emerge in early February but grow to peak biomass in August. Lower-elevation species such as Nelumbo lutea may not emerge until up to late March, such that their live biomass may not be

captured in imagery acquired in January or February. However, even during periods of senescence, dead vegetation stems and leaves from the previous year will remain emergent in places of former abundance.

The convolution of seasonal characteristics of vegetation with seasonal characteristics of flow and sediment delivery likely is an overwhelmingly important factor in the establishment of ecogeomorphic feedbacks (Nardin and Edmonds 2014). Vegetation may not have much influence on sedimentation during winter cold fronts when it is senesced, nor at the peak of summer when it is most abundant but sediment delivery events are rare, with the exception of hurricanes and tropical storms. Conversely, river flood events may represent the optimal convergence of sediment delivery with marsh vegetation biomass. Based on topographic surveys, Bevington found that prolonged, moderate- to high-discharge river floods dominate sedimentation on the Wax Lake Delta, whereas cold fronts are overwhelmingly associated with erosion (Bevington, Twilley et al. 2017). Tropical storms, on the other hand, contribute to net sediment aggradation. However, large floods and tropical storms may also uproot or otherwise stress vegetation, promoting community shifts or changing competition dynamics (Kalliola and Puhakka 1988, Tabacchi, Correll et al. 1998, Francis 2006).

3 Methods

3.1. Overview

Here we analyzed causal links between elevation/elevation change and vegetation biovolume/biovolume change within distinct classes of vegetation found across the Wax Lake Delta. First, we extracted bare-earth elevation and vegetation biovolume from lidar imagery collected before and after the 2011 flood. We identified which of these points coincided with the boundaries of each vegetation class of interest by overlaying preexisting vegetation classification maps (Carle et al., 2014) corresponding to periods of time before and after the flood. Then, within each of these vegetation classes, we used an information entropy analysis to identify and quantify causal linkages between elevation and biovolume variables to quantify the magnitude and direction of forcing or identify the existence of feedback. Though the information entropy analysis identifies causal linkages and how strong they are, it does not identify whether each forcing is positive (i.e., an increase (decrease) in the "source" variable produces an increase (decrease) in the "sink variable) or negative (i.e., the two variables change in the opposite sense). To gain further insight into the nature of each pairwise coupling, we also plotted scatterplots of each bivariate pairing and performed a traditional vegetation and topography transition analysis. Each of our data sources and analysis steps are detailed below.

3.2. Data sets

3.2.1. LiDAR source imagery

We used LiDAR imagery of the Wax Lake Delta to obtain delta-scale information about topographic change and vegetation canopy characteristics, two critical components of ecogeomorphic feedback in river deltas. Airborne LiDAR source imagery was obtained through the National Center for Airborne Laser Mapping (NCALM) and Bureau of Economic Geology in the Jackson School of Geosciences at the University of Texas-Austin. Imagery that spanned the spatial extent of the Wax Lake Delta (https://doi.org/10.5069/G9SF2T41; https://doi.org/10.5069/G95M63M8) was obtained

on January 14, 2009 with 1.69 pts/m2 point density, and again on February 13, 2013 with 14.27 pts/m2 point density. The vertical errors are 5.5 cm and 3.4 cm respectively.

Although the one-month offset in LiDAR image acquisition in 2009 compared to 2013 may have resulted in some of the emergent vegetation communities exhibiting slightly different physical characteristics associated with their stage of reemergence from senescence, this effect is expected to be small due to the fact that both images were acquired during the dominant period of senescence. Rather, we expect that image-to-image variability in elevation and vegetation class and characteristics was controlled dominantly by sedimentation and vegetation shifts resulting from the 2011 flood and smaller seasonal floods during the intervening years (Fig. 3.3). An additional potential source of error lies in the quantification of vegetation biovolume characteristics as a potential control on elevation during the period of vegetation senescence. In doing so, we assume that the volume of remnant stems observable from the previous season's growth scales monotonically (but not necessarily linearly) with total biovolume (stem + leaves) averaged over the periods of sediment delivery.

3.2.2. Surrogate bio-volume and topography from LiDAR imagery

Biomass is one of the most significant parameters related to the health and growth status of vegetation and its potential influence on topographic change. Because of its high spatial resolution in three dimensions, LiDAR imagery can be used to calculate surrogate vegetation bio-volume, itself a proxy for biomass (Figure 3.4). To do so, we used the LiDAR return order and number of returns. Laser pulses emitted from the LiDAR can return to the sensor more than one time from encounters with multiple reflective surfaces. The first returned laser pulse is usually reflected from the top of vegetation canopies or manmade structures. The last returned pulse is associated with the ground. The total number of returns of a given pulse can be used to classify the imaged area as open water or vegetation. Water has a lower number of returns, as it scatters the pulse. Meanwhile, vegetation has a higher number of returns.

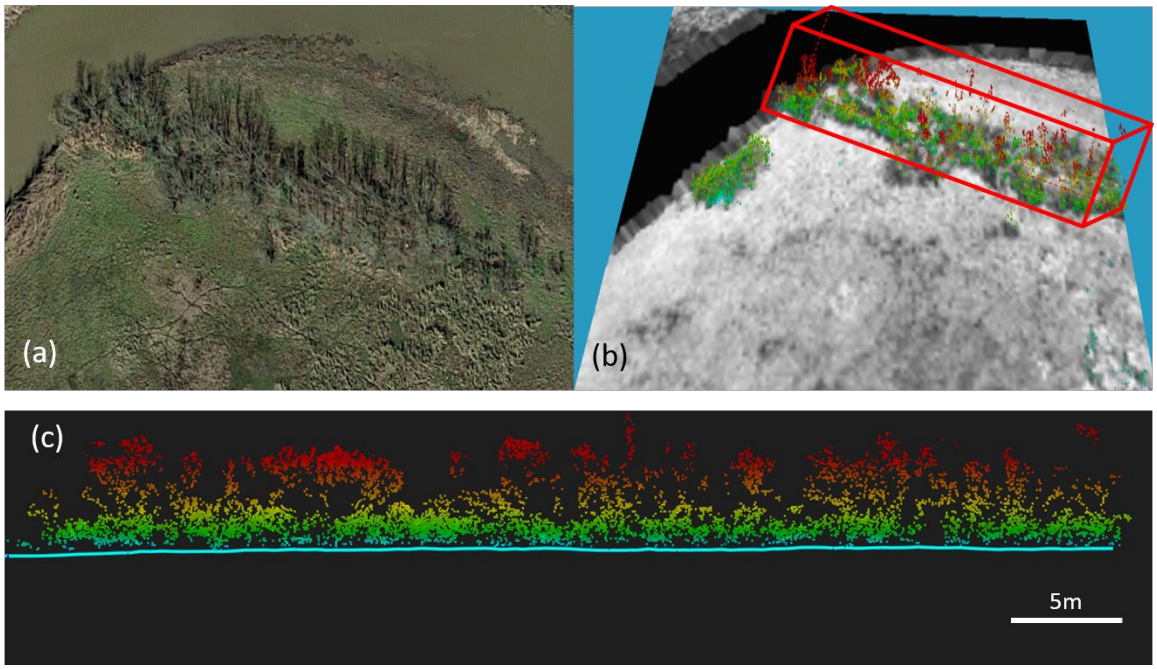

Figure 3.4. The figures show the 3D view (b) and the cross-section view (c) of segmented LiDAR cloud points. (a) is the corresponding aerial photograph. The color of points represents the height.

As the water returns only once, the non-water and water can be separated (Figure 3.5). To generate the vegetation-only LiDAR data, the points with last return are deleted, as they represent bare ground. The surrogate bio-volume is calculated by multiplying the average height of the point cloud in each unit cell that contains vegetation, relative to bare ground, with the area of unit cell, and the topography is estimated by calculating the average height of the point cloud in each unit cell that represents bare ground.

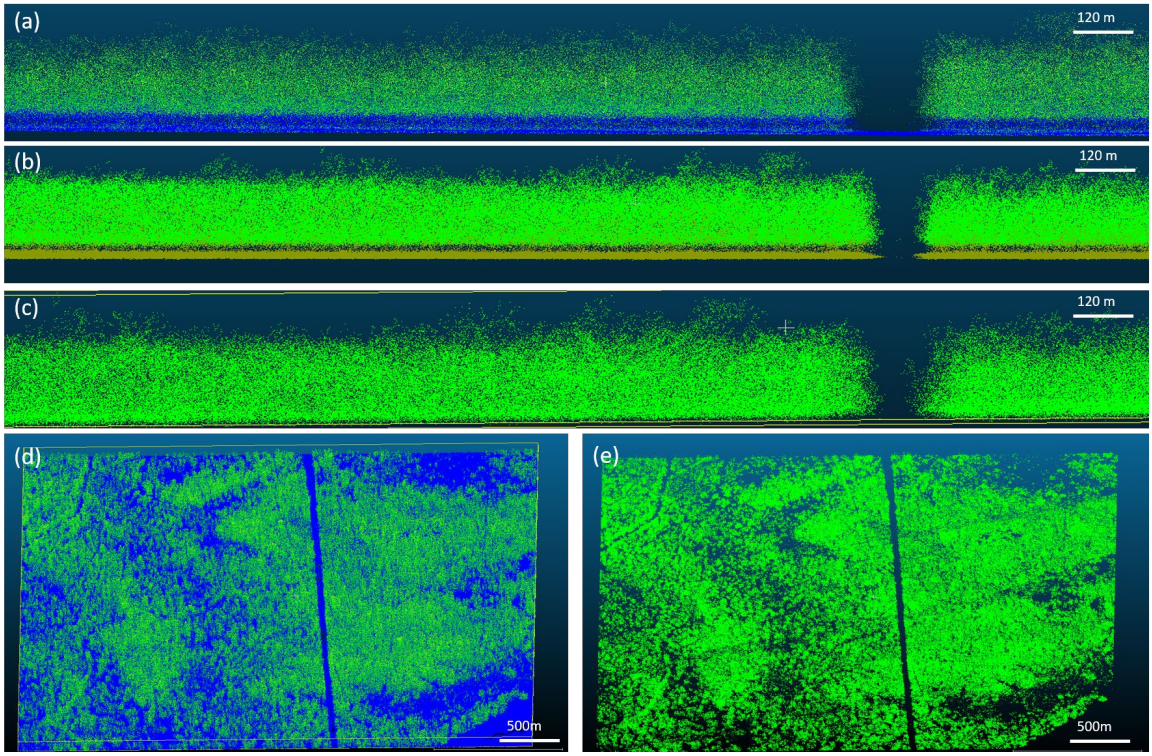

Figure 3.5. (a) Number of returns is used to separate open water and vegetation. Here, the blue points represent water, and the green points represent non-water. An open-water channel, visible on the right side of the image, is associated with a low number of returns. (b) Return number is used to separate bare land and vegetation. The yellow points represent bare land, and the green points represent vegetation. (c) is the cross section of extracted vegetation points. (d) and (e) are the planform (d) and oblique (e) views of LiDAR cloud points of vegetation (shown in green) with and without non-vegetation shown in blue.

3.2.3. Vegetation classification

We used existing vegetation classification maps (Figure 4 in Carle et al. 2014) to segment the surrogate biovolume and elevation data by vegetation class, such that ecogeomorphic feedbacks within distinct classes could be resolved. Carle et al. (2014) implemented a maximum likelihood supervised classification method on WorldView-2 and Landsat 5 TM remote sensing images to produce vegetation classification maps before and after the 2011 Mississippi River flood. The WorldView-2 images were taken on June 15, 2010 and October 16, 2011 with 2-m spatial resolution. The Landsat 5 TM images were taken on August 27, 2010 and August 30, 2011 with 30-m spatial resolution. Comparing with field validation, the overall classification accuracy was 75%, and the average classification accuracy of the vegetation classes that are a focus in this paper was 82%.

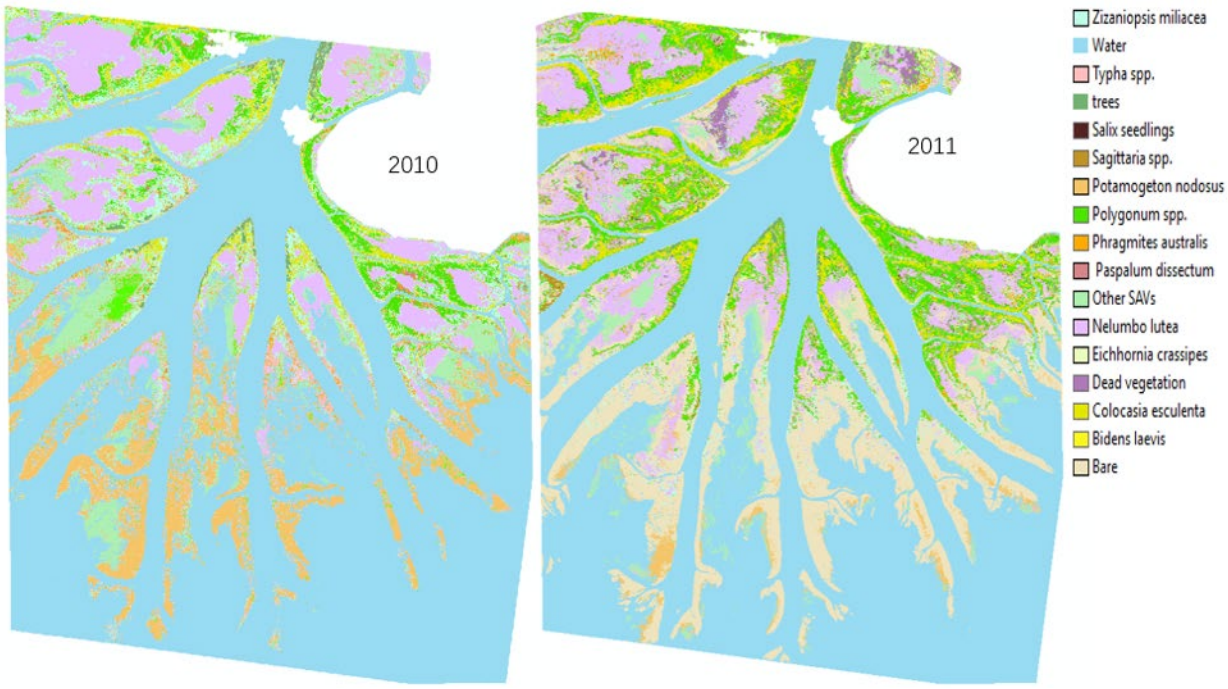

Figure 3.6. Vegetation types are classified using WorldView-2 remote sensing images from 2010 and 2011. Modified from vegetation classification maps of Carle et al. (2015). In the legend, SAV = submersed aquatic vegetation.

Although Carle et al.'s (2015) classification scheme encompassed 17 different classes, we worked with the most dominant subset, a total of seven vegetation classes (Tables 1 and S3). These seven vegetation types, as well as bare land and water, account for 91.16% of the WLD area. A rule of thumb is that transfer entropy calculations should be performed on datasets containing at least 500 points (Ruddell and Kumar 2009), so calculations performed on less dominant classes of vegetation would not be considered statistically robust. For the vegetation classes that we considered, pixel counts exceeded this value by several orders of magnitude (Table 3.1). To evaluate effects of individual pixels behaving non-independently (i.e., pseudoreplication), we performed an additional sensitivity analysis in which we randomly subsampled the data at ratios of 90%, 80%, 70%, and 50% for the information entropy analyses. Results (Table 3.2) indicated that our conclusions were robust to the subsampling.

Vegetation Type	2010 Pixel Count	2011 Pixel Count	2011-2010 Change	Vegetation Class	Elevation Range
Trees (*Salix nigra*)	93320	138723	45403	7	0.68 – 0.98
Colocasia esculenta	329978	518902	188924	6	0.39 – 0.81
Polygonum spp.	424198	1198920	774722	5	0.19 - 0.72
Eichhornia crassipes	25127	78869	53742	4	0.07 – 0.63

Nelumbo lutea	1596107	1558448	-37659	3	0.07 – 0.50
Potamogeton nodosus	1102374	217467	-884907	2	-0.18 – 0.31
SAVs	887136	428140	-458996	1	-0.18 – 0.45
Bare	118764	2576786	2458022	0	~0
Water	9058876	7876718	-1182158	0	~0

Table 3.1. Data classes considered in transfer entropy calculations, elevation ranges, and class-specific pixel counts before and after the 2011 flood. Each pixel corresponds to an area of 4 m2. The vegetation class is in rank order in accordance with the elevation range. Elevation ranges are with respect to the NAVD88 datum. SAV = submersed aquatic vegetation.

3.3. Resolution of bidirectional feedbacks with mutual information and transfer entropy

3.3.1. Mutual information and Transfer entropy computations

Transfer entropy is an information-theoretical method that statistically identifies directionalities of forcing and feedback by measuring information transfer among pairs of variables. Information is defined as the Shannon entropy, H, or total uncertainty present in a variable's distribution (Shannon 1949):

$H = -\sum_i p(i) log_2 p(i).$ [3.1]

where $p(i)$ denotes the probability that i th event happened. H measures uncertainty in units of bits.

The mutual information measures the reduction in one variable's uncertainty by knowing the other variable. It is calculated as

$I(X_t, Y_t) = \sum_{x_t, y_t} p(x_t, y_t) log \frac{p(x_t, y_t)}{p(x_t)p(y_t)}.$ [3.2]

where x_t, y_t are values in time series X_t and Y_t.

Transfer entropy measures how much information is transferred between two variables, quantifiable as the reduction in uncertainty in the distribution of variable Y based on knowing the value of variable X at a time lag □, conditioned on Y's own history. Typically, (Schreiber 2000, Ruddell and Kumar 2009), it is formulated from time-series X_t and Y_t as follows:

$$T(X_t \to Y_t, k, l, \omega, \tau) = \sum_{y_t, y_{t-\omega\Delta t}^{[k]}, x_t^{[l]}} p(y_t, y_{t-\omega\Delta t}^{[k]}, x_{t-\tau\Delta t}^{[l]}) \; log_2 \frac{p(y_t | (y_{t-\omega\Delta t}^{[k]}, x_{t-\tau\Delta t}^{[l]}))}{p(y_t | y_{t-\omega\Delta t}^{[k]})}. \quad [3.3]$$

Here $x_{t-\tau\Delta t}^{[l]}$ and $y_{t-\omega\Delta t}^{[k]}$ are the immediate history of $x_{t-\tau\Delta t}$ and $y_{t-\omega\Delta t}$ with block length of l and k respectively, where $x_{t-\tau\Delta t}$ and $y_{t-\omega\Delta t}$ are the values of x_t and y_t at τ and ω time steps earlier respectively. The assumption that setting $k = l = 1$ is conservatively biased as it neglects the information transferred to Y_t with block lengths $k > 1$ and $l > 1$ (Marschinski and Kantz 2002, Sabesan, Narayanan et al. 2003).

However, it is commonly employed in practice to reduce the dimensionality of the probability distributions in equation 2 to three-dimensional distributions (as shown in Figure 2.7A), to make them computationally tractable (Ruddell and Kumar 2009, Larsen, Newman et al. 2017).

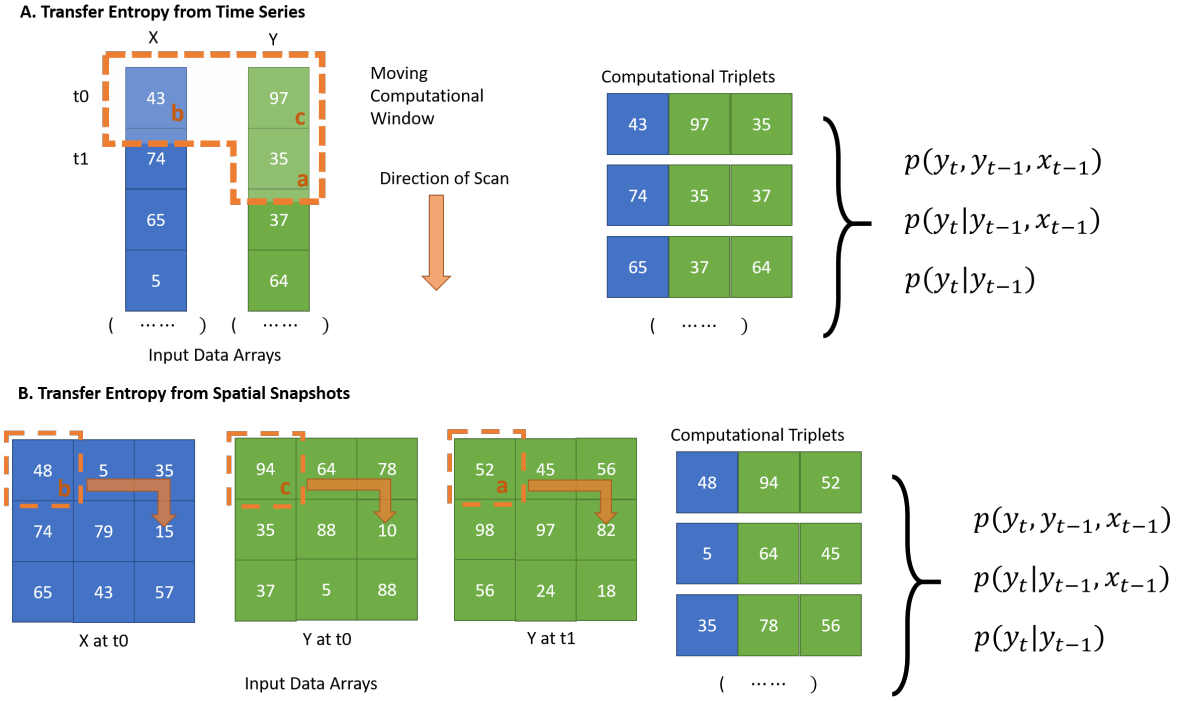

Figure 3.7. Transfer entropy is calculated from joint and conditional probability distributions based on triplets (a-c) of points: It measures the reduction of uncertainty in a dependent variable *Y* at a time t_1 (a) that is attributable to knowing the value of variable *X* at time t_0 (b), conditioned on the reduction of uncertainty attributable to knowing the value of *Y* at t_0 (c). In the traditional version of transfer entropy used to analyze time series (A), joint and conditional probability distributions based on these triplets are computed by scanning down the time-series (orange arrow). In the spatial version of transfer entropy (B), the triplets are taken from three spatial matrices, and joint and conditional probability distributions are computed by scanning the spatial matrices over all row, column (i.e., *i,j*) coordinates (orange arrow).

For remote sensing data that are intensive in space but sparse in time, a simple modification of equation 3 is necessary (Figure 3.7B). Whereas equation 3 results in high transfer entropy when certain ranges of values in variable X promote transitions in variable Y that are consistent over the time series, our modification (equation 3.4) results in high transfer entropy when certain states of variable Y result in particular transitions in variable X from one time point to another consistently over space. Hence, assuming that dominant interactions between X and Y are spatially stationary, the probability distributions in equation 3.3 can be reformulated using a space-for-time substitution:

$$T(X \to Y) = \sum_{y_{t1}^{(i,j)}, y_{t0}^{(i,j)}, x_{t0}^{(i,j)}} p(y_{t1}^{(i,j)}, y_{t0}^{(i,j)}, x_{t0}^{(i,j)}) \; log_2 \frac{p(y_{t1}^{(i,j)} | y_{t0}^{(i,j)}, x_{t0}^{(i,j)}))}{p(y_{t1}^{(i,j)} | y_{t0}^{(i,j)})}, \quad [3.4]$$

where X_{t0} and Y_{t1} are random variables of spatial data with time stamps $t0$ and $t1$ (e.g., sequential remote sensing image acquisition dates), and $x_{t0}^{(i,j)} \in X_{t0,}$ where i, j are the two-dimensional spatial coordinates.

To resolve the strength of bidirectional ecogeomorphic feedbacks in the Wax Lake Delta, we implemented two sets of computations with equation 3.4 to resolve 1) feedback between sedimentation and physical canopy characteristics, and 2) feedback between sedimentation and vegetation class. In the first set of computations, to evaluate the effect of surrogate biovolume on topography we initially solved equation 4 with X = surrogate biovolume and Y = elevation. Subsequently, we evaluated the effect of topography on surrogate biovolume by setting X = elevation and Y = surrogate bio-volume. For each of these computations, we segmented the data by vegetation class, as delineated in the 2009 - 2010 vegetation classification maps of Carle et al. (2015). Meanwhile, t0 and t1 coincided with the pre-flood 2009 and post-flood 2013 LiDAR imagery. Within each image, aggregate surrogate bio-volume and topography each have more than 18 million spatially distributed data points.

In the second set of computations, we initially solved equation 4 with X = vegetation class (categorical) and Y = elevation. Subsequently, we solved the equation with Y = vegetation class and X = elevation.

3.3.2. Statistical significance testing

The method of shuffled surrogates, which tells whether or not the information flow in a coupling is significantly higher than that randomly occurring between unrelated variables, is used to evaluate the statistical significance of information transferred among variables (Kantz and Schürmann 1996, Marschinski and Kantz 2002, Sabesan, Narayanan et al. 2003). To destroy the spatial correlations, X^S and Y^S are formed from randomly shuffled X and Y. Surrogate transfer entropy $T^S(X^S \to Y^S)$ is computed 500 times by using Monte Carlo simulations. A one-tailed hypothesis test is used, in which T is deemed significant if:

$$T > \mu(T^S) + c \cdot \sigma(T^S), \qquad [3.5]$$

where $\mu(T^S)$ and $\sigma(T^S)$ are the mean and standard deviation of distribution of T^S. c =1.66 corresponds to 95% confidence and c=2.36 corresponds to 99% (Ruddell and Kumar 2009). Here we considered the directional relationship between pairs of variables strong if the transfer entropy passed the shuffled surrogates significance test with at least 99% confidence and weak if it passed the test with between 95% and 99% confidence. We considered the directional relationship not significant if the transfer entropy did not pass the test with at least 95% confidence.

Once the threshold transfer entropy is computed, we compute a quantity that we heretofore refer to as the relative significant transfer entropy, for which the amount of uncertainty reduction above the threshold (T') is normalized by the total uncertainty present in the "sink" variable:

$$\big(T(X \to Y) - T'(X \to Y)\big)/H(Y). \qquad [3.6]$$

We similarly calculate the relative significant mutual information as follows:

$$\big(I(X,Y) - I'(X,Y)\big)/H(Y). \quad [3.7]$$

3.3.3 Validation of modified spatial transfer entropy

Because the spatial implementation of transfer entropy is new, we developed two proof-of-concept scenarios for validation purposes. In the first scenario, spatially intensive data X and Y were randomly and independently generated on a 500 x 500 grid

at times t0 and t1, with values ranging from -4 to 4. In the second scenario, X and Y were randomly and independently generated at t0. However, at t1, Y exhibits dependence on the t0 values of X and Y according to the following rules:

$$if\ X_{T0}^{(x,y)} > 0,\ \ Y_{T1}^{(x,y)} = Y_{T0}^{(x,y)} + \epsilon, \quad [3.8]$$

$$if\ X_{T0}^{(x,y)} < 0,\ \ Y_{T1}^{(x,y)} = Y_{T0}^{(x,y)} - \epsilon, \quad [3.9]$$

where ϵ is a random positive number ranging from 0 to 2 and (x, y) is the coordinate in the two-dimensional spatial field.

Transfer entropy from X to Y in the first scenario is 0.0046 bits. The threshold with 95% confidence of one-tailed hypothesis test is 0.005 bits, which means that there is no significant information transferred or no notable impact from X to Y. Transfer entropy from X to Y in the second scenario is 0.0056 bits, and the threshold with 95% confidence is 0.0043 bits, which means that significant information flow from X to Y is detected, or, in other words, that Y is impacted by X. These results are consistent with expectations, given the setup of the two scenarios. In the second scenario, the transfer entropy represents a significant reduction in the relative uncertainty in variable Y of 0.05%. Though this represents a relatively small reduction in uncertainty, it is consistent with expectations given the stochasticity inherent in equations 8-9 and with previous applications of transfer entropy to noisy environmental systems (Larsen and Harvey 2017).

3.3.4. Implementation

Transfer entropy and significance computations were implemented in MATLAB. The source and sink variables were alternately elevation, elevation change in time, surrogate biovolume (continuous), and vegetation class (categorical). Our initial set of analyses evaluated the feedback between elevation and vegetation canopy characteristics over all vegetation classes, as well as the feedback between elevation and vegetation class. The second set of analyses evaluated feedback among the continuous variables within each vegetation class, as detailed below.

We use both mutual information and transfer entropy to quantify different aspects of ecogeomorphic feedbacks between vegetation characteristics and landscape evolution. First, we quantify the significant relative mutual information between surrogate bio-volume of the vegetation in 2009 and the change in elevation between 2009 and 2013. Mutual information is not a directional quantity in the sense that it represents shared information between two variables. However, because the 2009 surrogate biovolume precedes the change in elevation, we interpret the mutual information between the two variables as an indicator of the impact of vegetation canopy characteristics on elevation change. A higher normalized mutual information implies a greater importance of vegetation canopy characteristics compared to other factors (such as variability in sediment supply, or flow characteristics) in explaining the variability in elevation change over the four years spanned by image acquisition.

To infer the impact of elevation change on vegetation canopy characteristics, we compute the transfer entropy from elevation change to 2013 surrogate biovolume. Here, we use transfer entropy rather than mutual information because we expect high correlation between 2013 surrogate biovolume and 2009 surrogate biovolume, the latter of which is expected to drive elevation change. Thus, it is important to condition the shared information between elevation change and 2013 surrogate biovolume on the 2009 surrogate biovolume to distinguish between cause and effect.

A stronger test of the impact of sedimentation attributable directly to physical interactions with vegetation canopies on the distribution of elevations within the delta is whether significant transfer entropy exists between the 2009 surrogate biovolume and 2013 elevations, once the effect of historical (2009) elevations is accounted for. Significant transfer entropy between these variables implies that vegetation canopy structural characteristics have an overriding influence on the distribution of raw elevations (and not just the change in elevation). In other words, transfer entropy from surrogate biovolume to elevation will be significant only if biovolume itself—independent of the extent to which biovolume is a reflection of elevation—has an overriding influence on elevation four years into the future, irregardless of historical trajectories, and thus is a dominant factor driving the short-term evolution of deltaic landscapes. While we expected that most vegetation classes would have a significant relationship between biovolume and elevation change due to known physical impacts of canopies on flow and sedimentation, we hypothesized that fewer vegetation classes would exhibit a significant transfer of information from surrogate biovolume to elevation.

Likewise, use transfer entropy to quantify the independent reduction in uncertainty in 2013 surrogate biovolume due to knowledge of 2009 elevations. Significant transfer entropy implies that vertical position relative to the tidal range influences future vegetation canopy characteristics. The magnitude of the transfer entropy indicates, in other words, the strength of zonation, or the control of elevation on vegetation characteristics, typically attributed to redox potential gradients or gradients in seed dispersal by flow, superimposed on competition dynamics (Bertness, 1991; Leck and Simpson, 1994). Meanwhile, transfer entropy from elevation change to surrogate biovolume provides insight into the effects of abiotic forcing on vegetation distinct from that gained from quantifying the transfer entropy from elevation to surrogate biovolume. Namely, it indicates the incremental effect of deposition on productivity, attributable to particulate nutrient inputs, or, if a negative relationship, to light blocking or burial.

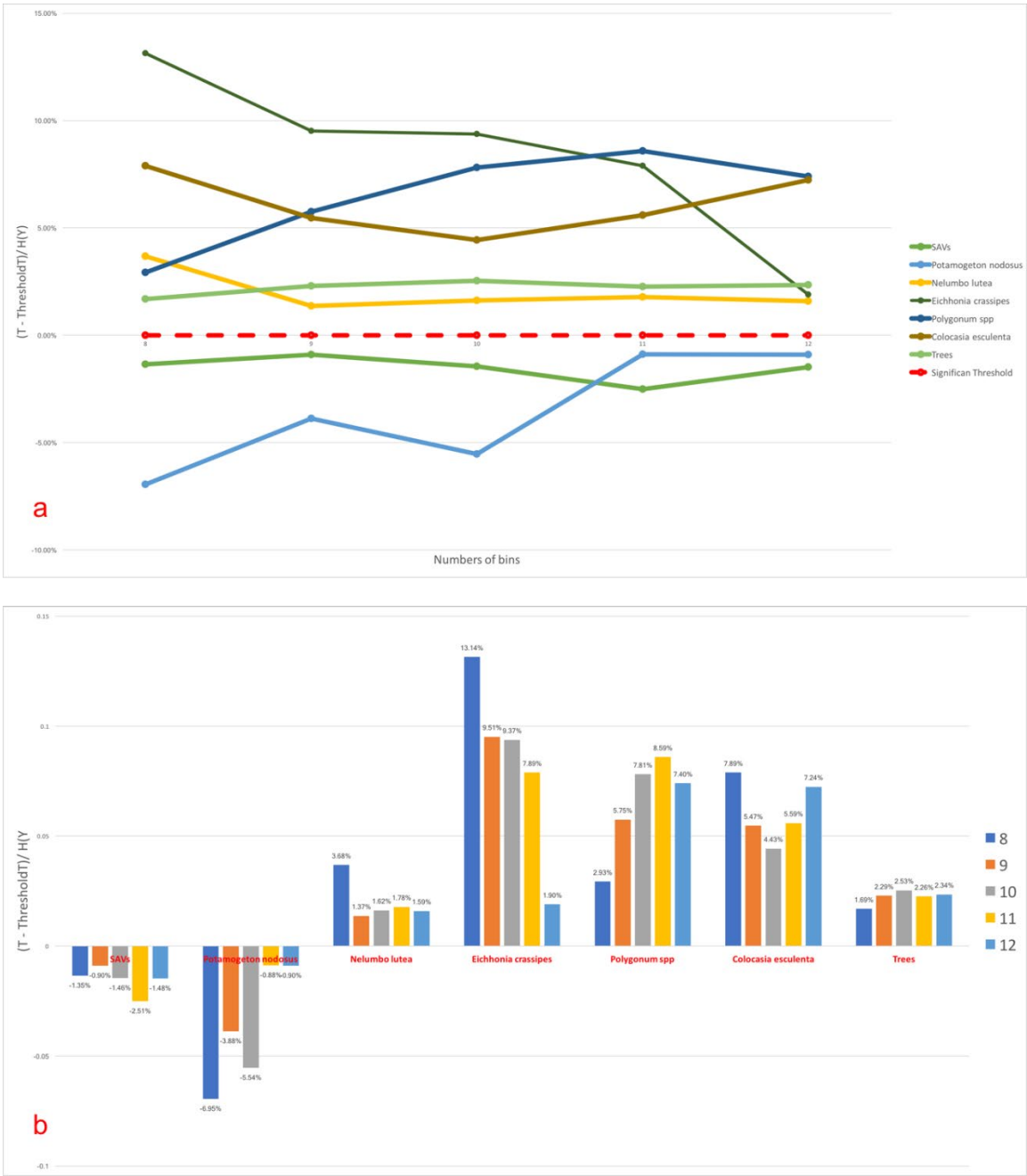

Figure 3.8. a. The probability density function of the relative transfer entropy of each vegetation by choosing different numbers of bins. The red dashed line represents the 95% confidence level. b. The histogram of relative transfer entropy of each vegetation by choosing different numbers of bins.

Probability distributions were estimated through discrete binning, using eight bins to estimate the marginal and joint probability distributions involving vegetation class, corresponding to the eight categories evaluated (seven vegetation classes, plus open water and all of Carle et al.'s (2015) categories not depicted in Figure 3.6 that were lumped together as a single class). Probability distributions for the continuous variables were estimated using 10 evenly spaced bins (Ruddell and Kumar 2009) in the first set of computations. Tests of the sensitivity of the information entropy calculations to number of bins (Figure 2.8) revealed limited sensitivity to choose bin number within the range of 8-12. Though there was slight variability in the magnitude of transfer entropy with changes in the number of bins, within all classes of vegetation evaluated, whether the information transferred was significant or not remained unchanged, and the direction(s) of information transferred between elevation and surrogate biovolume also remained unchanged. Because 10 bins generally produced the smallest differences in relative transfer entropy compared to computations with one bin less or more (Table 3.3), our reported analyses use the 10-bin convention.

We did a supplemental test to validate the sufficiency of the data. In the test, we randomly sample the data with four different ratios (90%, 80%, 70% and 50%), and run the same analysis as in the paper. The results (Table 3.2) from all different ratios, even when only 50% is used, agree with the results in the paper. It is reasonable to conclude that the data we used in the paper is sufficient to estimate the joint probability and measure the information flow between the variables. We also did another supplemental test to address the sensitivity of the results to the number of bins used. In the test, we evaluate different numbers of bins (8, 9, 11 and 12). The relative transfer entropy showed limited sensitivity to the selection of number of bins used in the resolution of probability density functions within the range of 8-12 bins (Figs. 3.8A and 3.8B). Though there was slight variability in the magnitude of transfer entropy with changes in the number of bins, within all classes of vegetation evaluated, whether the information transferred was significant or not remained unchanged, and the direction(s) of information transferred between elevation and surrogate biovolume also remained unchanged. Because 10 bins generally produced the smallest differences in relative transfer entropy compared to computations with one bin less or more (Table 3.3), our reported analyses use the 10-bin convention.

All code, based on the toolbox by Ruddell and Kumar (2009), and datasets used in the analysis are available on GitHub (https://github.com/Hongxuma/SpatialTransferEntropy.git).

			90% data	
Vegetation		T	Threshold T	(T-ThresholdT)/H(Y)
SAVs	X(Topography) ->Y(Biomass)	0.1379	0.1984	Not Significant
	X(Biomass) ->Y(Topography)	0.4139	0.2809	4.96%
Potamogeton nodosus	X(Topography) ->Y(Biomass)	0.5188	0.5736	Not Significant
	X(Biomass) ->Y(Topography)	0.5198	0.773	Not Significant
Nelumbo lutea	X(Topography) ->Y(Biomass)	0.014	0.000493	1.64%
	X(Biomass) ->Y(Topography)	0.0698	0.00086	2.68%

Eichhonia crassipes	X(Topography) ->Y(Biomass)	0.4591	0.2931	7.44%
	X(Biomass) ->Y(Topography)	0.1015	0.2805	Not Significant
Polygonum spp	X(Topography) ->Y(Biomass)	0.0067	0.000203	7.76%
	X(Biomass) ->Y(Topography)	0.004	0.000613	0.19%
Colocasia esculenta	X(Topography) ->Y(Biomass)	0.046	0.000628	5.69%
	X(Biomass) ->Y(Topography)	0.000423	0.000636	Not Significant
Trees	X(Topography) ->Y(Biomass)	0.0362	0.0038	2.52%
	X(Biomass) ->Y(Topography)	0.000457	0.000568	Not Significant
			80% data	
Vegetation		T	Threshold T	(T-ThresholdT)/H(Y)
SAVs	X(Topography) ->Y(Biomass)	0.2056	0.2476	Not Significant
	X(Biomass) ->Y(Topography)	0.3349	0.2292	4.06%
Potamogeton nodosus	X(Topography) ->Y(Biomass)	0.5443	0.6549	Not Significant
	X(Biomass) ->Y(Topography)	0.4717	0.7949	Not Significant
Nelumbo lutea	X(Topography) ->Y(Biomass)	0.0137	0.000552	1.60%
	X(Biomass) ->Y(Topography)	0.0466	0.0011	1.85%
Eichhonia crassipes	X(Topography) ->Y(Biomass)	0.715	0.5115	7.26%
	X(Biomass) ->Y(Topography)	0.0531	0.3428	Not Significant
Polygonum spp	X(Topography) ->Y(Biomass)	0.0406	0.000362	12.97%
	X(Biomass) ->Y(Topography)	0.0013	0.000793	0.03%
Colocasia esculenta	X(Topography) ->Y(Biomass)	0.0444	0.00048	4.26%
	X(Biomass) ->Y(Topography)	0.000777	0.000783	Not Significant
Trees	X(Topography) ->Y(Biomass)	0.0323	0.0042	2.47%
	X(Biomass) ->Y(Topography)	0.000412	0.000471	Not Significant
			70% data	
Vegetation		T	Threshold T	(T-ThresholdT)/H(Y)
SAVs	X(Topography) ->Y(Biomass)	0.2142	0.2538	Not Significant
	X(Biomass) ->Y(Topography)	0.3666	0.2682	3.82%
Potamogeton nodosus	X(Topography) ->Y(Biomass)	0.4936	0.7096	Not Significant
	X(Biomass) ->Y(Topography)	0.6	0.7772	Not Significant
Nelumbo lutea	X(Topography) ->Y(Biomass)	0.0181	0.00066	2.13%
	X(Biomass) ->Y(Topography)	0.0953	0.0013	3.64%
Eichhonia crassipes	X(Topography) ->Y(Biomass)	0.6402	0.5223	4.33%
	X(Biomass) ->Y(Topography)	0.063	0.2852	Not Significant
Polygonum spp	X(Topography) ->Y(Biomass)	0.0052	0.000262	6.36%
	X(Biomass) ->Y(Topography)	0.001	0.000584	0.03%
Colocasia esculenta	X(Topography) ->Y(Biomass)	0.0465	0.00055	4.81%
	X(Biomass) ->Y(Topography)	0.000646	0.000753	Not Significant
Trees	X(Topography) ->Y(Biomass)	0.0373	0.005	2.58%

	X(Biomass) ->Y(Topography)	0.00057	0.000572	Not Significant
		50% data		
Vegetation		T	Threshold T	(T-ThresholdT)/H(Y)
SAVs	X(Topography) ->Y(Biomass)	0.2369	0.3399	Not Significant
	X(Biomass) ->Y(Topography)	0.3721	0.3262	1.77%
Potamogeton nodosus	X(Topography) ->Y(Biomass)	0.5398	0.7599	Not Significant
	X(Biomass) ->Y(Topography)	0.5895	0.927	Not Significant
Nelumbo lutea	X(Topography) ->Y(Biomass)	0.0136	0.000837	1.56%
	X(Biomass) ->Y(Topography)	0.0993	0.0018	3.77%
Eichhonia crassipes	X(Topography) ->Y(Biomass)	0.4537	0.4381	0.71%
	X(Biomass) ->Y(Topography)	0.2491	0.7451	Not Significant
Polygonum spp	X(Topography) ->Y(Biomass)	0.0123	0.000468	5.38%
	X(Biomass) ->Y(Topography)	0.0034	0.00094	0.14%
Colocasia esculenta	X(Topography) ->Y(Biomass)	0.017	0.000994	1.56%
	X(Biomass) ->Y(Topography)	0.000797	0.000875	Not Significant
Trees	X(Topography) ->Y(Biomass)	0.0342	0.0055	2.56%
	X(Biomass) ->Y(Topography)	0.000219	0.000791	Not Significant

Table 3.2. Transfer entropy (T) with different percentage data used for each vegetation class considered in the analysis. The T, Threshold T are in unit of bits, and H(Y) denotes the Shannon entropy of the sink variable. Threshold T is calculated with 95% confidence. For all of the transfer entropy statistics, the X dataset comes from 2009 (with the exception of elevation change, which is computed as the 2013-2009 difference), while the Y dataset comes from 2013.

			Bins = 8	
Vegetation		T	Threshold T	(T-ThresholdT)/H(Y)
SAVs	X(Topography) ->Y(Biomass)	0.0663	0.0984	Not Significant
	X(Biomass) ->Y(Topography)	0.201	0.0943	4.70%
Potamogeton nodosus	X(Topography) ->Y(Biomass)	0.2857	0.43	Not Significant
	X(Biomass) ->Y(Topography)	0.3084	0.4579	Not Significant
Nelumbo lutea	X(Topography) ->Y(Biomass)	0.0181	0.000274	3.68%
	X(Biomass) ->Y(Topography)	0.0317	0.000437	1.38%
Eichhonia crassipes	X(Topography) ->Y(Biomass)	0.4215	0.176	13.14%
	X(Biomass) ->Y(Topography)	0.0454	0.1636	Not Significant
Polygonum spp	X(Topography) ->Y(Biomass)	0.001	0.000109	2.93%
	X(Biomass) ->Y(Topography)	0.000514	0.000438	0.01%
Colocasia esculenta	X(Topography) ->Y(Biomass)	0.0375	0.00023	7.89%
	X(Biomass) ->Y(Topography)	0.000281	0.000354	Not Significant
Trees	X(Topography) ->Y(Biomass)	0.017	0.0018	1.69%

	X(Biomass) ->Y(Topography)	0.000149	0.000214	Not Significant
			Bins = 9	
Vegetation		T	Threshold T	(T-ThresholdT)/H(Y)
SAVs	X(Topography) ->Y(Biomass)	0.141	0.143	Not Significant
	X(Biomass) ->Y(Topography)	0.243	0.1335	4.54%
Potamogeton nodosus	X(Topography) ->Y(Biomass)	0.4368	0.5179	Not Significant
	X(Biomass) ->Y(Topography)	0.3876	0.5521	Not Significant
Nelumbo lutea	X(Topography) ->Y(Biomass)	0.0096	0.000371	1.37%
	X(Biomass) ->Y(Topography)	0.0516	0.0009	2.09%
Eichhonia crassipes	X(Topography) ->Y(Biomass)	0.4017	0.2133	9.51%
	X(Biomass) ->Y(Topography)	0.0637	0.1833	Not Significant
Polygonum spp	X(Topography) ->Y(Biomass)	0.0032	0.000143	5.75%
	X(Biomass) ->Y(Topography)	0.000423	0.00035	0.01%
Colocasia esculenta	X(Topography) ->Y(Biomass)	0.0463	0.000331	5.47%
	X(Biomass) ->Y(Topography)	0.000344	0.000476	Not Significant
Trees	X(Topography) ->Y(Biomass)	0.0262	0.0025	2.29%
	X(Biomass) ->Y(Topography)	0.000192	0.000309	Not Significant
			Bins = 11	
Vegetation		T	Threshold T	(T-ThresholdT)/H(Y)
SAVs	X(Topography) ->Y(Biomass)	0.1547	0.2249	Not Significant
	X(Biomass) ->Y(Topography)	0.2726	0.2166	2.09%
Potamogeton nodosus	X(Topography) ->Y(Biomass)	0.4677	0.6702	Not Significant
	X(Biomass) ->Y(Topography)	0.4767	0.7856	Not Significant
Nelumbo lutea	X(Topography) ->Y(Biomass)	0.0169	0.000589	1.78%
	X(Biomass) ->Y(Topography)	0.073	0.000994	2.67%
Eichhonia crassipes	X(Topography) ->Y(Biomass)	0.5388	0.357	7.89%
	X(Biomass) ->Y(Topography)	0.0994	0.3453	Not Significant
Polygonum spp	X(Topography) ->Y(Biomass)	0.0109	0.000225	8.59%
	X(Biomass) ->Y(Topography)	0.001	0.000588	0.02%
Colocasia esculenta	X(Topography) ->Y(Biomass)	0.0544	0.000507	5.59%
	X(Biomass) ->Y(Topography)	0.0016	0.000791	0.04%
Trees	X(Topography) ->Y(Biomass)	0.0333	0.0043	2.26%
	X(Biomass) ->Y(Topography)	0.000318	0.000592	Not Significant
			Bins = 12	
Vegetation		T	Threshold T	(T-ThresholdT)/H(Y)
SAVs	X(Topography) ->Y(Biomass)	0.2203	0.2634	Not Significant
	X(Biomass) ->Y(Topography)	0.3177	0.2458	2.65%

Potamogeton nodosus	X(Topography) ->Y(Biomass)	0.5669	0.7884	Not Significant
	X(Biomass) ->Y(Topography)	0.6565	0.9032	Not Significant
Nelumbo lutea	X(Topography) ->Y(Biomass)	0.0164	0.000713	1.59%
	X(Biomass) ->Y(Topography)	0.0841	0.0012	2.93%
Eichhonia crassipes	X(Topography) ->Y(Biomass)	0.4335	0.429	1.90%
	X(Biomass) ->Y(Topography)	0.098	0.4304	Not Significant
Polygonum spp	X(Topography) ->Y(Biomass)	0.0148	0.000298	7.40%
	X(Biomass) ->Y(Topography)	0.0018	0.00073	0.05%
Colocasia esculenta	X(Topography) ->Y(Biomass)	0.0566	0.000589	7.24%
	X(Biomass) ->Y(Topography)	0.0027	0.00097	0.07%
Trees	X(Topography) ->Y(Biomass)	0.0376	0.0051	2.34%
	X(Biomass) ->Y(Topography)	0.000359	0.000654	Not Significant

Table 3.3. Transfer entropy (T) with different number of bins for each vegetation class considered in the analysis. The T, Threshold T are in unit of bits, and H(Y) denotes the Shannon entropy of the sink variable. Threshold T is calculated with 95% confidence. For all of the transfer entropy statistics, the X dataset comes from 2009 (with the exception of elevation change, which is computed as the 2013-2009 difference), while the Y dataset comes from 2013.

3.4. Vegetation and topography transition analysis

While transfer entropy establishes the non-independence of pairs of variables (i.e., the existence of a "causal" relationship between them), it says nothing about how variables influence other variables (e.g. whether the relationship is positive, negative, or piecewise). To grapple with the nature of the dynamic interactions between topography and vegetation classes, we complemented the transfer entropy analysis with a vegetation and topography transition analysis. First, to evaluate temporal changes in vegetation classes, a vegetation transition matrix was calculated based on the vegetation classification maps. The number of 2 × 2-m cells transitioning from each class (Table 3.4) to each other class between 2010 and 2011 was tabulated and recorded in an 8 × 8 transition matrix.

Subsequently, a topographic change matrix was computed to evaluate how much elevation changed for each transition type. Within the cells undergoing each of the 64 (i.e., 8 × 8) possible transitions, the change in elevation between 2009 and 2013 was computed. Negative values represented a loss in elevation, and positive values represented a gain. The total elevation change for each transition type was then normalized by the total area of the transition type.

4 Results

4.1 Trends and transitions in elevation, surrogate biovolume, and vegetation class

Across the imaged area, sediment accreted by an average of 24.9 mm between 2009 and 2013, but with large variability across the delta (standard deviation of 25.2 mm). Net positive elevation changes occurred in all vegetation classes and were generally

highest in the lower portions of the delta (Table 3.4). Areas occupied consistently by open water and floating Potamogeton nodosus increased in elevation by 44-47 mm, while the highest areas, occupied by Salix nigra, increased by an average of just 2 mm. Meanwhile, across the whole study area biovolume changed by 1.47 % ± 19.47% from 2009 to 2013.

From 2009 to 2013, 32.6% of the imaged vegetation area transitioned to other vegetation classes (Table 2.4; Figure 2.9; and as discussed in Carle et al., 2014). Within individual vegetation classes, the percentage of areal coverage transitioning between 2010 and 2011 ranged from 5.60% (Salix nigra) to 98.63% (Colocasia esculenta). Most transitions happened between species with a similar topographic range and primarily at lower elevations within the tidal wedge. Transitions from lower-elevation classes to higher-elevation classes tended to occur in places where elevation gains were greater than average for that vegetation class (i.e., cells to the right of the diagonal in Table 2, with the exception of transitions from intertidal classes to Nelumbo lutea). Gains in elevation within SAV prompted shifts to Potamogeton nodosus and Nelumbo lutea, with a particularly large proportion (26.2%) transitioning to Nelumbo lutea. For example, the nonnative invasive species Eichhornia crassipes exhibited a relatively large increase in area, overtaking 48.9% of the 2010 area of Colocasia esculenta.

From \ To	Water and Others	SAVs	*Potamogeton nodosus*	*Nelumbo lutea*	*Eichhornia crassipes*	*Polygonum spp.*	*Colocasia esculenta*	Trees (*Salix nigra*)	Spatially Averaged
Water and Others	49.6 (82.84%)	29.7 (1.40%)	42.6 (0.59%)	42.0 (4.78%)	26.5 (7.12%)	32.4 (2.56%)	25.7 (0.38%)	18.5 (0.32%)	46.6 (17.16%)
SAVs	37.6 (53.73%)	12.5 (10.34%)	35.6 (1.88%)	24.4 (26.18%)	35.9 (5.71%)	33.0 (0.30%)	33.6 (1.49%)	28.3 (0.37%)	31.3 (89.66%)
Potamogeton nodosus	47.5 (72.38%)	27.7 (8.36%)	40.9 (10.66%)	42.3 (7.22%)	28.5 (1.11%)	44.2 (0.05%)	54.5 (0.20%)	42.5 (0.01%)	44.6 (89.34%)
Nelumbo lutea	33.6 (32.33%)	28.2 (6.82%)	27.5 (0.85%)	24.6 (50.19%)	34.6 (6.97%)	33.2 (0.22%)	34.1 (1.59%)	29.5 (1.03%)	28.7 (49.81%)
Eichhornia crassipes	27.0 (10.70%)	13.8 (0.17%)	67.6 (0.02%)	29.3 (5.20%)	11.3 (65.70%)	16.2 (15.85%)	11.9 (1.55%)	24.7 (0.81%)	14.8 (34.30%)
Polygonum spp.	20.2 (4.06%)	25.6 (0.06%)	26.5 (0.01%)	28.1 (1.26%)	13.2 (28.75%)	15.8 (64.77%)	11.8 (0.70%)	19.6 (0.39%)	15.4 (35.33%)
Colocasia esculenta	13.7 (33.76%)	21.2 (0.37%)	38.2 (0.10%)	29.0 (3.78%)	10.5 (48.92%)	7.9 (10.91%)	8.6 (1.37%)	6.8 (0.78%)	12.0 (98.63%)
Trees (*Salix nigra*)	4.4 (2.62%)	17.7 (0.06%)	-1.1 (<0.01%)	13.1 (0.79%)	9.6 (1.46%)	6.3 (0.55%)	10.5 (0.12%)	1.1 (94.40%)	1.5 (5.6%)

Table 3.4. The matrix of the mean elevation change (unit in mm/ m^2). The degree of change is colored from red (gain) to white (loss) for each vegetation type. The percentage of each class transitioning to the other classes is also calculated and shown in brackets. The spatially averaged elevation changes also calculated. The degree of change is represented by saturation of green and the percentage of area that underwent a transition to other type are shown in brackets.

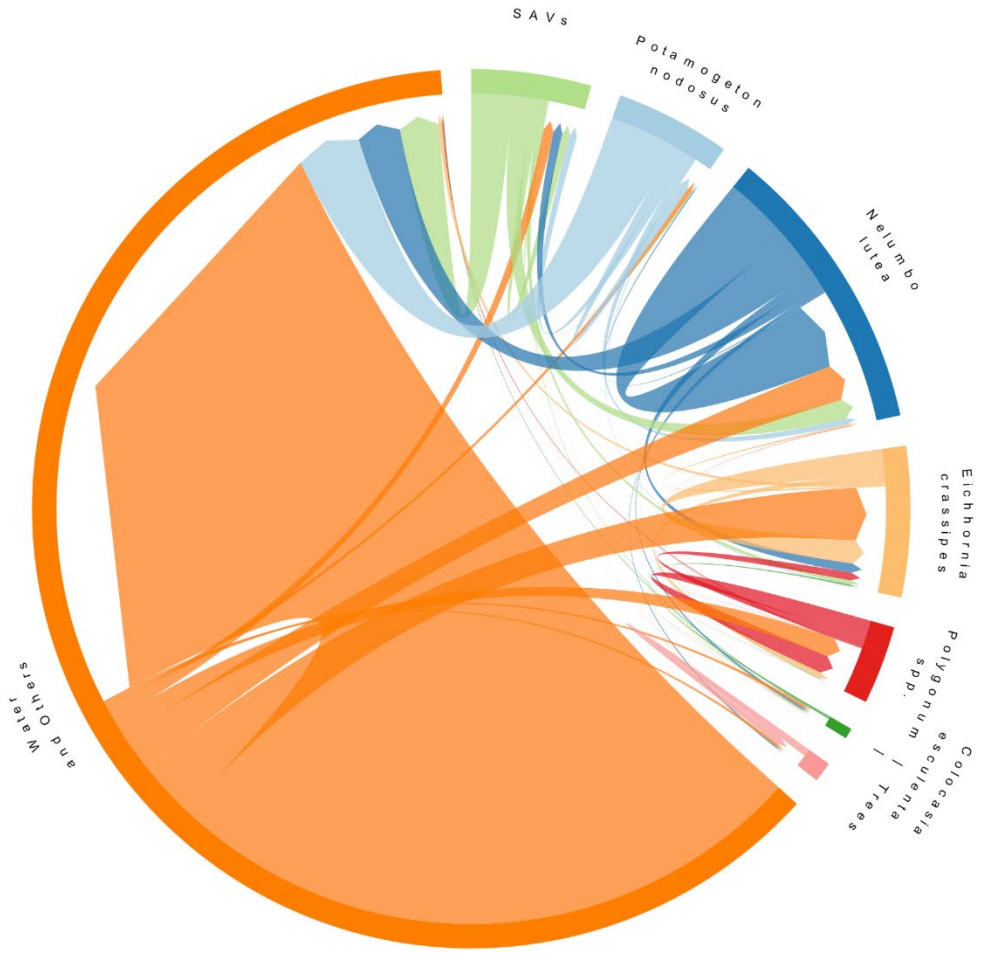

Figure 3.9. The vegetation transition map of each vegetation types. The color bar on the edge represents the vegetation type and the size of arrow represents the number of pixels for each transition. The arrows which point to themselves represent the pixels that remained unchanged.

4.2. Resolution of feedbacks and forcings between vegetation and sediment

Transfer entropy-based resolution of vegetation-sediment feedbacks indicated strong feedback between elevation and surrogate biovolume over all vegetation classes (Fig. 3.10A, Table 3.5). The transfer entropy from elevation to surrogate bio-volume exceeded the 95% confidence threshold and explains 1.30% uncertainty of bio-volume, and that from surrogate bio-volume to elevation explains 0.48% uncertainty of elevation. Meanwhile, elevation also exerted strong feedback with vegetation class. The transfer entropy from elevation to vegetation class exceeded the 95% confidence threshold and explains 1.61% uncertainty of vegetation class, while that from vegetation class to elevation exceeded the threshold and explains 2.36% uncertainty of elevation.

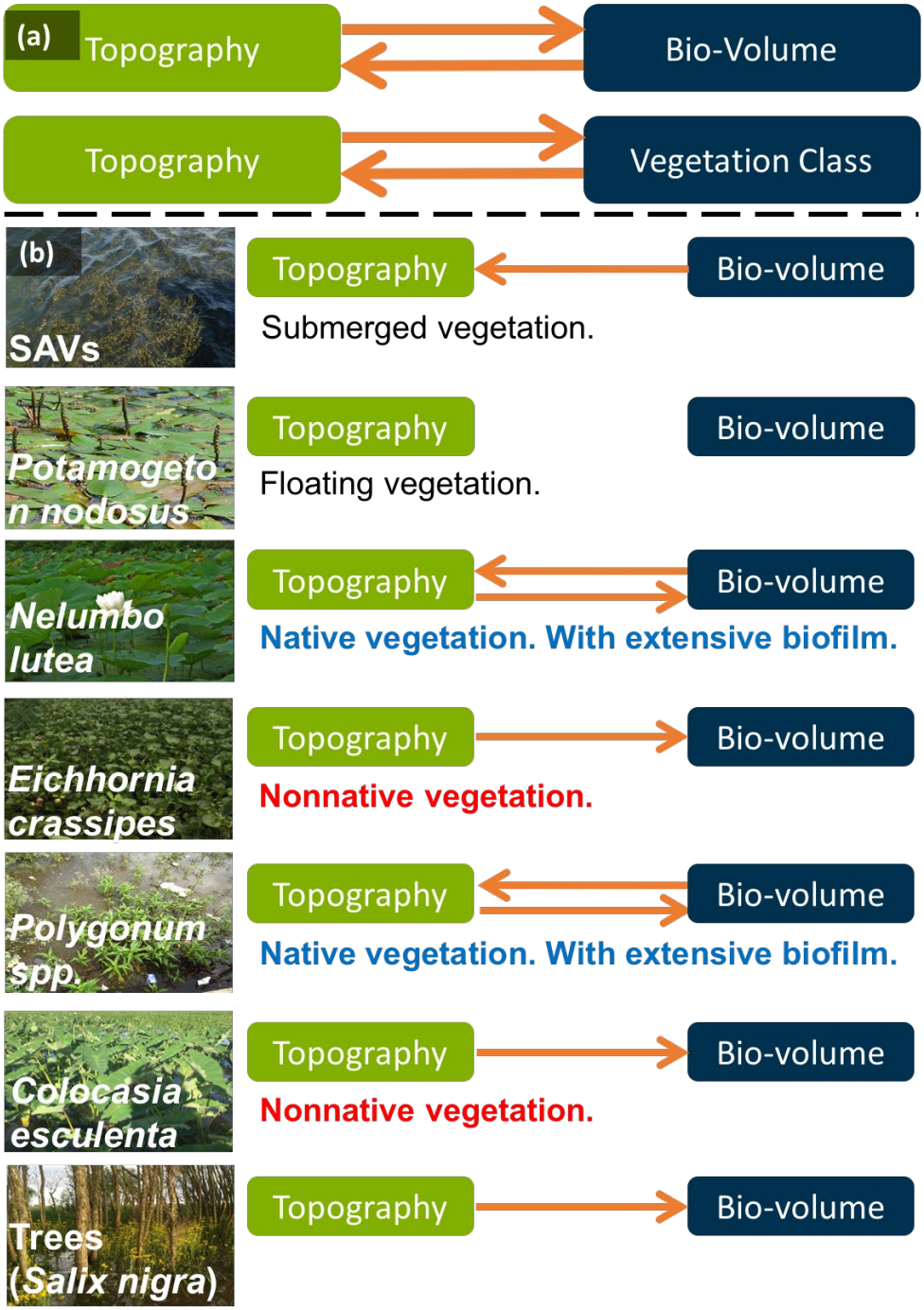

Figure 3.10. a) Feedback and forcing between elevation, surrogate bio-volume, and vegetation class, based on a transfer entropy analysis. b) Transfer entropy between elevation and surrogate bio-volume for each vegetation class considered. The orange line represents transfer entropy that passes the significance test with 95% confidence. The time lag between all depicted causal relationships is four years, as constrained by the LiDAR image acquisition in 2009 and 2013.

Transfer Entropy

Vegetation		T	Threshold T	(T-ThresholdT) /H(Y)	p-value
SAVs	X(Elevation) ->Y(Bio-volume)	0.1419	0.1811	Not Significant	-
	X(Bio-volume) ->Y(Elevation)	0.2261	0.1732	3.57%	<0.001
	X(Elevation change) ->(Bio-Volume)	0.6998	0.1697	22.44%	<0.001
Potamogeton nodosus	X(Elevation) ->Y(Bio-volume)	0.4681	0.5891	Not Significant	-
	X(Bio-volume) ->Y(Elevation)	0.5106	0.6756	Not Significant	-
	X(Elevation change) ->(Bio-Volume)	0.6725	0.5214	5.29%	<0.001
Nelumbo lutea	X(Elevation) ->Y(Bio-volume)	0.0138	0.000467	1.62%	<0.001
	X(Bio-volume) ->Y(Elevation)	0.0701	0.000766	2.69%	<0.001
	X(Elevation change) ->(Bio-Volume)	0.3278	0.00063	23.94%	<0.001
Eichhonia crassipes	X(Elevation) ->Y(Bio-volume)	0.4841	0.2712	9.37%	<0.001
	X(Bio-volume) ->Y(Elevation)	0.0652	0.2527	Not Significant	-
	X(Elevation change) ->(Bio-Volume)	0.2559	0.2891	Not Significant	-
Polygonum spp	X(Elevation) ->Y(Bio-volume)	0.0066	0.000183	7.81%	<0.001
	X(Bio-volume) ->Y(Elevation)	0.000702	0.00046	0.01%	<0.001
	X(Elevation change) ->(Bio-Volume)	0.0044	0.00026	3.45%	<0.001
Colocasia esculenta	X(Elevation) ->Y(Bio-volume)	0.046	0.0004	4.43%	<0.001
	X(Bio-volume) ->Y(Elevation)	0.000596	0.000597	Not Significant	0.051*
	X(Elevation change) ->(Bio-Volume)	0.055	0.000487	11.06%	<0.001
Trees (*Salix nigra*)	X(Elevation) ->Y(Bio-volume)	0.0326	0.0033	2.53%	<0.001
	X(Bio-volume) ->Y(Elevation)	0.000262	0.000418	Not Significant	-
	X(Elevation change) ->(Bio-Volume)	0.00051	0.00023	0.01%	<0.001

Vegetation	Mutual Information of Elevation Change & Bio-volume at 2009 I	Threshold I	(I-Threshold I)/$\overline{H(Y)}$
SAVs	1.1869	0.045	41.94%
Potamogeton nodosus	0.4291	0.2089	8.81%
Nelumbo lutea	0.6095	0.00013	45.56%

Eichhonia crassipes	0.8028	0.00013	28.68%
Polygonum spp	0.526	0.0012	56.44%
Colocasia esculenta	0.5714	0.00011	76.89%
Trees (*Salix nigra*)	0.8735	0.0618	46.58%

Table 3.5. Transfer entropy (T) and mutual information (I) for each vegetation class considered in the analysis. The T, Threshold T, I and Threshold I are in unit of bits, and H(Y) denotes the Shannon entropy of the sink variable. Threshold T and Threshold I are calculated with 95% confidence. For all of the transfer entropy statistics, the X dataset comes from 2009 (with the exception of elevation change, which is computed as the 2013-2009 difference), while the Y dataset comes from 2013.

* The transfer entropy from bio-volume to elevation of Colocasia esculenta is just below the 95% confidence level.

Vegetation classes exhibited a range of resolvable feedbacks and/or forcings. For the weak test of vegetation's influence on elevation (i.e., mutual information in Table 3.5), all vegetation classes had a significant influence on the change in elevation, with the classes highest in elevation having the strongest influence. Of these classes, Colocasia esculenta featured the highest significant relative mutual information, with an average of 76.89% of the information present in the temporal elevation change shared with that of the 2009 surrogate biovolume.

For the stronger test of feedback or forcing between vegetation canopy structure and topography (i.e., transfer entropies between elevation and biovolume), only a single, floating, vegetation class (Potamogeton nodosus) exhibited no resolvable feedback or forcing (Table 3.5). With the exception of Potamogeton and communities of submersed aquatic vegetation, elevation exerted a significant impact on surrogate biovolume within all vegetation classes. However, only classes at low to moderate (SAV, Nelumbo lutea, Polygonum spp.) elevation ranges had resolvable forcing from surrogate biovolume to elevation. In a spatial sense, the subtidal island interiors in younger parts of the delta exhibited one-way forcing from surrogate biovolume to elevation, while supratidal island heads and along-channel levees exhibited one-way forcing from elevation to surrogate biovolume. Meanwhile, bidirectional feedback occurred at moderate elevations intermediate between island interiors and higher-elevation near-channel levees, which occupied a larger proportion of older islands at the upstream end of the delta than the younger islands downstream (Figure 3.11).

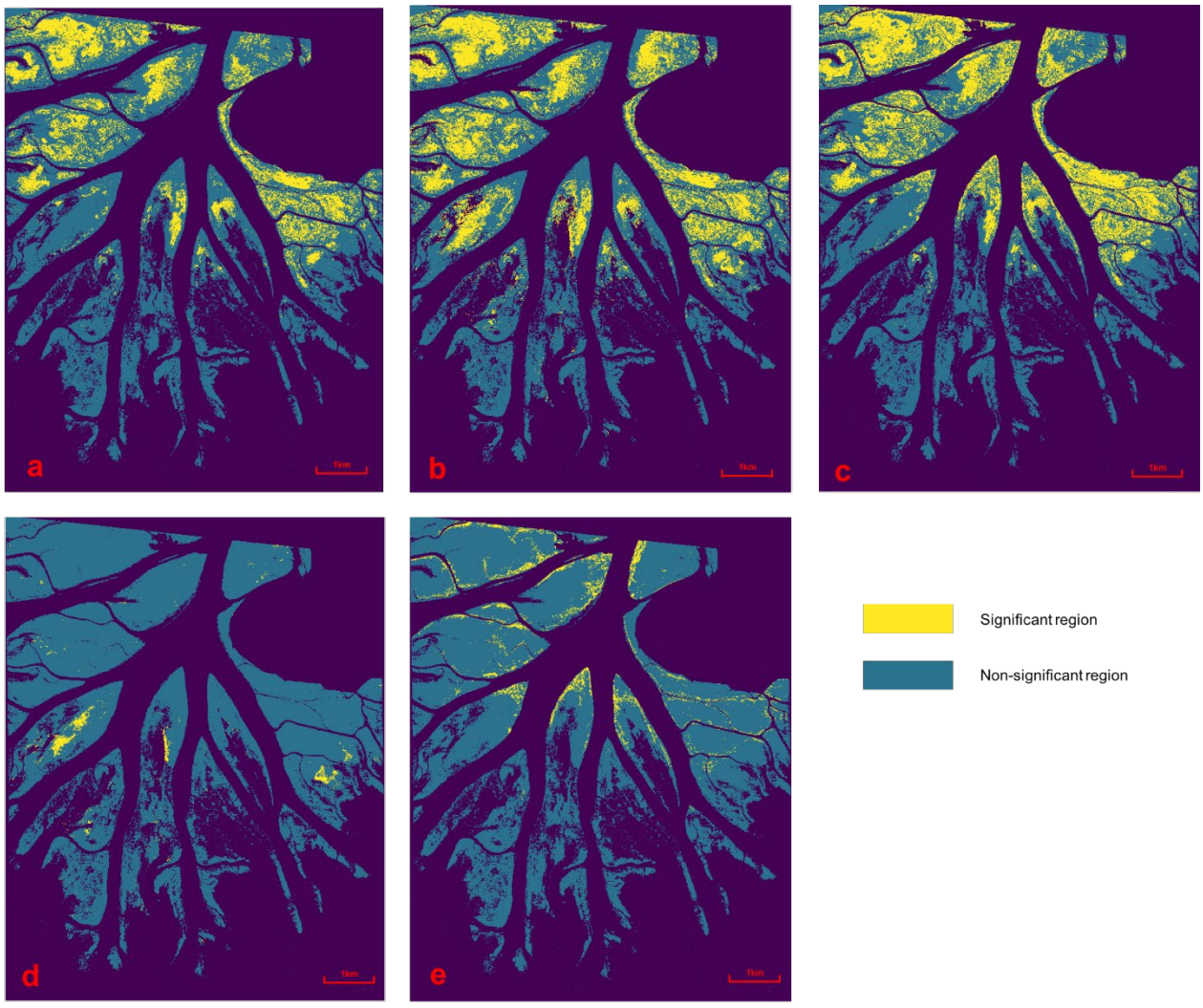

Figure 3.11. a) The map of the region with significant feedback between elevation and bio-volume. b) The map of the region with information significantly transferred from bio-volume to elevation. c) The map of the region with information significantly transferred from elevation to bio-volume. d) The map of the region with one-way forcing from bio-volume to elevation. e) The map of the region with one-way forcing from elevation to bio-volume.

Finally, in the test of how incremental deposition or erosion influenced vegetation surrogate biovolume characteristics (third row in each set of transfer entropy statistics in Table 3.5), elevation change significantly reduced uncertainty in the 2013 surrogate biovolume, independent of the 2009 biovolume, of all vegetation classes except for Eichhornia crassipes, with the caveat that for Salix nigra, the reduction in uncertainty was very small (0.01% of the uncertainty in biovolume). Within all vegetation classes, correlations between elevation change and the change in biovolume were positive (Figure 3.12), suggesting that deposition of sediment enhanced the volumetric growth of the canopy. The strength of the forcing was strongest for Nelumbo lutea and SAV, with a >20% reduction in the uncertainty of biovolume in both classes (Table 3.5). The relationship was slightly less strong in Colocasia esculenta, with an 11% reduction in the uncertainty of biovolume.

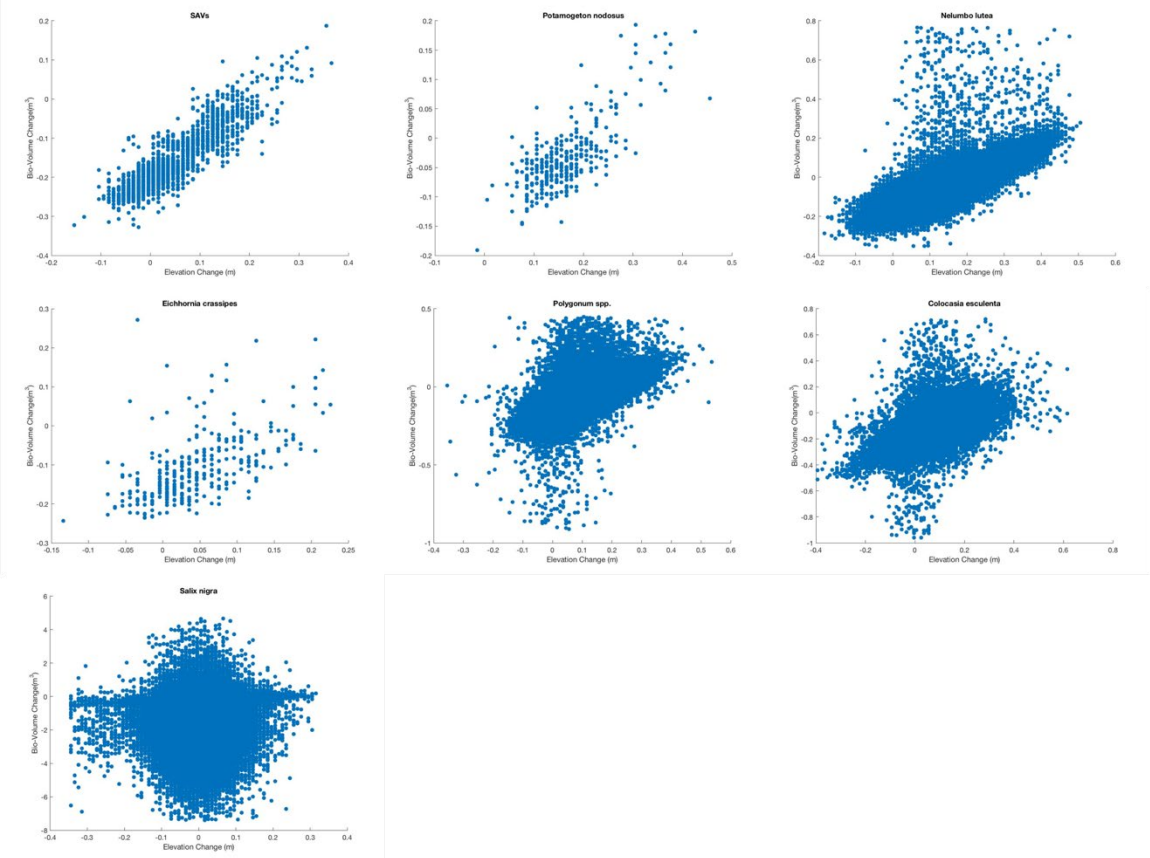

Figure 3.12. The relationship between topography change and surrogate Bio-Volume change of each vegetation type.

In summary, vegetation biovolume had a resolvable impact on deposition or erosion within all vegetation classes, but it was a dominant influence on marsh elevation only within rooted classes that occupy lower elevations (i.e., Nelumbo lutea and SAV). Strong ecogeomorphic feedback loops (i.e., bidirectional forcing between surrogate biovolume and elevation) were resolvable for classes only at moderate elevation ranges. At lower elevations (within SAV), only directional forcing from surrogate bio-volume to elevation was resolvable, whereas at higher elevations (within Colocasia esculenta and Salix nigra) and within the widely ranging floating invasive Eichhornia crassipes, forcing from elevation to surrogate biovolume was resolvable. While vegetation communities had a dominant influence on elevation over the four-year timescale of the experiment only at moderate elevations, nearly all vegetation canopies reduced uncertainty in deposition. Conversely, deposition amounts had a significant influence on surrogate biovolume in nearly all vegetation classes, particularly those low in the tidal range.

5 Discussion

5.1 Delta-scale resolution of ecogeomorphic feedbacks with information theory

The linkage between elevation, vegetation community composition, and canopy characteristics has been long recognized for coastal marshes. In the classic example, mean high water marks the elevation at which Spartina alterniflora, which occupies low elevations,

transitions to Spartina patens, a superior competitor that is limited by low rhizosphere oxygen content, in New England salt marshes (Bertness 1991). More recent studies have shown that the factors influencing salt marsh zonation are often complex, and that saturated and unsaturated flow and groundwater discharge may interact with salinity and elevation in determining vegetation distribution patterns (Silvestri, Defina et al. 2005, Wilson and Gardner 2006). Freshwater marshes, including deltaic freshwater marshes, have more diverse community compositions and even more complex patterns of zonation, often with overlap between communities. Nevertheless, the influence of elevation on species composition remains discernible and regionally consistent (Odum 1988, Leck and Simpson 1994).

The basic concept of marsh zonation is concerned with the one-way influence of elevation or other abiotic factors on vegetation distribution. Understanding of the feedback between vegetation species and topography along different portions of the marsh elevation/zonation gradient is less well developed, particularly for freshwater, deltaic marshes. In part, this knowledge gap is due to difficulties in resolving ecogeomorphic feedback from data. Primary difficulties include a disparity in the timescales over which vegetation-to-topography (slower) and topography-to-vegetation (faster) forcings act and high spatial variability in the effects of vegetation on topography, which are convolved with spatial variability in sediment supply and flow characteristics.

A spatial transfer entropy analysis based on LiDAR imagery is able to overcome many of the difficulties in resolving bidirectional feedback between vegetation and topography. The approach is particularly well suited for detection of noisy relationships (e.g., section 3.2.3). Transfer entropy does not presume the nature of the relationship between the pair of variables but provides a means to statistically distinguish between apparent correlations between variables A and B that are due to 1) A causing B, 2) B causing A, 3) a third factor C causing apparent synchrony between A and B or 4) feedback (bi-directional causality between A and B).

Here, the transfer entropy analysis was consistent with widespread understanding of marsh zonation, yet produced additional insight into which vegetation communities had the most dominant impacts on topographic change. With respect to the former, knowledge of marsh elevation at a previous time step reduced uncertainty in future vegetation class to a greater extent than knowledge of vegetation class at the previous time step (Figure 3.10A), suggesting that physical habitat had a dominant influence over biological facilitation (i.e., seed bank) in the dynamics of vegetation community distribution. This finding complements previous studies on vegetation succession in the Atchafalaya Delta (Shaffer, Sasser et al. 1992). The vegetation/topographic transition analysis provided additional support for this interpretation, showing that transitions in communities structured along an elevation gradient tended to be associated with consistent changes in elevation (Table 3.4). Further, in the transfer entropy analysis, elevation had a resolvable impact on the surrogate bio-volume of almost every vegetation class, except for those adapted to submersed conditions (SAV) and the floating Potamogeton nodosus class.

With vegetation class-specific analysis, surrogate biovolume shared significant mutual information with elevation change in all vegetation classes examined (Table 3.5), consistent with our hypothesis that canopy characteristics serve as a control on sedimentation and erosion. The normalized mutual information is greatest in Colocasia esculenta, suggesting that canopy characteristics are the primary factor explaining variability in sedimentation and that variability in sediment supply or flow characteristics plays a more minor role, unless correlated with the surrogate biovolume of Colocasia. On the channel-side and inner-side margins of the high marsh

platform (Salix nigra and Polygonum spp., respectively), the normalized significant mutual information decreases relative to Colocasia, but remains high compared to the low island interiors, where exposure to deeper waters or a wider range of flow velocities may coincide with more variability in sediment delivery or erosion. In particular, Salix nigra exhibits both areas of erosion and of deposition (Figure 3.12), consistent with observations and models of high-velocity routing of water around island heads and edges, which triggers erosion, together with deposition on the natural levees (Olliver and Edmonds 2017, Wagner, Lague et al. 2017, Bevington and Twilley 2018).

In the stronger test of the impact of ecogeomorphic feedback on marsh elevations (i.e., transfer entropies in Table 3.5), far fewer vegetation classes emerge as providing significant information to (i.e., reducing uncertainty in) elevation that is independent of past elevations. Although the mutual information analysis suggested that canopy characteristics are the dominant driver of variability in sedimentation within the high marsh platform, the transfer entropy analysis on elevation data suggests that, because of the higher rates of sedimentation in the low marsh, it is only within these vegetation classes that biovolume serves as a dominant driver of absolute elevation over the four-year timescale of analysis. On the other hand, in the high marsh and near channel edges, consistent spatial variability in flow patterns or production of organic matter (measured to be much greater in the high marsh than low marsh) may be more dominant controls on absolute elevation (Bevington and Twilley 2018).

Nevertheless, the absence of statistically significant transfer entropy from vegetation to elevation does not necessarily reflect a lack of ecogeomorphic feedback. For example, mats of Eichhornia crassipes are highly mobile, prone to transport by wind, tides, and, particularly, storm events. Its distribution at a snapshot in time, therefore, may not be representative of its distribution during the period of sediment accumulation captured between LiDAR image acquisitions. Further, the highly variable range of elevations over which Eichhornia crassipes occurs results in highly uncertain values of the elevation at which a canopy of particular biovolume will occur at a future time step, regardless of the sedimentation directly attributable to the vegetation canopy. Thus, significant transfer entropy may be a sufficient, while not necessary, requirement for resolution of ecogeomorphic feedback.

2.5.2 Do nonnative vegetation communities have similar ecogeomorphic function to native communities?

Our transfer entropy analysis suggests that ecogeomorphic feedback that has a substantial short-term impact on evolving topography was resolvable only within native vegetation communities that occur over low to moderate elevations (subtidal to intertidal) within the Wax Lake Delta. Within higher elevation ranges, Colocasia esculenta, which displaces a mixture of species such as Polygonum and Sagittaria spp., responds to elevation but does not significantly influence it (though its canopy structure does significantly impact spatial variability in deposition). Within lower vegetation ranges, Eichhornia crassipes and Potamogeton nodosus, which displace Nelumbo lutea and SAV, exhibit no resolvable influence on elevation, though as discussed above, their mobility may explain the lack of statistically significant transfer entropy.

Within lower vegetation ranges, Eichhornia crassipes and Potamogeton nodosus, which displace Nelumbo lutea and SAV, exhibit no resolvable control on elevation, despite the fact that they occur in zones with among the highest rates of deposition (Table 3.4). Though, as discussed above, their mobility may explain the lack of statistically significant transfer entropy, this analysis suggests that unmeasured factors such as variability in sediment supply or flow may

serve as a stronger control on elevations in the areas occupied by these vegetation classes than the biovolume of the vegetation canopy.

Vegetation morphology and the presence/absence of epiphyton may explain why, in the Wax Lake Delta, nonnative vegetation communities are not as functional at accreting sediment as native communities. The underwater biomass and blockage factors (important controls on sedimentation (Chen, Ortiz et al. 2012)) of floating Eichhornia crassipes and Potamogeton nodosus are low compared to SAV. Because the biomass of floating vegetation is concentrated in the upper portion of the water column, flows are forced preferentially closer to the bed, where they may inhibit sediment deposition (Wharton, Cotton et al. 2006). Studies in lakes and streams show that, for this reason, floating vegetation induces substantially lower sedimentation than emergent or submersed vegetation (Horppila and Nurminen 2005, Li, Pan et al. 2016). Colocasia esculenta contrasts with Eichhornia crassipes in that it is emergent in addition to having high densities, thus resulting in a high blockage factor and strong potential to promote accretion by decreasing flows and enhancing settling. However, its stem diameters are large (8-10 mm), particularly near the bed, where two distinct stems characteristically join into one large culm. Large-diameter stems may inhibit particle settling by setting a large characteristic eddy scale and promoting high turbulence intensities (Leonard and Luther 1995, Nepf 1999), which inhibit deposition within the patch (Chen, Ortiz et al. 2012, Follett and Nepf 2012, Ortiz, Ashton et al. 2013). Furthermore, direct capture efficiencies—defined as the ratio of particles transported within the upstream projected area of the vegetation stems to the particles that are permanently captured on vegetation stems—are inversely proportional to stem diameter (Palmer, Nepf et al. 2004).

Indeed, direct particle interception by stems, an often-neglected and/or potentially underestimated component of sedimentation budgets (Fauria, Kerwin et al. 2015) may contribute substantially to the resolved differences between vegetation classes in ecogeomorphic feedback strength. All of the classes with a statistically significant influence of surrogate bio-volume on topography have extensive epiphytic biofilm coverage, which, in our observations and in studies elsewhere (Gerbersdorf and Wieprecht 2015), has been noted to be associated with substantial fine sediment capture. In contrast, Colocasia esculenta stems are devoid of biofilm and hydrophobic, though both of these properties change when they senesce.

Though it remains unclear whether the mechanism behind differences in ecogeomorphic feedback strength is the purely physical effect of vegetation biovolume on flow or the presence/ absence of epiphytic biofilm, our results clearly suggest that efforts to control invasive Eichhornia crassipes in coastal marshes will likely have a payoff in higher sedimentation rates. Less sedimentation occurs at higher elevations, but if Colocasia esculenta could be prevented from invading high marsh vegetation communities, higher rates of sedimentation may also result, though investigations into belowground differences in organic matter production between Colocasia and the communities it displaces are warranted (Bevington and Twilley 2018).

5.3 Ecogeomorphic functional types and ecogeomorphic models of delta evolution

Above all, our analyses suggest that different vegetation communities play functionally different roles in landscape evolution. This insight contrasts with the common practice of representing vegetation in ecogeomorphic models as a single entity, even over a range of aquatic to upland elevations (Bertoldi, Siviglia et al. 2014). For example, models of river-floodplain evolution typically consider only the ecogeomorphic effects of trees (Murray and Paola 1997, Nicholas and Quine 2007, Nicholas 2013, Manners, Schmidt et al. 2013) whereas ecogeomorphic marsh models typically consider a single species of emergent marsh grass

(Kirwan and Murray 2007, Mariotti and Fagherazzi 2010, Larsen and Harvey 2011, Fagherazzi, Kirwan et al. 2012). In our data-driven analysis of the Wax Lake Delta, it was apparent that trees played a role different from that typically assigned in models of river/floodplain evolution, in which they typically act as stabilizing agents, diminishing erosion. Here, no significant forcing relationship from tree surrogate bio-volume to topography was resolved, consistent with others' observations of the erosion of island heads in the Wax Lake Delta (Carle, Sasser et al. 2013), and with the physically based understanding that large-diameter, sparse stems tend to enhance erosion rather than stimulate deposition (Follett and Nepf 2012, Liu and Nepf 2016). Numerical models suggest that, unless delta island heads are populated with vegetation with a high blockage factor, erosion within the heads may be high (Nardin, Edmonds et al. 2016).

Given the increasing availability of LiDAR data and principles and practices of open science that have made several transfer entropy toolboxes readily available (Ruddell and Kumar 2009, Larsen, Newman et al. 2017), it may become practical for modelers to use spatial transfer entropy as a screening tool to define the relevant ecogeomorphic functional types that should be included in a model of a particular floodplain or wetland of interest. Here, our analyses would suggest that almost every vegetation class considered has a distinct ecogeomorphic role that should be differentiated in a model, with the exception of Potamogeton nodosus, which could be reasonably left out of an ecogeomorphic model. Within such a model, it would be most critical to resolve detailed flow characteristics at lower to low-middle island elevations, where SAV and Nelumbo are abundant, as these communities exert the strongest influence on topographic change. Furthermore, within elevation zones, it is likely important to differentiate between the roles of multiple vegetation classes (e.g., Nelumbo vs. Eichhornia) rather than treating the entire elevation zone as a single ecogeomorphic entity. Whether interception or settling-dominated sedimentation is the most important process to represent within these classes, however, remains an open question.

5.4. Data and analysis limitations

In any attempt to detect or quantify feedbacks and forcings from data, it is important to be aware of sensitivities to timescale (Turnbull, Hochstrasser et al. 2014). One potential limitation of our study is that our analysis is derived from just two points in time (spaced four years apart). Limited sampling in time presents the risk that the period sampled is not representative of the set of external drivers that activate feedback and forcing over the timescale of delta evolution. Our analysis period was dominated by a major river flood that presented the opportunity to observe flow-sediment interactions in response to sediment delivery and/or erosion typical of major flood events and of intervening average cold front-induced disturbances (Figure 3.3) but not infrequent hurricane-type disturbance.

Information entropy analyses will also be sensitive to the time step evaluated. Short time steps (e.g., source images at a resolution of less than one year, or on the order of several years with below-average sedimentation events) may pose challenges in detecting feedback and forcing with transfer entropy, as the previous time step would expectedly reduce most of the uncertainty in the variable of interest, obscuring reductions in uncertainty by exogenous variables. On the other hand, with long time steps (e.g., five or more years, or even as little as a few years with several major disturbances), processes other than local ecogeomorphic feedbacks (e.g., localized patterns in wind, flow, or sediment deliver) may contribute more substantially to uncertainty in the response variable, manifesting as noise in an information entropy analysis and reducing the likelihood of detecting statistically significant ecogeomorphic interactions. At the same time, longer timescales of observation may allow for more sediment delivery to higher-

elevation locations, potentially resulting in detection of significant information flow from surrogate biovolume to elevation (though presumably with a lower magnitude of information transfer than for lower-elevation areas).

Last, it is also important to recognize that the ecogeomorphic feedbacks we have quantified here apply to the local (i.e., patch) scale, and that larger-scale feedbacks may be relevant to the evolution of deltaic islands. Olliver and Edmonds (Olliver and Edmonds 2017), for instance, found evidence supporting the hypothesis that intertidal (the elevation range from SAV and up to, but not including, Colocasia) and subaerial (the elevation range from Colocasia to Salix nigra) elevation platforms are alternative stable states, which self-organize to remarkably consistent elevations. This self-organization, in the face of local variability in the strength of ecogeomorphic feedbacks, may reflect larger-scale ecogeomorphic feedbacks, such as those arising from the effect of landscape configuration on regional flow fields (Larsen, Ma et al. 2017) or on the sediment (Nardin and Edmonds 2014) or particulate nutrient supply (Bouma, Van Duren et al. 2007) delivered to vegetated platforms. Prediction of delta evolution will ultimately require understanding of both the large-scale and local-scale ecogeomorphic feedbacks, with spatial transfer entropy providing an efficient means of identifying and quantifying local-scale feedbacks and interactions.

6 Conclusions

Here we have addressed questions about the strength of ecogeomorphic feedbacks responsible for vertical delta growth within different vegetation classes. To do so, we extended the transfer entropy approach for extracting causal interactions to spatial systems. The approach enables measurement of the relative strength, directionality and statistical significance of interactions between state variables of interest—here, surrogate bio-volume and elevation.

Based on our quantification of statistically significant feedbacks, we found that, in a spatially averaged sense, elevation exhibits strong feedback with surrogate biovolume in the Wax Lake Delta, a river-dominated delta ecosystem. In addition to bidirectional feedback between surrogate bio-volume and topography, we also resolved statistically significant forcing from topography to vegetation class, which is consistent with existing understanding of delta vegetation succession associated with elevation change. Within individual vegetation classes, the type of coupling between surrogate biovolume and elevation reflects the magnitude of sedimentation within vegetation canopies and the importance of elevation for plant growth. Here, native species tended to have strong feedback-dominated couplings, while invasive species had a forcing-dominated coupling, from elevation to biovolume. Native species with feedback-dominated couplings contributed most of the observed increase in elevation over the course of the study, whereas species with the forcing-dominated couplings contributed little to the observed elevation growth.

Chapter 4

Dust mediates CO2 - Temperature feedbacks over Pleistocene glacial - interglacial cycles

4.1 INTRODUCTION

The climate system has moved between glacial and interglacial stages in relatively consistent ~100 kyr cycles during the late Pleistocene (Petit et al. 1999), begging the question: What mechanisms control this consistent synchrony? These cycles are of significant interest because they imply self-regulation within the climate system and have significant implications for understanding and predicting potentially abrupt climate changes (Lenton et al. 2008).

The correlation analysis among greenhouse gases, temperature and other paleoclimate records have been well studied. The directionality, relative strength and statistical significance of each causal effects is still challenging to identify. CO2 is originally believed to lead the change of Antarctic temperatures based on the temporal scale (Fischer et al. 1999; Shackleton 2000). However, the lag used to identify the causality from CO2 to temperature is not able to be identified in the last deglaciation (Pedro et al. 2012; Shakun et al. 2012). The relation between variables could have different feedback status when system stationary changed. Even more complex, two variables could have mixed opposite feedbacks at the same time, instead of simple one-way forcing effect (Nes et al. 2015). For example, high CO2 concentration will amplify photosynthesis which will lead a negative feedback since photosynthesis takes up CO2. However, high temperature will amplify respiration, the release of CO2, leading to a positive feedback (Cramer et al. 2001). Additionally, high temperatures decrease the CO2-consuming process and CaCO3 neutralization process (Archer et al. 2004), and lastly will lead a positive feedback through releasing methane from the hydrate storages (Archer et al. 2009). But Martinez-Boti et al. (2015) have found carbon release from the oceans that precede the temperature changes in deglaciation. This complex system with multiple feedback scheme remains a major challenge to identify the causality roles of each paleoclimate variable.

The climate history as revealed by proxies from the Antarctic Vostok ice core shows a clear pattern during the past 420 kyr, in which glacial-interglacial cycles occurred with about 100 kyr periodicity (Petit et al. 1999) (Figure 3.1). The timing of glacial-interglacial transitions was previously found to be “closely correlated” with external orbital forcings such as the earth’s orbital eccentricity, whose average period is 93,000 years (Hays, Imbrie, and Shackleton 1976). Other studies have shown that climatic cycles “strongly correspond” to orbital precession and obliquity cycles (Berger 1978; Imbrie et al. 1992). However, none of those analyses were technically able to demonstrate the causal link between orbital and climate changes, which we address here for the first time by quantifying the direction and magnitude of information transfer within the system (see Chapter 1.).

Paleoclimate reconstructions record long-term climate dynamics, thus providing the opportunity to assess the evolutionary history of the climate system. Further, paleoclimate data can help reveal controlling mechanisms that regulate and stabilize the climate system (Washington et al. 2009). Most research has focused on the evolution of temperature and greenhouse gases, in particular CO2, suggesting that greenhouse gases principally drove temperature changes (Shakun et al. 2012; van Nes et al. 2015). Others linked dust directly to temperature by showing a highly synchronous relationship between the two (Lambert et al. 2008;

Martínez-Garcia et al. 2011; Winckler et al. 2008). Motivated by previous findings, we explore the role of atmospheric aerosols: in particular, how dust, through its enhancement of carbon sequestration, which capture carbon and storage CO2 and other form carbon in the long term, acts as a key mediator in the coupling between CO2 and temperature.

Dust has been hypothesized to regulate climate changes via two distinct mechanisms. First, dust directly affects the earth's energy balance through reflecting solar radiation (Claquin et al. 2003) and nucleating clouds, which then reflect incoming shortwave radiation and release long wave radiation (Yue et al. 2011). Second, dust carries macro- and micro-nutrients such as iron which can fertilize marine (Martin 1990) and terrestrial (Yu et al. 2015) ecosystem productivity. Subsequent settling of marine organisms and lithification of ocean sediments can sequester carbon from the short-term to the long-term carbon cycle. By affecting earth's CO2 balance via productivity, dust also indirectly exerts relatively short-term control on temperature.

Although the tight dust-to-climate connection has been widely perceived in various paleoclimate data and well acknowledged (Lambert et al. 2008; Winckler et al. 2008), the cause-and-effect relationships between dust and climate change, and their relevant time scales, have never been rigorously demonstrated (Martínez-Garcia et al. 2011). Previous studies largely relied on pairwise analysis (e.g., dust to temperature or dust to CO2) and linear regression with non-directional and non-causal analysis frameworks (Shakun et al. 2012; Lambert et al. 2008; Kohfeld et al. 2005). However, the climate system is characterized by nonlinear interactions that control directional feedbacks and emergent climate responses (van Nes et al. 2015) over a range of timescales. Here, we address these issues by applying a nonlinear technique used widely in information theory analyses to identify causal dynamics in complex systems, to directly "map" the interactions that constitute a climate network and the timescales over which they occur, and to identify drivers and regulators of climate changes during the last four climate cycles.

4.2 METHODS AND DATA

We used the Vostok ice core (Petit et al. 1999) records of local temperature, CO2, CH4, dust, Na, and July insolation at 65°N, eccentricity, obliquity, and precession (Ashkenazy et al. 2003) for the transfer entropy analysis. All-time series were interpolated to 1 kyr estimates. Transfer entropy is a causal inference technique that identifies forcing, feedback, or synchronous relationships via directed information transfer among pairs of variables. Information is defined here using Shannon's [1949] approach:

$$H = -\sum_i p(i) log_2 p(i). \qquad [4.1]$$

where p(xi) denotes the probability of the i th event in the series and H is in units of bits. Transfer entropy (T) is an asymmetric measure of information transfer between two random variables (Schreiber 2000). Given two-time series X = {x1, x2, . . ., xn}and Y = {y1, y2, . . ., yn}, T from X to Y can be computed using the following conditional entropies:

$$T_{X->Y} = \sum_{y_i, y_{i-k\Delta t}, x_{i-l\Delta t}} p(y_i, y_{i-k\Delta t}, x_{i-l\Delta t}) log_2 \frac{p(y_i \mid y_{i-k\Delta t}, x_{i-l\Delta t})}{p(y_i \mid y_{i-k\Delta t})} \qquad [4.2]$$

Where i is an instant in time, k and l are the block lengths of past values in X and Y, respectively, and τ and t are the time lags in X and Y, respectively.

The method of shuffled surrogates, which tells whether or not the information flow in a coupling is significantly higher than that randomly occurring between unrelated variables, is used to evaluate the statistical significance of information transferred among variables (Kantz and Schürmann 1996, Marschinski and Kantz 2002, Sabesan, Narayanan et al. 2003). To destroy

the spatial correlations, X^S and Y^S are formed from randomly shuffled X and Y. Surrogate transfer entropy $T^S(X^S \rightarrow Y^S)$ is computed 500 times by using Monte Carlo simulations. A one-tailed hypothesis test is used, in which T is deemed significant if:

$$T > \mu(T^S) + c \cdot \sigma(T^S), \qquad [4.3]$$

where $\mu(T^S)$ and $\sigma(T^S)$ are the mean and standard deviation of distribution of T^S. c =1.66 corresponds to 95% confidence (Ruddell and Kumar 2009). Here we considered the directional relationship between pairs of variables strong if the transfer entropy passed the shuffled surrogates significance test with at 95% confidence. When both directions are significant, the maximum information in the interested time range is used to determine the directionality. For example, if max (Tx → y) > max (Ty→ x), then X forces Y.

Theoretically, a complex system could be modeled with multiple transmitters and receivers between which information flows. The amount of information sent out by a transmitter is not necessarily equal to the amount of information received by the corresponding receiver, because information commonly is modified or lost during transfer. The actual amount of information transfer (from X to Y) is measured by the shared information between Y and time-lagged X minus the shared information between Y and its own history at a given time step.

Analogously, climate relevant variables including internal and external states and fluxes can be treated as information transmitters and receivers. The actual amount of information transfer between climate relevant states can then be mathematically quantified. More importantly, the information transfer from one climate variable to another is modified by other agents, as well as by system nonlinear and chaotic features. As a result, information can become distorted, lagged, or even dissipated during transfer, which might make the traditional linear-based causality inference technique (e.g., Granger causality) fail.

A climate feedback is defined as a bidirectional interaction such that a change of one state or flux can cause a change of another state or flux and vice versa. For example, atmospheric CO2 concentration affects temperature, and in return, temperature also affects atmospheric CO2 concentration. By definition, climate feedback is a bidirectional causality problem, which can be quantitatively and rigorously solved by bidirectional information transfer. “Information provider” means its information production is higher than information consumption. The net information transfer is always from provider to sink, meaning the former drives changes in the latter. The net information is calculated by subtracting total information significantly transferred from this variable from the total information significantly transferred to this variable. Similarly, in this study, information providers (Figures 4.2 pink nodes) drive the changes in information sinks (Figures 4.2 green nodes).

Time lag (τ) of information transfer from X to Y (Tx →y) means that when a certain event occurred in X, after time τ, Y responds. The observed time lag of information transfer is a mixture of several components. First is a physical time lag. For example, it takes time for Saharan dust to affect Amazon rainforest phosphorus dynamics (e.g., from atmospheric transportation time). Secondly, the observed time lag also contains the effects coming from climate system nonlinearity, chaos, and randomness that are not quantifiable by traditional lagged linear correlation analysis.

We analyzed climate system feedbacks by considering nonlinear interactions among variables hypothesized to affect climate that are recorded in the Vostok ice core (78°S, 106 °E) and orbital reconstruction histories, including: (1) external forcing: orbital and insolation changes; (2) greenhouse gases: CO2 and CH4; (3) climate state indicators: temperature and ice volume, which are directly from Vostok ice core (Lorius et al., 1985), based on the age model

from Bornola et al. (Bornola et al., 1991).and (4) aerosols: sea salt aerosol and dust (Figure 4.1). The abbreviation and the units of the variables used in this analysis are shown in Table 4.1.

We use first difference method to remove the trend of CH4, CO2, Dust, O18 and Na. Transfer entropy is implemented on the delta change among the climatological variables. Variable pairs that are obviously physically related (e.g. Insolation and Precession) are ignored in transfer entropy analysis. For physically obvious reasons, the directional transfer entropy from climatological variables to external forcing variables (e.g. from CO2 to Eccentricity) are also ignored.

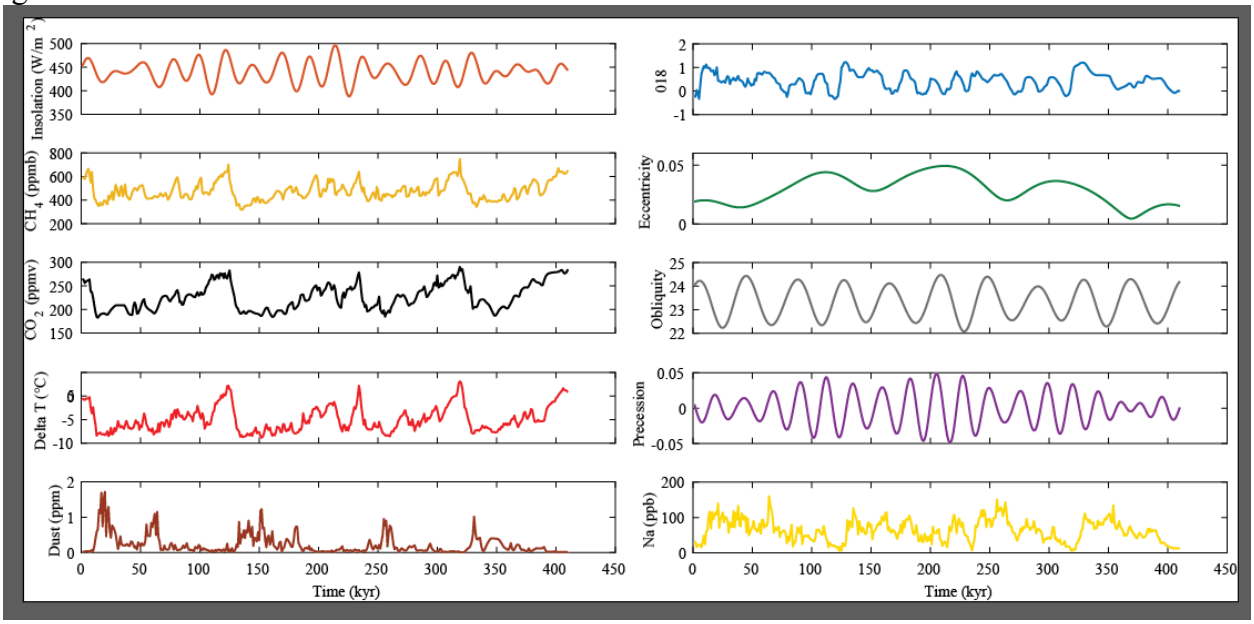

Figure 4.1: Time series data for Vostok ice core and orbital variables used in this study.

Table 4.1. The abbreviation and units of the variables used in this analysis

Variable	Abbreviation	Unit
Eccentricity	ECC	-
Obliquity	OBL	Degree (°)
Precession	PREC	Rad
Insolation	JanInsoS65	W/m^2
CO2	CO2	Parts per million by volume
CH4	CH4	Parts per billion
Delta T	T	$°C$
O18	O18	‰, parts per thousand

Na	Na	Parts per billion
Dust	Dust	Parts per million

4.3 RESULTS & DISCUSSION

4.3.1 OVERALL CLIMATE SYSTEM FEEDBACK

Here we use a process network (Ruddell and Kumar, 2009) to delineate the feedback patterns considering all possible variables. In the process network, variables are represented by nodes and the couplings between variables are represented as weighted directional links (Figure 4.2.). The process network captures the critical time scale, relative strength and directionality of the couplings in a complex system as a whole at the same time. The process network is able to identify the relationships that are usually not able to be detected using those methods analyzing one relationship at a time (Ruddell and Kumar, 2009). Despite more than four decades of research on ice and ocean sediment cores (Hays, Imbrie, and Shackleton 1976; Johnsen et al. 1972), a unifying framework for quantitatively analyzing dynamic climate system feedbacks has not been demonstrated.

The patterns of information flow within the climate system dynamically evolve, and are complicated by nonlinearity and chaotic features (Shukla 1998; Stenseth and Mysterud 2002; Ashkenazy et al. 2003). Our analysis reveals that, on average over all of the timescales analyzed (~o (100 kyr)), drivers of the climate system are the external forcings (eccentricity, precession, obliquity, and insolation), sea salt aerosol (Na), and ice volume (18O); responders to these drivers are temperature, greenhouse gases, and dust (Figure 4.2). Over these long timescales, dust is a central mediator (therefore its location in the middle of the network), collecting and re-distributing information within the climate system and consequently governing interactions between other variables. Historically, bidirectional feedbacks between temperature and CO2 have been widely investigated in terms of identifying driver-responder relationships (Shakun et al. 2012). In contrast, the system-scale feedback resolved here suggests that CO2 and temperature are not as simply coupled as previously thought (Shakun et al. 2012; van Nes et al. 2015; Lüthi et al. 2008); rather, their coupling is strongly mediated by the effects of dust, as described below.

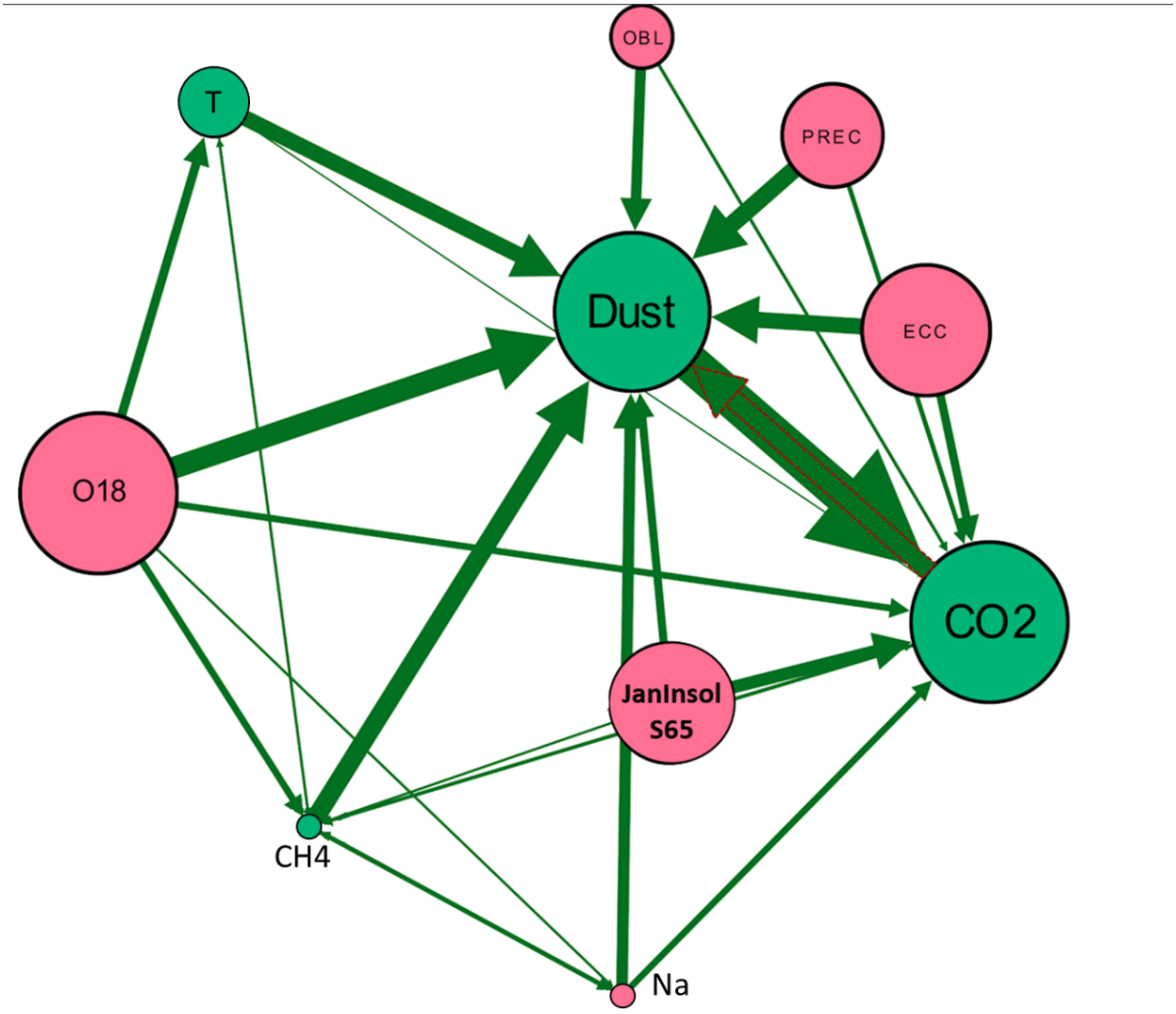

Figure 4.2. Feedback pattern of the climate system during the past 420 kyr. Size of each node represents net information flow divided by the number of connected nodes. Arrow size denotes magnitude of net information transfer over all timescales (also see **Figure 4.3**). Green nodes are information sinks (responders) and pink nodes are information sources (drivers). The distance between any two nodes is scaled with magnitude of net information transferred. (An arrow from CO_2 to Dust is edged as red dash line for visualization purpose)

4.3.2 EVOLUTIONARY VIEW OF CLIMATE SYSTEM FEEDBACKS

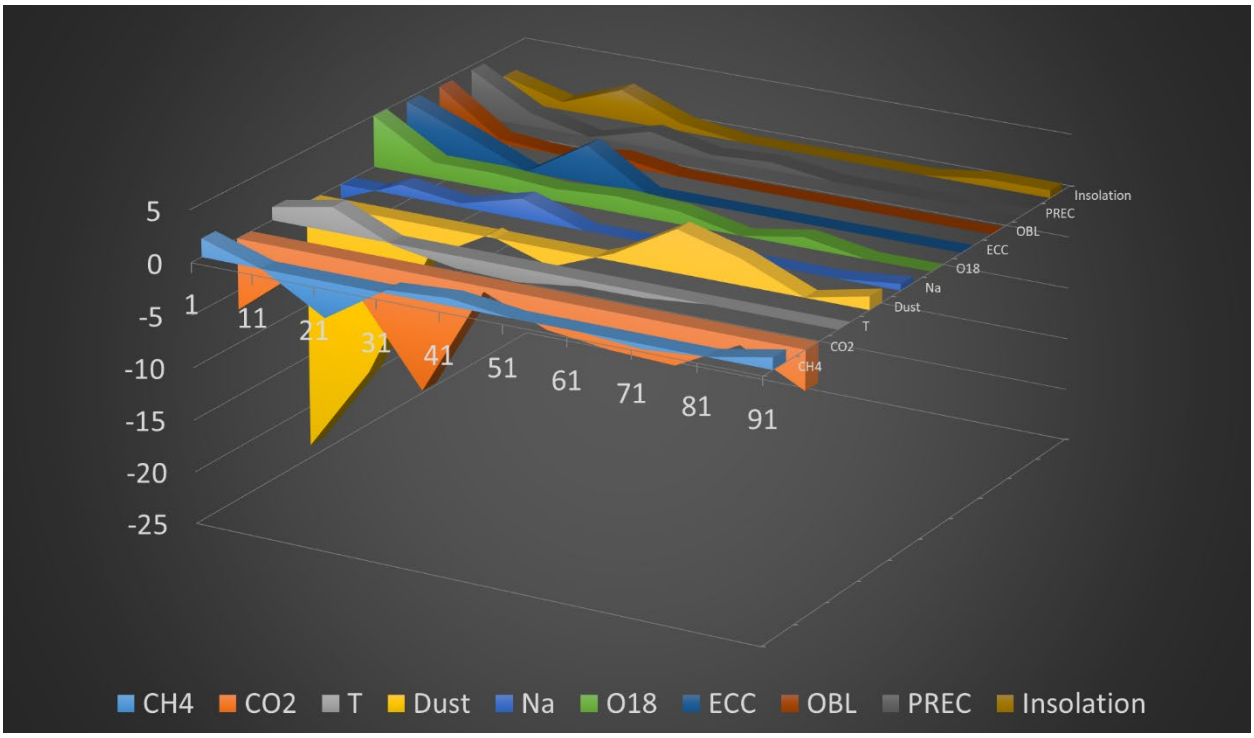

Figure 4.3. Time series of net information flow (positive means net production; negative means net consumption) for all variables.

Significant amounts of information originated from solar insolation, orbital obliquity, precession, and eccentricity (Figure 4.3) and flowed to dust and CO2 as shown by the arrows in Figure 4.2 and the net information flow in Figure 4.3. Information transfer metrics confirm that external forcings initially drove climate change. The information production from perturbations associated with those orbital forcings sharply declines with time lag, indicating that external forcings only initiated but were not responsible for sustaining the long-term climate system responses to changes in external drivers. Consistent with external forcings, ice volume (as inferred from ice 18O content) continued to amplify the initial orbital and insolation perturbations via ice-albedo feedbacks (McGehee and Lehman 2012; Wang and Mysak 2002; Gallée et al. 1992).

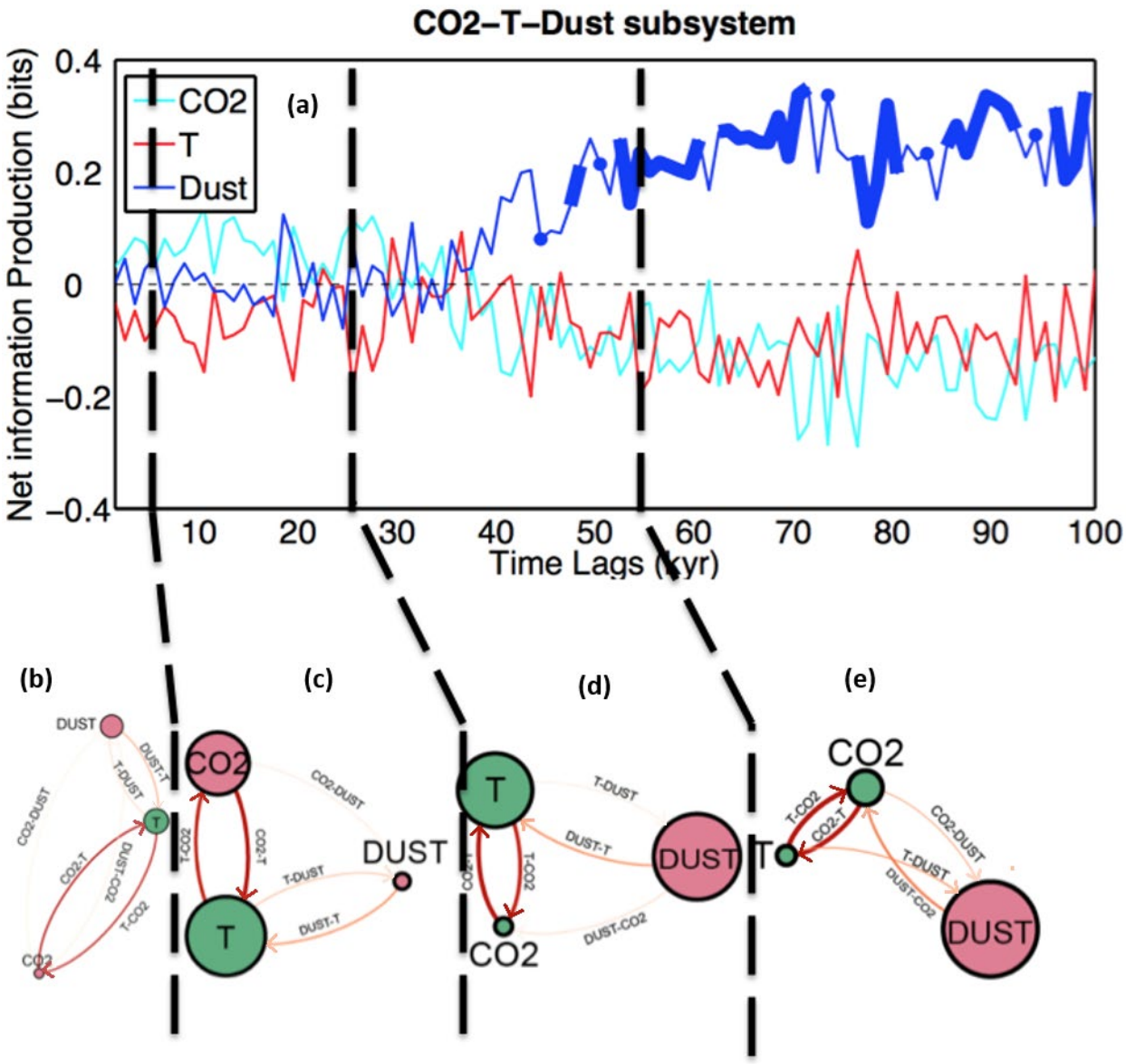

Figure 4.4. (a) Net information flow within CO_2-T-Dust tripartite subsystem. Thick lines indicate statistically significant (at the alpha = 0.05 level). (b - e) Thickness of lines represent strength of directional feedback, size of node denotes net information. Green nodes are information sinks (responders) and pink nodes are information sources (drivers). The CO_2-T-Dust tripartite exhibits dynamic behavior and involves four distinct stages: (b) initially, CO_2 and T exhibit loose coupling and CO_2 drove T; (c) strong internal coupling between CO_2 and T is established; (d) dust starts to affect both T and CO_2 significantly; and (e) dust dominates the system and supplied large amounts of information (about 40-60%; **Figure 4.5**) to sustain the strong coupling between T and CO_2.

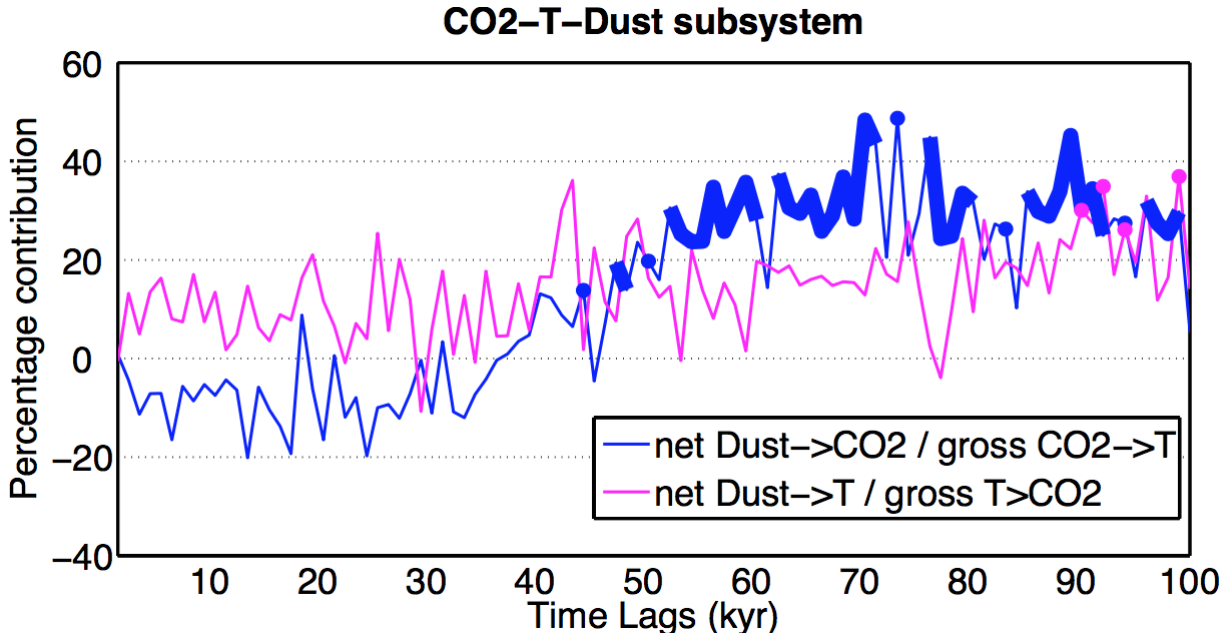

Figure 4.5. Relative contribution of dust to sustaining T and CO_2 coupling. The relative contribution is calculated through dividing net information that gain from dust by the gross information that transfer to the other. This relative contribution of dust delineates what the percentage of information that sustaining CO2 and T coupling is supplied by dust. Approximately 40-60% of information exchange between CO_2 and T is supplied by dust at long timescales. Thick lines indicate statistically significant (at the alpha = 0.05 level).

However, the effects of ice volume on the climate system are much weaker than those of dust over longer time lags (50 ~ 100 kyr beyond the initial perturbation). By analyzing the sum of the information flow over a band of 0 – 2kyrs lags of each climatological variable pair, external forcing variables (ECC, OBL, PREC) and O18 are serving as the primary information sources (Figure 4.3) and most of the information go to and storage in dust and CO2. Over times lags of up to 35 kyr beyond perturbations, CO2 and dust absorbed the most information in the climate system (Figure 4.2, Figure 4.3). Transfer entropy analysis is implemented on the tripartite subsystem formed by CO2, temperature and dust (Figure 4.4a, Figure 4.5). As shown in the series subplots in Figure 4.4 (b) to (e), the information flow accumulated within bands of relatively short time lag shows CO2 has a strong feedback correlation with temperature (represented by the arrows in figure 4.4(b)). Meanwhile, CO2 and dust serving as an information sources, which has positive net information flow (represented by pink circle) and temperature serve as the information sink (represented by green circle), which absorbs more information than it gains. The correlation of the tripartite subsystem changes along with taking a band of longer lags, as well as the role of dust and CO2. However, the temperature consistently serves as the information sink and drove by the dust and CO2 in this tripartite subsystem during each ~ 100 kyr climate cycle.

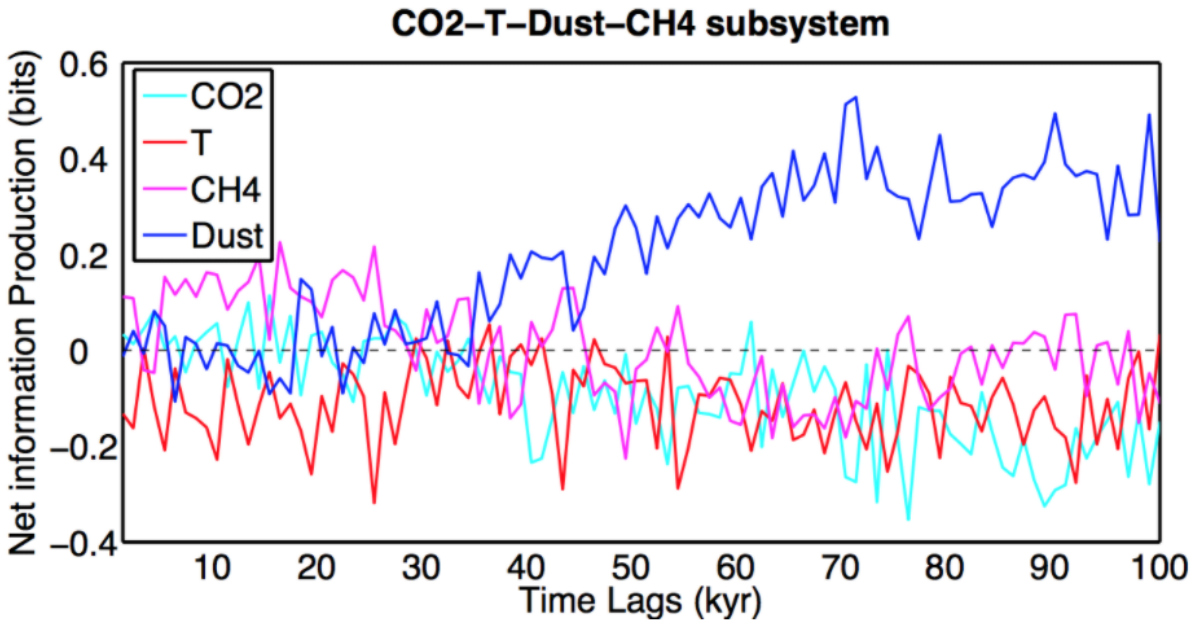

Figure 4.6. Net information flow within CO_2-T-Dust-CH_4 tripartite.

4.3.3 DYNAMICS OF CO_2-T-DUST TRIPARTITE SUBSYSTEM

Previous hypotheses that CO2 leads or causes temperature change were derived from lagged correlation analyses designed for linear systems (Montgomery, Peck, and Vining 2015) and may not be sufficient to resolve nonlinear (Ashkenazy et al. 2003), dynamic, two-way interactions between these variables (Shakun et al. 2012; Lüthi et al. 2008). Recent advances based on dynamical systems analysis demonstrate that CO2 and temperature have two-way interactions (van Nes et al. 2015), (i.e., temperature and CO2 mutually affect each other at different times within the last 420 kyr). Our results are consistent with this finding (Figure 4.7 (a) bar 12 CO2->delta T and (b) bar 11 delta T -> CO2) and further highlight that dust acted as a key mediator of more complex interactions between temperature and CO2 (Figure 4.4a).

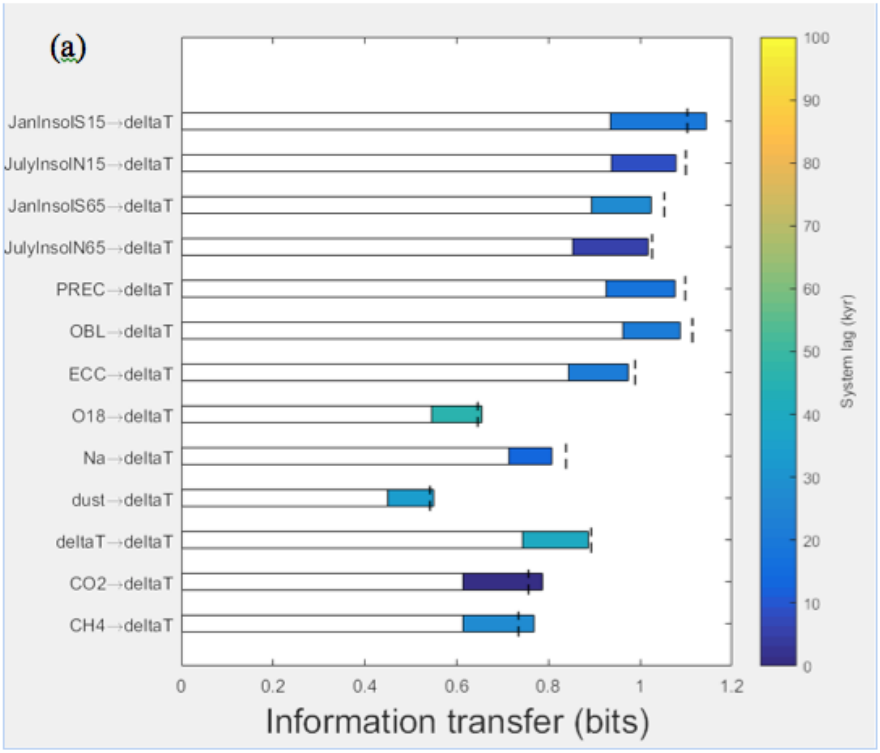
(a)
JanInsolS15→deltaT
JulyInsolN15→deltaT
JanInsolS65→deltaT
JulyInsolN65→deltaT
PREC→deltaT
OBL→deltaT
ECC→deltaT
O18→deltaT
Na→deltaT
dust→deltaT
deltaT→deltaT
CO2→deltaT
CH4→deltaT
0
0.2
0.4
0.6
0.8
1
1.2
Information transfer (bits)
System lag (kyr)
100
90
80
70
60
50
40
30
20
10
0

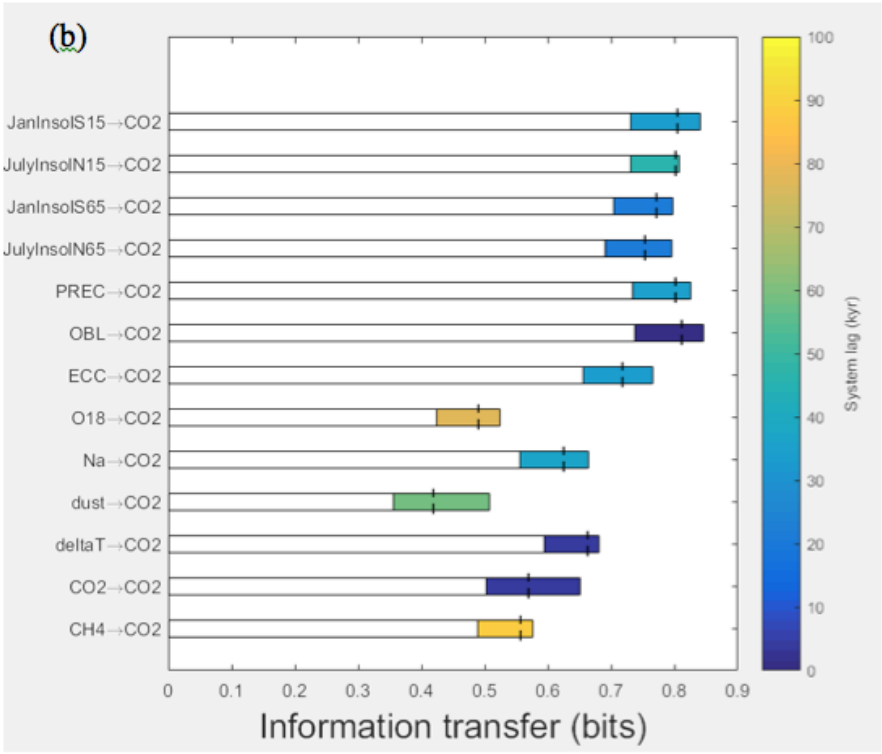
(b)
JanInsolS15→CO2
JulyInsolN15→CO2
JanInsolS65→CO2
JulyInsolN65→CO2
PREC→CO2
OBL→CO2
ECC→CO2
O18→CO2
Na→CO2
dust→CO2
deltaT→CO2
CO2→CO2
CH4→CO2
0
0.1
0.2
0.3
0.4
0.5
0.6
0.7
0.8
0.9
Information transfer (bits)
System lag (kyr)
100
90
80
70
60
50
40
30
20
10
0

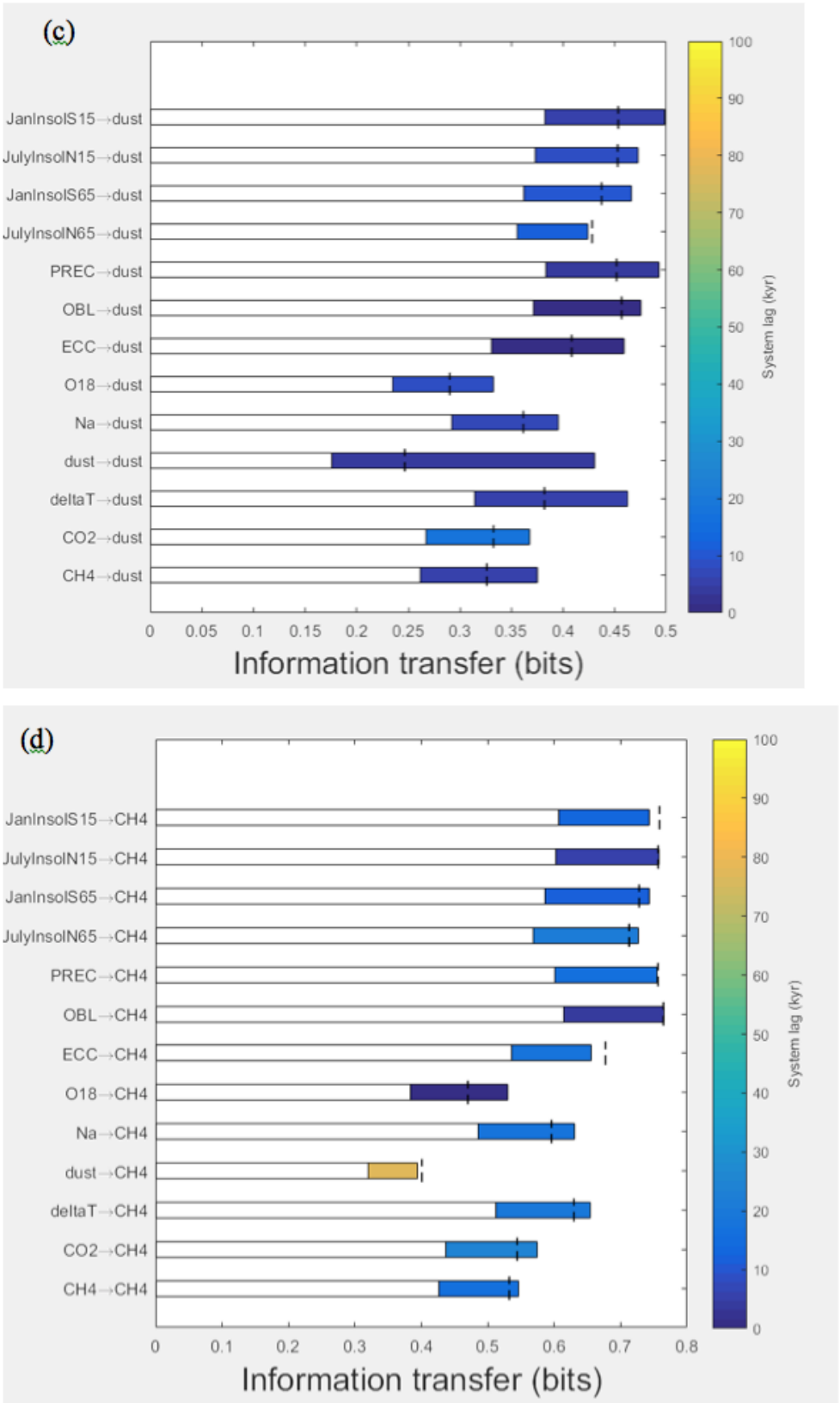

Figure 4.7. Information transfer from all variables to (a) temperature, (b) CO_2, (c) dust, and (d) CH_4.

Importantly, components of feedbacks within the CO2-T-Dust tripartite subsystem exhibit four distinct timescales (Figure 4.4b). First, within the band of short time lag (0-2 kyr), which accumulate the information flow from 0 time lag to 2 kyr time lag, temperature and CO2 were loosely coupled compared with later stages, indicated by the information flow between variables (thickness of lines connecting CO2 and temperature in Figure 4.4b). At this stage, temperature is jointly driven by CO2 and dust, through direct radiative forcing effects (Claquin et al. 2003; Takemura et al. 2009; Yue et al. 2011). During the second stage (time lag 3-25 kyr), the strong coupling between temperature and CO2 was fully established (Shakun et al. 2012) with CO2 surpassing dust as the predominant driver for temperature. However, at the third stage (time lag 26-55 kyr), dust drove both CO2 and temperature and their internal coupling (note that CO2 and temperature became information sinks (green nodes)). Finally, in the fourth stage, (time lag 56-100 kyr), dust overwhelmingly regulated changes in CO2 and temperature, accounting for 40 - 60% of the information flow between CO2 and temperature (Figure 4.5). The impact of dust on temperature is relatively consistent over a broad band of time lags (56-100 kyr) (Figure 4.5 magenta line). However, dust impacts on CO2 tended to accumulate and become more significant over longer time periods. This increasing trend highlights long-term impacts of dust on land and ocean biological CO2 sequestration, and might be more significant than previously thought (Lambert et al. 2008; Winckler et al. 2008; Kohfeld et al. 2005; Maher et al. 2010; Wolff et al. 2006; Legrand et al. 1991). The accumulated information flow analysis is not necessarily mean the information is consistently transferred to the target variable with a uniform strength and velocity. The information could be hold by a third variable (information carrier) for a relatively long time and then released back to the system. For example, the dust could serve as an information carrier and be trapped in the ice during the glacier period and then released back to the system during the interglacial period.

Dust could potentially serve as a direct control on CO2 over long glacial-to-interglacial timescales for multiple hypotheses. First, dust could control CO2 through biogeochemical processes by changing of CaCO3 cycle and changing in marine productivity. By promoting sequestration of C in ocean sediments through the biological carbon pump. Carbon has higher transfer effectiveness into the deep ocean and taken away from the sea surface once fixed in the euphotic zone (Bopp et al. 2003). Both an increasement of major nutrients (PO_4^{3-} and NO_3^-) (Broecker, 1982) and increasement of utilization of surface nutrients by marine ecosystem could amplify the biological carbon pump and the reduce the atmospheric CO2 during the glacial times (Knox and McElroy, 1984; Sarmiento and Toggweiler, 1984; Siegenthaler and Wenk, 1984). Marine biota, like phytoplankton, which is depends on the supply of iron-rich dust, could lower the atmospheric CO2 in a dusty glacial period (Martin and Fitzwater, 1988; Coale et al, 1996; Boyd et al., 2000). Meanwhile, when followed by lithification, dust would make less C available for the short-term C cycle during the next interglacial. Second, high dust, especially for high iron-rich dust, could lower diatom Si/N or Si/C uptake ratios. (Brzezinski et al. 2002; Takeda, 1998) It could drive the Antarctic toward N-depletion with excess silicate remaining in surface waters. Matsumoto et al (2002) postulate the silicate rich water could be transported to the subtropics and lowers the CO2 by favoring diatoms growth.

4.4 CONCLUSIONS

The overall- and sub-system feedback patterns demonstrate that temperature and CO2 exhibit short-term (5 kyr) responses to external forcings (orbital eccentricity, precession, obliquity, and solar insolation) but that an internal feedback, the CO2-T-Dust subsystem, exerts control over the band of longer time lags (26-55 kyr). It implied that previous analyses of pairwise feedback between only temperature and CO2 may miss the role of internal feedbacks

involving other variables, thus hindering our understanding of the relative importance of a network of cause and effect relationships within the climate system.

Remarkably high dust deposition during glaciation has been observed and confirmed by different paleoclimate reconstructions (e.g., ice cores, marine sediments) (Martínez-Garcia et al. 2011; Petit et al. 1999; Winckler et al. 2008). However, the relationships between dust and climate are uncertain (Lambert et al. 2008; Martínez-Garcia et al. 2011; Kohfeld et al. 2005; Saigne and Legrand 1987; Legrand et al. 1991), ranging from, e.g., linearly synchronous (Lambert et al. 2008) to nonlinear (Martínez-Garcia et al. 2011). Here, we quantitatively demonstrated that (1) dust's role in regulating climate was asynchronous and more importantly, (2) dust's role dynamically evolved within ~100 kyr climate cycles and could potentially serve as a direct control on CO2 over long glacial-to-interglacial timescales.

Chapter 5:
Climate teleconnection revealed by transfer entropy

5.1 Background

Global and regional precipitation are associated with local water balance as well as interacting with remote forcings, such as large-scale circulation and advective moisture supply. The latter is often known as teleconnection of the climate system (Daniel et., al 1991). Understanding the remote control on regional precipitation is essential to better understand the local dynamics of precipitation trend and variability. For example, previous work has shown that climate indices (e.g. Pacific/ North American, Southern Oscillation Index, Niño series) have a significant correlation with precipitation in U.S. (Daniel et., al 1991; Ropelewski and Halpert 1988; Mock 1995; Barlow et., al 2000; Redmond and Koch 1991; and McCabe and Dettinger 1999), and that precipitation has an especially strong connection with sea surface temperature (Haylock et., al 2005).

Climate teleconnection often interacts with local precipitation feedbacks and thus raise critical challenges in quantitatively partitioning the driving factors of regional precipitation variation. For example, for West Sahel precipitation, two interacting mechanisms are widely studied: 1) warming SSTs weaken the land-ocean temperature contrast and force deep convection towards the ocean (Giannini et al., 2003), leading to reduction in continental moisture convergence, with its impacts intensified by 2) variation in moisture-driven vegetation interactions induced by the interrupted recycling of moisture through precipitation and evapotranspiration (Zeng et al., 1999). Charney (1977) and Zeng (1999) also proposed that barren soil with larger albedo leads to increased atmospheric subsidence and thereby decreased moisture convection and precipitation. Aerosols such as dust have relatively smaller effects on precipitation through increased mid-troposphere radiative heating, surface cooling, and ice and cloud condensation nuclei in comparison to SST and vegetation's impact (Huang et al., 2009; Hui et al., 2008). Some studies also conclude that the West African Monsoon influences the amount of moisture transported from the Atlantic to the Sahel region (Taylor, 2008). These remote and local feedback mechanisms associated with West Sahel precipitation warrant rigorous statistical analysis to accurately attribute the local precipitation variation to certain processes or factors.

However, most of the previous work only test the correlation between remote/local climate factors and the precipitation over region of interest; and map the spatial distribution of the correlation. Linear correlation could theoretically fail to detect teleconnections due to two major reasons: (1) climate system is highly nonlinear; (2) The effect on precipitation from climate factors is not necessary happened immediately, it could have time lag before anomalies 'effect reach different location and cause the change in precipitation (Schepen et., al 2011). For example, the linkage between El Niño sea surface temperature anomalies and precipitation in the US fluctuation has been proved by many studies (Ropelewski and Halpert 1986; Trenberth et al. 1988; Trenberth and Guellimot 1996; Bunkers et al. 1996;). The primary physical mechanism in this linkage is the change in tropical convection associated with the El Niño/ La Niña conditions and the subsequent change in atmospheric circulation through Rossby wave dispersion from the anomalous tropical convection (Hoskins and Karoly 1983). The signals of SST anomalies may not immediately affect the precipitation in the US, but absorbed and held

by the positive feedback with atmospheric circulation rather than direct moisture transport (Ting and Wang, 1997).

Even lagged correlations analysis has been used in many studies to detect teleconnections (Oldenborgh et al., 2000; Nicholls 1987; Mo and Livezey, 1986). The linear-based analysis still not able to detect the non-linear correlations (see Chapter 2) and distinguish the direct or indirect components (Zhou et al. 2015). Some nonlinear based approaches have been proved to be more effective in detecting teleconnections (Boers et al. 2013; Mukhin et al. 2018). For example, complex network has been used in analyzing climate time series data effectively (Tsonis et al., 2007; Yamasaki et al., 2008; Donges et al., 2009a; Malik et al., 2011; Steinhaeuser et al., 2012; Berezin et al., 2012). Nonlinear generalizations of PCA are also successfully applied in climate analysis (Ross et al. (2008); Gámez et al. (2004); Hannachi and Turner (2013); Hlinka et al. (2014); Pires and Ribeiro (2017). Meanwhile, transfer entropy method is ideal to analysis the time lagged correlation between climate factors and precipitation. It has been shown to be effective and efficient in broad range research (Vicente et., al 2011; Rubinov and Sporms 2010; Verdes 2005; Kleeman 2007; Hannisdal and Peters 2011). The time lag could be easily introduced into this computation to detect the effect time lag in analyzing these correlations (Schreiber 2000; Ruddell and Kumar 2009).

5.2 Case study 1. Sahel precipitation*

(*Liu, B. Y., Zhu, Q., Riley, W. J., Zhao, L., Ma, H., Van Gordon, M., & Larsen, L. (2019). Using Information Theory to Evaluate Directional Precipitation Interactions Over the West Sahel Region in Observations and Models. *Journal of Geophysical Research: Atmospheres*, *124*(3), 1463-1473.)

This case study published on Journal of Geophysical Research: Atmospheres in 2019 by Bessie Liu, Qing Zhu, William Riley, Lei Zhao, Hongxu Ma, Mollie Van Gordon and Laurel Larsen. Hongxu contribute to the design of methodology and results analysis. Here, part of the materials is included in this section as a use case for the application of transfer entropy in climate system with global spatial scale and decadal temporal scale. (Liu et al., 2019)

Water availability has historically been one of the most significant threats to African regional social and economic well-being. Over the Sahel region, a megadrought during the 1960s and 1970s induced by an abrupt and substantial rainfall reduction caused widespread famine and death. The post-drought recovery, which is still ongoing, has been characterized by gradual increases in rainfall, but with dramatic fluctuations. The large negative human impacts, slow recovery, and variability raise important questions of why and how rainfall dynamics evolve and interact with other components of the regional climate system. In this case study, we provide an observational assessment of regional mechanisms (informed by directional transfer of information entropy) that regulate Sahel rainfall.

5.2.1 Hypotheses

We focused on two prevailing hypotheses potentially responsible for West Sahel precipitation variation (Figure 5.1). First, warm sea surface temperatures weaken land-ocean temperature contrast and transfer deep convection to the ocean, which leads to precipitation decreases over land (Giannini et al., 2003). Second, terrestrial vegetation dynamics control water

(evapotranspiration) and energy (surface albedo) fluxes into the atmosphere and thus impact local precipitation (Zeng et al., 1999). Each hypothesized interactive pattern was upheld or falsified by quantifying directional information entropy transfer between West Sahel precipitation and (1) Sea Surface Temperature and (2) Leaf Area Index (LAI).

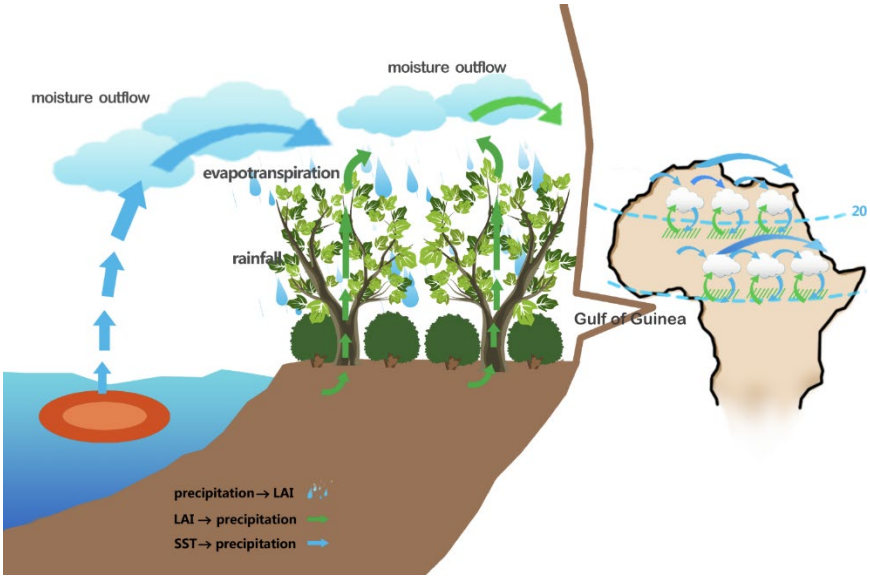

Figure 5.1. Conceptual model of hypothesized mechanisms that control variability in Sahelian precipitation: (1) The African West Sahel region receives moisture through low-level southwesterly flow from the Gulf of Guinea. Therefore, West Sahel precipitation is strongly controlled by SST variation over the Gulf of Guinea. (2) Vegetation growth in the West Sahel region is influenced by water availability and land surface vegetation dynamics that control water and energy fluxes into the atmosphere and therefore affect local precipitation. (Liu et al., 2019)

5.2.2 Data and model

Sea Surface Temperature in the Gulf of Guinea was provided by NOAA Optimum Interpolation (OI) Sea Surface Temperature (SST) V2 (Reynolds et al., 2002). This dataset combines daily in situ, bias corrected satellite retrieval (Smith and Reynolds, 1998), as well as modeled SST starting from 1981, and interpolates to a monthly time scale at a 1°×1° resolution. Since advective moisture from the Gulf of Guinea strongly controls West Sahel precipitation (Sultan and Janicot, 2003), we extracted and averaged the SST over the Gulf of Guinea (1W-8E, 0-5N) for our analysis.

For vegetation dynamics, we used GLASS Leaf Area Index (LAI) as a proxy, which was derived from Advanced Very High Resolution Radiometer (AVHRR) LAI, Moderate Resolution Imaging Spectroradiometer (MODIS) LAI, and CYCLOPES LAI using a neural network approach (Liang and Xiao, 2012). We defined the West Sahel region to be between 10 °N and 20 °N, and between 20 °W and 10 °E. The LAI product over this region, available since 1982, was extracted for each individual grid cell at a 0.5°×0.5° degree resolution.

Precipitation data came from Climate Research Unit (CRU ts3.2) from 1901 to 2014 (Harris et al., 2014). This product is gridded over two thousand precipitation stations onto

0.5°×0.5° resolution regular grids and provided a monthly climatology mean and anomaly over the West Sahel region.

Similar to the observations, we analyzed the monthly precipitation, LAI over the West Sahel region, and SST over the Gulf of Guinea from nine Earth System Models (ESMs) that participated in the CMIP5. We used historical emission-driven fully coupled simulations (esmhistorical) from bcc-csm1-1-m, CanESM2 (Chylek et al., 2011), CESM1-BGC (Lindsay et al., 2014), GFDL-ESM2G (Dunne et al., 2012), HadGEM2-ES (Collins et al., 2011), inmcm4 (Volodin et al., 2010), IPSL-CM5A-LR (Cattiaux et al., 2013), MPI-ESM-LR (Brovkin et al., 2013), and NorESM1-ME (Tjiputra et al., 2013).

Since we focused on precipitation variation and its underlying controls and interactions, we detrended all datasets by first removing the long-term trend with a 10-year moving average and then the seasonal cycle by subtracting the mean seasonal cycle averaged across the whole-time series. Next, we investigated the information entropy transfer between the residual (anomaly) time series.

Based on information theory, directional interactions (or causation) can be quantitatively measured by how much information entropy is transferred between variables (Schreiber, 2000; Shannon, 2001). First, we calculate Shannon Information Entropy (H, a measure of uncertainty, quantified in bits) of a variable (X) (i.e., SST over the Gulf of Guinea, LAI, or Precipitation):

$$H = -\sum_{x_i} p(x_i) log_2 p(x_i) \tag{5.1}$$

where xi is a possible value of variable X and p(xi) is the probability of xi within the whole time series X. Given two time series X [xi : i = 1:n] and Y [yj : j = 1:n] (e.g., Precipitation and SST), the directional information entropy transfer from X to Y (TX->Y) is a measure of the extent to which knowledge of X independently reduces uncertainty in Y's future behavior, once the reduction of uncertainty derived from knowledge of Y's own past behavior is accounted for. It is calculated as:

$$T_{X->Y} = \sum_{y_i, y_{i-k\Delta t}, x_{i-l\Delta t}} p(y_i, y_{i-k\Delta t}, x_{i-l\Delta t}) log_2 \frac{p(y_i \mid y_{i-k\Delta t}, x_{i-l\Delta t})}{p(y_i \mid y_{i-k\Delta t})} \tag{5.2}$$

where k and l refer to the block-length history of y and x on which estimates of uncertainty reduction of yi are conditioned. Here, we use k and l = one time step as a conservative choice (Ruddell and Kumar, 2009) and drop the superscript in future reference to these variables. $l\Delta t$ is the time lag over which X transfers information to Y. If the transferred entropy (in bits) is larger than a significance threshold, the directional impact was interpreted as statistically robust. The significance threshold is calculated by randomly shuffling the time series X and Y to destroy temporal relationships between the variables and computing the transfer entropy. The significance threshold is then selected as the α= 0.05 value from the Monte Carlo distribution of transfer entropies.

For this study, we define "interactions" under the climate change context to be significant bidirectional information exchange between two climate relevant variables; while "control" is unidirectional information flow from the source process to sink process. For example, if patterns in the precipitation time series ($x_{i-l\Delta t}$) significantly reduce uncertainty in future values of the LAI time series (y_i) beyond the reduction in uncertainty due to knowledge of LAI's history (yi-1), then unidirectional control of precipitation on LAI is identified. If directional control of LAI on local precipitation is similarly identified, a bidirectional "interaction" is identified. We evaluated information transfer between all pairs of variables at all possible lags $l\Delta t$ to test for the existence of hypothesized hydro-climatological interactions at the scale of the West Sahel. Here

we report the maximum amount of information transferred over all lags examined and its associated timescale.

5.2.3 Results and discussion

The African Sahel region receives moisture through low-level southwesterly flow from the South Atlantic Gulf of Guinea across the Southwestern coast of West Africa (Lamb, 1978; Sultan and Janicot, 2000). Strong advection of moisture over the West Sahel region and Guinea Coast often leads to corresponding precipitation changes (Nicholson and Webster, 2007). Therefore, to assess the influence of convection-driven moisture controls on precipitation, and vice-versa, we take a spatial range for the Gulf of Guinea to be [1 °W - 8 °E and 0 - 5 ° N].

Information transfer from SST over the Gulf of Guinea (averaged the SST values within [1 °W - 8 °E and 0 - 5 ° N]) to West Sahel precipitation was significant over 93% of analyzed West Sahel grid cells (Figure 5.2). In contrast, information transfer from West Sahel precipitation to SST over the Gulf of Guinea was much smaller; less than 1% of the grid cells transferred significant information, which is well below the experiment-wide false positive rate of $\alpha = 0.05$ (Figure 5.3). Therefore, our information transfer-based analysis supports the hypothesis that SST variation over the Gulf of Guinea unidirectionally controls precipitation variation over the West Sahel region. This observed directional control from SST to West Sahel precipitation was consistent with modeling studies (Biasutti et al., 2008; Folland et al., 1986; Giannini et al., 2003; Lamb, 1978; Vizy and Cook, 2001). For example, Giannini et al. (2003) suggested that the oceanic warming around Africa might have reduced the difference in temperature between land and ocean, making deep convection migrate to the ocean while reducing precipitation on land.

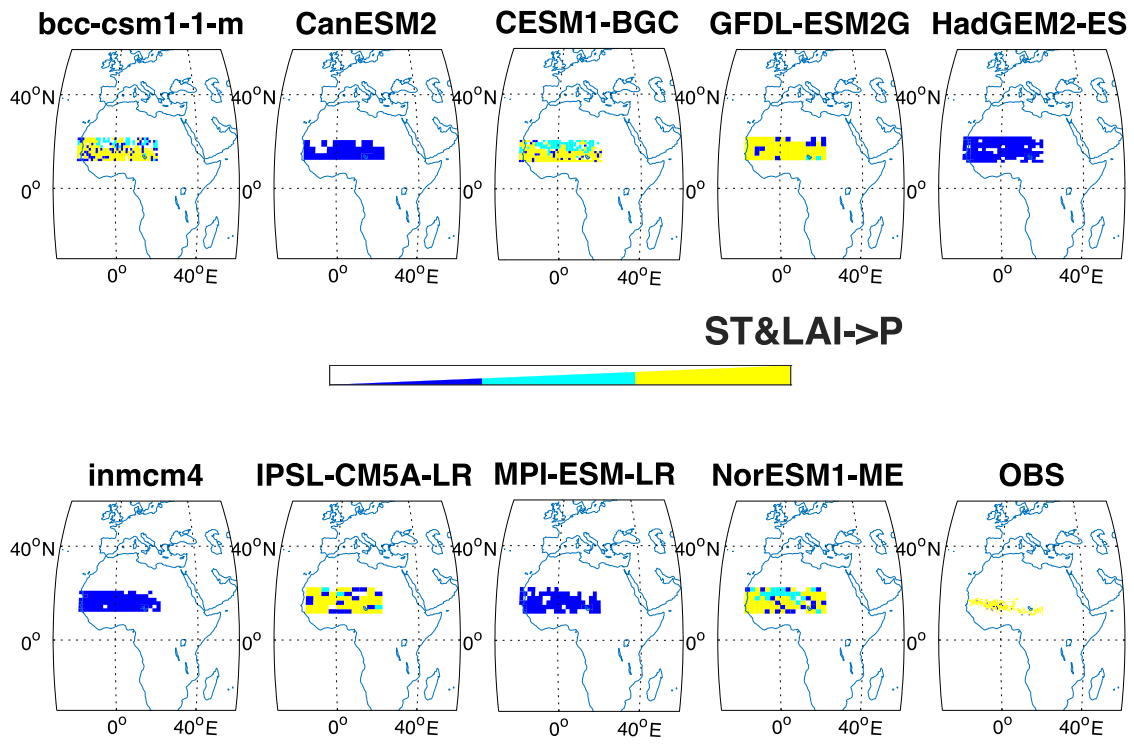

Figure 5.2. Directional interaction (1) only from Leaf Area Index (LAI) (blue), (2) only from Gulf of Guinea Sea Surface Temperature (SST) (cyan), or (3) from both LAI and SST (yellow) to West Sahel precipitation. Only statistically significant grid cells are shown in color. (Liu et al., 2019)

Another widely acknowledged hypothesis is that local vegetation-precipitation interactions control West Sahel precipitation (Wang and Eltahir, 2000; Zeng et al., 1999; Zheng and Eltahir, 1998). For example, using an ecosystem model, Hickler et al. (2005) showed that vegetation growth in the West Sahel region was mostly influenced by water availability but not by temperature variability. Another modeling study showed that variation in precipitation was closely related to variation in vegetation cover (Zeng et al., 1999). However, there is a general lack of observational demonstration of vegetation – precipitation interactions.

Here, we used observed LAI as an indicator for local vegetation coverage and variation, reducing uncertainties caused by solely relying on simulation data as in previous studies. Over 99% of the study's grid cells showed significant information transfer from precipitation to LAI, suggesting the importance of precipitation to LAI inter-annual variability in the West Sahel region (Figure 5.3). Further, over 99% of the study's grid cells showed a significant amount of information transfer from LAI to precipitation (Figure 5.2), suggesting that local variation in evapotranspiration and its impact on the surface energy balance contributes to changes in atmospheric moisture and energy for convection, and therefore to changes in regional precipitation.

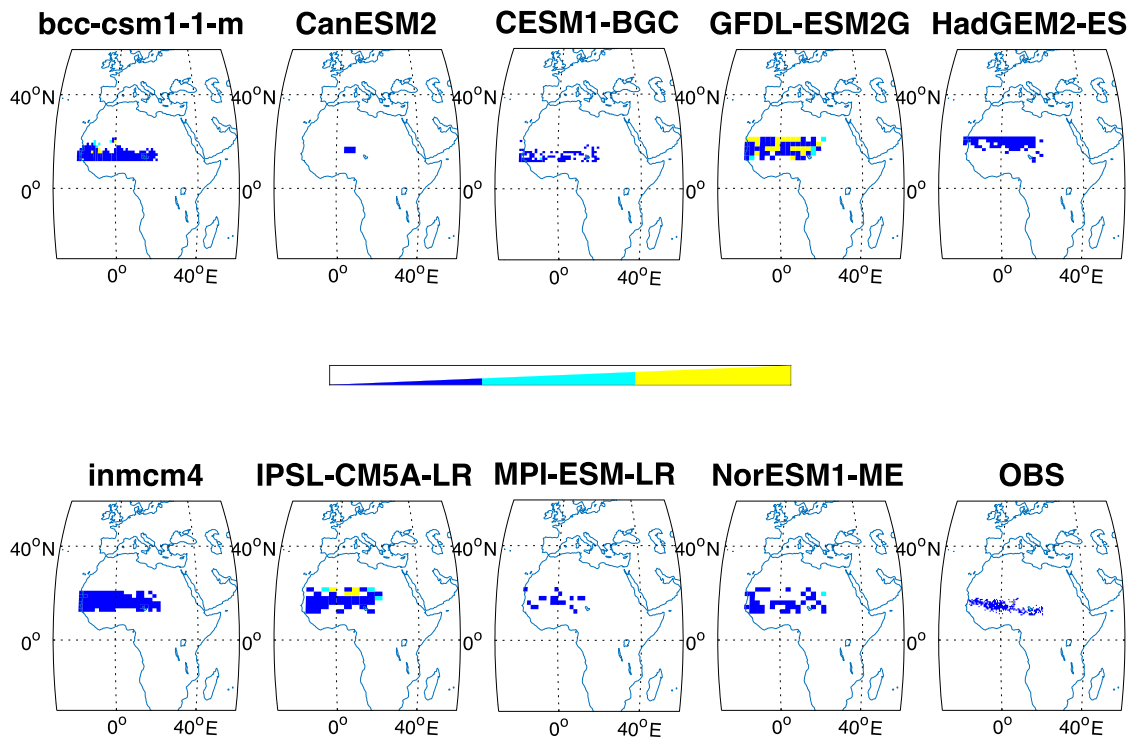

Figure 5.3. Directional interaction from West Sahel precipitation to (1) only Leaf area index (LAI) (blue), (2) only Gulf of Guinea Sea Surface Temperature (SST) (cyan), or (3) both SST and LAI (yellow). Only statistically significant grid cells are shown in color. (Liu et al., 2019)

Charney et al. (1977) first proposed that overgrazing in the West Sahel region may be the cause of persistent drying by enhancing a positive biogeophysical interaction. In particular, the reduced amount of vegetation leads to an increase in albedo and a cooler land surface over which air descends and dries, consequently suppressing precipitation. This dynamic was seen in many subsequent studies that used coupled biosphere-atmosphere models, suggesting that reduction in vegetation intensifies West Sahel drying, although the triggering mechanism of West Sahel drought may include changes in a combination of controls, including land cover and SST (Wang and Eltahir, 2000). However, the coupled climate models used in previous studies applied a wide variety of underlying assumptions and process representations. Observational demonstration of Charney's hypothesis is challenging due to the fact that regression-based (R2) or lead/lag correlations assume linear relationships between variables, although the system is inherently nonlinear. As a formal non-linear causal inference framework, transfer entropy can address such challenges. Here, the data demonstrate a causal relationship among observed precipitation, SST, and LAI. Our approach provides a first observational evaluation of directional interaction patterns affecting West Sahel precipitation. These resolved interactions can serve as useful model evaluation benchmarks, as discussed below.

Following our analysis above, we used the observed information transfer between modeled (1) SST and precipitation and (2) LAI and precipitation as quantitative benchmarks for the underlying mechanisms affecting West Sahel precipitation. Although the observational data showed that 93% of grid cells transfer significant information from both LAI and SST to precipitation (Figure 5.2, 5.4), GFDL-ESM2G, IPSL-CM5A-LR, CESM1-BGC, bcc-csm1-1-m, and NorESM1-ME predict that 77%, 65%, 55%, 51%, and 56% of the grid cells transfer significant information from both factors, respectively, while other models generally failed (significant entropy transfer appeared over less than 1% of grid cells) to capture either LAI or SST's observed impact on precipitation. We also found that only one third of the ESMs captured the precipitation control on LAI over at least half of their grid cells (Figure 5.3, 5.4). The models that most closely reproduce the observed relationship were inmcm4, IPSL-CM5A-LR, bcc-csm1-1-m, and GFDL-ESM2G with 86%, 56%, 50%, and 49% of the studied grid cells being statistically significant, respectively.

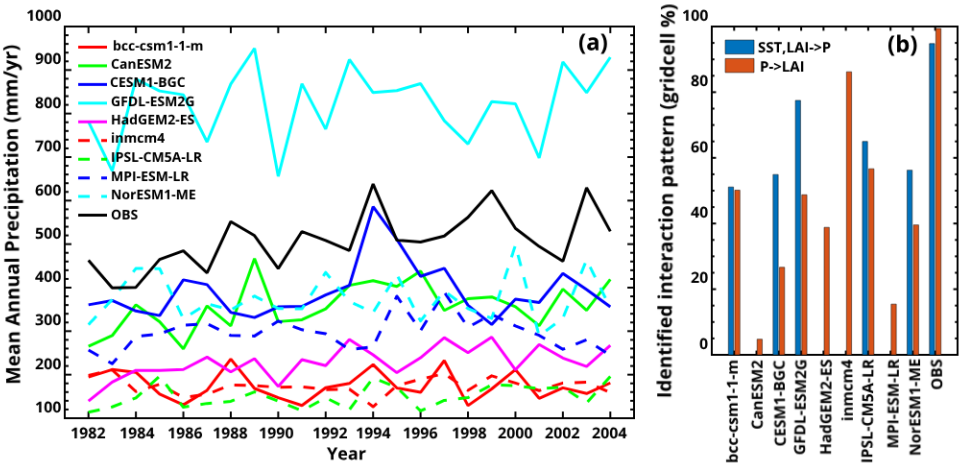

Figure 5.4. (a) Emergent benchmarks (here, mean annual precipitation) for West Sahel precipitation from observations and CMIP5 ESMs. (b) Percentage of model grid cells exhibiting interactions consistent with the observed mechanistic benchmark for West Sahelian precipitation. SST, LAI, and P are sea surface temperature, leaf area index, and precipitation, respectively. (Liu et al., 2019)

In summary, GFDL-ESM2G and IPSL-CM5A-LR most accurately reproduced observed interactions in more than 50% of the study's grid cells. All tested CMIP5 models generally captured the precipitation control on vegetation but largely failed to reproduce both LAI and SST's influence on precipitation. Although GFDL-ESM2G and IPSL-CM5A-LR relatively well reproduced the observed mechanistic interactions, they either dramatically overestimated (GFDL-ESM2G) or underestimated (IPSL-CM5A-LR) precipitation amount for the West Sahel region, suggesting that capturing both the interaction patterns and the emergent precipitation amount is challenging and important. Our results suggest that a full evaluation of climate models requires a combination of mechanistic and traditional emergent pattern benchmarks.

5.3 Case study 2. U.S. precipitation

Oceanic and atmospheric climate indices are potentially useful predictors of precipitation (Schepen et al., 2011). Understanding the temporal and spatial aspects of correlation between climate indices and precipitation is essential to understanding the ocean-continental dynamic system. Previous work has demonstrated that climate indices (e.g. Pacific/ North American, Southern Oscillation Index, Niño series) have a significant correlation with precipitation in U.S. (Daniel et., al 1991; Ropelewski and Halpert 1988; Mock 1995; Barlow et., al 2000; Redmond and Koch 1991; and McCabe and Dettinger 1999). In particular, precipitation has strong connection with sea surface temperature (Haylock et., al 2005). However, most of the previous work only test the correlation between anomalies and three-months average precipitation and map the spatial distribution. The effect on precipitation from climate anomalies is not necessarily immediate, but could have a time lag. Schepen used a rigorous Bayesian joint probability modeling approach to find the cross-validation predictive densities of gridded Australian seasonal rainfall totals using lagged climate indices as predictors throughout 1950-2009. They found lagged climate indices derived from sea surface temperature anomalies in the Pacific region (e.g., Niño3, Niño3.4, and Niño 4) show a significant relationship with Australian seasonal rainfall total. The lag between SST and rainfall could go up to 3 months (Schepen et al., 2011). Yang et al. (2006) applied wavelet analysis and the least squares method to depict the time-frequency features and the dominant oscillating time scales of Great Plains precipitation variation, and then analyze the characteristics of lead-lag correlation with central-eastern Pacific SST. They found that the associations are strongest when the SST leads the precipitation by one month and the significant SST-precipitation relationship appears over a wide range of time in which SST leads the precipitation up to 10 months with 95% confidence level.

Thus, temporal scale characteristic of these correlation is also important.

Meanwhile, transfer entropy method is an ideal method to perform time lagged correlation between climate indices and precipitation in different locations in U.S. Transfer entropy is a method that measures how much uncertainty of one system decreased by introducing another system. It has been shown to be effective in a broad range of research (Vicente et., al 2011; Rubinov and Sporms 2010; Verdes 2005; Kleeman 2007; Hannisdal and Peters 2011). The time lag could be easily introduced into this computation to detect the time lag inherent in these correlations (Schreiber 2000; Ruddell and Kumar 2009).

Thus, mapping the effect time lag from climate anomalies for precipitation from different locations is important step to understand the temporal and spatial aspect of correlations.

5.3.1 Data and model

The Niño series indices are used in this study (Table 5.1). The Niño series indices measure sea surface temperature (SST) over different locations in the Pacific Ocean (http:// www.esrl.noaa.gov /psd /data /climateindices/list/). These sea surface temperature indices are commonly used in studying ENSO teleconnection and the connection to the US climate (Bjerknes 1969, Rasmussen and Carpenter 1982, Wyrtki 1985). Niño series indices depict the sea surface temperature anomalies in the ENSO region. Niño 1+2 region (0-10S, 90W-80W) is the eastern-most of the Niño SST regions and corresponds with the region of coastal South America where El Niño phenomenon was first recognized. This index tends to have the most

considerable variance of the Niño SST indices (Trenberth and Stepaniak, 2000). Niño3 region (5N-5S, 150W-90W) use to be the primary focus for monitoring and predicting El Niño. Trenberth (1997) later found that the critical region for coupled ocean-atmosphere interactions for ENSO lies further west. Niño3.4 region (5N-5S, 170W-120W) represents the average equatorial SSTs across the Pacific from about the dateline to the South American coast. The Niño 3.4 index typically uses a 5-month running mean, and El Niño or La Niña events are quantified in terms of this index as corresponding to times when SST exceed +/- 0.4C for six months or more (Trenberth, 1997). Niño4 (5N-5S, 160E-150W) measures SST anomalies in the central equatorial Pacific with less variance than the other Niño indices.

Beyond the sea surface temperature anomalies, other climate indices are also highly correlated with ENSO. For example, the oldest index for ENSO is the Southern Oscillation Index (SOI) which measures the difference between the atmospheric pressure at sea level at Tahiti and Darwin (Bliss, 1932). However, the SOI can be affected by shorter-term fluctuations unrelated to ENSO since it is only considered two individual stations, and because it uses sea level pressure which as a meteorological quantity is affected by weather. The outgoing longwave radiation indexes are introduced by continuous satellite data (Chiodi and Harrison, 2013). However, the data only extends back to 1979, which may not be able to provide enough data for our study.

Thus, we choose to use all four Niño series indices that measure the sea surface temperature anomalies in different regions. They are well-known to have a strong correlation to US precipitation (Yang et al., 2007; Wang and Ting, 1999; Lee et al., 2008; Ting and Wang, 1997). Meanwhile, the precipitation patterns depend on the whole SST field, including gradients of SST. By considering the four neighboring regions, it allows for an evolutional perspective by comparing the difference in results between these indices.

The period used is from 1960 to 2015. The regions of each climate indices are shown in Figure 5.8.(a) and Figure 5.9.(a). While Table 4.1 describe the characteristics of each climate indices.

Table 5.1. Climate indices used as the information provider of U.S. precipitation

Climate Indices	Description	Region	Location
Niño1+2	Average SST anomaly over 80°-90°W and 0°-10°S	Pacific	80°W-90°W, 0°-10°S
Niño3	Average SST anomaly over 150°-90° W and 5°N-5°S	Pacific	150°W-90° W, 5°N-5°S
Niño3.4	Average SST anomaly over 170°-120° W and 5°N-5°S	Pacific	170°W-120° W, 5°N-5°S
Niño4	Average SST anomaly over 150°-160° E and 5°N-5°S	Pacific	150°W-160° E, 5°N-5°S

The precipitation data investigated in this study are collected from National Oceanic and Atmospheric Administration Monthly Climate Data Pool (http://www.ncdc.noaa.gov/cdo-web/search). 2595 precipitation stations are selected because they have records from 1960 to 2015, and have less than 10 percent missing data. The spatial distribution of these stations (Figure 5.5) are relatively more concentrated over both coasts.

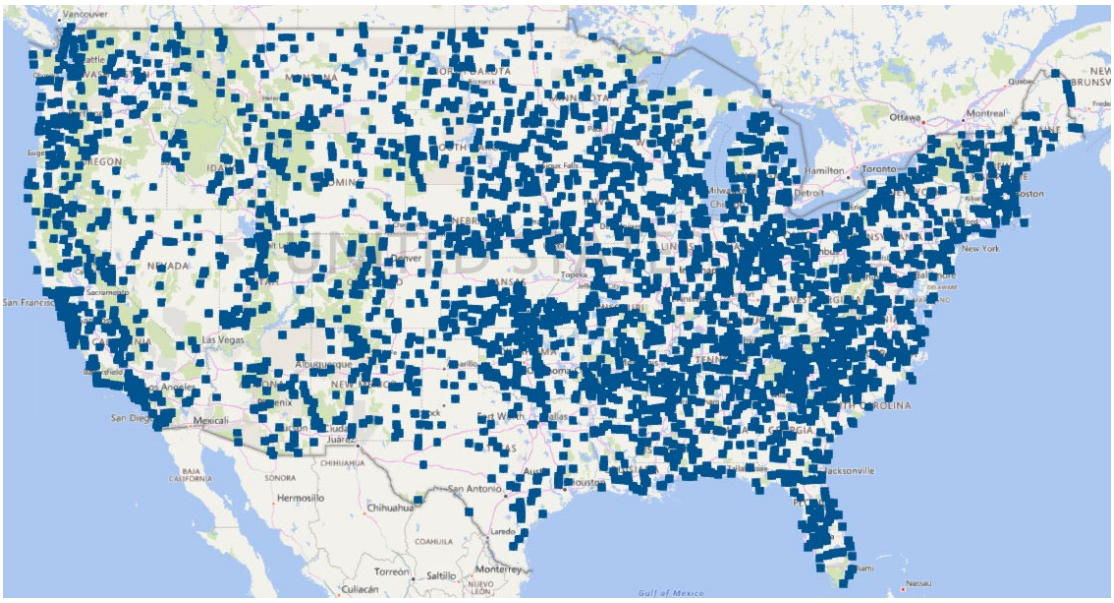

Figure 5.5. The locations of 2595 precipitation stations in U.S.

For two systems, $X_t = \{x_t\}\ t = 1,2,\dots,n$ and $Y_t = \{y_t\}\ t = 1,2,\dots,n$. x_t and y_t represent the state of system X and Y at time t respectively. In this study, climate indices are noted as system X, while precipitation data are noted as system Y. Transfer entropy of each climate indices to each precipitation are calculated with 12 time lags (from 1-month time lag to 12-month). The τ with largest significant transfer entropy $T(X_{i,t}>Y_{n,t})$ of each pair of climate indices ($i = 1,\dots,4$) and precipitation data ($n = 1,\dots,2595$) are noted to represent the significant time lag. If all 12 transfer entropy with different τ are non-significant, the correlation will be noted as non-significant.

The significant region (region with significant transfer entropy from climate indices to precipitation) map was made by using ordinary Kriging method (Georges Matheron, 1960). Meanwhile, the significant time lag of each stations was also used as input for making time lag spatial distribution map of each climate indices by using ordinary Kriging method.

5.3.2 Results

5.3.2.1 Sub-regions

First, we focus on eight pre-defined sub-regions (Figure 5.6) and 21 remote climate indices of interest based on empirical knowledge and literature survey. The sub-region are defined following the US Census Bureau. We have compared with the subregions used by Bukovsky (2012) and NOAA. However, precipitation stations are not evenly distributed. To make sure the number of stations of each sub-region to be roughly the same, we choose to use the US Census Bureau plan. The middle Atlantic region and New England region are merged for this reason as well.

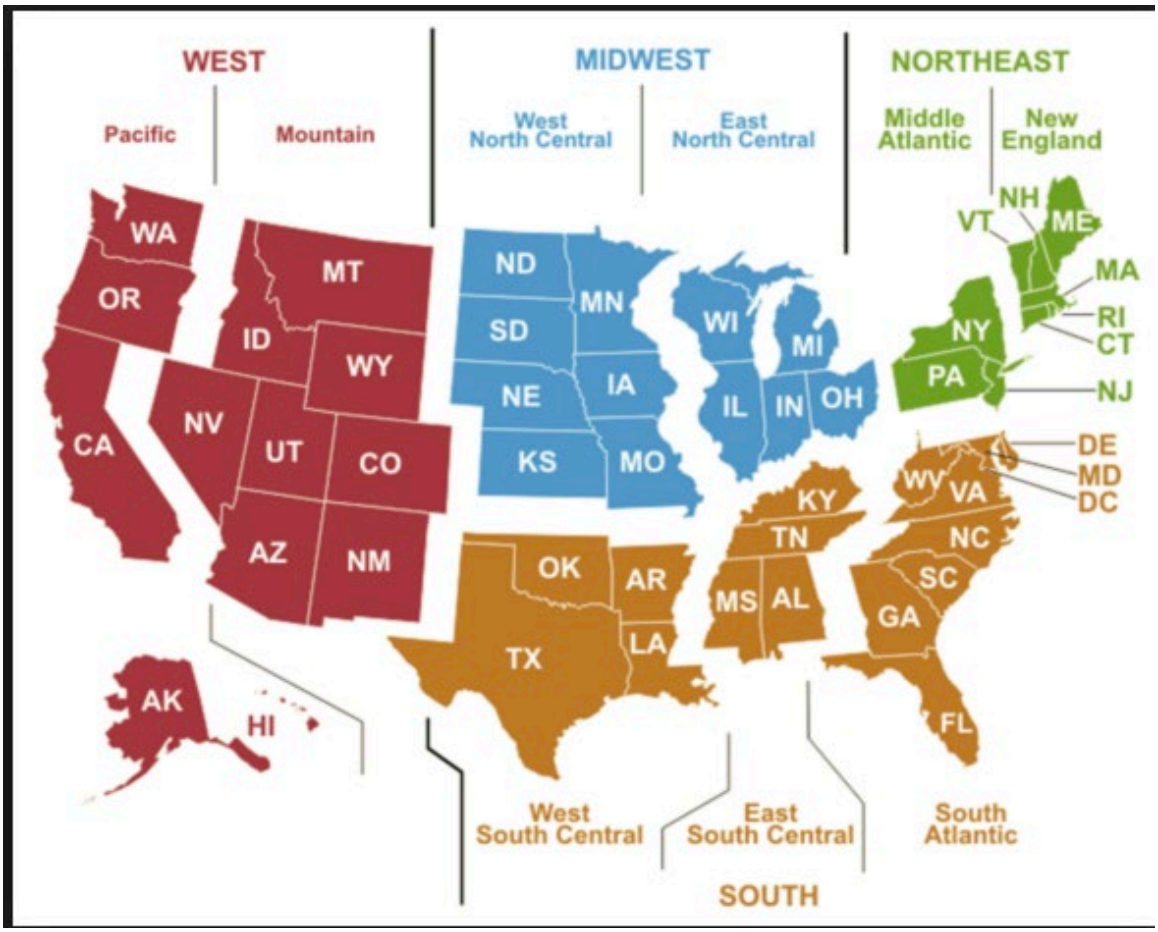

Figure 5.6. Pre-defined sub-region used in this study.

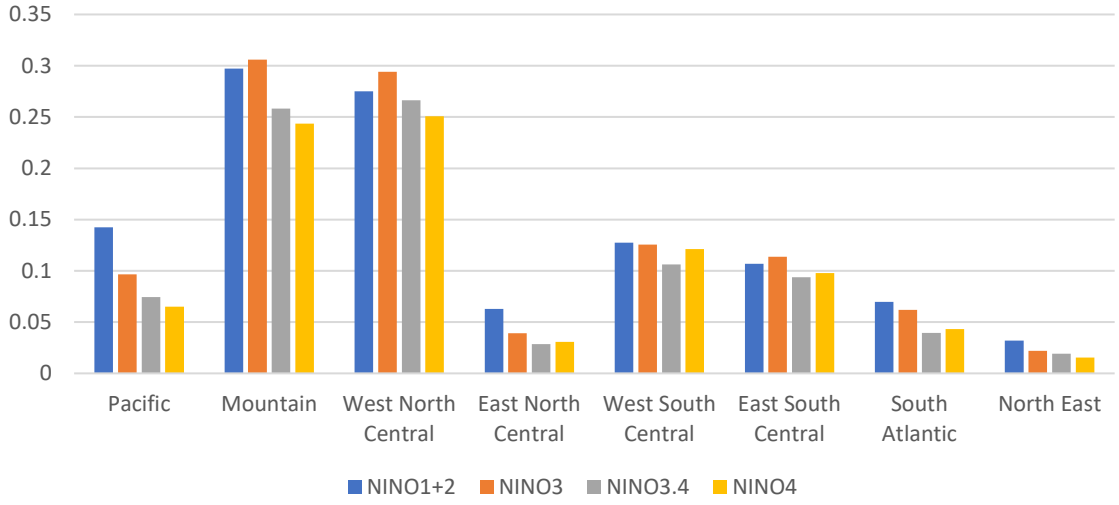

Figure 5.7. The percentages of weather stations, whose precipitation variation are identified to be significant information sinks of the various Niño climate indices.

El Niño dynamics potentially affect precipitation intensity over a large portion of United States. Here we quantify the significance of information entropy transfer from El Niño indices (including, Niño1+2, Niño3, Niño3.4, and Niño4) to the observed precipitation variation across

different sub-regions. We find that 25-30% of weather stations over the Mountain and West North Central US regions show significant information transfer, while only less than 5% of weather stations over the East North Central and North East US regions (i.e., less than the chance of a random positive with a significance threshold of 0.05) are significant information sinks (Figure 5.7.). It reveals a clear spatial pattern of how Niño indices impact US regional precipitation dynamics.

5.3.2.2 Niño Climate Indices Series

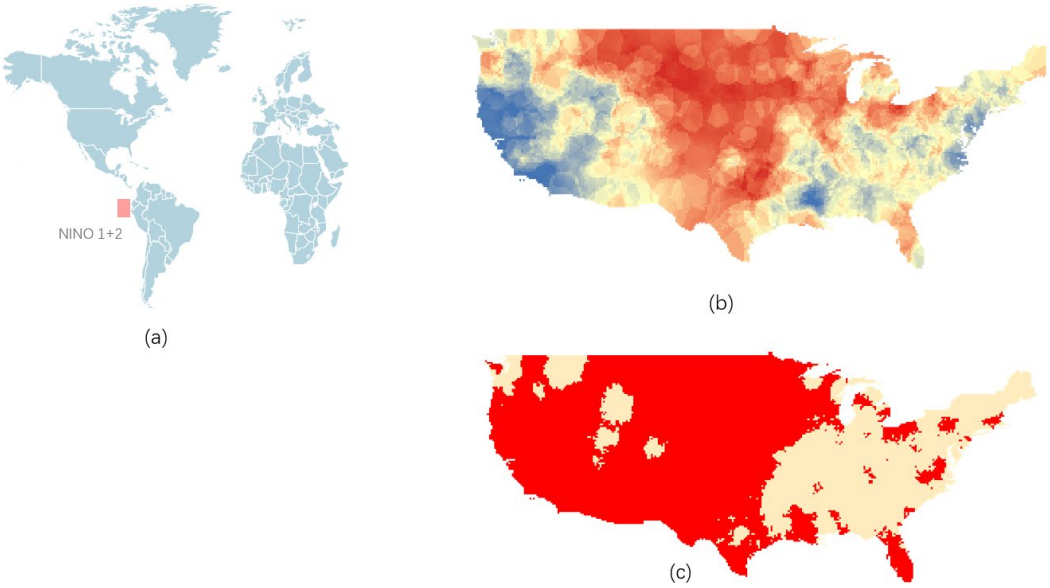

Figure 5.8. (a) Niño1+2 is the sea surface temperature (SST) averaged over the area 80°W-90°W, 0°-10°S. (b) is the ordinary kriging map of time lag of each stations with significant transfer entropy from Niño1+2 to precipitation. The red area represents short time lag (1-3 months), yellow area represents intermediate time lag (4-7 months) and the blue area represents long time lag (more than 7 months) (c) is the map of region with significant transfer entropy (shown in red).

We first discuss in detail the results from using Nino 1+2. From 5.8.(b), a clear time lag pattern is depicted. The precipitation over the middle of the continental US has relatively short time lag response to Niño1+2, while east and west coast have long ones. The topography also affects the time lag spatial patterns. The Rocky Mountains divide the spatial distribution of teleconnected changes into an eastern portion with short time lag, and a western portion with a larger lag.

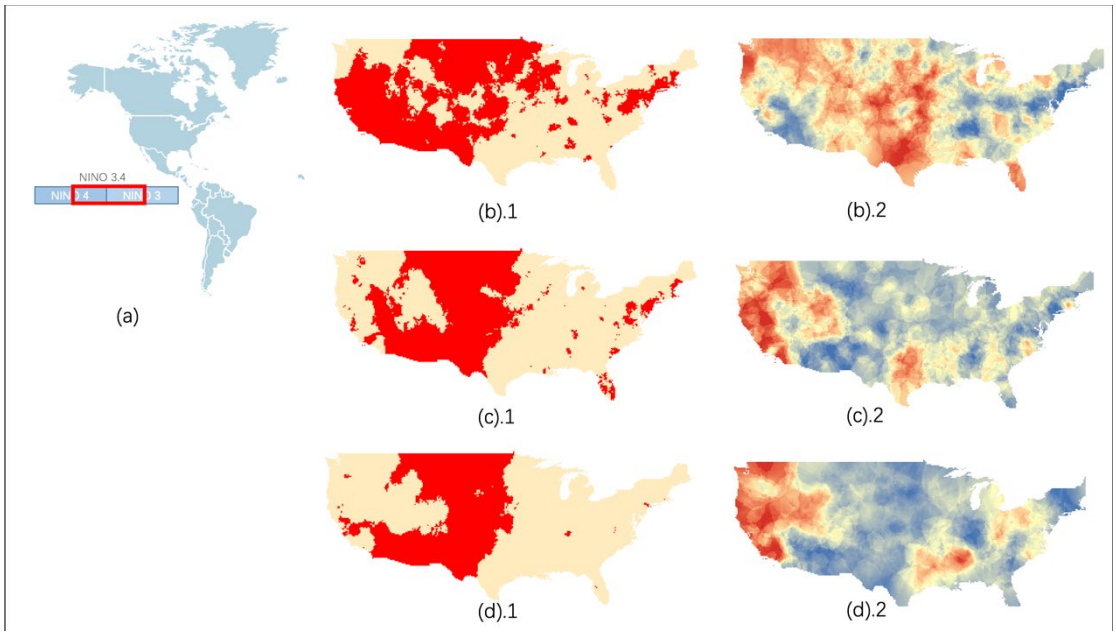

Figure 5.9. (a) Niño3, Niño3.4 and Niño4 measure the sea surface temperature of region of 150°W-90° W, 5°N-5°S, 170°W-120° W, 5°N-5°S and 160°E-150° W, 5°N-5°S respectively. (b).1, (c).1 and (d).1 are the map of region with significant transfer entropy from Niño3, Niño3.4 and Niño4 respectively. (b).2, (c).2 and (d).2 are the map of time lag spatial distribution of each climate indices. The legend is same as figure 5.8.(b).

We now discuss Niño3, 3+4, and 4. From Niño4 to Niño3, the index region moves eastwards towards the US mainland, while Niño3.4 located between the two. Figure 5.9(b-d) show that the significant region expands from Niño4 to Niño3. The precipitation has strong connection with Niño series climate indices. The maps shown in (b).2, (c).2, and (d).2 show that the short time lag region (shown in red) also expands from Niño4 to Niño3. These spatial pattern shows that in 5°N-5°S latitudinal zone the distance between SST anomalies region with U.S. mainland has a positive correlation with the region area with significant transfer entropy and with the region are with short time lag.

Meanwhile, the topography also affects the spatial pattern. The longitude of Rocky Mountain is around 110°W. The short time lag region for Nino3.4 and Nino4 (shown as red in 5.9.(c).2 and 5.9.(d).2) is on the west side of the Rocky Mountain. On the eastern side of the Rocky Mountain, most of the precipitation stations have no significant response to the Niño3.4 and Niño 4. It is affected by the rain shadow effect (Poage and Chamberlain, 2002). The topography in the mountain region uplifts the moist air mass. Along with uplifting, it expands and cools, which is no longer able to hold the moistures comparing its' relatively warm status. Clouds are formed and will drop rain and snow as it rises a mountain. After the air mass passes over the mountain and move downstream, the air mass becomes warm and carry less moisture, resulting in low precipitation rate on the other side of the mountain. However, as the region of Niño3 range from 150°W-90°, the short time lag region is expanding to the east side of Rocky Mountain, which also contributes to the increase of region with a short time lag. The vertically integrated total moisture flux from the Gulf of Mexico could be a potential source to the precipitation in the east side of Rocky Mountain (Trenberth and Guillemon, 1996).

Niño 3.4 and Niño 4 has a significant connection to the precipitation/drought of the western coast with a 0-2-month time lag. The linkage is explained by the change in tropical

convection associated with the El Niño/ La Niña conditions and the subsequent change in atmospheric circulation through Rossby wave propagation from the anomalous tropical convection (Hoskins and Karoly 1983). However, the signals of SST anomalies may not immediately affect the precipitation in the US. The information flow from the SST to the precipitation is absorbed and hold by the positive feedback with atmospheric circulation rather than direct moisture transport (Ting and Wang, 1997). The warm (cold) sea surface temperature will reduce (intensify) the meridional surface temperature gradient, which in turn leads to a smaller (larger) meridional gradient in the surface air temperature. The smaller (larger) meridional surface temperature gradient maintains a weaker (stronger) Pacific jet stream (Ting and Wang, 1997). Thus, the pacific jet stream altered by the sea surface anomalies connects the precipitation over the West coast to Niño 3.4 and Niño 4, thus establishing the physical basis for the information connection between the two.

The west coast region responds significantly faster to the Niño 4 and Niño 3.4 but relatively slow, or even insignificantly, to the Niño 3 and Niño 1+2. The middle region of the continental US has the opposite behavior, responding faster to Niño3 and Niño 1+2 but slower, or even insignificantly, to Niño 4 and Niño 3.4. To identify the reasons why there is a significant response spatial patterns to Niño 4 and Niño 1+2, we implement a transfer entropy analysis from the Niño 4 index to Niño 1+2 index. The result shows that Niño 1+2 lags Niño 4 by 0-1 month. It could partially explain those locations with less than the 1-month response time difference between to Niño 4 and Niño 1+2.

Two other reasons could explain the difference in teleconnections to the Nino indicies in the other locations. First, there is a difference of the response to La Niña and El Niño between Niño 4 and Niño1+2. Niño4 has a strong response to La Niña, but a relatively small response to El Niño, while the Niño 1+2 has the opposite characteristics (Hanley et al., 2003). The west coast region has much lower average precipitation than the middle continental US region. The precipitation signals of these two regions would thus be affected differently by El Niño or La Niña. For example, it is easier for a wet year to make a significant difference in precipitation in the west coast than a dry year, considering most of the year in California has near zero precipitation. Moreover, as previously stated, Niño 4 has a stronger response to La Niña, and Niño 1+2 has a stronger response to El Niño. Second, the topography could also exaggerate the difference in spatial response patterns between Niño 4 and Niño 1+2. Direct moisture transport by the Pacific jet stream could explain the short response time of coast region to Niño 4. But because of the presence of the Rockies Mountain, the middle continental US region has no direct connection to the moisture transport by the Pacific jet stream (and hence to Niño 4). However, direct moisture flux from the Gulf of Mexico could be a potential source for explaining the short response time of the middle continental US region to Niño 1+2(Trenberth and Guillemon, 1996). Future work will implement transfer entropy analysis on the Gulf of Mexico and the precipitation in the US to further answer this question.

5.4 Conclusions

We conclude that Transfer Entropy is an effective approach to quantify directional relationship between climate factors (including local and remote ones) and regional precipitation. In the Sahel precipitation study, we applied information theory to evaluate two widely acknowledged hypotheses regarding controls on West Sahel region precipitation variability: (1) unidirectional control of Sea Surface Temperatures over the Gulf of Guinea on West Sahel

precipitation and (2) bidirectional interactions between West Sahel precipitation and local vegetation dynamics. Based on information transfer between observed variables, we developed mechanistic benchmarking metrics for CMIP5 ESM predicted precipitation over the West Sahel region. In combination with traditional emergent pattern benchmarks (e.g., mean and trends in annual precipitation), we found that most ESMs were able to capture either the directional control of SST on precipitation or bidirectional interactions between vegetation and precipitation. However, none of the models captured both interactive patterns and the emergent mean and trends of regional precipitation. We recommend that a combination of mechanistic and traditional emergent pattern benchmarks should be used to better assess and inform processes that require improved representation in climate models. In the US precipitation study, we found that different climate indices have dramatically different teleconnections with US local precipitation, thus, there is no single climate indices could be used to understand precipitation over the whole US.

The spatial distribution map of time lag with most significant transfer entropy also shows the clear trend of each climate indices tested in this research. By analyzing the results of transfer entropy, we found that the signals of SST anomalies may not immediately affect the precipitation in the US, the hold by the positive feedback with atmospheric circulation rather than direct moisture transport. The Niño 3+4 and Niño 4 have a relatively short time lag with significant transfer entropy to west coast and have insignificant information transferred to the middle continental US. The Niño 1+2 and Niño 3 have a relatively short time lag with significant information transferred to the middle region but insignificant information transferred to the west coast. Normally the linkage explained by the change in tropical convection associated with the El Niño/ La Niña conditions and the subsequent change in atmospheric circulation through Rossby wave propagation from the anomalous tropical convection (Hoskins and Karoly 1983). The Niño 3+4 and Niño 4 have a relatively short time lag with significant transfer entropy to the west coast and have insignificant information transferred to the middle US. The Niño 1+2 and Niño 3 have a relatively short time lag with significant information transferred to the middle region but insignificant information transferred to the west coast. The precipitation signals in these two regions have different sensitivity to the El Niño and La Niña effect.

Reference

Labrinidis, A., & Jagadish, H. V. (2012). Challenges and opportunities with big data. Proceedings of the VLDB Endowment, 5(12), 2032-2033.

Chen, C. P., & Zhang, C. Y. (2014). Data-intensive applications, challenges, techniques and technologies: A survey on Big Data. Information Sciences, 275, 314-347.

Rodell, M., Chen, J., Kato, H., Famiglietti, J. S., Nigro, J., & Wilson, C. R. (2007). Estimating groundwater storage changes in the Mississippi River basin (USA) using GRACE. Hydrogeology Journal, 15(1), 159-166.

Shannon, C. E. (1949). Communication theory of secrecy systems. Bell system technical journal, 28(4), 656-715.

Schreiber, T. (2000). Measuring information transfer. Physical review letters, 85(2), 461.

Ruddell, B. L., & Kumar, P. (2009). Ecohydrologic process networks: 1. Identification. Water Resources Research, 45(3).

Ruddell, B. L., & Kumar, P. (2009). Ecohydrologic process networks: 2. Analysis and characterization. Water Resources Research, 45(3).

Ruddell, B. L., Brunsell, N. A., & Stoy, P. (2013). Applying information theory in the geosciences to quantify process uncertainty, feedback, scale. Eos, Transactions American Geophysical Union, 94(5), 56-56.

Pechlivanidis, I. G., Jackson, B., & McMillan, H. (2010). The use of entropy as a model diagnostic in rainfall-runoff modelling.

Reid, W. V., Chen, D., Goldfarb, L., Hackmann, H., Lee, Y. T., Mokhele, K., ... & Whyte, A. (2010). Earth system science for global sustainability: grand challenges. Science, 330(6006), 916-917.

Takens, F. (1981). Detecting strange attractors in turbulence. In Dynamical systems and turbulence, Warwick 1980 (pp. 366-381). Springer, Berlin, Heidelberg.

Tibshirani, R. (1996). Regression shrinkage and selection via the lasso. Journal of the Royal Statistical Society. Series B (Methodological), 267-288.

James, G., Witten, D., Hastie, T., & Tibshirani, R. (2013). An introduction to statistical learning (Vol. 112). New York: springer.

Chatterjee, S., Steinhaeuser, K., Banerjee, A., Chatterjee, S., & Ganguly, A. (2012, April). Sparse group lasso: Consistency and climate applications. In Proceedings of the 2012 SIAM International Conference on Data Mining (pp. 47-58). Society for Industrial and Applied Mathematics.

Kim, H., Eykholt, R., & Salas, J. D. (1999). Nonlinear dynamics, delay times, and embedding windows. Physica D: Nonlinear Phenomena, 127(1-2), 48-60.

Reference

Giannini, A., R. Saravanan and P. Chang (2003). "Oceanic forcing of Sahel rainfall on interannual to interdecadal time scales." Science 302(5647): 1027-1030.

Zeng, N., J. D. Neelin, K.-M. Lau and C. J. Tucker (1999). "Enhancement of interdecadal climate variability in the Sahel by vegetation interaction." Science 286(5444): 1537-1540.

Charney, J., W. J. Quirk, S. h. Chow and J. Kornfield (1977). "A comparative study of the effects of albedo change on drought in semi–arid regions." Journal of the Atmospheric Sciences 34(9): 1366-1385.

Huang, J., C. Zhang and J. M. Prospero (2009). "Aerosol-induced large-scale variability in precipitation over the tropical Atlantic." Journal of Climate 22(19): 4970-4988.

Hui, W. J., B. I. Cook, S. Ravi, J. D. Fuentes and P. D'Odorico (2008). "Dust‐rainfall feedbacks in the West African Sahel." Water Resources Research 44(5).

Taylor, C. M. (2008). "Intraseasonal land–atmosphere coupling in the West African monsoon." Journal of Climate 21(24): 6636-6648.

Taylor, C. M., E. F. Lambin, N. Stephenne, R. J. Harding and R. L. Essery (2002). "The influence of land use change on climate in the Sahel." Journal of Climate 15(24): 3615-3629.

Schepen, A., Wang, Q. J., & Robertson, D. (2012). Evidence for using lagged climate indices to forecast Australian seasonal rainfall. Journal of Climate, 25(4), 1230-1246.

Vicente, R., Wibral, M., Lindner, M., & Pipa, G. (2011). Transfer entropy—a model-free measure of effective connectivity for the neurosciences. Journal of computational neuroscience, 30(1), 45-67.

Rubinov, M., & Sporns, O. (2010). Complex network measures of brain connectivity: uses and interpretations. Neuroimage, 52(3), 1059-1069.

Verdes, P. F. (2005). Assessing causality from multivariate time series. Physical Review E, 72(2), 026222.

Hannisdal, B., & Peters, S. E. (2011). Phanerozoic Earth system evolution and marine biodiversity. science, 334(6059), 1121-1124.

Hays, James D., John Imbrie, and Nicholas J. Shackleton. 1976. “Variations in the Earth’s Orbit: Pacemaker of the Ice Ages.” Science 194 (4270): 1121–32.

Shakun, Jeremy D., Peter U. Clark, Feng He, Shaun A. Marcott, Alan C. Mix, Zhengyu Liu, Bette Otto-Bliesner, Andreas Schmittner, and Edouard Bard. 2012. “Global Warming Preceded by Increasing Carbon Dioxide Concentrations during the Last Deglaciation.” Nature 484 (7392): 49–54.

Petit, Jean-Robert, Jean Jouzel, Dominique Raynaud, Narcisse I. Barkov, J. M. Barnola, Isabelle Basile, Michael Bender, J. Chappellaz, M. Davis, and G. Delaygue. 1999. “Climate and Atmospheric History of the Past 420,000 Years from the Vostok Ice Core, Antarctica.” Nature 399 (6735): 429–36.

Reference

Claquin, T., C. Roelandt, Kohfeld Kohfeld, S. Harrison, I. Tegen, I. Prentice, Y. Balkanski, G. Bergametti, M. Hansson, and N. Mahowald. 2003. "Radiative Forcing of Climate by Ice-Age Atmospheric Dust." Climate Dynamics 20 (2-3): 193–202.

Takemura, T., M. Egashira, K. Matsuzawa, H. Ichijo, R. O'ishi, and A. Abe-Ouchi. 2009. "A Simulation of the Global Distribution and Radiative Forcing of Soil Dust Aerosols at the Last Glacial Maximum." Atmospheric Chemistry and Physics 9 (9): 3061–73.

Lambert, Fabrice, Barbara Delmonte, Jean-Robert Petit, Matthias Bigler, Patrick R. Kaufmann, Manuel A.

Larsen, L. G., & Harvey, J. W. (2017). Disrupted carbon cycling in restored and unrestored urban streams: Critical timescales and controls. Limnology and Oceanography, 62(S1).

Martínez-Garcia, Alfredo, Antoni Rosell-Melé, Samuel L. Jaccard, Walter Geibert, Daniel M. Sigman, and Gerald H. Haug. 2011. "Southern Ocean Dust-Climate Coupling over the Past Four Million Years." Nature 476 (7360): 312–15.

Schreiber, T. (2000). Measuring information transfer. Physical review letters, 85(2), 461.

Ver Steeg, G., & Galstyan, A. (2013, February). Information-theoretic measures of influence based on content dynamics. In Proceedings of the sixth ACM international conference on Web search and data mining (pp. 3-12). ACM.

Wibral, M., Vicente, R., & Lindner, M. (2014). Transfer entropy in neuroscience. In Directed Information Measures in Neuroscience (pp. 3-36). Springer, Berlin, Heidelberg.

Barnett, L., Barrett, A. B., & Seth, A. K. (2009). Granger causality and transfer entropy are equivalent for Gaussian variables. Physical review letters, 103(23), 238701.

Vicente, R., Wibral, M., Lindner, M., & Pipa, G. (2011). Transfer entropy—a model-free measure of effective connectivity for the neurosciences. Journal of computational neuroscience, 30(1), 45-67.

Bauer, M., Cox, J. W., Caveness, M. H., Downs, J. J., & Thornhill, N. F. (2007). Finding the direction of disturbance propagation in a chemical process using transfer entropy. IEEE transactions on control systems technology, 15(1), 12-21.

Dimpfl, T., & Peter, F. J. (2013). Using transfer entropy to measure information flows between financial markets. Studies in Nonlinear Dynamics and Econometrics, 17(1), 85-102.

Baek, S. K., Jung, W. S., Kwon, O., & Moon, H. T. (2005). Transfer entropy analysis of the stock market. arXiv preprint physics/0509014.

Sendrowski, A., & Passalacqua, P. (2017). Process connectivity in a naturally prograding river delta. Water Resources Research, 53(3), 1841-1863.

Rinderer, M., McGlynn, B. L., & van Meerveld, H. J. (2017). Groundwater similarity across a watershed derived from time-warped and flow-corrected time series. Water Resources Research, 53(5), 3921-3940.

Reference

Goodwell, A. E., Kumar, P., Fellows, A. W., & Flerchinger, G. N. (2018). Dynamic process connectivity explains ecohydrologic responses to rainfall pulses and drought. Proceedings of the National Academy of Sciences, 115(37), E8604-E8613.

Goodwell, A. E., & Kumar, P. (2017). Temporal Information Partitioning Networks (TIPNets): A process network approach to infer ecohydrologic shifts. Water Resources Research, 53(7), 5899-5919.

Allison, M. A., et al. (2012). "A water and sediment budget for the lower Mississippi–Atchafalaya River in flood years 2008–2010: implications for sediment discharge to the oceans and coastal restoration in Louisiana." Journal of Hydrology 432: 84-97.

Balke, T., et al. (2014). "Critical transitions in disturbance-driven ecosystems: identifying Windows of Opportunity for recovery." Journal of Ecology 102(3): 700-708.

Bertness, M. D. (1991). "Zonation of Spartina patens and Spartina alterniflora in New England salt marsh." Ecology 72(1): 138-148.

Bertoldi, W., et al. (2014). "Modeling vegetation controls on fluvial morphological trajectories." Geophysical Research Letters 41(20): 7167-7175.

Bevington, A. E. and R. R. Twilley (2018). "Island edge morphodynamics along a chronosequence in a prograding deltaic floodplain wetland." Journal of Coastal Research.

Bevington, A. E., et al. (2017). "Contribution of river floods, hurricanes, and cold fronts to elevation change in a deltaic floodplain, northern Gulf of Mexico, USA." Estuarine, Coastal and Shelf Science 191: 188-200.

Blum, M. D. and H. H. Roberts (2009). "Drowning of the Mississippi Delta due to insufficient sediment supply and global sea-level rise." Nature Geoscience 2(7): 488.

Bouma, T., et al. (2007). "Spatial flow and sedimentation patterns within patches of epibenthic structures: Combining field, flume and modelling experiments." Continental Shelf Research 27(8): 1020-1045.

Bouma, T. J., et al. (2009). "Density-dependent linkage of scale-dependent feedbacks: A flume study on the intertidal macrophyte Spartina anglica." Oikos 118(2): 260-268.

Boumans, R. M. and J. W. Day (1993). "High precision measurements of sediment elevation in shallow coastal areas using a sedimentation-erosion table." Estuaries and Coasts 16(2): 375-380.

Butler, D. R. (1995). Zoogeomorphology: animals as geomorphic agents, Cambridge University Press.

Cahoon, D. R., et al. (2002). "High-precision measurements of wetland sediment elevation: II. The rod surface elevation table." Journal of Sedimentary Research 72(5): 734-739.

Cahoon, D. R., et al. (2011). "Sediment infilling and wetland formation dynamics in an active crevasse splay of the Mississippi River delta." Geomorphology 131(3-4): 57-68.

Carle, M. V., et al. (2013). "Accretion and vegetation community change in the Wax Lake Delta following the historic 2011 Mississippi River flood." Journal of Coastal Research 31(3): 569-587.

Reference

Carle, M. V., et al. (2014). "Mapping freshwater marsh species distributions using WorldView-2 high-resolution multispectral satellite imagery." International journal of remote sensing 35(13): 4698-4716.

Chen, Z., et al. (2012). "The wake structure behind a porous obstruction and its implications for deposition near a finite patch of emergent vegetation." Water Resources Research 48(9).

Coniglio, M. and N. P. James (1985). "Calcified algae as sediment contributors to early Paleozoic limestones; evidence from deep-water sediments of the Cow Head Group, western Newfoundland." Journal of Sedimentary Research 55(5): 746-754.

Corenblit, D. and J. Steiger (2009). "Vegetation as a major conductor of geomorphic changes on the Earth surface: toward evolutionary geomorphology." Earth Surface Processes and Landforms 34(6): 891-896.

Corenblit, D., et al. (2007). "Reciprocal interactions and adjustments between fluvial landforms and vegetation dynamics in river corridors: a review of complementary approaches." Earth-Science Reviews 84(1-2): 56-86.

Curran, J. C. and W. C. Hession (2013). "Vegetative impacts on hydraulics and sediment processes across the fluvial system." Journal of Hydrology 505: 364-376.

DeLaune, R., et al. (1983). "Relationships among vertical accretion, coastal submergence, and erosion in a Louisiana Gulf Coast marsh." Journal of Sedimentary Research 53(1).

Diehl, R. M., et al. (2017). "Applying functional traits to ecogeomorphic processes in riparian ecosystems." BioScience 67(8): 729-743.

Edmonds, D. A. and R. L. Slingerland (2010). "Significant effect of sediment cohesion on delta morphology." Nature Geoscience 3(2): 105.

Eichel, J., et al. (2016). "Conditions for feedbacks between geomorphic and vegetation dynamics on lateral moraine slopes: a biogeomorphic feedback window." Earth Surface Processes and Landforms 41(3): 406-419.

Fagherazzi, S., et al. (2012). "Numerical models of salt marsh evolution: Ecological, geomorphic, and climatic factors." Reviews of Geophysics 50(1).

Fauria, K. E., et al. (2015). "Suspended particle capture by synthetic vegetation in a laboratory flume." Water Resources Research 51(11): 9112-9126.

Fei, S., et al. (2014). "Biogeomorphic impacts of invasive species." Annual review of ecology, evolution, and systematics 45.

Feng, Z. and C. Li (2010). "Cold-front-induced flushing of the Louisiana Bays." Journal of Marine Systems 82(4): 252-264.

Folkard, A. M. (2011). "Vegetated flows in their environmental context: a review." Proceedings of the Institution of Civil Engineers-Engineering and Computational Mechanics 164(1): 3-24.

Reference

Follett, E. M. and H. M. Nepf (2012). "Sediment patterns near a model patch of reedy emergent vegetation." Geomorphology 179: 141-151.

Francis, R. A. (2006). "Allogenic and autogenic influences upon riparian vegetation dynamics." Area 38(4): 453-464.

Gerbersdorf, S. and S. Wieprecht (2015). "Biostabilization of cohesive sediments: revisiting the role of abiotic conditions, physiology and diversity of microbes, polymeric secretion, and biofilm architecture." Geobiology 13(1): 68-97.

Goodwell, A. E. and P. Kumar (2017). "Temporal Information Partitioning Networks (TIPNets): A process network approach to infer ecohydrologic shifts." Water Resources Research.

Goodwell, A. E. and P. Kumar (2017). "Temporal information partitioning: Characterizing synergy, uniqueness, and redundancy in interacting environmental variables." Water Resources Research.

Gurnell, A. (2014). "Plants as river system engineers." Earth Surface Processes and Landforms 39(1): 4-25.

Gurnell, A. M., et al. (2012). "Changing river channels: The roles of hydrological processes, plants and pioneer fluvial landforms in humid temperate, mixed load, gravel bed rivers." Earth-Science Reviews 111(1): 129-141.

Gurnell, A. M., et al. (2012). "Changing river channels: The roles of hydrological processes, plants and pioneer fluvial landforms in humid temperate, mixed load, gravel bed rivers." Earth-Science Reviews 111(1-2): 129-141.

Hardy, J. W. and K. G. Henderson (2003). "Cold front variability in the southern United States and the influence of atmospheric teleconnection patterns." Physical geography 24(2): 120-137.

Heppell, C., et al. (2009). "Sediment storage in the shallow hyporheic of lowland vegetated river reaches." Hydrological Processes: An International Journal 23(15): 2239-2251.

Heuner, M., et al. (2015). "Ecosystem engineering by plants on wave-exposed intertidal flats is governed by relationships between effect and response traits." Plos one 10(9): e0138086.

Horppila, J. and L. Nurminen (2005). "Effects of different macrophyte growth forms on sediment and P resuspension in a shallow lake." Hydrobiologia 545(1): 167-175.

Johnson, W., et al. (1985). "Succession of vegetation in an evolving river delta, Atchafalaya Bay, Louisiana." The Journal of Ecology: 973-986.

Kalliola, R. and M. Puhakka (1988). "River dynamics and vegetation mosaicism: a case study of the River Kamajohka, northernmost Finland." Journal of Biogeography: 703-719.

Kantz, H. and T. Schürmann (1996). "Enlarged scaling ranges for the KS-entropy and the information dimension." Chaos: An Interdisciplinary Journal of Nonlinear Science 6(2): 167-171.

Kirwan, M. L. and A. B. Murray (2007). "A coupled geomorphic and ecological model of tidal marsh evolution." Proceedings of the National Academy of Sciences 104(15): 6118-6122.

Reference

Kirwan, M. L., et al. (2016). "Overestimation of marsh vulnerability to sea level rise." Nature Climate Change 6(3): 253.

Larsen, L. and J. Harvey (2017). "Disrupted carbon cycling in restored and unrestored urban streams: Critical timescales and controls." Limnology and Oceanography 62(S1).

Larsen, L. G. and J. W. Harvey (2011). "Modeling of hydroecological feedbacks predicts distinct classes of landscape pattern, process, and restoration potential in shallow aquatic ecosystems." Geomorphology 126(3-4): 279-296.

Larsen, L. G., et al. (2017). "How important is connectivity for surface water fluxes? A generalized expression for flow through heterogeneous landscapes." Geophysical Research Letters 44(20).

Larsen, L. G., et al. (2017). "Complex networks of functional connectivity in a wetland reconnected to its floodplain." Water Resources Research.

Leck, M. A. and R. L. Simpson (1994). "Tidal freshwater wetland zonation: seed and seedling dynamics." Aquatic Botany 47(1): 61-75.

Leonard, L. A. and M. E. Luther (1995). "Flow hydrodynamics in tidal marsh canopies." Limnology and Oceanography 40(8): 1474-1484.

Li, C., et al. (2011). "Wind surge and saltwater intrusion in Atchafalaya Bay during onshore winds prior to cold front passage." Hydrobiologia 658(1): 27-39.

Li, F., et al. (2016). "Different roles of three emergent macrophytes in promoting sedimentation in Dongting Lake, China." Aquatic sciences 78(1): 159-169.

Liu, C., et al. (2017). "Vortex Structure and Sediment Deposition in the Wake behind a Finite Patch of Model Submerged Vegetation." Journal of Hydraulic Engineering 144(2): 04017065.

Liu, C. and H. Nepf (2016). "Sediment deposition within and around a finite patch of model vegetation over a range of channel velocity." Water Resources Research 52(1): 600-612.

Lorenzo-Trueba, J., et al. (2012). "Exploring the role of organic matter accumulation on delta evolution." Journal of Geophysical Research: Earth Surface 117(F4).

Luhar, M. and H. M. Nepf (2013). "From the blade scale to the reach scale: A characterization of aquatic vegetative drag." Advances in Water Resources 51: 305-316.

Ma, S. and H. J. Bohnert (2007). "Integration of Arabidopsis thaliana stress-related transcript profiles, promoter structures, and cell-specific expression." Genome biology 8(4): R49.

Manners, R., et al. (2013). "Multiscalar model for the determination of spatially explicit riparian vegetation roughness." Journal of Geophysical Research: Earth Surface 118(1): 65-83.

Marani, M., et al. (2013). "Vegetation engineers marsh morphology through multiple competing stable states." Proceedings of the National Academy of Sciences 110(9): 3259-3263.

Mariotti, G. and S. Fagherazzi (2010). "A numerical model for the coupled long-term evolution of salt marshes and tidal flats." Journal of Geophysical Research: Earth Surface 115(F1).

Reference

Marschinski, R. and H. Kantz (2002). "Analysing the information flow between financial time series." The European Physical Journal B-Condensed Matter and Complex Systems 30(2): 275-281.

Merritt, D. M., et al. (2010). "Theory, methods and tools for determining environmental flows for riparian vegetation: riparian vegetation-flow response guilds." Freshwater biology 55(1): 206-225.

Mossa, J. and H. H. Roberts (1990). "Synergism of riverine and winter storm-related sediment transport processes in Louisiana's coastal wetlands."

Murray, A. B. and C. Paola (1997). "Properties of a cellular braided-stream model." Earth Surface Processes and Landforms 22(11): 1001-1025.

Nardin, W., et al. (2016). "Influence of vegetation on spatial patterns of sediment deposition in deltaic islands during flood." Advances in Water Resources 93: 236-248.

Nardin, W. and D. A. Edmonds (2014). "Optimum vegetation height and density for inorganic sedimentation in deltaic marshes." Nature Geoscience 7(10): 722.

Nardin, W., et al. (2018). "Tradeoffs among hydrodynamics, sediment fluxes and vegetation community in the Virginia Coast Reserve, USA." Estuarine, Coastal and Shelf Science.

Nepf, H. (1999). "Drag, turbulence, and diffusion in flow through emergent vegetation." Water Resources Research 35(2): 479-489.

Nicholas, A. and T. Quine (2007). "Crossing the divide: Representation of channels and processes in reduced-complexity river models at reach and landscape scales." Geomorphology 90(3-4): 318-339.

Nicholas, A. P. (2013). "Modelling the continuum of river channel patterns." Earth Surface Processes and Landforms 38(10): 1187-1196.

Nyman, J., et al. (1990). "Wetland soil formation in the rapidly subsiding Mississippi River deltaic plain: Mineral and organic matter relationships." Estuarine, Coastal and Shelf Science 31(1): 57-69.

O'Hare, M., et al. (2015). "Plant traits relevant to fluvial geomorphology and hydrological interactions." River Research and Applications 32(2): 179-189.

Odum, W. E. (1988). "Comparative ecology of tidal freshwater and salt marshes." Annual Review of Ecology and Systematics 19(1): 147-176.

Olliver, E. A. and D. A. Edmonds (2017). "Defining the ecogeomorphic succession of land building for freshwater, intertidal wetlands in Wax Lake Delta, Louisiana." Estuarine, Coastal and Shelf Science 196: 45-57.

Olliver, E. A. and D. A. Edmonds (2017). "Defining the ecogeomorphic succession of land building for freshwater, intertidal wetlands in Wax Lake Delta, Louisiana." Estuarine, Coastal and Shelf Science.

Ortiz, A. C., et al. (2013). "Mean and turbulent velocity fields near rigid and flexible plants and the implications for deposition." Journal of Geophysical Research: Earth Surface 118(4): 2585-2599.

Palmer, M. R., et al. (2004). "Observations of particle capture on a cylindrical collector: Implications for particle accumulation and removal in aquatic systems." Limnology and Oceanography 49(1): 76-85.

Paola, C., et al. (2011). "Natural processes in delta restoration: Application to the Mississippi Delta." Annual Review of Marine Science 3: 67-91.

Percha, B., et al. (2005). "Transition from local to global phase synchrony in small world neural network and its possible implications for epilepsy." Physical Review E 72(3): 031909.

Perucca, E., et al. (2006). "Influence of river meandering dynamics on riparian vegetation pattern formation." Journal of Geophysical Research: Biogeosciences 111(G1).

Phillips, J. D. (2009). "Biological energy in landscape evolution." American Journal of Science 309(4): 271-289.

Pluntke, T. and H.-P. Kozerski (2003). "Particle trapping on leaves and on the bottom in simulated submerged plant stands." Hydrobiologia 506(1-3): 575-581.

Reed, D. J. (2002). "Sea-level rise and coastal marsh sustainability: geological and ecological factors in the Mississippi delta plain." Geomorphology 48(1-3): 233-243.

Roberts, H., et al. (1997). "Evolution of sedimentary architecture and surface morphology: Atchafalaya and Wax Lake Deltas, Louisiana (1973-1994)."

Roberts, H. H., et al. (2015). "Floods and cold front passages: impacts on coastal marshes in a river diversion setting (Wax Lake Delta Area, Louisiana)." Journal of Coastal Research 31(5): 1057-1068.

Rosen, T. and Y. J. Xu (2013). "Recent decadal growth of the Atchafalaya River Delta complex: Effects of variable riverine sediment input and vegetation succession." Geomorphology 194: 108-120.

Ruddell, B. L. and P. Kumar (2009). "Ecohydrologic process networks: 1. Identification." Water Resources Research 45: 22.

Ruddell, B. L. and P. Kumar (2009). "Ecohydrologic process networks: 1. Identification." Water Resources Research 45(3).

Sabesan, S., et al. (2003). Improved Measure of Information Flow in Coupled Nonlinear Systems. Modelling and Simulation.

Schreiber, T. (2000). "Measuring information transfer." Physical review letters 85(2): 461.

Schuerch, M., et al. (2018). "Future response of global coastal wetlands to sea-level rise." Nature 561(7722): 231.

Sendrowski, A. and P. Passalacqua (2017). "Process connectivity in a naturally prograding river delta." Water Resources Research 53(3): 1841-1863.

Reference

Sendrowski, A., et al. (2018). "Transfer Entropy as a Tool for Hydrodynamic Model Validation." Entropy 20(1): 58.

Shaffer, G. P., et al. (1992). "Vegetation dynamics in the emerging Atchafalaya Delta, Louisiana, USA." Journal of Ecology: 677-687.

Shannon, C. E. (1949). "Communication theory of secrecy systems." Bell Labs Technical Journal 28(4): 656-715.

Silvestri, S., et al. (2005). "Tidal regime, salinity and salt marsh plant zonation." Estuarine, Coastal and Shelf Science 62(1-2): 119-130.

Stallins, J. A. (2005). "Stability domains in barrier island dune systems." Ecological Complexity 2(4): 410-430.

Stallins, J. A. (2006). "Geomorphology and ecology: unifying themes for complex systems in biogeomorphology." Geomorphology 77(3-4): 207-216.

Tabacchi, E., et al. (1998). "Development, maintenance and role of riparian vegetation in the river landscape." Freshwater biology 40(3): 497-516.

Temmerman, S., et al. (2007). "Vegetation causes channel erosion in a tidal landscape." Geology 35(7): 631-634.

Turnbull, L., et al. (2014). Approaches to modelling ecogeomorphic systems. Patterns of Land Degradation in Drylands, Springer: 171-209.

van de Koppel, J., et al. (2012). "The influence of local-and landscape-scale processes on spatial self-organization in estuarine ecosystems." Journal of Experimental Biology 215(6): 962-967.

Van der Wal, D., et al. (2008). "Spatial patterns, rates and mechanisms of saltmarsh cycles (Westerschelde, The Netherlands)." Estuarine, Coastal and Shelf Science 76(2): 357-368.

Vandenbruwaene, W., et al. (2011). "Flow interaction with dynamic vegetation patches: Implications for biogeomorphic evolution of a tidal landscape." Journal of Geophysical Research: Earth Surface 116(F1).

Vinent, O. D. and L. J. Moore (2015). "Barrier island bistability induced by biophysical interactions." Nature Climate Change 5(2): 158.

Wagner, W., et al. (2017). "Elevation change and stability on a prograding delta." Geophysical Research Letters 44(4): 1786-1794.

Wharton, G., et al. (2006). "Macrophytes and suspension-feeding invertebrates modify flows and fine sediments in the Frome and Piddle catchments, Dorset (UK)." Journal of Hydrology 330(1-2): 171-184.

White, D. A. (1993). "Vascular plant community development on mudflats in the Mississippi River delta, Louisiana, USA." Aquatic Botany 45(2-3): 171-194.

Reference

Wilson, A. M. and L. R. Gardner (2006). "Tidally driven groundwater flow and solute exchange in a marsh: numerical simulations." Water Resources Research 42(1).

Yager, E. and M. Schmeeckle (2013). "The influence of vegetation on turbulence and bed load transport." Journal of Geophysical Research: Earth Surface 118(3): 1585-1601.

Zinke, P., et al. (2011). "Three-dimensional numerical modelling of levee depositions in a Scandinavian freshwater delta." Geomorphology 129(3-4): 320-333.

Ashkenazy, Yosef, Don R. Baker, Hezi Gildor, and Shlomo Havlin. 2003. “Nonlinearity and Multifractality of Climate Change in the Past 420,000 Years.” Geophysical Research Letters 30 (22).

Barnola, J. M., Pimienta, P., Raynaud, D., & Korotkevich, Y. S. (1991). CO2-climate relationship as deduced from the Vostok ice core: A re-examination based on new measurements and on a re-evaluation of the air dating. Tellus B, 43(2), 83-90.

Berger, Andrél. 1978. “Long-Term Variations of Daily Insolation and Quaternary Climatic Changes.” Journal of the Atmospheric Sciences 35 (12): 2362–67.

Bopp, L., Kohfeld, K. E., Le Quéré, C., & Aumont, O. (2003). Dust impact on marine biota and atmospheric CO2 during glacial periods. Paleoceanography, 18(2).

Boyd, P. W., Watson, A. J., Law, C. S., Abraham, E. R., Trull, T., Murdoch, R., ... & Charette, M. (2000). A mesoscale phytoplankton bloom in the polar Southern Ocean stimulated by iron fertilization. Nature, 407(6805), 695.

Barnola, J. M., Pimienta, P., Raynaud, D., & Korotkevich, Y. S. (1991). CO2-climate relationship as deduced from the Vostok ice core: A re-examination based on new measurements and on a re-evaluation of the air dating. Tellus B, 43(2), 83-90.

Broecker, W. S. (1982). Ocean chemistry during glacial time. Geochimica et Cosmochimica Acta, 46(10), 1689-1705.

Brzezinski, M. A., Pride, C. J., Franck, V. M., Sigman, D. M., Sarmiento, J. L., Matsumoto, K., ... & Coale, K. H. (2002). A switch from Si (OH) 4 to NO3− depletion in the glacial Southern Ocean. Geophysical research letters, 29(12), 5-1.

Claquin, T., C. Roelandt, Kohfeld Kohfeld, S. Harrison, I. Tegen, I. Prentice, Y. Balkanski, G. Bergametti, M. Hansson, and N. Mahowald. 2003. “Radiative Forcing of Climate by Ice-Age Atmospheric Dust.” Climate Dynamics 20 (2-3): 193–202.

Coale, K. H., Johnson, K. S., Fitzwater, S. E., Gordon, R. M., Tanner, S., Chavez, F. P., ... & Steinberg, P. (1996). A massive phytoplankton bloom induced by an ecosystem-scale iron fertilization experiment in the equatorial Pacific Ocean. Nature, 383(6600), 495.

Gallée, H., J. P. Van Yperselb, Th Fichefet, I. Marsiat, Ch Tricot, and A. Berger. 1992. “Simulation of the Last Glacial Cycle by a Coupled, Sectorially Averaged Climate-ice Sheet Model: 2. Response to Insolation and CO2 Variations.” Journal of Geophysical Research, D: Atmospheres 97 (D14): 15713–40.

Reference

Hansen, James, Larissa Nazarenko, Reto Ruedy, Makiko Sato, Josh Willis, Anthony Del Genio, Dorothy Koch, Andrew Lacis, Ken Lo, and Surabi Menon. 2005. "Earth's Energy Imbalance: Confirmation and Implications." Science 308 (5727): 1431–35.

Hays, James D., John Imbrie, and Nicholas J. Shackleton. 1976. "Variations in the Earth's Orbit: Pacemaker of the Ice Ages." Science 194 (4270): 1121–32.

Imbrie, John, E. A. Boyle, S. C. Clemens, A. Duffy, W. R. Howard, G. Kukla, J. Kutzbach, 735dg Martinson, A. McIntyre, and A. C. Mix. 1992. "On the Structure and Origin of Major Glaciation Cycles 1. Linear Responses to Milankovitch Forcing." Paleoceanography 7 (6): 701–38.

Johnsen, S. J., Willi Dansgaard, H. B. Clausen, and Chester C. Langway. 1972. "Oxygen Isotope Profiles through the Antarctic and Greenland Ice Sheets." Nature 235 (5339): 429–34.

Knox, F., & McElroy, M. B. (1984). Changes in atmospheric CO2: Influence of the marine biota at high latitude. Journal of Geophysical Research: Atmospheres, 89(D3), 4629-4637.

Kohfeld, Karen E., Corinne Le Quéré, Sandy P. Harrison, and Robert F. Anderson. 2005. "Role of Marine Biology in Glacial-Interglacial CO2 Cycles." Science 308 (5718): 74–78.

Lambert, Fabrice, Barbara Delmonte, Jean-Robert Petit, Matthias Bigler, Patrick R. Kaufmann, Manuel A.

Hutterli, Thomas F. Stocker, Urs Ruth, Jørgen Peder Steffensen, and Valter Maggi. 2008. "Dust-Climate Couplings over the Past 800,000 Years from the EPICA Dome C Ice Core." Nature 452 (7187): 616–19.

Legrand, M., C. Feniet-Saigne, E. S. Sattzman, C. Germain, N. I. Barkov, and V. N. Petrov. 1991. "Ice-Core Record of Oceanic Emissions of Dimethylsulphide during the Last Climate Cycle." Nature 350: 144–46.

Lenton, Timothy M., Hermann Held, Elmar Kriegler, Jim W. Hall, Wolfgang Lucht, Stefan Rahmstorf, and Hans Joachim Schellnhuber. 2008. "Tipping Elements in the Earth's Climate System." Proceedings of the National Academy of Sciences 105 (6): 1786–93.

Lorius, C., Jouzel, J., Ritz, C., Merlivat, L., Barkov, N. I., Korotkevich, Y. S., & Kotlyakov, V. M. (1985). A 150,000-year climatic record from Antarctic ice. Nature, 316(6029), 591.

Lüthi, Dieter, Martine Le Floch, Bernhard Bereiter, Thomas Blunier, Jean-Marc Barnola, Urs Siegenthaler, Dominique Raynaud, Jean Jouzel, Hubertus Fischer, and Kenji Kawamura. 2008. "High-Resolution Carbon Dioxide Concentration Record 650,000–800,000 Years before Present." Nature 453 (7193): 379–82.

Maher, B. A., J. M. Prospero, Doug Mackie, Diego Gaiero, Paul Phillip Hesse, and Yves Balkanski. 2010. "Global Connections between Aeolian Dust, Climate and Ocean Biogeochemistry at the Present Day and at the Last Glacial Maximum." Earth-Science Reviews 99 (1): 61–97.

Martínez-Garcia, Alfredo, Antoni Rosell-Melé, Samuel L. Jaccard, Walter Geibert, Daniel M. Sigman, and Gerald H. Haug. 2011. "Southern Ocean Dust-Climate Coupling over the Past Four Million Years." Nature 476 (7360): 312–15.

Reference

Martin, John H. 1990. “Glacial-interglacial CO2 Change: The Iron Hypothesis.” Paleoceanography 5 (1): 1–13.

Martin, J. H., & Fitzwater, S. E. (1988). Iron deficiency limits phytoplankton growth in the north-east Pacific subarctic. Nature, 331(6154), 341.

Matsumoto, K., Sarmiento, J. L., & Brzezinski, M. A. (2002). Silicic acid leakage from the Southern Ocean: A possible explanation for glacial atmospheric pCO2. Global Biogeochemical Cycles, 16(3), 5-1.

McGehee, Richard, and Clarence Lehman. 2012. “A Paleoclimate Model of Ice-Albedo Feedback Forced by Variations in Earth’s Orbit.” SIAM Journal on Applied Dynamical Systems 11 (2): 684–707.

Montgomery, Douglas C., Elizabeth A. Peck, and G. Geoffrey Vining. 2015. Introduction to Linear Regression Analysis. John Wiley & Sons.

Nes, Egbert H. van, Marten Scheffer, Victor Brovkin, Timothy M. Lenton, Hao Ye, Ethan Deyle, and George Sugihara. 2015. “Causal Feedbacks in Climate Change.” Nature Climate Change 5 (5): 445–48.

Petit, Jean-Robert, Jean Jouzel, Dominique Raynaud, Narcisse I. Barkov, J. M. Barnola, Isabelle Basile, Michael Bender, J. Chappellaz, M. Davis, and G. Delaygue. 1999. “Climate and Atmospheric History of the Past 420,000 Years from the Vostok Ice Core, Antarctica.” Nature 399 (6735): 429–36.

Rind, David. 1999. “Complexity and Climate.” Science 284 (5411): 105–7.

Sarmiento, J. L., & Toggweiler, J. R. (1984). A new model for the role of the oceans in determining atmospheric pCO2. Nature, 308(5960), 621.

Saigne, C., and M. Legrand. 1987. “Measurements of Methanesulphonic Acid in Antarctic Ice.” Nature 330: 240–42.

Schreiber, Thomas. 2000. “Measuring Information Transfer.” Physical Review Letters 85 (2): 461.

Shakun, Jeremy D., Peter U. Clark, Feng He, Shaun A. Marcott, Alan C. Mix, Zhengyu Liu, Bette Otto-Bliesner, Andreas Schmittner, and Edouard Bard. 2012. “Global Warming Preceded by Increasing Carbon Dioxide Concentrations during the Last Deglaciation.” Nature 484 (7392): 49–54.

Shannon, Claude Elwood. 2001. “A Mathematical Theory of Communication.” ACM SIGMOBILE Mobile Computing and Communications Review 5 (1): 3–55.

Shukla, Jagadish. 1998. “Predictability in the Midst of Chaos: A Scientific Basis for Climate Forecasting.” Science 282 (5389): 728–31.

Siegenthaler, U., & Wenk, T. (1984). Rapid atmospheric CO2 variations and ocean circulation. Nature, 308(5960), 624.

Stenseth, Nils Chr, and Atle Mysterud. 2002. “Climate, Changing Phenology, and Other Life History Traits: Nonlinearity and Match–mismatch to the Environment.” Proceedings of the National Academy of Sciences 99 (21): 13379–81.

Reference

Takeda, S. (1998). Influence of iron availability on nutrient consumption ratio of diatoms in oceanic waters. Nature, 393(6687), 774.

Takemura, T., M. Egashira, K. Matsuzawa, H. Ichijo, R. O'ishi, and A. Abe-Ouchi. 2009. "A Simulation of the Global Distribution and Radiative Forcing of Soil Dust Aerosols at the Last Glacial Maximum." Atmospheric Chemistry and Physics 9 (9): 3061–73.

Wang, Zhaomin, and Lawrence A. Mysak. 2002. "Simulation of the Last Glacial Inception and Rapid Ice Sheet Growth in the McGill Paleoclimate Model." Geophysical Research Letters 29 (23).

Washington, Richard, Christel Bouet, Guy Cautenet, Elisabeth Mackenzie, Ian Ashpole, Sebastian Engelstaedter, Gil Lizcano, Gideon M. Henderson, Kerstin Schepanski, and Ina Tegen. 2009. "Dust as a Tipping Element: The Bodélé Depression, Chad." Proceedings of the National Academy of Sciences 106 (49): 20564–71.

Winckler, Gisela, Robert F. Anderson, Martin Q. Fleisher, David McGee, and Natalie Mahowald. 2008. "Covariant Glacial-Interglacial Dust Fluxes in the Equatorial Pacific and Antarctica." Science 320 (5872): 93–96.

Wolff, Eric W., Hubertus Fischer, Felix Fundel, Urs Ruth, Birthe Twarloh, Geneviève C. Littot, R.

Mulvaney, Regine Röthlisberger, Martine De Angelis, and Claude F. Boutron. 2006. "Southern Ocean Sea-Ice Extent, Productivity and Iron Flux over the Past Eight Glacial Cycles." Nature 440 (7083): 491–96.

Yue, Xu, Huijun Wang, Hong Liao, and Dabang Jiang. 2011. "Simulation of the Direct Radiative Effect of Mineral Dust Aerosol on the Climate at the Last Glacial Maximum." Journal of Climate 24 (3): 843–58.

Yu, Hongbin, Mian Chin, Tianle Yuan, Huisheng Bian, Lorraine A. Remer, Joseph M. Prospero, Ali Omar, David Winker, Yuekui Yang, and Yan Zhang. 2015. "The Fertilizing Role of African Dust in the Amazon Rainforest: A First Multiyear Assessment Based on Data from Cloud-Aerosol Lidar and Infrared Pathfinder Satellite Observations." Geophysical Research Letters 42 (6): 1984–91.

Chiang, J. C. H., & Vimont, D. J. (2004). Analogous meridional modes of atmosphere–ocean variability in the tropical Pacific and tropical Atlantic. J. Climate, 17(21), 4143-4158.

Jones, P. D., Jonsson, T., & Wheeler, D. (1997). Extension to the North Atlantic Oscillation using early instrumental pressure observations from Gibraltar and south-west Iceland. International Journal of Climatology: A Journal of the Royal Meteorological Society, 17(13), 1433-1450.

Trenberth, K. E., & Stepaniak, D. P. (2001). Indices of el Niño evolution. Journal of climate, 14(8), 1697-1701.

Biasutti, M., I. M. Held, A. Sobel and A. Giannini (2008). "SST forcings and Sahel rainfall variability in simulations of the twentieth and twenty-first centuries." Journal of Climate 21(14): 3471-3486.

Reference

Brovkin, V., L. Boysen, T. Raddatz, V. Gayler, A. Loew and M. Claussen (2013). "Evaluation of vegetation cover and land-surface albedo in MPI-ESM CMIP5 simulations." Journal of Advances in Modeling Earth Systems 5(1): 48-57.

Cattiaux, J., H. Douville, A. Ribes, F. Chauvin and C. Plante (2013). "Towards a better understanding of changes in wintertime cold extremes over Europe: a pilot study with CNRM and IPSL atmospheric models." Climate dynamics 40(9-10): 2433-2445.

Chappell, A. and C. T. Agnew (2004). "Modelling climate change in West African Sahel rainfall (1931–90) as an artifact of changing station locations." International Journal of Climatology 24(5): 547-554.

Charney, J., W. J. Quirk, S. h. Chow and J. Kornfield (1977). "A comparative study of the effects of albedo change on drought in semi–arid regions." Journal of the Atmospheric Sciences 34(9): 1366-1385.

Chylek, P., J. Li, M. Dubey, M. Wang and G. Lesins (2011). "Observed and model simulated 20th century Arctic temperature variability: Canadian earth system model CanESM2." Atmospheric Chemistry and Physics Discussions 11(8): 22893-22907.

Collins, W., N. Bellouin, M. Doutriaux-Boucher, N. Gedney, P. Halloran, T. Hinton, J. Hughes, C. Jones, M. Joshi and S. Liddicoat (2011). "Development and evaluation of an Earth-System model-HadGEM2." Geoscientific Model Development 4(4): 1051.

Cook, K. H. and E. K. Vizy (2006). "Coupled model simulations of the West African monsoon system: twentieth-and twenty-first-century simulations." Journal of climate 19(15): 3681-3703.

Druyan, L. M. (2011). "Studies of 21st-century precipitation trends over West Africa." International Journal of Climatology 31(10): 1415-1424.

Dunne, J. P., J. G. John, A. J. Adcroft, S. M. Griffies, R. W. Hallberg, E. Shevliakova, R. J. Stouffer, W. Cooke, K. A. Dunne and M. J. Harrison (2012). "GFDL's ESM2 global coupled climate–carbon earth system models. Part I: Physical formulation and baseline simulation characteristics." Journal of Climate 25(19): 6646-6665.

Folland, C., T. Palmer and D. Parker (1986). "Sahel rainfall and worldwide sea temperatures, 1901–85." Nature 320(6063): 602-607.

Giannini, A., R. Saravanan and P. Chang (2003). "Oceanic forcing of Sahel rainfall on interannual to interdecadal time scales." Science 302(5647): 1027-1030.

Grodsky, S. A. and J. A. Carton (2003). "The intertropical convergence zone in the South Atlantic and the equatorial cold tongue." Journal of Climate 16(4): 723-733.

Hagos, S. M. and K. H. Cook (2008). "Ocean warming and late-twentieth-century Sahel drought and recovery." Journal of Climate 21(15): 3797-3814.

Harris, I., P. Jones, T. Osborn and D. Lister (2014). "Updated high-resolution grids of monthly climatic observations–the CRU TS3. 10 Dataset." International Journal of Climatology 34(3): 623-642.

Reference

Held, I., T. Delworth, J. Lu, K. u. Findell and T. Knutson (2005). "Simulation of Sahel drought in the 20th and 21st centuries." Proceedings of the National Academy of Sciences of the United States of America 102(50): 17891-17896.

Hickler, T., L. Eklundh, J. W. Seaquist, B. Smith, J. Ardö, L. Olsson, M. T. Sykes and M. Sjöström (2005). "Precipitation controls Sahel greening trend." Geophysical Research Letters 32(21).

Hill, S. A., Y. Ming and M. Zhao (2018). "Robust responses of the Sahelian hydrological cycle to global warming." Journal of Climate 31(24): 9793-9814.

Huang, J., C. Zhang and J. M. Prospero (2009). "Aerosol-induced large-scale variability in precipitation over the tropical Atlantic." Journal of Climate 22(19): 4970-4988.

Hui, W. J., B. I. Cook, S. Ravi, J. D. Fuentes and P. D'Odorico (2008). "Dust-rainfall feedbacks in the West African Sahel." Water Resources Research 44(5).

Jung, M., M. Reichstein, H. A. Margolis, A. Cescatti, A. D. Richardson, M. A. Arain, A. Arneth, C. Bernhofer, D. Bonal and J. Chen (2011). "Global patterns of land-atmosphere fluxes of carbon dioxide, latent heat, and sensible heat derived from eddy covariance, satellite, and meteorological observations." Journal of Geophysical Research: Biogeosciences (2005–2012) 116(G3).

Kirchner, J. W. (2006). "Getting the right answers for the right reasons: Linking measurements, analyses, and models to advance the science of hydrology." Water Resources Research 42(3).

Kumar, S., V. Merwade, J. L. Kinter III and D. Niyogi (2013). "Evaluation of temperature and precipitation trends and long-term persistence in CMIP5 twentieth-century climate simulations." Journal of Climate 26(12): 4168-4185.

Lamb, P. J. (1978). "Large-scale Tropical Atlantic surface circulation patterns associated with Subsaharan weather anomalies." Tellus 30(3): 240-251.

Liang, S. and Z. Xiao (2012). "Global land surface products: Leaf area index product data collection (1985–2010)." Beijing Normal University.

Lindsay, K., G. B. Bonan, S. C. Doney, F. M. Hoffman, D. M. Lawrence, M. C. Long, N. M. Mahowald, J. Keith Moore, J. T. Randerson and P. E. Thornton (2014). "Preindustrial-control and twentieth-century carbon cycle experiments with the Earth system model CESM1 (BGC)." Journal of Climate 27(24): 8981-9005.

Nicholson, S. E. (2005). "On the question of the “recovery” of the rains in the West African Sahel." Journal of Arid Environments 63(3): 615-641.

Nicholson, S. E. (2013). "The West African Sahel: A Review of Recent Studies on the Rainfall Regime and Its Interannual Variability." ISRN Meteorology 2013: 1-32.

Nicholson, S. E. and J. P. Grist (2003). "The seasonal evolution of the atmospheric circulation over West Africa and equatorial Africa." Journal of Climate 16(7): 1013-1030.

Nicholson, S. E. and P. J. Webster (2007). "A physical basis for the interannual variability of rainfall in the Sahel." Quarterly Journal of the Royal Meteorological Society 133(629): 2065-2084.

Reference

Patricola, C. M. and K. H. Cook (2010). "Northern African climate at the end of the twenty-first century: an integrated application of regional and global climate models." Climate Dynamics 35(1): 193-212.

Pu, B. and K. H. Cook (2012). "Role of the West African westerly jet in Sahel rainfall variations." Journal of Climate 25(8): 2880-2896.

Reynolds, R. W., N. A. Rayner, T. M. Smith, D. C. Stokes and W. Wang (2002). "An improved in situ and satellite SST analysis for climate." Journal of climate 15(13): 1609-1625.

Rowell, D. P., C. K. Folland, K. Maskell and M. N. Ward (1995). "Variability of summer rainfall over tropical North Africa (1906–92): Observations and modelling." Quarterly Journal of the Royal Meteorological Society 121(523): 669-704.

Ruddell, B. L. and P. Kumar (2009). "Ecohydrologic process networks: 1. Identification." Water Resources Research 45(3).

Schär, C., D. Lüthi, U. Beyerle and E. Heise (1999). "The soil–precipitation feedback: A process study with a regional climate model." Journal of Climate 12(3): 722-741.

Shannon, C. E. (2001). "A mathematical theory of communication." ACM SIGMOBILE Mobile Computing and Communications Review 5(1): 3-55.

Smirnov, D. A. (2013). "Spurious causalities with transfer entropy." Physical Review E 87(4): 042917.

Smith, T. M. and R. W. Reynolds (1998). "A high-resolution global sea surface temperature climatology for the 1961–90 base period." Journal of Climate 11(12): 3320-3323.

Sultan, B. and S. Janicot (2000). "Abrupt shift of the ITCZ over West Africa and intra-seasonal variability." Geophysical Research Letters 27(20): 3353-3356.

Sultan, B. and S. Janicot (2003). "The West African monsoon dynamics. Part II: The “preonset” and “onset” of the summer monsoon." Journal of climate 16(21): 3407-3427.

Sultan, B., S. Janicot and A. Diedhiou (2003). "The West African monsoon dynamics. Part I: Documentation of intraseasonal variability." Journal of Climate 16(21): 3389-3406.

Schepen, A., Wang, Q. J., & Robertson, D. (2012). Evidence for using lagged climate indices to forecast Australian seasonal rainfall. Journal of Climate, 25(4), 1230-1246.

Taylor, C. M. (2008). "Intraseasonal land–atmosphere coupling in the West African monsoon." Journal of Climate 21(24): 6636-6648.

Taylor, C. M., E. F. Lambin, N. Stephenne, R. J. Harding and R. L. Essery (2002). "The influence of land use change on climate in the Sahel." Journal of Climate 15(24): 3615-3629.

Tjiputra, J., C. Roelandt, M. Bentsen, D. Lawrence, T. Lorentzen, J. Schwinger, Ø. Seland and C. Heinze (2013). "Evaluation of the carbon cycle components in the Norwegian Earth System Model (NorESM)." Geoscientific Model Development 6(2): 301-325.

Ting, M., & Wang, H. (1997). Summertime US Precipitation Variability and Its Relation toPacific Sea Surface Temperature. Journal of Climate, 10(8), 1853-1873.

Reference

Trenberth, K. E., & Guillemot, C. J. (1996). Physical processes involved in the 1988 drought and 1993 floods in North America. Journal of Climate, 9(6), 1288-1298.

Vizy, E. K. and K. H. Cook (2001). "Mechanisms by which Gulf of Guinea and eastern North Atlantic sea surface temperature anomalies can influence African rainfall." Journal of Climate 14(5): 795-821.

Volodin, E., N. Dianskii and A. Gusev (2010). "Simulating present-day climate with the INMCM4. 0 coupled model of the atmospheric and oceanic general circulations." Izvestiya, Atmospheric and Oceanic Physics 46(4): 414-431.

Wang, G. and E. A. Eltahir (2000). "Role of vegetation dynamics in enhancing the low-frequency variability of the Sahel rainfall." Water Resources Research 36(4): 1013-1021.

Yoshioka, M., N. M. Mahowald, A. J. Conley, W. D. Collins, D. W. Fillmore, C. S. Zender and D. B. Coleman (2007). "Impact of desert dust radiative forcing on Sahel precipitation: Relative importance of dust compared to sea surface temperature variations, vegetation changes, and greenhouse gas warming." Journal of Climate 20(8): 1445-1467.

Zeng, N., J. D. Neelin, K.-M. Lau and C. J. Tucker (1999). "Enhancement of interdecadal climate variability in the Sahel by vegetation interaction." Science 286(5444): 1537-1540.

Zheng, X. and E. A. Eltahir (1998). "The role of vegetation in the dynamics of West African monsoons." Journal of Climate 11(8): 2078-2096.

Schepen, A., Wang, Q. J., & Robertson, D. (2012). Evidence for using lagged climate indices to forecast Australian seasonal rainfall. Journal of Climate, 25(4), 1230-1246.

Vicente, R., Wibral, M., Lindner, M., & Pipa, G. (2011). Transfer entropy—a model-free measure of effective connectivity for the neurosciences. Journal of computational neuroscience, 30(1), 45-67.

Rubinov, M., & Sporns, O. (2010). Complex network measures of brain connectivity: uses and interpretations. Neuroimage, 52(3), 1059-1069.

Verdes, P. F. (2005). Assessing causality from multivariate time series. Physical Review E, 72(2), 026222.

Hannisdal, B., & Peters, S. E. (2011). Phanerozoic Earth system evolution and marine biodiversity. science, 334(6059), 1121-1124.

Tsonis, A. A., Swanson, K., & Kravtsov, S. (2007). A new dynamical mechanism for major climate shifts. Geophysical Research Letters, 34(13).

Berezin, Y., Gozolchiani, A., Guez, O., & Havlin, S. (2012). Stability of climate networks with time. Scientific reports, 2, 666.

Mukhin, D., Gavrilov, A., Loskutov, E., Feigin, A., & Kurths, J. (2018). Nonlinear reconstruction of global climate leading modes on decadal scales. Climate dynamics, 51(5-6), 2301-2310.

Reference

Ross, I., Valdes, P. J., and Wiggins, S. (2008). ENSO dynamics in current climate models: an investigation using nonlinear dimensionality reduction, Nonlin. Processes Geophys., 15, 339-363.

Pires, C. A., & Ribeiro, A. F. (2017). Separation of the atmospheric variability into non-Gaussian multidimensional sources by projection pursuit techniques. Climate dynamics, 48(3-4), 821-850.

Gámez, A. J., Zhou, C. S., Timmermann, A., and Kurths, J. (2004). Nonlinear dimensionality reduction in climate data, Nonlin. Processes Geophys., 11, 393-398.

Malik, N., Bookhagen, B., Marwan, N., & Kurths, J. (2012). Analysis of spatial and temporal extreme monsoonal rainfall over South Asia using complex networks. Climate dynamics, 39(3-4), 971-987.

Hlinka, J., Hartman, D., Vejmelka, M., Novotná, D., & Paluš, M. (2014). Non-linear dependence and teleconnections in climate data: sources, relevance, nonstationarity. Climate dynamics, 42(7-8), 1873-1886.

Hannachi, A., & Turner, A. G. (2013). 20th century intraseasonal Asian monsoon dynamics viewed from Isomap. Nonlinear Processes in Geophysics, 20(5), 725-741.

Vera, C., Higgins, W., Amador, J., Ambrizzi, T., Garreaud, R., Gochis, D., ... & Nogues-Paegle, J. (2006). Toward a unified view of the American monsoon systems. Journal of climate, 19(20), 4977-5000.

Steinhaeuser, K., Ganguly, A. R., & Chawla, N. V. (2012). Multivariate and multiscale dependence in the global climate system revealed through complex networks. Climate dynamics, 39(3-4), 889-895.

Donges, J. F., Zou, Y., Marwan, N., & Kurths, J. (2009). The backbone of the climate network. EPL (Europhysics Letters), 87(4), 48007.

Van Oldenborgh, G. J., Burgers, G., & Tank, A. K. (2000). On the El Niño teleconnection to spring precipitation in Europe. International Journal of Climatology: A Journal of the Royal Meteorological Society, 20(5), 565-574.

Nicholls, N. (1987). The use of canonical correlation to study teleconnections. Monthly Weather Review, 115(2), 393-399.

Bjerknes, J. (1969). Atmospheric teleconnections from the equatorial Pacific. *J. Phys. Oceanog.,* **97**, 163-172.

Rasmussen, E. M. and T. H. Carpenter 1982: Variations in tropical sea surface temperature and surface wind fields associated with the Southern Oscillation/El Niño. *Mon. Wea. Rev*., **110**, 354-384.

Wyrtki, K., 1985: Water displacements in the Pacific and the genesis of El Niño cycles. *J. Geophys. Res., 90, 7129-7132.*

Trenberth, K. E., & Stepaniak, D. P. (2001). Indices of el niño evolution. Journal of climate, 14(8), 1697-1701.

Reference

Poage, M. A., & Chamberlain, C. P. (2002). Stable isotopic evidence for a Pre-Middle Miocene rain shadow in the western Basin and Range: Implications for the paleotopography of the Sierra Nevada. Tectonics, 21(4), 16-1.

Mo, K. C., & Livezey, R. E. (1986). Tropical-extratropical geopotential height teleconnections during the Northern Hemisphere winter. Monthly Weather Review, 114(12), 2488-2515.

Zhou, D., Gozolchiani, A., Ashkenazy, Y., & Havlin, S. (2015). Teleconnection paths via climate network direct link detection. Physical review letters, 115(26), 268501.

Boers, N., Bookhagen, B., Marwan, N., Kurths, J., & Marengo, J. (2013). Complex networks identify spatial patterns of extreme rainfall events of the South American Monsoon System. Geophysical Research Letters, 40(16), 4386-4392.

Matheron, G. (1960). Krigeage d'un Panneau Rectangulaire par sa Périphérie. Note géostatistique, 28.

Leathers, D. J., Yarnal, B., & Palecki, M. A. (1991). The Pacific/North American teleconnection pattern and United States climate. Part I: Regional temperature and precipitation associations. Journal of Climate, 4(5), 517-528.

Wang, H., Ting, M., & Ji, M. (1999). Prediction of seasonal mean United States precipitation based on El Niño sea surface temperatures. Geophysical research letters, 26(9), 1341-1344.

Appendices

Study case: The utility of information flow in formulating discharge forecast models: a case study from an arid snow-dominated catchment*

*This work is done by Christopher Tennant, Laurel Larsen, Dino Bellugi, Edom Moges, Hongxu Ma, and Liang Zhang. Hongxu Ma majorly contribute to the methodology part, which is an extension of Chapter 2.

1 Introduction

Forecasting river flows is a cornerstone of operational hydrology and an important research topic due to the substantial impacts of flooding on life and the economy (average cost of $4.5 billion/flood event; https://www.ncei.noaa.gov/news/calculating-cost-weather-and-climate disasters). Forecasting is also an important facet of water resources planning such as predicting summer low flows (Godsey et al., 2014), anticipating drought conditions (Kapnick et al., 2018), or managing reservoir systems (Rhoades et al., 2018). Hydrologic forecasts can, in many instances, achieve a high degree of accuracy and utility but often perform more poorly at certain times of year (e.g., baseflow or peak flow) or for certain types of catchments. For example, in a national-scale evaluation of the predictability of different streamflow metrics, Eng et al. (2017) found that although data-driven forecasts typically predict mean annual runoff and the number of hydrograph peaks well, low flows are generally poorly predicted. Well-performing models are often labor-intensive, requiring years for model development, and/or might not perform well under climate conditions different from those under which the model was calibrated (Pechlivanidis et al., 2011).

Hydrologic forecasts are typically formulated at one end or another of what we refer to as the hydrologic modeling pendulum (Figure 1). The hydrologic pendulum analogy alludes to the fact that, like a physical pendulum that spends most of its time at its extremes, the hydrologic modeling community has tended to segregate its efforts into mechanistic, physically based modeling or empirical, data-driven modeling. Physically-based models are grounded in first principles and use differential equations to describe the physics of water movement and transport throughout the atmosphere, biosphere, bedrock, soil, and river channels. Both the parameterization of catchment properties and representation of 81 hydrologic processes span a range of complexity in physically-based models, with lumped parameters and tipping bucket representations exemplifying the simpler end of the spectrum and distributed parameters and detailed flow routing exemplifying the complex end. This representational complexity participates in a tradeoff with model computational and developmental tractability, performance for an individual catchment, and generalizability to a range of catchments (Larsen et al., 2016). Presently, agency-sponsored efforts to develop continental-extent models for producing hydrologic forecasts at the catchment scale are grounded in physical modeling approaches with high representational complexity (Hipsey et al., 2015; Newman et al., 2015; Xia et al., 2012).

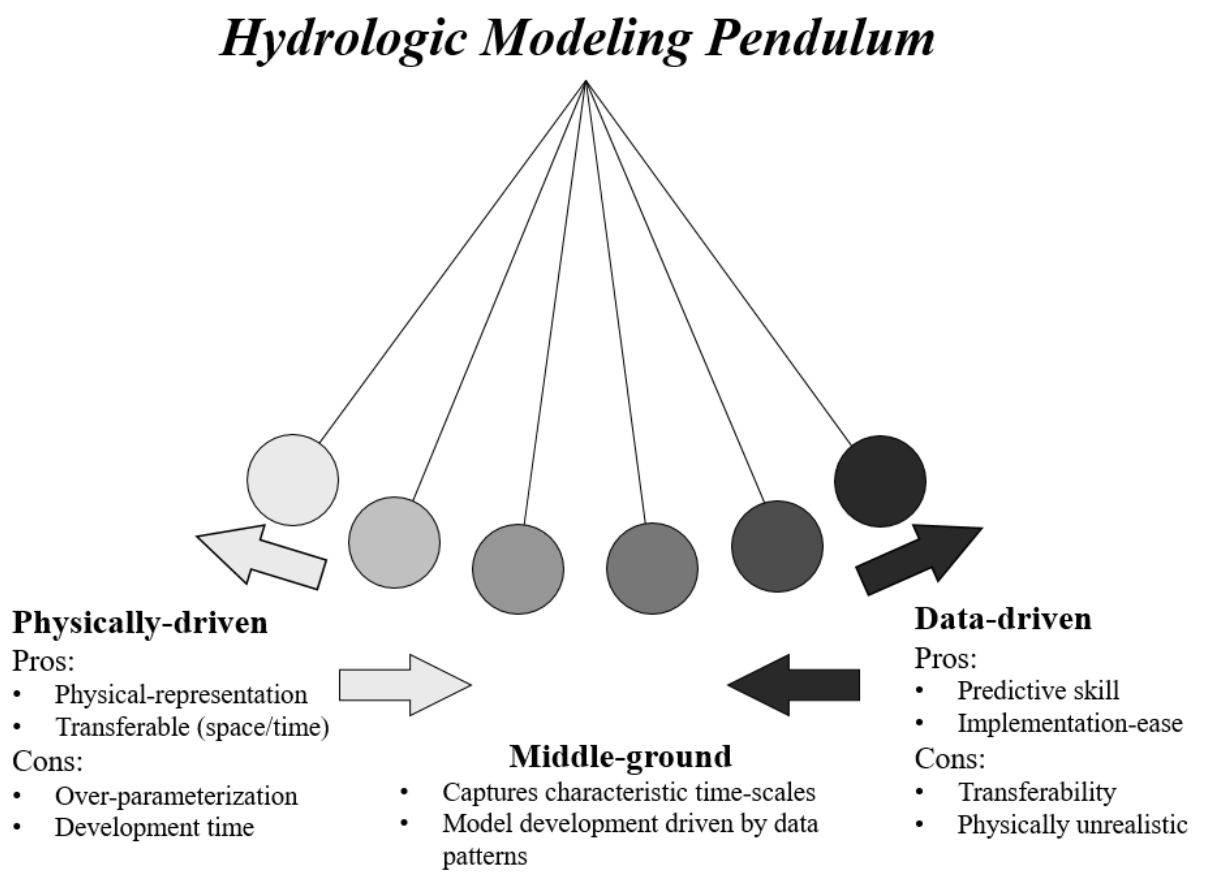

Figure 1. The *hydrologic modeling pendulum*. Hydrologic model efforts often fall into either physically based or data-driven approaches. We argue that a middle-ground between the two approaches will lead to better model performance and optimal learning.

At the opposite end of the hydrologic pendulum, data-driven, or machine-learning modeling approaches have been shown to perform as well (if not better) than process-based models (Shrestha and Nestmann, 2009; Todini, 2007; De Vos and Rientjes, 2005), yet they have important limitations. One is that they are quite sensitive to the training set employed; a model calibrated for a given time period will not predict well if there is a shift in system state or if the model encounters an event that is not contained within the training set. Furthermore, data-driven models can easily lose sight of first principles and lack physical interoperability, and many machine learning approaches are often based on discharge alone (Tokar & Johnson, 1999; Rasouli et al., 2012; Kisi & Cimen, 2011). Like a pendulum that has greatest momentum between the extrema, hydrologic forecasting may be most fruitful when it combines data-driven and physically-based strategies for modeling. Indeed, there have been many recent calls for this approach within the hydrology community (Lettenmaier, 2018; Lopez et al., 2016; Yucel et al., 2015). For example, Fatichi et al. (2016), issuing a strong call for model-data fusion, identify one of the primary opportunities for advancement of modeling efforts as the use of the hyperresolution data coming online from hydrologic observatories in a two-way exchange with large-scale modeling to formulate and test hypotheses.

Several analysis techniques not commonly used in the earth sciences and with roots in the data and information sciences may provide opportunities for resolving major uncertainties in hydrologic forecasts formulated at either end of the hydrologic modeling pendulum. These uncertainties include model feature selection (i.e., selection or representation of the variables dominant in driving catchment behavior) and identification of the appropriate timescales over which hydrologic processes occur (Benettin et al., 2015; Gibson et al., 2002; McGuire & McDonnell, 2006; McNamara et al., 2011; Skøien et al., 2003).

Streamflow is a result of complex interactions among climatic forcing, storage units, topography, land cover, and hydrogeological variables at different timescales (Bloschl & Sivapalan, 1995). Hydrologists generally recognize several types of timescales as critically important for discharge forecasting. Transit time lags represent the time parcels of water spend in storage (e.g., snowpack, in soils or groundwater) before reaching the catchment outlet, whereas hydraulic response timescales, governed by the celerity of the pressure wave, represent the time between a precipitation signal and a discharge response (McDonnell & Beven, 2014). Transit time lags are orders of magnitude larger than hydraulic response timescales (Beven, 1982) and are likely the most significant unknown for developing viable hydrologic forecast models (Kirchner, 2003; Kirchner et al., 2000).

Isotope-based studies and correlation analyses suggest these lags may be surprisingly long. For example, McGuire and McDonnell (2006) reported transit time lags ranging from less than one to five years, though these lags may be highly variable within single catchments (Benettin et al., 2015; Godsey et al., 2014; Nippgen et al., 2016). Also, Godsey et al. (2014) found that in some catchments, low flows depend not only on the current year's snowpack but the previous year's peak snow water equivalent (SWE) as well. An inability to account for these long transit times may be why estimates of catchment storage derived from continental-extent models exhibit substantial mismatches to satellite-derived estimates of storage (Scanlon et al., 2018). Further, Dawson and Wilby (2001) found that determination of interaction timescales (lags) between predictors and target variables is one of the critical factors governing performance of data driven models, while Yu et al. (2006) showed improved performance in a support vector machine model by considering timescales that are associated with hydrological response times. These studies highlight the need for a systematic guide in identifying interaction timescales in model development.

In this work we examine the potential for critical timescale detection through transfer entropy analyses to improve hydrologic forecasts. This analysis, grounded in information theory, quantifies the flow of information between pairs of time series. We argue that "info-flow informed" forecasts offer a number of benefits in different modeling contexts (e.g., avoidance of relying on subjective judgements and/or trial and error analysis in identifying timescales), discuss what these analyses reveal about watershed processes, and lay the groundwork for how our approach could be extended to inform physically-based models and ensure that they properly represent process time scales. We apply this approach to the Dry Creek Experimental Watershed (DCEW), a catchment with openly available time-series data (McNamara et al., 2017; McNamara, 2017), for which soil-water (McNamara et al., 2005, 2011; Williams et al., 2009; Smith et al., 2011) and groundwater (Aishlin, 2006; Miller et al., 2008) storage processes and the catchment water balance (Kelleners et al., 2009, 2010; Stratton et al., 2009) have been studied extensively.

Our specific questions are as follows: (1) What are the characteristic timescales between measures of hydrometeorological predictors (e.g. precipitation, snowmelt, shallow and deep soil moisture) and streamflow response? (2) How does the explicit inclusion (or omission) of the dominant timescales affect streamflow prediction skill? (3) How do differences in the temporal variability of hydrologic inputs and stores affect their ability to reduce uncertainty in discharge? We hypothesize that: (1) forecasting models that use input data lagged at the timescale for which predictor variables transfer the most information to discharge will improve prediction skill over uninformed null models. (2) Variables with a high frequency of variation (e.g., precipitation) will reduce a greater amount of uncertainty in discharge when aggregated over time compared to their non-aggregated form. (3) Hydrometeorological fluxes will influence streamflow primarily over short-term lags (i.e., < 1 year), reflecting characteristic hydrologic response timescales of the watershed. However, longer transit-time lags, due to groundwater storage processes, will also be resolvable.

2 Site Description and Data

The DCEW is located in southwestern Idaho just north of the city of Boise and within the northern portion of the Snake River Basin (Figure 2). The DCEW drains 27 km2 of semi-arid mountainous terrain that ranges from ~ 1000 m up to 2100 m in elevation. The majority of precipitation occurs during winter months, with snow being dominant at higher elevations and rain at lower elevations; approximately 54% of the basin's annual average precipitation of 57 cm is in the form of snow (Stratton et al., 2009; Williams et al 2009). Snow can persist at high elevations from November through March, though interannual variability is high, and in warm years precipitation can fall dominantly as rain (Tyler et al., 2008). Rain-on-snow events are common in late autumn and early spring, while

summers are hot and dry, with infrequent thunderstorms (Williams et al., 2009). According to the van Koppen climate classification system, upper elevations are characterized as moist continental climate and dry summers (Dsa), and lower elevations as steppe summer dry climate (Bsa) (Henderson-Sellers & Robinson, 2001). Vegetation within the catchment varies with aspect, elevation, and soil type, with grass and shrubland being the most common at lower elevations and and Douglas-fir (Pseudotsuga Menziesii), lodgepole pine (Pinus contorta), and aspen (Populus tremuloides) dominating the upper elevations (>1500 m). Riparian areas feature dense brush along perennial portions of Dry Creek and its tributaries and around low-elevation seeps, consisting of cottonwoods (Populus fremontii), water birch (Betula occidentalis), yellow willow (Salix lutea), mountain alder (Alnus viridus), and mountain maple (Acer spicatum). The geology of DCEW is predominantly biotite granodiorite of the Atlanta Lobe of the Idaho Batholith which is Cretaceous in age (Johnson et al., 1988), Soils tend to be relatively thin (max depths of 1.2 m) (Williams et al., 2009) and coarse-grained and are classified as loamy sands and sandy loams (Gribb et al., 2009); a thin veneer of wind-blown loess covers portions of the basin (McNamara et al., 2017). Soil characteristics also vary with aspect, with steeper north-facing slopes having thicker soil depths, more organic matter and silt, higher porosity, and greater water storage than gentler south-facing slopes (Geroy et al., 2011). Because of limited soil moisture storage capacity (Smith et al., 2011) and no groundwater flow contribution (Yenko, 2003), high-elevation portions of Dry Creek are intermittent and lose flow (Aislin, 2006) to deep (> 100 m) groundwater (Miller et al., 2008), though one tributary (Shingle Creek, with a drainage area of 8.6 km2) and the lower-elevation mainstem are perennial, sustained by groundwater (Stratton et al., 2009).

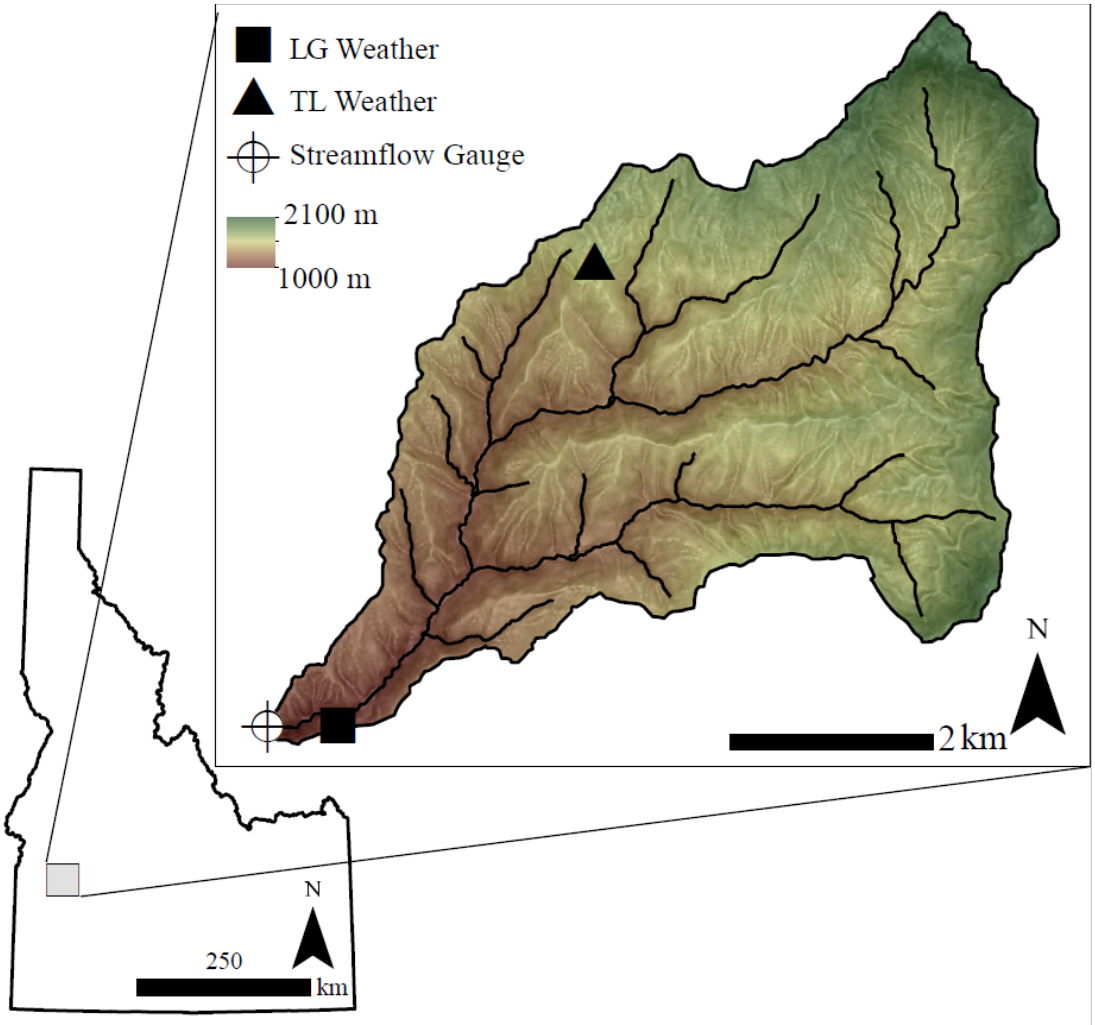

Figure 2. Dry Creek Experimental Watershed in Idaho, USA. Discharge data were obtained from the catchment outlet (cross symbol), while hydrometeorological and soil moisture data were obtained from the Treeline (TL) station (triangle) and Lower Gauge (LG) station.

The DCEW has been operational since 1998, with hydrometeorological and soil moisture sensors supplying data at an hourly time increment. Hydrometeorological sensors are positioned at a treeline (TL) and lower-elevation gauge (LG) station. Soil moisture sensors are distributed at four locations across the catchment, on north-facing and south-facing slopes adjacent to each hydrometeorological station. Discharge is monitored at the catchment outlet at the LG station (Figure 2).

2.1 Data

Initially, all variables monitored at the TL and LG meteorological stations (McNamara, 2017; Table 1), which span the longest observational period of all the catchment sensors, were considered as candidate variables for the discharge forecasting models and critical timescales analysis. Discharge measured at the LG station (McNamara et al., 2017) was the response variable in the forecasting analysis. Raw data from 1 January 2001 through 19 July 2017 were obtained from Boise State University (https://earth.boisestate.edu/drycreek/data/; data links to each station provided in Acknowledgements section). In addition, evaporation, a derived variable, was estimated for the TL and LWR stations using the Priestley-Taylor model. The Priestley-Taylor method (Priestley and Taylor, 1972) for estimating evaporation is based on radiation and is a simplification of the Penman-Monteith combination equation (Penman, 1948; Monteith, 1981). An α of 1.72 was used instead of the commonly used 1.26 to reflect the higher moisture stress of the arid conditions within the catchment. We compared mean monthly estimates of evaporation between the Priestley-Taylor and Penman-Monteith methods with long term (1916 - 2005) pan observations from the nearby Arrowrock Dam, Boise River, Idaho (https://wrcc.dri.edu/Climate/comp_table_show.php?stype=pan_evap_avg), and found better qualitative agreement with the Priestly-Taylor estimates. Evaluation of a broader range of crop coefficients would likely have improved evaporative estimates from the Penman-Monteith method; however, since the timing (as opposed to total amounts) of evaporative-demand was most salient for our analysis we used the Priestley-Taylor estimates.

All data were carefully quality controlled and any outliers or spurious patterns in the data were identified and removed by hand. Gaps in the data were filled using interpolation, multiple linear regression, and autoregressive models. When possible, multiple linear regression was used to fill gaps as this provided a synthetic record based on observations from within the catchment. When gaps occurred over small-time scales at both meteorological stations (LG and TL) autoregressive or linear interpolation was used to in-fill the records. Overall, only a small portion of the time series (< 6% on average) required gap in-filling. Gap-filled data products are also provided to the reader, with a link in the Acknowledgements.

Raw data, originally provided on an hourly time step, were aggregated to the daily time scale, the minimum time step included in our analysis. We also aggregated the data to 1-week, 2-weeks, 1-month, 2-month, 3-month, 6-month, 1-year, and 2-year timescales using a back-looking moving window to smooth out higher frequencies of variability (e.g., for precipitation, whose daily time-series is dominated by zeros). To remove periodic/seasonal trends from the time series we computed an anomaly for each variable at each aggregation length by computing the day of water year (DOWY) mean (based on the full period of record) and then differencing the DOWY mean from the daily and aggregated values. These anomaly time series were used for our transfer entropy analysis and allowed us to detect causal interactions between hydrologic variables that were not driven by synoptic changes in seasonal conditions.

Appendices

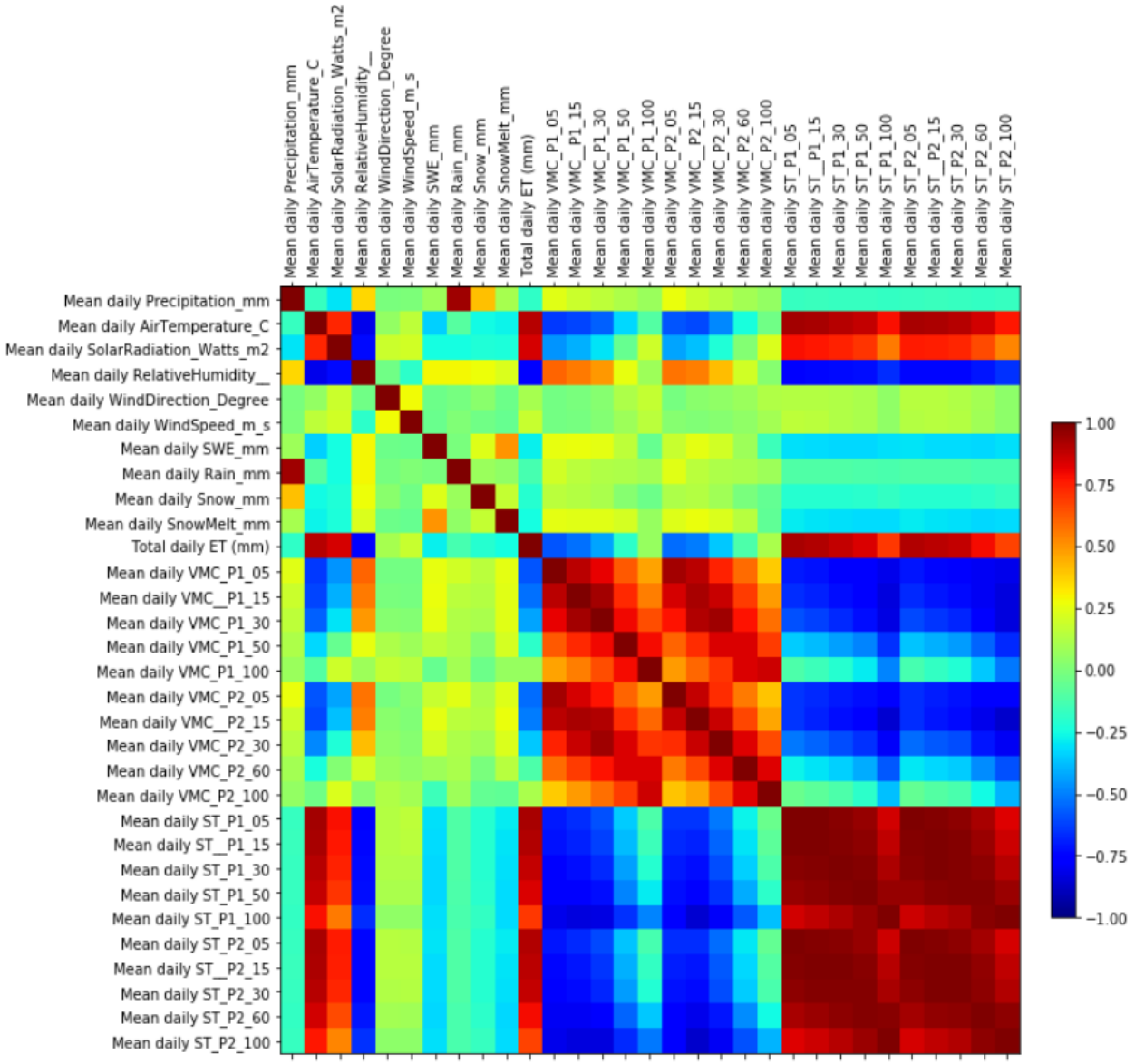

Figure 3. Correlation-heat-map for Treeline station. See Table 1 for a description of the variables.

Appendices

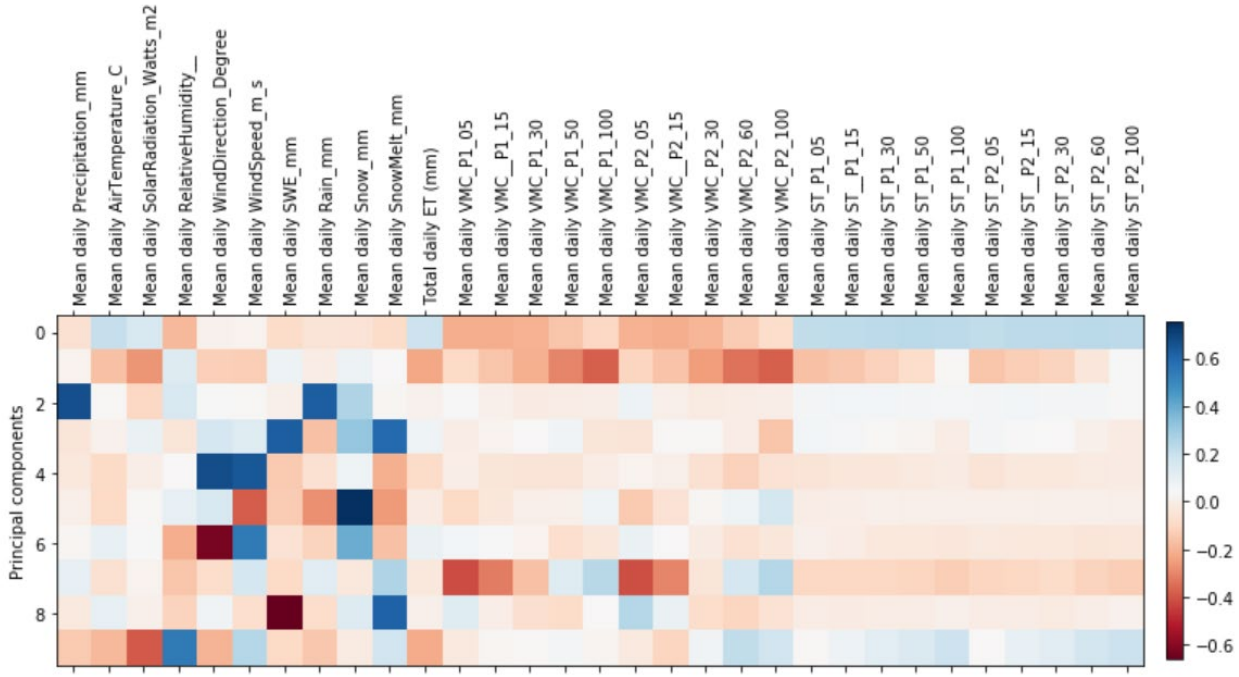

Figure 4. Principal components analysis for the Treeline station. Colors show relative magnitudes of the loading of each variable on nine principal components scores.

Appendices

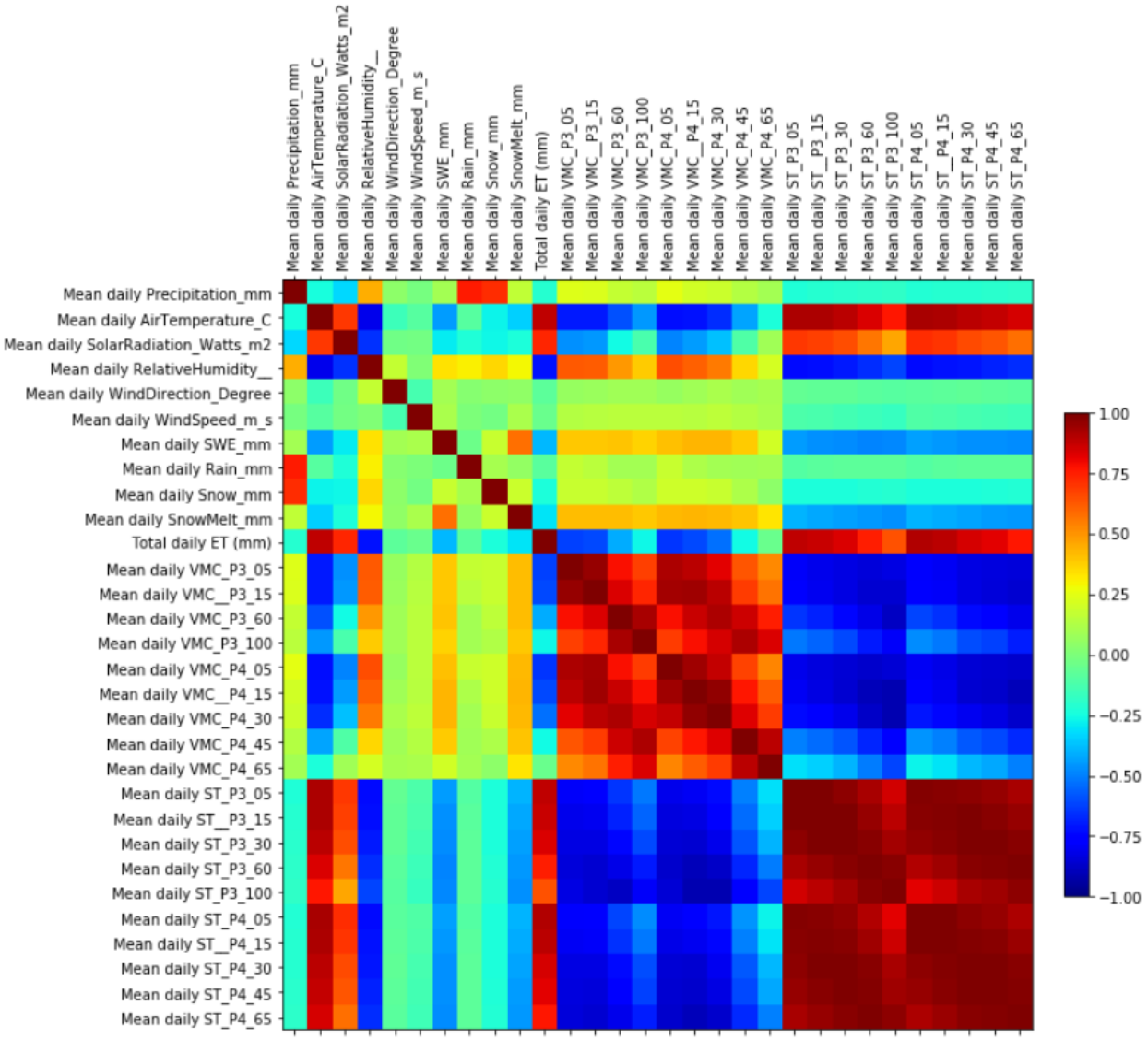

Figure 5. Correlation-heat-map for Lower gauge station. See Table 1 for a description of the variables.

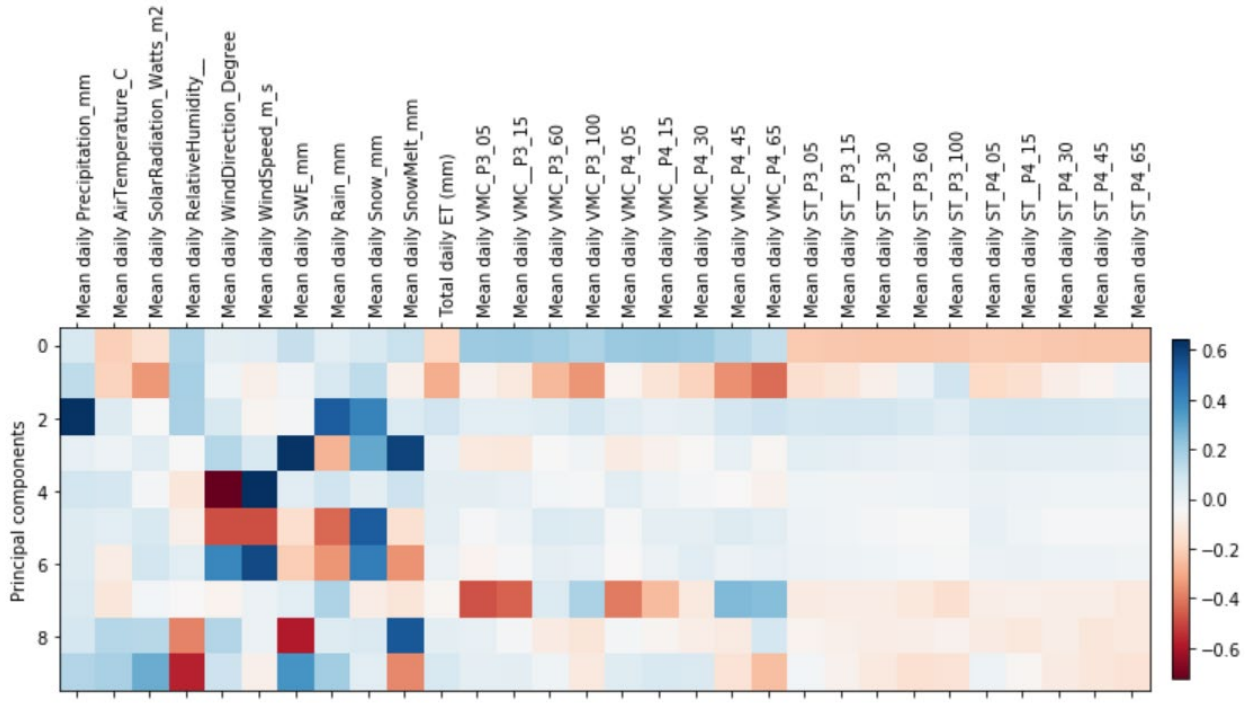

Figure 6. Principal components analysis for the Lower gauge station. Colors show relative magnitudes of the loading of each variable on nine principal components scores.

Following the data preprocessing, a subset of predictor variables was selected for further analysis. Selection of predictor variables is important for removing redundant data, avoiding over-parameterization, and discarding non-informative predictors (May et al., 2011). For each meteorological station, we conducted a correlation analysis and principal components analysis to identify variables that exhibited collinearity (Figure 3-2.14 and Table 1). We discarded the collinear variables least relevant to the physical water balance of the catchment from further analysis, with a few exceptions (Table 1). Although air temperature, shallow soil moisture, and evapotranspiration exhibited high correlations with each other, the principal components analysis suggested that components of these variables exhibited orthogonal behavior, so all three variables were retained (Figure 4, 2.14). Also, although soil moisture from north-facing slopes was strongly correlated to that from south-facing slopes, we retained both sets of variables because of prior physical understanding of salient differences in mechanisms that drive soil moisture availability as a function of aspect (Geroy et al., 2011; Smith et al., 2011; McNamara et al., 2018). Last, both snow-water equivalent (SWE) and snowmelt were retained despite their high correlation because of the understanding that instantaneous melt rate (i.e., snowmelt) measures a process that could have different implications for discharge from total water available within the snowpack (SWE). In total, we identified 9 predictor variables per station for our final analysis (Table 1), resulting in a total of 18.

Notably, unlike many other machine-learning based forecasts of discharge discussed in the literature (Erdal and Karakurt, 2013; Hsu et al., 1995; Besaw et al., 2010; Kisi and Cigizoglu, 2007; Jeong and Kim, 2005), we did not consider past discharge as a predictor. Our rationale was that our analysis was intended to evaluate the type of forecasts that might be generated from projections of hydroclimatic information for ungauged basins from land-surface models or available through remote sensing, for longer forecast timescales than a single day in advance.

Table 1. Hydroclimatic and hydrologic variables considered for discharge forecast model

Variable(s)[1]	**Description**	**Unit**	**Used as input?**[2]	**Behavior category from TE analysis**[3]
Precipitation		mm day^{-1}	Yes	3

Rain		mm day^{-1}	No	--
Snow		mm day^{-1}	No	--
Air temperature		^{o}C	Yes	3
Evapotranspiration		mm day^{-1}	Yes	2, 3 (TL) 3, 2 (LG)
VMC_P1_05 (LG)	Volumetric moisture content at 5 (10, 15, 30, 50) cm, south-facing	%	Yes	3
VMC_P1_15 (LG)		%	No	--
VMC_P1_30 (LG)		%	No	--
VMC_P1_50 (LG)		%	No	--
VMC_P2_05 (LG)	Volumetric moisture content at 5 (10, 15, 30, 60) cm, north-facing	%	Yes	3
VMC_P2_10 (LG)		%	No	--
VMC_P2_15 (LG)		%	No	--
VMC_P2_30 (LG)		%	No	--
VMC_P2_50 (LG)		%	No	--
VMC_P3_05 (TL)	Volumetric moisture content at 5 (15, 60) cm, south-facing	%	Yes	3
VMC_P3_15 (TL)		%	No	--
VMC_P3_60 (TL)		%	No	--
VMC_P4_05 (TL)	Volumetric moisture content at 5 (15, 30, 45) cm, north-facing	%	Yes	3
VMC_P4_15 (TL)		%	No	--
VMC_P4_30 (TL)		%	No	--
VMC_P4_45 (TL)		%	No	--
ST_P1 at all depths (LG)	Soil temperature, south-facing	^{o}C	No	--
ST_P2 at all depths (LG)	Soil temperature, north-facing	^{o}C	No	--
ST_P3 at all depths (TL)	Soil temperature, south-facing	^{o}C	No	--
ST_P4 at all depths (TL)	Soil temperature, north-facing	^{o}C	No	--
Solar radiation		Wm^{-2}	No	--
Net radiation		Wm^{-2}	No	--
Relative humidity		%	No	--
VMC_P1_100 (LG)	Volumetric moisture content at 100 cm, south-facing	%	Yes	2

VMC_P2_100 (LG)	Volumetric moisture content at 100 cm, north-facing	%	Yes	1
VMC_P3_100 (TL)	Volumetric moisture content at 100 cm, south-facing	%	Yes	3
VMC_P4_65	Volumetric moisture content at 65 cm, north-facing	%	Yes	1
Wind speed		m s^{-1}	No	--
Wind direction		Degrees	No	--
SWE	Snow-water equivalent	mm	Yes	1
Snowmelt		mm day^{-1}	Yes	2 (TL) 2,3 (LG)

[1]Unless otherwise indicated, includes variables measured at both the Lower Gage (LG) and Treeline (TL) sites.
[2]Based on a principal components analysis and correlation analysis performed on variables from each station individually. Clustered rows group variables that are collinear with each other (with the caveat that the collinearity of data from the LG station with data from the TL station was not evaluated).
[3]See Section 3.4.1.2. Where multiple categories are listed, the primary category is listed first.

3 Methods

3.1 Information-flow analysis to identify causal interactions and critical timescales

Here we use the transfer entropy to identify causal interactions and critical timescales as discussed in the previous chapter. We calculate TE for time lags up to 730 days (i.e., two years), which meets the criterion for the minimum number of overlapping data points between the discharge and predictor time-series for a robust TE analysis (500 datapoints, according to the rule of thumb proposed by Ruddell and Kumar (2009a)). We quantify the relative significant TE at each lag τ as $T'_{rel,\tau} = (T_\tau - T_{0,\tau})/H_Q$ where $T_{0,\tau}$ is the significance threshold at that time lag and HQ is the total uncertainty in the sink variable, discharge. $T'_{rel,\tau}$ is a normalized version of the TE that quantifies the significant reduction in the uncertainty of discharge relative to the total uncertainty in discharge. The τ associated with the highest $T'_{rel,\tau}$ within the first 180 lags was selected as the critical timescale (i.e., most significant lag) to be used in the machine-learning forecast models. Although use of just a single time lag in these analyses captures only the timescale of the most dominant mechanism through which each independent variable controls discharge, ignoring multi-year and/or less dominant processes, the decision to apply one time lag to each variable allows us to cleanly test the hypothesis that incorporating information about critical timescales improves a model's forecast skill, without applying arbitrary thresholds for peak selection. Further, by limiting the τ selected for the machine learning analysis to 180 days, we minimize the number of training days that must be discarded (i.e., since the first portion of the time series up to the maximum number of lag days considered cannot be modeled).

3.2 Forecasting models

As a simplest first test of our hypotheses, we generated machine-learning model forecasts of discharge in the DCEW. Although these models lie on the purely data-driven end of the hydrologic modeling pendulum, they offer the advantage here of providing a straightforward means through which to adjust the critical timescales represented in the model (i.e., through adjustment of the predictor variable lags and aggregation timescales used in model training).

Unlike physically based models, the performance of machine-learning models is not a function of the quality of measurements of physical properties of the catchment nor of calibration of hydrologic parameters, resulting in a simpler test of the hypotheses.

We selected two commonly used machine-learning strategies to generate discharge forecasts. Random forest regression (RFR) was selected as an example of a machine-learning algorithm that is readily interpretable, in that it

is possible to extract the relative importance of variables in predicting an output and even to generate a predictive equation that is a linear combination of variables in a partitioned state-space. Support vector machine regression (SVR), in contrast, was selected as an example of a machine-learning algorithm that generates black-box predictions (making it difficult to estimate the "importance" of predictor variables) but that, relative to other common machine-learning algorithms such as artificial neural networks, exhibits improved generalization ability and performance, particularly for highly nonlinear systems (Vapnik, 1998). SVR always converges upon global (not local) minima but, in comparison to RFR, is more computationally intensive. Collectively, we refer to the RFR and SVR forecasts as the machine learning models (MLMs).

Both MLMs were trained and tested in an identical manner. In both cases, the first 75% of the discharge time series was designated the training dataset (from 01/01/2001 to 12/31/2012), while the last 25% (from 01/01/2013 to 12/31/2016) served as the "test" dataset for evaluating model performance. In the training phase, the training data were randomly partitioned into 5 disjoint subsets, and in turn each subset is used as a test set while the other k-1 sets are used for training. Parameters used within the MLMs (described below) were also optimized through k-fold cross-validation grid searching, which tests discrete combinations of parameters within the search range. The parameters resulting in the best average performance across the k iterations are used to train the SVR on the entire training set. The resulting model is then evaluated on the test dataset. Performance within the training dataset was assessed through the root-mean squared error. As described in section 3.3.2.3, performance within the test dataset was assessed through a suite of metrics.

3.2.1 Random Forest Regression

RFR is an ensemble learning technique that combines a number of decision trees into an additive model to generate a predicted value (here, streamflow). Each base or tree model is trained on a random sample of the training dataset. The prediction is the average of all the outputs from the trees, which controls for overfitting. RFR is typically valued for the accuracy and stability of the output models (Ho, 1995; Breiman, 2001).

Here we used the scikit-learn python package to implement the RFR (Pedregosa, 2011), splitting the branches based on the Gini impurity coefficient (Liaw & Wiener, 2002). Five algorithmic parameters were optimized through the cross-validation grid searching: 1) the number of individually trained regression tree models in the ensemble, 2) the number of features to be considered when searching for the best split strategy, 3) the minimum number of samples needed to generate leaf nodes, 4) the minimum number of samples needed for a leaf node, which will make sure the model will have enough historical data to learn for a certain scenario, and 5) the threshold to stop the growth of the tree. The node will stop splitting if this split induces a decrease of the impurity smaller than this threshold.

3.2.2 Support Vector Regression

Support Vector Machines (SVM) are a class of non-parametric semi-supervised learning algorithms (Vapnik & Chervonenkis, 1974; Vapnik, 1995). They can be applied to highly non-linear problems by mapping the input data via a kernel function to a much higher dimensional space where the original nonlinear problem can be transformed into a linear one (Drucker et al., 1997). For robustness, the learning algorithm for SVR introduces a cost function to penalize deviations from the learned continuous function, which is minimized via convex quadratic optimization. The most widely used cost function in SVR is the ε-insensitive loss function (Vapnik, 1995; Müller et al., 1999), whereby data points inside a "tube" of radius epsilon do not contribute to the cost. SVMs thus require choosing a kernel function (here, a radial basis function) and its hyper-parameter (i.e., the width γ of the radial basis), a hyper-parameter C that controls the error penalty, and in the case of ε-SVR, the hyper-parameter ε. Due to the computational intensiveness of training the SVR, the grid search and k-fold cross-validation procedure to obtain values for the hyper-parameters gamma, C, and epsilon were initially performed with a coarse grid resolution (0.5 increments in log2 space) to find neighborhoods of the parameter space that were subsequently tested in detail with a fine grid resolution (0.05 increments in log2 space) 5-fold cross-validation procedure. Ultimately, these choices control the complexity of the non-linear mapping and the tradeoff between training error vs. model complexity, and thus the tradeoff between training and prediction performance. We adopted the epsilon-SVR described in Smola and Schölkopf (1998) and implemented in the package LIBSVM (Chang & Lin, 2011) (software available at http://www.csie.ntu.edu.tw/~cjlin/libsvm).

3.2.3 Assessment of model performance

The use of multiple model performance measures is important to reveal model goodness of fit for the different segments of a hydrograph. Here, we considered three statistical performance measures (1) Nash-Sutcliffe efficiency

(NSE), which emphasizes model performance in capturing high flow segments, (2) the log transformed Nash-Sutcliffe (logNSE) metric, which emphasizes model performance in low flow regimes, and (3) Root mean square error (RMSE), which reveals performance in capturing the overall model fitting. Mathematically, the formulations are:

$$NSE = 1 - \frac{\sum_i^N (Q_i - \hat{Q}_i)^2}{\sum_i^N (Q_i - \bar{Q}_i)^2} \quad [2.6]$$

$$logNSE = 1 - \frac{\sum_i^N (logQ_i - log\hat{Q}_i)^2}{\sum_i^N (logQ_i - log\bar{Q}_i)^2} \quad [2.7]$$

$$RMSE = \sqrt{\frac{\sum_i^N (Q_i - \hat{Q}_i)^2}{N}} \quad [2.8]$$

In the above equations, Q_i and $\hat{Q}_i$represent observed and simulated streamflow over a total record length of N data points, while $\bar{Q}_i$ represents the mean of the discharge time series.

Generally, we found that the results from the NSE metric mirrored those of the logNSE metric, so while we show both metrics in our table of MLM results, we heretofore discuss only the NSE metric.

3.3. Experimental design

We tested the performance of TE-informed hydrological forecasts against several important benchmarks (Table 2). The "null" model benchmark is a forecast formulated as a simple day-of-year (DOY) average. This model predicts that discharge at any DOY in the test period is equal to the average discharge measured in the same DOY during the training period. The "expert's" model benchmark, meanwhile, is an MLM developed through traditional (i.e., not info-flow informed) approaches, in which the expert recognizes the importance of timescale in model performance but lacks a robust way of detecting critical timescales. In this model, a combination of professional judgement and trial-and-error was used to select input variable characteristics, prior to examining the results of the TE analysis. Last, each of the "informed" MLMs was compared to a companion "uninformed" MLM, which used the same combination of input variables and aggregation timescales but in which the inputs were not time-lagged.

Table 2 Classes of discharge forecast models evaluated. The shading of the rows indicates the color used to depict each class of model throughout the paper.

Model Terminology	Model description	TE-informed components	Number of predictor variables
Null	Prediction formulated from day-of-year average flow	None	N/A
Cumulative, informed	MLM with full set of predictor variables from Table 1, aggregated at specified timescale and all smaller timescales	Lags	18 x number of aggregation scales
Cumulative, uninformed	MLM with full set of predictor variables from Table 1, aggregated at specified timescale and all smaller timescales	None	18 x number of aggregation scales
Non-cumulative, informed	MLM with full set of predictor variables from Table 1, aggregated at specified timescale	Lags	18
Non-cumulative, uninformed	MLM with full set of predictor variables from Table 1, aggregated at specified timescale	None	18

Limited, informed	MLM with only temperature and precipitation as predictors, aggregated at specified timescale and all smaller timescales	Lags	2 x number of aggregation scales
Limited, uninformed	MLM with only temperature and precipitation as predictors, aggregated at specified timescale	None	2 x number of aggregation scales
Expert's	MLM with Lower Gauge and Treeline precipitation, air temperature, and soil moisture (deep + shallow, north-facing + south-facing) as predictors, aggregated at 7 days of daily data, the subsequent 2 weeks of weekly data, and subsequent 2 months of monthly data	None	12 x (7 + 2 + 2) = 121
Fully informed	MLM with full set of predictor variables from Table 1, each aggregated and lagged at the timescales that coincide with the maximum transfer of information to discharge	Lags, aggregation scale	18

Several classes of MLMs were developed for comparison, mainly to assess the independent contributions of appropriate selection of the lag timescale and aggregation timescale(s). "Cumulative" MLMs included variables aggregated at multiple timescales, whereas "non-cumulative" MLMs featured only a single timescale of aggregation. A separate set of "limited" MLMs was developed to evaluate whether TE-informed models developed only using the most widely available sensor datasets (air temperature and precipitation, also available as remote sensing products) exhibited improved performance relative to uninformed models. Last, a set of "fully informed" models, in which a unique aggregation timescale and lag that maximized information transfer to discharge were selected for each variable.

4 Results

4.1 Characteristic timescales of interaction between discharge and its hydrometeorological predictors

4.1.1 Critical timescales for daily-aggregated predictors of streamflow

All daily predictor variables transferred significant information to discharge over lags from several days up to 120 days, though with considerable variability across variables and within that span of time (Figure. 2.15 and 2.16). While several variables consistently transferred significant information to discharge within the first day (precipitation, snow-water equivalent, and some soil moisture pits) across the two measurement stations, other variables (air temperature, evapotranspiration, other soil moisture stations) consistently transferred significant information only after several days of lag, with the delay being greatest for air temperature.

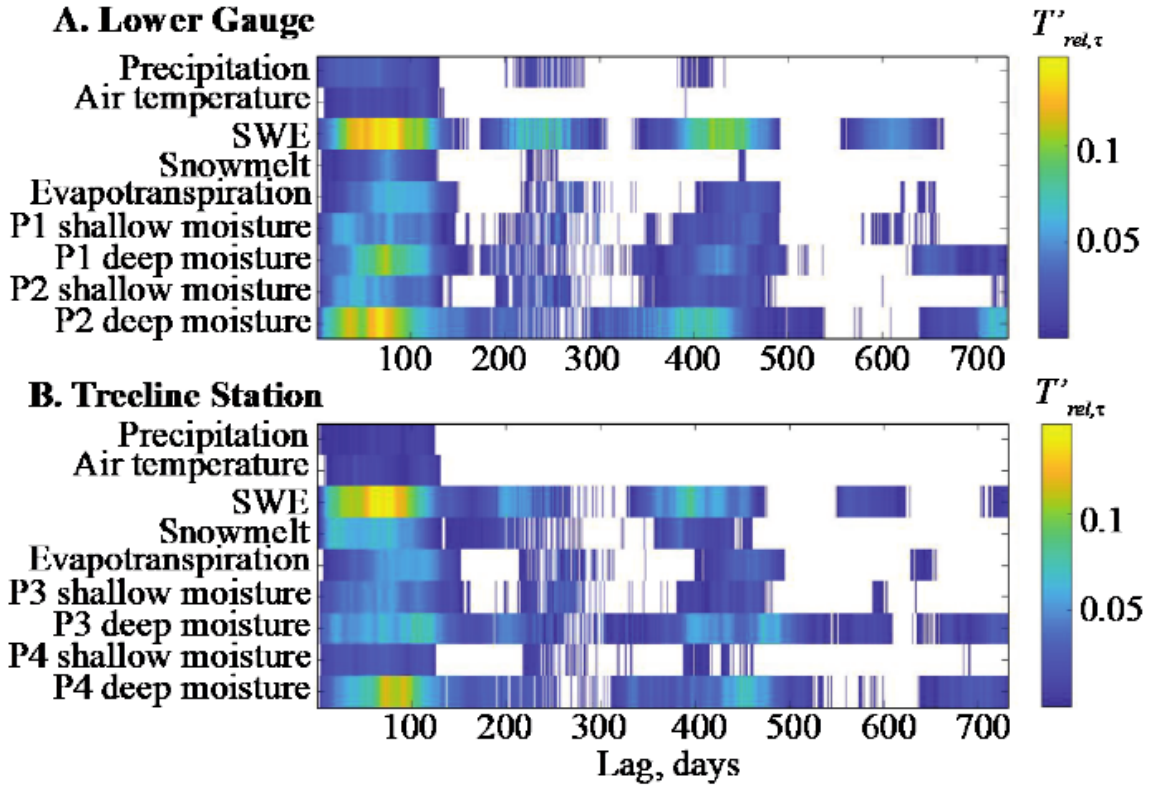

Figure 7. Relative significant transfer entropy of daily hydroclimatic predictor variables to discharge. The color indicates the value of $T'_{rel,\tau}$ over a range of variables (y-axis), and lag days τ (x-axis) for the Lower Gauge (A) and Treeline Station (B). White areas indicate lag times for which no significant information was transferred to discharge.

Within the 120-day "seasonal" timescale, snow-water equivalent (SWE) by far transferred the most information to discharge (Figure 7), peaking at an approximately 90-day lag. Deep soil moisture measured on the north-facing slope (P2 and P4) transferred the next highest amount of significant information, with a nearly equivalent lag for the treeline pits and a shorter lag (~70 days) for the lower-elevation pits. Deep moisture on the south-facing slopes transferred the third-highest amount of significant information, with a lag equivalent to that of the north-facing slopes at lower elevations and a slightly longer lag (>100 days) than the critical timescales of SWE or soil moisture on the north-facing slope at the Treeline station. Among the remaining daily-aggregated variables, precipitation and air temperature transferred the lowest amounts of significant information to discharge.

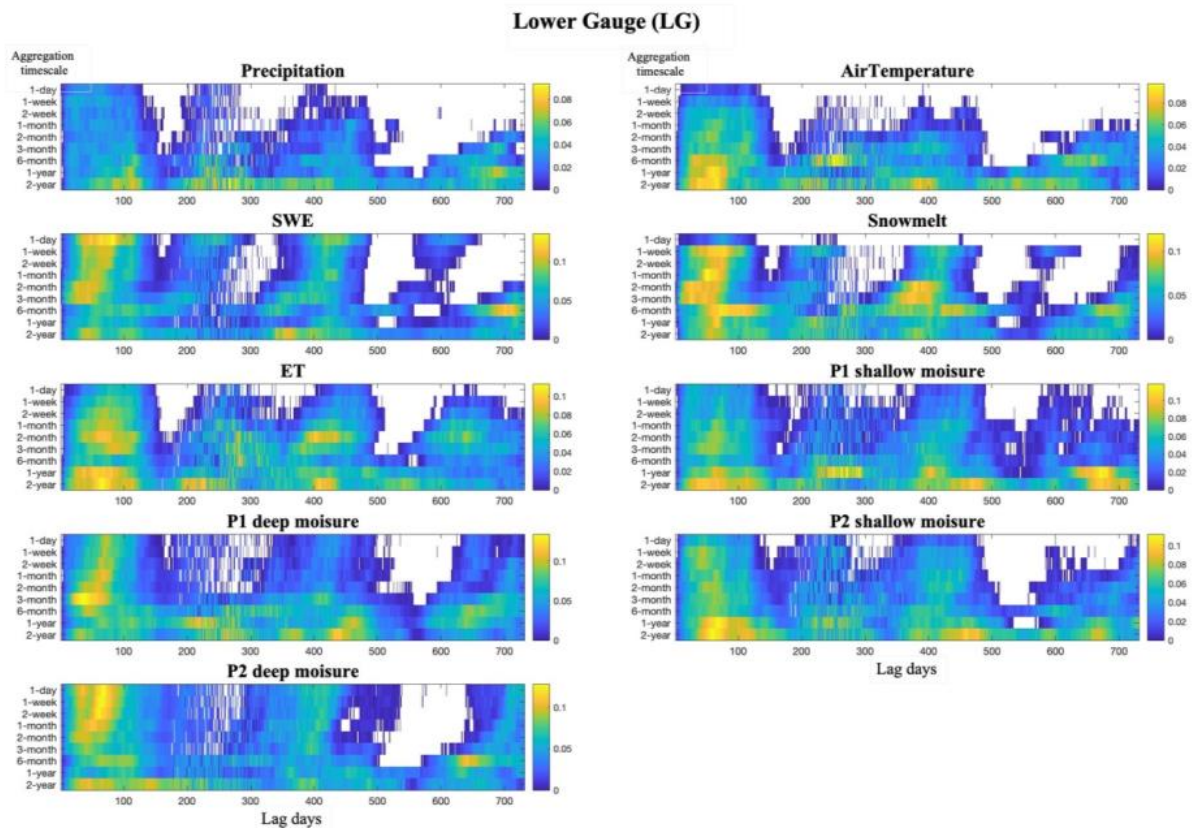

Figure 8. Relative significant transfer entropy of daily hydroclimatic predictor variables to discharge over all aggregation timescales for the Lower gauge station. The color indicates the value of $T'_{rel,\tau}$ over a range of variables (subplots), lag days τ (x-axis) and aggregation timescales(y-axis). White areas indicate lag times for which no significant information was transferred to discharge.

At timescales longer than the 120-day "seasonal" timescale but still less than one year, many of the variables exhibited some transfer of significant information to discharge, interspersed with many non-significant lags, except for SWE, which consistently transferred significant information over a band spanning 180-320 days. Within this band of timescales, the transfer of information peaked approximately half a year after the seasonal timescale peak. Because of this symmetry and the lack of an underlying physical mechanism, we interpret significant information transfer within this band as an artifact due to incomplete removal of each year's seasonal signal through the day-of-year anomaly filter, as previously noted by Larsen and Harvey (2017). In other words, if an intra- and interannually variable signal is consistently low in summer but high in winter (or vice-versa), and that pattern is incompletely removed through subtraction of a typical year's signal (as performed here, see section 3.2.1), the remnant summer-low values will be associated with remnant winter-high values half a year later, thereby reducing uncertainty. For this reason, we do not further discuss significant information transfer within this band of timescales. Notably, other short bands of significant information transfer surrounded by bands without significant information transfer may be attributed to random processes, as one in 20 randomly shuffled samples in a time series would be expected to yield a false positive when using a significance threshold of alpha = 0.05.

At one year past the ~90-day information transfer peak, SWE and deep soil moisture (particularly on the north-facing slope) transferred notable amounts of information to discharge, while air temperature and Treeline precipitation transferred no significant information. Among the predictor variables with substantial information transfer at these timescales, the magnitude of information transfer was higher than that exhibited in the "false" half-year harmonic discussed above. Because of the high probability of interannual variability, artifacts in information transfer are less likely for the one-year harmonic than the half-year harmonic. Thus, these greater-than-one-year lags in significant information transfer are likely interpretable as physically important.

4.1.2. Critical timescales for multiday-aggregated predictors of streamflow

At aggregation timescales of greater than one day, the behavior of predictor variables fell into roughly three different categories (Figure. 2.16 and 2.17). First, variables with high significant information transfer to discharge at the daily timescale (SWE, deep moisture on north-facing slopes) continued to transfer high amounts of information to discharge up to aggregation timescales of 1-3 months, with similar but slightly shorter peak lags (i.e., the "seasonal" critical timescale), consistent with adjustment for the centroid of the backwards-looking window used for the aggregation. Over longer timescales of aggregation, their importance fades.

The second category includes variables for which significant information transfer to discharge peaks at intermediate timescales, of 2-6 months (snowmelt, ET). Although the first peak lag for these variables is consistent with the seasonal critical timescale, these variables have equally or almost-equally strong peak information transfer at the multi-year timescale (i.e., ~90-day critical lag + 365 days).

The third category includes variables that have some of the lowest significant information transfer to discharge but peak in their information transfer at long (1-2 year) timescales of aggregation (precipitation, air temperature, deep moisture on south-facing slopes, shallow moisture on both north-facing and south-facing slopes). Information transfer peaks tend to be broader for these variables and spread over a wider range of lags than the consistent seasonal critical timescale previously identified. These lags range from approximately 50 to 150 days. Notably, these variables transfer significant information to discharge over all time lags and also feature broad secondary peaks at the two-year harmonic.

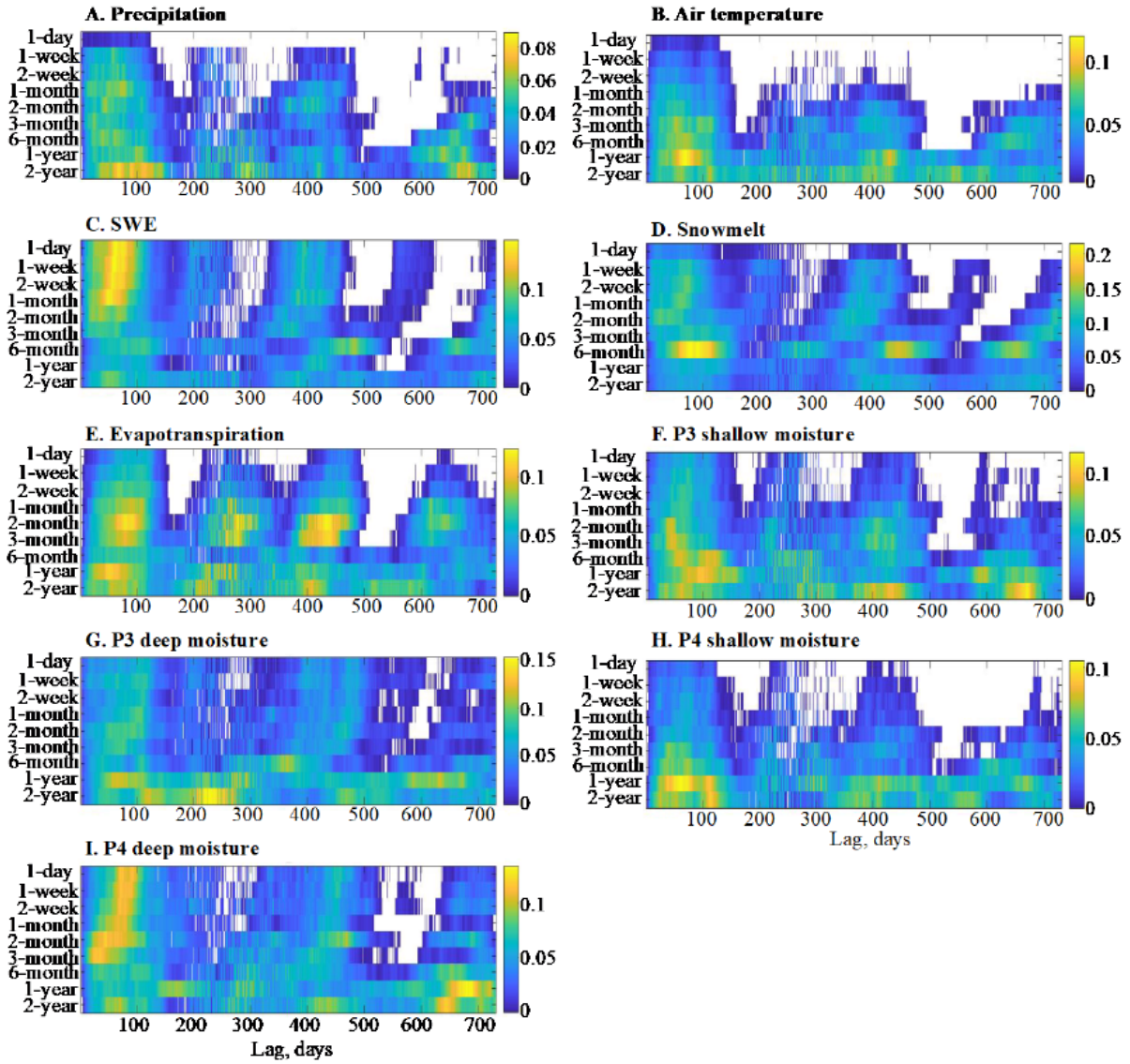

Figure 9. Relative significant transfer entropy of hydroclimatic predictor variables to discharge over all aggregation timescales for the Treeline site. The color indicates the value of $T'_{rel,\tau}$ over a range of predictor variables (subplots), lag days τ (x-axis), and aggregation timescales (y-axis). White areas indicate lag times for which no significant information was transferred to discharge.

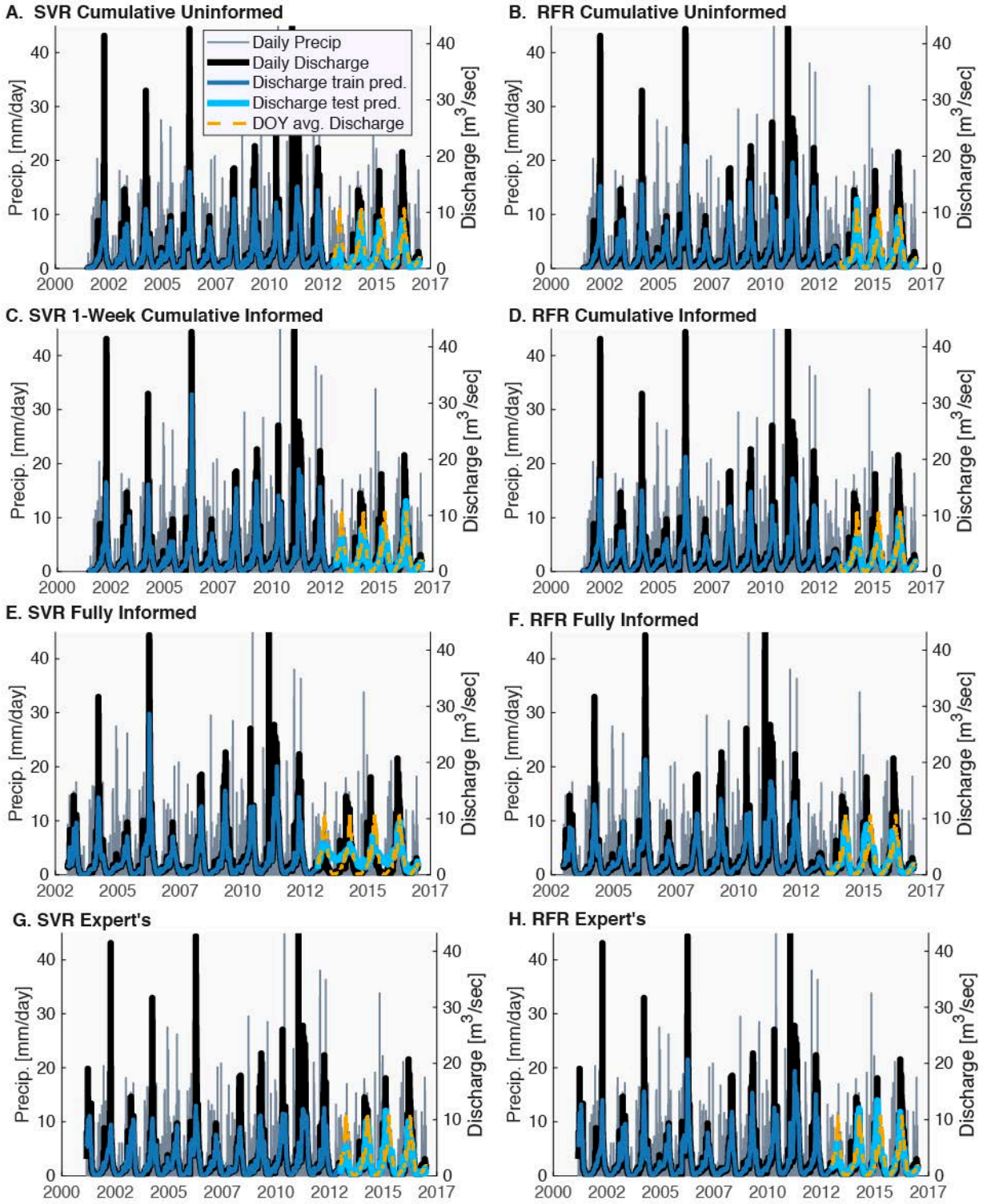

Figure 10. Measured and modeled hydrographs for the best-performing support vector regression (SVR) and random forest regression (RFR) forecast models in select model classes. Model classes (subfigure rows) are described in Table 2. Precipitation is displayed in the background of the hydrographs, and predictions for the null (day-of-year) model are shown for the model test period (2012-2017). The training period extends from 2000-2012.

4.2 Comparative Performance of Machine-learning Models

4.2.1 General model performance

While forecast performance varied substantially across the different MLMs in our experimental design, some generalities were observed. Both the RFR and SVR models tended to capture baseflow relatively well and underpredict peakflow, though the timing of peakflow was generally well predicted (Figure. 2.18). For both the RFR and SVR models, the uninformed daily (i.e., same-day, unlagged) model exhibited similar or worse performance compared to the null (day-of-year mean) model, with an RMS error of approximately 0.13 $m^3 d^{-1}$ (0.15 $m^3 d^{-1}$ for the RFR) and a NSE of 0.44-0.46 (-0.33 for the RFR).

Table 3. Performance metrics for the complete set of discharge forecasting models. Models are shaded by class, in accordance with the experimental design (Table 2)

Model	SVR (or Null Model) RMSE Test	RFR RMSE Test	SVR (or Null Model) NSE Test	RFR NSE Test	SVR (or Null Model) logNSE Test	RFR logNSE Test
Null	0.13300		0.44400		0.43500	
1D Uninformed	0.15006	0.12500	-0.32858	0.45900	-0.06413	0.54800
1W Cumulative Uninformed	0.12106	0.10100	0.13523	0.64600	0.69717	0.69500
2W Cumulative Uninformed	0.09980	0.09100	0.41233	0.71800	0.68214	0.74700
1M Cumulative Uninformed	0.07485	0.08300	0.66947	0.76100	0.67549	0.78500
2M Cumulative Uninformed	0.06738	0.07800	0.73216	0.79100	0.70419	0.82000
3M Cumulative Uninformed	0.06710	0.07900	0.73433	0.78600	0.67748	0.82500
6M Cumulative Uninformed	0.06503	0.07700	0.75047	0.79500	0.79406	0.83300
1D Informed	0.08629	0.10700	0.56072	0.60700	0.58714	0.65700
1W Cumulative Informed	0.08096	0.10500	0.61328	0.62200	0.59680	0.68300
2W Cumulative Informed	0.08270	0.10100	0.59646	0.64900	0.48961	0.69500
1M Cumulative Informed	0.08409	0.10100	0.58280	0.64800	0.50894	0.69600
2M Cumulative Informed	0.08920	0.10000	0.53060	0.65700	0.47922	0.70600
3M Cumulative Informed	0.08802	0.09900	0.54283	0.66600	0.59246	0.71300
6M Cumulative Informed	0.08583	0.09700	0.56540	0.67700	0.61268	0.72400
1D Non-Cumulative Uninformed	0.15006	0.12500	-0.32858	0.45900	-0.06413	0.54800
1W Non-Cumulative Uninformed	0.10059	0.09200	0.40297	0.78600	0.45382	0.74000
2W Non-Cumulative Uninformed	0.09421	0.09500	0.47637	0.69100	0.51980	0.71700
1M Non-Cumulative Uninformed	0.09932	0.08500	0.41802	0.75000	0.45249	0.78500
2M Non-Cumulative Uninformed	0.11045	0.08500	0.28023	0.75500	0.30677	0.79700
3M Non-Cumulative Uninformed	0.11458	0.09600	0.22542	0.68100	0.25151	0.73700
6M Non-Cumulative Uninformed	0.12924	0.09000	0.01445	0.72200	0.01455	0.76100
1Y Non-Cumulative Uninformed	0.13316	0.16700	-0.04622	0.04700	-0.08689	0.03900
1D Non-Cumulative Informed	0.08629	0.10700	0.56072	0.60700	0.58714	0.65700
1W Non-Cumulative Informed	0.07986	0.10600	0.62372	0.60900	0.65095	0.66300
2W Non-Cumulative Informed	0.08901	0.09800	0.53252	0.67000	0.56163	0.71500
1M Non-Cumulative Informed	0.10526	0.10800	0.34622	0.59900	0.36078	0.65000
2M Non-Cumulative Informed	0.12064	0.10800	0.14125	0.59800	0.12748	0.65500
3M Non-Cumulative Informed	0.12525	0.09800	0.07442	0.67000	0.07080	0.71100

6M Non-Cumulative Informed	0.12986	0.11800	0.00502	0.52500	-0.00426	0.58000
1Y Non-Cumulative Informed	0.13041	0.17200	-0.00344	-0.01400	-0.01577	-0.01500
1D Limited Uninformed	0.12237	0.15300	0.11646	0.20000	0.25573	0.22700
1W Limited Uninformed	0.11329	0.13000	0.24277	0.41900	0.25573	0.44000
2W Limited Uninformed	0.11137	0.11700	0.26824	0.52700	0.27660	0.54100
1M Limited Uninformed	0.10473	0.09900	0.35282	0.66100	0.60607	0.68100
2M Limited Uninformed	0.08465	0.09000	0.57721	0.72300	0.61223	0.75900
3M Limited Uninformed	0.08579	0.08000	0.56578	0.78300	0.59731	0.81300
6M Limited Uninformed	0.08605	0.08100	0.56309	0.77600	0.60607	0.81300
1D Limited Informed	0.12232	0.13100	0.11721	0.41200	0.35333	0.47200
1W Limited Informed	0.10949	0.12200	0.29265	0.48700	0.35333	0.55300
2W Limited Informed	0.10999	0.11100	0.28626	0.57400	0.28714	0.62700
1M Limited Informed	0.10761	0.10700	0.31681	0.61000	0.36987	0.65400
2M Limited Informed	0.10260	0.10200	0.37891	0.64600	0.43111	0.68900
3M Limited Informed	0.09520	0.09800	0.46521	0.67300	0.49696	0.71300
6M Limited Informed	0.09520	0.09300	0.46521	0.70300	0.41038	0.73500
Expert's	0.06504	0.06900	0.75041	0.71400	0.77926	0.74400
Fully Informed	0.10463	0.11600	0.35412	0.54300	0.31480	0.60200

4.2.2. Informed vs. uninformed models

Using the lagged daily data instead of the unlagged daily data improved performance statistics by 19-37% (Table 3). Improvement was more marked in both the informed and uninformed models when longer-term aggregations (1 wk+) were used in the input predictor variables. The best performing of the cumulative models were those with the largest number of aggregation timescales considered (models 3 and 6, Table 4), with one exception: the 1-week cumulative informed SVR model (model 5) outperformed those with additional aggregation timescales. However, contrary to our hypothesis, the informed cumulative models did not consistently outperform the uninformed cumulative models. In fact, the informed cumulative models outperformed the uninformed models for relatively short aggregation timescales (up to 2 weeks for SVR and up to 1 day only for RFR), after which the uninformed models performed better (Figure 11). This pattern also held for the non-cumulative models and was similar to that observed in the limited models. Within the limited models, the informed models outperformed the uninformed models for up to 2-week aggregations with respect to RMSE (SVR and RFR) and up to 1 week with respect to NSE (for RFR only; NSE was never better for the informed limited SVR models compared to their uninformed counterparts) (Figure 11). Within individual classes of models, the best-performing uninformed models always outperformed the best-performing informed models with respect to RMSE and NSE (Table 4).

Table 4. Performance metrics for select discharge forecast models. Rows are shaded by class (see Table 2), and the best-performing value of each metric for each class of models (support vector regression or random forest regression) is indicated in boldface font.

No.	Model	SVR (or Null) RMSE	RFR RMSE	SVR (or Null) NSE	RFR NSE	SVR (or Null) LogNSE	RFR logNSE
1	Null Model	**0.133**		**0.444**		**0.435**	
2	1D Cumulative Uninformed	0.150	0.125	-0.329	0.459	-0.064	0.548
3	6M Cumulative Uninformed	**0.065**	**0.077**	**0.750**	**0.795**	0.794	**0.833**
4	1D Cumulative Informed	0.086	0.107	0.561	0.607	0.587	0.657
5	1W Cumulative Informed	**0.081**	0.105	**0.613**	0.622	**0.597**	0.683

6	6M Cumulative Informed	0.086	**0.097**	0.565	**0.677**	0.613	**0.724**
7	1W Non-Cumulative Uninformed	0.101	0.092	0.403	**0.786**	**0.454**	0.740
8	1M Non-Cumulative Uninformed	**0.099**	**0.085**	**0.418**	0.750	0.452	0.785
9	2M Non-Cumulative Uninformed	0.110	0.085	0.280	0.755	0.307	**0.797**
10	1W Non-Cumulative Informed	**0.080**	0.106	**0.624**	0.609	**0.651**	0.663
11	2W Non-Cumulative Informed	0.089	**0.098**	0.533	**0.670**	0.562	**0.715**
12	2M Limited Uninformed	**0.085**	0.090	**0.577**	0.723	**0.612**	0.759
13	3M Limited Uninformed	0.086	**0.080**	0.566	**0.783**	0.597	**0.813**
14	1M Limited Informed	0.108	0.107	0.317	0.610	0.370	0.654
15	3M Limited Informed	**0.095**	0.098	**0.465**	0.673	**0.497**	0.713
16	6M Limited Informed	0.095	**0.093**	0.465	**0.703**	0.410	**0.735**
17	Expert's	**0.065**	**0.069**	**0.750**	**0.714**	**0.779**	**0.744**
18	Fully Informed	**0.089**	**0.116**	**0.538**	**0.543**	**0.531**	**0.602**

4.2.3 Performance of aggregation timescales in isolation

When individual timescales of aggregation were isolated with the non-cumulative models, the 1-week (NSE, RFR, model 7) or 1-month models (RMSE, RFR and SVR; NSE, SVR, model 8) performed best among the uninformed models, while the 1-week (SVR, model 10) or 2-week (RFR, model 11) timescales performed best among the informed models (Table 4). For the latter (informed) models, the top four most influential variables for the RFR were SWE or snowmelt from the two different stations, and evapotranspiration at Treeline (Tables 2.6 and 2.7), indicating that the model was dominated by the seasonal snowmelt dynamic. For the best-performing uninformed models, the top four most influential variables for the RFR were deep moisture at the four different stations (Tables 2.8 and 2.9), indicating that the range of hydrological processes influencing deep moisture throughout the catchment dominated in the prediction of discharge. In further contrast to the informed models, snowmelt and SWE were among the least influential variables for the uninformed models.

Table 5. Ranked variable importance metrics for the 1-week non-cumulative informed random forest regression discharge model.

Predictor variable	**Importance**
TL SWE_mm	0.18
TL ET (mm)	0.13
TL SnowMelt_mm	0.12
LG SnowMelt_mm	0.09
LG ET (mm)	0.08
LG SWE_mm	0.07
TL AirTemperature_C	0.06
LG AirTemperature_C	0.05
LG VMC_P2_05	0.04
LG VMC_P2_100	0.03
LG VMC_P1_100	0.03

TL VMC_P4_05	0.02
TL VMC_P3_100	0.02
TL VMC_P4_65	0.02
LG Precipitation_mm	0.02
LG VMC_P1_05	0.01
TL VMC_P3_05	0.01
TL Precipitation_mm	0.01

Table 6. Ranked variable importance metrics for the 2-week non-cumulative informed random forest regression discharge model.

Predictor variable	Importance
TL SWE_mm	0.18
LG SnowMelt_mm	0.11
LG SWE_mm	0.10
TL ET (mm)	0.10
TL AirTemperature_C	0.09
TL SnowMelt_mm	0.09
LG ET (mm)	0.07
LG VMC_P2_05	0.055
LG VMC_P1_100	0.04
LG VMC_P2_100	0.03
LG AirTemperature_C	0.03
LG Precipitation_mm	0.02
TL VMC_P4_65	0.02
TL VMC_P3_100	0.02
TL VMC_P4_05	0.02
TL VMC_P3_05	0.01
LG VMC_P1_05	0.01
TL Precipitation_mm	0.01

Table 7. Ranked variable importance metrics for the 1-week non-cumulative uninformed random forest regression discharge model.

Predictor variable	Importance
LG VMC_P2_100	0.18
LG VMC_P1_100	0.17
TL VMC_P3_100	0.17
TL VMC_P4_65	0.13
LG VMC_P1_05	0.05
LG ET (mm)	0.05
LG VMC_P2_05	0.04
TL VMC_P3_05	0.04

TL VMC_P4_05	0.04
TL ET (mm)	0.03
TL AirTemperature_C	0.02
LG AirTemperature_C	0.02
LG Precipitation_mm	0.02
TL Precipitation_mm	0.01
TL SnowMelt_mm	0.01
TL SWE_mm	0.01
LG SWE_mm	0.00
LG SnowMelt_mm	0.00

Table 8. Ranked variable importance metrics for the 1-month non-cumulative uninformed random forest regression discharge model.

Predictor variable	**Importance**
TL VMC_P3_100	0.19
TL VMC_P4_65	0.18
LG VMC_P1_100	0.13
LG VMC_P2_100	0.10
TL VMC_P4_05	0.08
LG VMC_P2_05	0.08
LG VMC_P1_05	0.05
TL VMC_P3_05	0.05
TL SnowMelt_mm	0.04
LG ET (mm)	0.02
TL SWE_mm	0.02
LG Precipitation_mm	0.01
TL Precipitation_mm	0.01
TL ET (mm)	0.01
TL AirTemperature_C	0.01
LG AirTemperature_C	0.01
LG SWE_mm	0.01
LG SnowMelt_mm	0.01

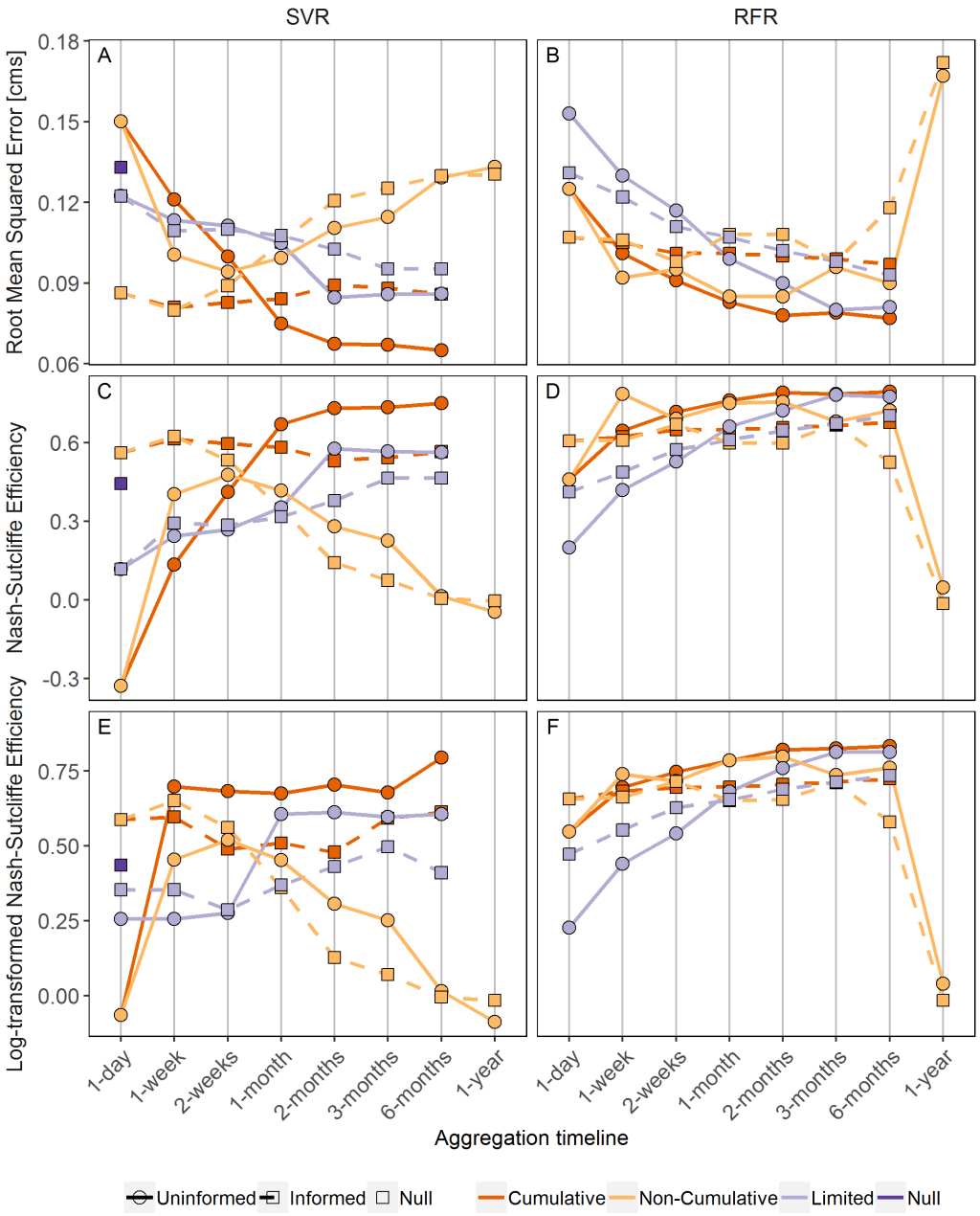

Figure 11. Comparison of forecast performance metrics between uninformed and informed models for the cumulative, non-cumulative, and limited classes of models and for support vector regression (A, C, E) and random forest regression (B, D, F), over a range of aggregation timescales. Values for the null (day-of-year) model are also shown for comparison.

4.2.4 Comparison of different model classes

Performance relative to expert model baseline.

Across the different classes of models, while all of the MLMs outperformed the day-of-year null model, very few of them outperformed the expert's model. The uninformed 6-month cumulative SVR model (model 3) exhibited performance metrics equivalent to the expert's model, though the RFR version performed slightly worse. All other models performed considerably worse (Table 4).

Cumulative vs. non-cumulative models.

Surprisingly, the best-performing informed non-cumulative models tended to outperform (SVR) or perform only slightly worse than (RFR) the best-performing informed cumulative models (Table 4). These results suggest that the additional timescales of aggregation may have induced overfitting and/or that the additional lagged, aggregated variables did not contain additional information useful for prediction. However, the outcome was reversed for the uninformed models, for which the multiple timescales of aggregation in the cumulative models resulted in considerably improved performance

Full vs. limited models.

For the SVR forecasts, the limited models consistently performed worse than either the cumulative or non-cumulative full models, regardless of performance metric. In contrast, for the RFR forecasts, the best-performing limited models tended to exhibit similar performance to the best-performing full models. Namely, the limited informed models exhibited better performance than both the cumulative and non-cumulative informed models, despite their much lower variable count compared to the cumulative models. Meanwhile, the best limited uninformed models performed slightly worse than the uninformed full models with respect to NSE and slightly better than the non-cumulative uninformed model but worse than the cumulative uninformed model with respect to RMSE.

Collectively, these findings suggest that precipitation and temperature alone were sufficient to capture the mechanisms represented within the MLM "black box" predictive of discharge and that additional variables did not contribute additional information useful for prediction, or that the MLMs were subject to overfitting with the addition of more variables. Curiously, fewer timescales of aggregation (up to 3 months) were needed to generate the best forecasts for the limited uninformed model compared to the full cumulative uninformed model (up to 6 months).

Relative performance of fully informed model.

In contrast to our hypotheses, the fully informed model (model 20 in Table 4) exhibited the worst performance of all the best-performing MLMs in each class with respect to all metrics. It should be noted that in contrast to all other models, the fully informed model considers lags up to two years, resulting in a limited training dataset. For the SVR models, the NSE was even worse for the fully informed model than for the null model (model 1), though the comparison was reversed for the RFR. For both the SVR and RFR, RMSE was better (i.e., lower) for the fully informed model than the null model.

4.2.5 Random forest regression vs. support vector regression

Comparing across equivalent models, RMSE was generally similar between the SVR and RFR models (Table 4), with the SVR models most often doing better with respect to RMSE. However, the RFR models consistently outperformed the SVR models with respect to NSE, suggesting that the SVR models may have been more biased for certain parts of the hydrograph, while fitting other parts of the hydrograph better than the RFR models.

5 Discussion

5.1 Discharge timing and controls inferred through information flow

The TE analysis is consistent with the knowledge that DCEW is a snowmelt-dominated watershed. Both the high peak magnitudes of the significant relative transfer entropy for variables that are indicators of melt-driven streamflow contributions and the remarkably consistent ~90-day "seasonal" critical timescale over which that information transfer occurs point to snowmelt as a dominant mechanism for streamflow generation.

Previous studies in the DCEW illuminate the mechanisms through which melt generates streamflow. As the melt begins, meltwater percolates downward to the shallow bedrock. Antecedent dry conditions may initially inhibit

gravity drainage to the deepest soil layers, so streamflow often remains disconnected from the dynamics of shallow soil moisture (McNamara et al., 2005; 2011). However, when hillslope-to stream connectivity of a near-bedrock, deep, saturated layer of soil is established, melt contributes to streamflow (McNamara et al., 2005). This mechanistic understanding of the primary driver of streamflow explains why integrated variables indicative of the water content of snow (SWE) and deep soil moisture of north-facing slopes (which contain the thickest, most sheltered soils) substantially reduce uncertainty in discharge approximately one season later. These are the category 1 variables discussed in section 3.4.1.2. The convergence of the seasonal critical timescale to around 90 days may be driven not just by the timescale of mean temperature changes but by the finding that at DCEW, spring rains may extend wet soil conditions by up to 90 days following snowmelt (Smith et al., 2011).

Category 2 variables (snowmelt, ET, and deep moisture from the LG south-facing slope) that significantly reduce uncertainty in discharge at 1-6 month timescales of aggregation and a seasonal lag are additional indicators of snowmelt-driven streamflow generation. Both melt rate and ET are substantially more variable at a daily frequency than SWE or deep soil moisture. Thus, while knowledge of a particular day's SWE or deep soil moisture may reduce substantial uncertainty in the next season's discharge, the same cannot be said of melt rate or ET, particularly since their signals must then be filtered through subsurface transport. Rather, it is the cumulative melt, together with the cumulative amount of ET depleting snow-water and moisture stores over the snowmelt season, that substantially reduce uncertainty in the next season's streamflow. In this case, intermediate timescales of aggregation smooth daily variability in the net contribution of meltwater to deep moisture stores, which is important as the primary reduction in uncertainty in spring discharge comes from knowledge of the total contribution of snowpack to deep moisture.

Category 3 variables (precipitation, air temperature, shallow soil moisture, and deep moisture for the TL south-facing slope), which reduce uncertainty in discharge only when aggregated over one-year+ timescales, likely reflect baseflow contributions via deep groundwater, as influenced by long-term energy fluxes that determine the catchment water balance. More specifically, these variables collectively reflect net long-term water inputs to the catchment that percolate into baseflow and reemerge over a year later as streamflow at LG (Aishlin, 2006). It is further likely that the secondary peak information transfer at > 1-year lags exhibited by some of the other variables, most notably SWE, also reflect this mechanism of streamflow generation. In addition, ET, although classified primarily as a category 2 variable because of its peak information transfer at intermediate timescales of aggregation, may additionally be classified as category 3, as its information transfer passes through a minimum at the 6-month aggregation timescale but then increases at the 1-year timescale (Figure. 2.18E). As with the other variables mentioned above, ET contains information that reflects the long-timescale net catchment water balance, potentially consuming up to 53% of annual precipitation (Kelleners et al., 2010). Previous chloride mass-balance studies conducted at DCEW revealed that at the catchment scale, up to 11% of annual precipitation recharges deep groundwater (Aishlin, 2006), primarily through fracture flow (Miller et al., 2008). Meanwhile, a water balance model of DCEW suggested that up to 36% of precipitation may percolate deeply to groundwater, with only 11-16% transformed over shorter timescales into streamflow (Kelleners et al., 2010). Our analysis is also consistent with previous findings that in high-relief catchments, streamflow has a long (multi-year) memory (Godsey et al., 2013; McGuire & McDonnell, 2006; Nippgen et al., 2016), and old groundwater may contribute substantially to baseflow (Jasechko et al., 2016).

Other, less-dominant processes also contribute to streamflow generation in the DCEW. Late-summer rains may generate streamflow if deep moisture connectivity is established prior to freezing (McNamara et al., 2005). Similarly, depending on the timing of spring rain events following the melt and whether they coincide with connected conditions in deep soil moisture, these rain events can also contribute to streamflow (Williams et al., 2009). These processes are spatially heterogeneous and highly variable interannually (Williams et al., 2009; McNamara et al., 2005) but may be partially represented in the low but significant transfer of information from water balance-relevant variables to discharge at short timescales. However, they are not captured by our machine-learning analysis, which uses predictor variables lagged only at the peak, as discussed below.

5.2 Effects of info-informed forecast on model performance

When considering short histories (i.e., one day, one week) of each predictor variable as inputs, our hypothesis that TE-informed MLMs performed better than uninformed MLMs was upheld. However, as longer variable histories were considered, either in isolation or together with other aggregation timescales, this hypothesis broke down, and unlagged, aggregated inputs primarily resulted in better forecasts than lagged, aggregated inputs. The one exception was that the informed non-cumulative SVR models outperformed their uninformed counterparts. A combination of factors may explain this surprising result, which we discuss in the subsections below.

5.2.1 Limited set of mechanisms for streamflow generation represented in informed models

First, the TE analysis suggested that, for the 6-month-or-less timescales of aggregation considered in the MLMs, the peak information transfer and peak lags associated with each variable were representative of the seasonal-scale snowmelt dynamics. Furthermore, at least some of the variables in the full models transfer large amounts of information to discharge at the seasonal-scale snowmelt lag for any of the aggregation timescales considered (Figure. 2.17). Thus, as additional aggregation timescales are added as candidate variables to a MLM and those variables are lagged in accordance with a TE analysis, the seasonal snowmelt dynamics may be better resolved, but those dynamics remain the only streamflow-generating process that can be captured by the model. Hence, the additional input variables introduced by including additional timescales of aggregation are redundant in the set of processes the MLM is able to represent. For this reason, in addition to the shortened training dataset required, the fully-informed model ended up being the worst-performing class of MLMs considered (Table 4), as it effectively was only able to represent the seasonal-scale snowmelt dynamic.

In contrast, as longer timescales of aggregation are added to a cumulative, uninformed (unlagged) MLM, streamflow-generating processes operating over a wider range of timescales may effectively be captured by the model. The longer timescales of aggregation (one-month+) begin to tap into the timescales that are part of the broad seasonal snowmelt peaks in the TE analysis, while the shorter timescales of aggregation enable the model to represent rapid streamflow-generating processes that compose a small fraction of the information contained in the annual-scale hydrograph but that may be highly important in determining the magnitude of peakflow events (Williams et al., 2009). Whether these processes generate streamflow and how much streamflow they generate may be a function of preexisting catchment connectivity (Smith et al., 2011), whether temperatures hit the freezing point before or after connectivity is established (McNamara et al., 2005), whether and for how long temperatures drop below freezing during the early snowmelt season (McNamara et al., 2011; Williams et al., 2009), and whether a snowpack exists during a rain event (Williams et al., 2009). Thus, depending on the recent histories of the spatial distribution of soil moisture, temperature, and snowpack, a precipitation event may generate large or very little amounts of streamflow at short to intermediate timescales. These dynamics may be well-represented in a MLM that considers the interaction of multiple variables at these timescales.

In contrast to the MLMs, TE does not highlight short-to-intermediate timescales as important. Indeed, the reduction in uncertainty in future discharge from knowing the recent history of any one of the involved variables in isolation may be small in a limited data record (e.g., just 16 years here), as the number of times any particular combination of connectivity, prior temperature, and prior snowpack present during a precipitation or melt event would presumably be small. Notably, almost all variables begin transferring significant information to discharge at lag times of over a week (Figure. 2.16 and 2.17), around the timescale of aggregation at which the uninformed models begin to perform better than the informed models. However, for the reasons articulated above, this information transfer is very low relative to the snowmelt peak, which unfailingly occurs in every year of the dataset.

5.2.2 Importance of interactive effects

The ability of the MLMs to represent interactive effects among predictor variables at short timescales, in contrast to the pairwise TE analysis, almost certainly plays a large role in explaining the surprising patterns in our results. Recent histories of a suite of variables that collectively reflect longer-term histories of water supply and spatial distribution (e.g., multiple soil moisture measurements, SWE) logically have high predictive power for streamflow in a way that knowledge of any one of these variables does not. As a case-in-point, the NSE for the non-cumulative uninformed 1-week model (0.786, RFR, model 7) was almost as high as that of the best-performing cumulative uninformed model (model 2.5), which included aggregation timescales of up to 6 months (0.795, RFR). Variable importance rankings for the 1-week non-cumulative uninformed RFR model (Table 5) indicated that the deep soil moisture values from all stations were the four most influential variables in the model, with moisture from the two LG stations the most influential.

In contrast to the RFR models, performance of the non-cumulative uninformed SVR models were consistently worse than their cumulative counterparts (Table 4), suggesting that RFR, with its decision-tree structure, may have modeled variable interactions (essential for predictive skill when considering a limited time range) more effectively than SVR. A superior ability to model variable interactions in physically meaningful ways may also explain why NSE metrics for the RFR models generally exceeded those of the SVR models.

With fewer variables, provided those variables are the ultimate drivers of streamflow generation, the interactive effects that are primarily responsible for individual peakflow events may be represented in a MLM through the inclusion of diverse timescales of aggregation. Among our limited, uninformed models, those with up to 3-month timescales of aggregation (i.e., up to the critical ~90-day seasonal timescales) were the best performing, with a performance only slightly lower than the best cumulative model for RFR (NSE of 0.783 for model 13 vs. 0.795 for model 3), though the difference was more pronounced for SVR (NSE of 0.577 for model 12 vs. 0.750 for model 3). In these models, presumably the longer aggregation timescales for precipitation and temperature would represent the total availability of snowpack and meltwater, while the shorter timescales may effectively capture the distribution of that water through the subsurface. Explicit inclusion of soil moisture, however, may improve the model's ability to represent catchment connectivity. This improvement is apparent in the performance of the expert's (which considers temperature, precipitation, and soil moisture) SVR (NSE of 0.779, model 17) relative to the best limited model (NSE of 0.612, model 12). However, for the RFR, the greater diversity of timescales in the best limited model (NSE of 0.783, model 13) appeared to be more important for representation of these dynamics than the inclusion of soil moisture in the expert's model (NSE of 0.716, model 17).

5.3 Information theory-informed machine learning models and the hydrologic modeling pendulum

On whole, the TE-informed identification of critical timescales is consistent with a conceptualization of the catchment as a nonlinear filter for signals from precipitation (Kirchner et al., 2000; 2001). Predictor variables tend to transfer significant amounts of information to discharge over a majority of timescales examined, reflecting both a range of mechanisms for streamflow generation and heterogeneous flow paths that encompass both active and passive storage (McNamara et al., 2005; 2011; Tetzlaff et al., 2014; 2011). Recognition of the physical importance of a wide range of timescales bodes poorly for the development of purely data-driven models at first glance, as practical considerations demand selection of a discrete set of timescales at which the input variables will be represented. When only the timescales of peak information transfer are used to guide the selection of inputs for MLMs, only the dominant streamflow-generating process or processes will be represented in the model, potentially resulting in predictions that capture the broad, low-frequency characteristics and timing of the annual hydrograph but missing higher-frequency components that are affected by interactions among several of the predictor variables. While an info-flow analysis may thus serve as a quantitative guide for ensuring representation of dominant processes in the simplest of models (e.g., here, those with very short histories of the variables considered), it may undercut the full predictive power of an MLM when only peaks of information transfer are considered in the curation of input datasets and timescales.

Rather, our analysis suggests that processes through which predictive variables causally impact streamflow generation occur over a wide range of timescales, implying that more timescales with significant information flow to discharge should be represented in the model, than just those that transfer the most information. Our initial restrictive approach may be a reason why the uninformed MLMs that spanned a wider range of hydrological process-relevant timescales generally outperformed the informed MLMs.

Several other possibilities exist for improving the potential for information-flow analyses to meaningfully inform MLMs. Partitioning information flow into synergistic, unique, and redundant components (Goodwell and Kumar, 2017a), or the use of partial transfer entropy statistics, which evaluate the reduction in uncertainty contributed by a predictor variable given knowledge of all other predictors (Rinderer et al., 2017), may help to resolve the effect of interactions between multiple predictor variables and discharge and illuminate important timescales that emerge when the combined effects of hydrologic drivers are considered . Including longer block-lengths (i.e., longer histories) in the computation of TE may result in a downweighting of the relative importance of the seasonal-timescale snowmelt dynamics compared to the intermediate-timescale rain or melt dynamics that both the MLMs and previous experiments (e.g., McNamara et al., 2005; Williams et al., 2009) indicate are important in this

catchment. Further, more years of data may allow discharge uncertainty reduction due to particular combinations of moisture/connectivity and precipitation or melt inputs to be better resolved. Unfortunately, all three of these options increase the data requirements for the TE analysis, making it less applicable to a wide range of catchments.

An alternative for improving the relevance of the TE analysis to MLM that does not increase data requirements would be to formulate additional composite variables that better represent the key hydrologic drivers of a catchment. For instance, soil moisture from all stations and depths, potentially in combination with other monitored variables, may be integrated into a metric representative of catchment connectivity. Soulsby et al. (2016), for example, used a dynamic saturation area as a measure of connectivity in a simple tipping-bucket physical model of the Girnock Burn catchment. Even though connectivity still must interact with rainfall or snowmelt to generate streamflow, this more proximal variable by itself may still be sufficient to reduce substantial uncertainty in discharge at short timescales in a way that single soil moisture measurements at specific locations within the catchment were not.

Despite the shortcomings of our present TE analysis for improving MLM-based forecasts of discharge, there remains strong potential for info-flow analyses to advance physically-based or data-driven models to more central locations in the hydrologic modeling pendulum through model benchmarking. Namely, a model that performs well for the "right" reasons (e.g., Kirchner, 2006) should exhibit similar patterns of information transfer among modeled variables as those resolved among sensor variables. In comparing timescales and relative magnitudes of information flow between models and data, a hydrologist takes advantage of a powerful tool for model selection and diagnostics. Such an analysis may particularly benefit selection from among multiple well-performing MLMs in which overfitting is a common hazard, such as those considered here.

6.Summary and Conclusions

In this work we evaluated the ability of transfer entropy to reveal the dominant catchment processes that drive streamflow and analyzed how the inclusion of these variables and the timescales over which they reduce uncertainty in discharge affected model performance. Our transfer entropy analysis suggested that the seasonal accumulation of snowpack and the interaction of snowmelt with soil moisture stores and energy fluxes driving evaporative losses were the dominant controls on seasonal discharge patterns, which agrees well with previous mechanistic-based studies that have evaluated controls on catchment discharge. Using the dominant variables and their timescales from the transfer entropy analysis, we formulated a number of classes of machine learning models to forecast catchment discharge. The effects of the info-informed versus uninformed model formulations were mixed. In general, the info-informed formulations improved the ability of the model to capture the dominant processes (i.e. accumulation, snowmelt, and evaporative losses) but limited the ability of the models to capture a wider range of processes known to be important for controlling streamflow generation (e.g. catchment connectivity and higher frequency variations driven by daily snowmelt and rainfall). Instead of models based on predictor variables lagged at the dominant timescale for transfer of information to discharge, models that included a wider range of timescales were better able to capture the range of processes relevant to local peakflow events. Furthermore, our modeling results also suggest that formulations using precipitation and temperature aggregated across multiple relevant timescales, when combined with the nonlinear architecture of machine learning models, perform close to, if not as well as more complex models that include variables known to be important in controlling discharge.

Although our simple test of the use of information theory to improve predictive models of discharge yielded mixed results, we suggest that transfer entropy will continue to be a useful tool in model formulation and evaluation. Rather than being used to identify a single dominant timescale for inclusion in the model, we suggest that info-flow analyses should be interpreted as highlighting a range of timescales that are important to include. These analyses may also improve forecasts through the identification of the dominant processes controlling catchment discharge and their potential use in model benchmarking and selection.

References

Aishlin, P. S. (2006). *Groundwater recharge estimation using chloride mass balance, Dry Creek Experimental Watershed* (PhD Thesis). Boise State University.

Benettin, P., Kirchner, J. W., Rinaldo, A., & Botter, G. (2015). Modeling chloride transport using travel time distributions at Plynlimon, Wales. *Water Resources Research*, *51*(5), 3259–3276. https://doi.org/10.1002/2014WR016600

Besaw, L. E., Rizzo, D. M., Bierman, P. R., & Hackett, W. R. (2010). Advances in ungauged streamflow prediction using artificial neural networks. *Journal of Hydrology*, *386*(1), 27–37. https://doi.org/10.1016/j.jhydrol.2010.02.037

Beven, K. (1982). On subsurface stormflow: Predictions with simple kinematic theory for saturated and unsaturated flows. *Water Resources Research*, *18*(6), 1627–1633.

Blöschl, G., & Sivapalan, M. (1995). Scale issues in hydrological modelling: a review. *Hydrological Processes*, *9*(3–4), 251–290.

Bossomaier, T., Barnett, L., Harré, M., & Lizier, J. T. (2016). Introduction. In *Introduction to Transfer Entropy* (pp. 1–10). Cham: Springer International Publishing. Retrieved from https://doi.org/10.1007/978-3-319-43222-9_1

Breiman, L. (2001). Random forests. *Machine Learning*, *45*(1), 5–32.

Chang, C.-C., & Lin, C.-J. (2011). LIBSVM: a library for support vector machines. *ACM Transactions on Intelligent Systems and Technology (TIST)*, *2*(3), 27.

Chen, Y.-C., Wei, C., & Yeh, H.-C. (2008). Rainfall network design using kriging and entropy. *Hydrological Processes: An International Journal*, *22*(3), 340–346.

Cover, T. M., & Thomas, J. A. (2006). *Elements of information theory*. NJ: John Wiley & Sons.

Dawson, C. W., & Wilby, R. L. (2001). Hydrological modelling using artificial neural networks. *Progress in Physical Geography*, *25*(1), 80–108.

Drucker, H., Burges, C. J., Kaufman, L., Smola, A. J., & Vapnik, V. (1997). Support vector regression machines. In M. Mozer, M. Jordan, & T. Petsche, *Advances in neural information processing systems* (Vol. 9, pp. 155–161). Cambridge, MA: MIT Press.

Eng, K., Grantham, T. E., Carlisle, D. M., & Wolock, D. M. (2017). Predictability and selection of hydrologic metrics in riverine ecohydrology. *Freshwater Science*, *36*(4), 915–926. https://doi.org/10.1086/694912

Erdal, H. I., & Karakurt, O. (2013). Advancing monthly streamflow prediction accuracy of CART models using ensemble learning paradigms. *Journal of Hydrology*, *477*, 119–128. https://doi.org/10.1016/j.jhydrol.2012.11.015

Fatichi, S., Vivoni, E. R., Ogden, F. L., Ivanov, V. Y., Mirus, B., Gochis, D., et al. (2016). An overview of current applications, challenges, and future trends in distributed process-based models in hydrology. *Journal of Hydrology*, *537*, 45–60. https://doi.org/10.1016/j.jhydrol.2016.03.026

Geroy, I. J., Gribb, M. M., Marshall, H.-P., Chandler, D. G., Benner, S. G., & McNamara, J. P. (2011). Aspect influences on soil water retention and storage. *Hydrological Processes*, *25*(25), 3836–3842.

Gibson, J. J., Aggarwal, P., Hogan, J., Kendall, C., Martinelli, L. A., Stichler, W., et al. (2002). Isotope studies in large river basins: A new global research focus. *Eos, Transactions American Geophysical Union*, *83*(52), 613–617. https://doi.org/10.1029/2002EO000415

Godsey, S. E., Kirchner, J. W., & Tague, C. L. (2014). Effects of changes in winter snowpacks on summer low flows: case studies in the Sierra Nevada, California, USA. *Hydrological Processes*, *28*(19), 5048–5064.

Goodwell, A. E., & Kumar, P. (2017). Temporal information partitioning: Characterizing synergy, uniqueness, and redundancy in interacting environmental variables. *Water Resources Research*, *53*(7), 5920–5942.

Goodwell, A. E., Kumar, P., Fellows, A. W., & Flerchinger, G. N. (2018). Dynamic process connectivity explains ecohydrologic responses to rainfall pulses and drought. *Proceedings of the National Academy of Sciences*, *115*(37), E8604–E8613.

Gribb, M. M., Forkutsa, I., Hansen, A., Chandler, D. G., & McNamara, J. P. (2009). The effect of various soil hydraulic property estimates on soil moisture simulations. *Vadose Zone Journal*, *8*(2), 321–331.

Henderson-Sellers, A., & Robinson, P. J. (1986). *Contemporary Climatology*. London, New York: Longman Scientific & Technical, Wiley.

Hipsey, M. R., Hamilton, D. P., Hanson, P. C., Carey, C. C., Coletti, J. Z., Read, J. S., et al. (2015). Predicting the resilience and recovery of aquatic systems: A framework for model evolution within environmental observatories. *Water Resources Research*, *51*(9), 7023–7043. https://doi.org/10.1002/2015WR017175

Ho, T. K. (1995). Random decision forests. In *Document analysis and recognition, 1995., proceedings of the third international conference on* (Vol. 1, pp. 278–282). IEEE.

Hsu, K., Gupta, H. V., & Sorooshian, S. (1995). Artificial Neural Network Modeling of the Rainfall-Runoff Process. *Water Resources Research*, *31*(10), 2517–2530. https://doi.org/10.1029/95WR01955

Jasechko, S., Kirchner, J. W., Welker, J. M., & McDonnell, J. J. (2016). Substantial proportion of global streamflow less than three months old. *Nature Geoscience*, *9*(2), 126–129. https://doi.org/10.1038/ngeo2636

Jeong, D.-I., & Kim, Y.-O. (2005). Rainfall-runoff models using artificial neural networks for ensemble streamflow prediction. *Hydrological Processes*, *19*(19), 3819–3835. https://doi.org/10.1002/hyp.5983

Johnson, K. M., Lewis, R. S., Bennett, E. H., & Kiilsgaard, T. H. (1988). Cretaceous and Tertiary intrusive rocks of south-central Idaho. In P. K. Link & W. R. Hackett (Eds.), *Guidebook to the Geology of Central and Southern Idaho* (Vol. 27, pp. 55–86). Boise, ID: Idaho Geologic Survey.

Kapnick, S. B., Yang, X., Vecchi, G. A., Delworth, T. L., Gudgel, R., Malyshev, S., et al. (2018). Potential for western US seasonal snowpack prediction. *Proceedings of the National Academy of Sciences*, 201716760.

Kelleners, T. J., Chandler, D. G., McNamara, J. P., Gribb, M. M., & Seyfried, M. S. (2009). Modeling the water and energy balance of vegetated areas with snow accumulation. *Vadose Zone Journal*, *8*(4), 1013–1030.

Kelleners, T. J., Chandler, D. G., McNamara, J. P., Gribb, M. M., & Seyfried, M. S. (2010). Modeling runoff generation in a small snow-dominated mountainous catchment. *Vadose Zone Journal*, *9*(3), 517–527.

Kirchner, J. W. (2003). A double paradox in catchment hydrology and geochemistry. *Hydrological Processes*, *17*(4), 871–874.

Kirchner, J. W. (2006). Getting the right answers for the right reasons: Linking measurements, analyses, and models to advance the science of hydrology. *Water Resources Research*, *42*(3). https://doi.org/10.1029/2005WR004362

Kirchner, J. W., Feng, X., & Neal, C. (2000). Fractal stream chemistry and its implications for contaminant transport in catchments. *Nature*, *403*(6769), 524–527. https://doi.org/10.1038/35000537

Kirchner, J. W., Feng, X., & Neal, C. (2001). Catchment-scale advection and dispersion as a mechanism for fractal scaling in stream tracer concentrations. *Journal of Hydrology*, *254*(1), 82–101. https://doi.org/10.1016/S0022-1694(01)00487-5

Kisi, O., & Cigizoglu, H. K. (2007). Comparison of different ANN techniques in river flow prediction. *Civil Engineering and Environmental Systems*, *24*(3), 211–231. https://doi.org/10.1080/10286600600888565

Kisi, O., & Cimen, M. (2011). A wavelet-support vector machine conjunction model for monthly streamflow forecasting. *Journal of Hydrology*, *399*(1), 132–140. https://doi.org/10.1016/j.jhydrol.2010.12.041

Knuth, K. H., Gotera, A., Curry, C. T., Huyser, K. A., Wheeler, K. R., & Rossow, W. B. (2013). Revealing relationships among relevant climate variables with information theory. *ArXiv Preprint ArXiv:1311.4632*.

Larsen, L. G., & Harvey, J. W. (2017). Disrupted carbon cycling in restored and unrestored urban streams: Critical timescales and controls. *Limnology and Oceanography*, *62*(S1).

Larsen, Laurel G., Eppinga, M. B., Passalacqua, P., Getz, W. M., Rose, K. A., & Liang, M. (2016). Appropriate complexity landscape modeling. *Earth-Science Reviews*, *160*, 111–130. https://doi.org/10.1016/j.earscirev.2016.06.016

Lettenmaier, D. P. (2018). Observational breakthroughs lead the way to improved hydrological predictions. *Reviews of Geophysics*, 2591–2597. https://doi.org/10.1002/2017WR020896@10.1002/(ISSN)1944-9208.COMHES1

Liaw, A., & Wiener, M. (2002). Classification and regression by randomForest. *R News*, *2*(3), 18–22.

Liu, B. Y., Zhu, Q., Riley, W. J., Zhao, L., Ma, H., Gordon, M. V., & Larsen, L. (2019). Using Information Theory to Evaluate Directional Precipitation Interactions Over The West Sahel Region In Observations and Models. *Journal of Geophysical Research: Atmospheres*, *in press*, https://doi.org/10.1029/2018JD029160. https://doi.org/10.1029/2018JD029160

López, P. L., Wanders, N., Schellekens, J., Renzullo, L. J., Sutanudjaja, E. H., & Bierkens, M. F. P. (2016). Improved large-scale hydrological modelling through the assimilation of streamflow and

downscaled satellite soil moisture observations. *Hydrology and Earth System Sciences*, *20*(7), 3059–3076. https://doi.org/10.5194/hess-20-3059-2016

Marković, I., Jurić-Kavelj, S., & Petrović, I. (2013). Partial mutual information based input variable selection for supervised learning approaches to voice activity detection. *Applied Soft Computing*, *13*(11), 4383–4391.

Markus, M., Knapp, H. V., & Tasker, G. D. (2003). Entropy and generalized least square methods in assessment of the regional value of streamgages. *Journal of Hydrology*, *283*(1–4), 107–121.

May, R., Dandy, G., & Maier, H. (2011). Review of input variable selection methods for artificial neural networks. In *Artificial neural networks-methodological advances and biomedical applications*. InTech.

McDonnell, J. J., & Beven, K. (2014). Debates—The future of hydrological sciences: A (common) path forward? A call to action aimed at understanding velocities, celerities and residence time distributions of the headwater hydrograph. *Water Resources Research*, *50*(6), 5342–5350.

McGuire, K. J., & McDonnell, J. J. (2006). A review and evaluation of catchment transit time modeling. *Journal of Hydrology*, *330*(3), 543–563. https://doi.org/10.1016/j.jhydrol.2006.04.020

McNamara, J. P. (2017). Long-term hydrometeorologic data time series, 1998-present, Dry Creek Experimental Watershed, Southwest Idaho. *Dry Creek Experimental Watershed Data*, https://doi.org/10.18122/B2BG6T.

McNamara, J. P., Chandler, D., Seyfried, M., & Achet, S. (2005). Soil moisture states, lateral flow, and streamflow generation in a semi-arid, snowmelt-driven catchment. *Hydrological Processes: An International Journal*, *19*(20), 4023–4038.

McNamara, J. P., Tetzlaff, D., Bishop, K., Soulsby, C., Seyfried, M., Peters, N. E., et al. (2011). Storage as a metric of catchment comparison. *Hydrological Processes*, *25*(21), 3364–3371.

McNamara, J. P., Flores, A. N., Benner, S. G., Pierce, J., & Aishlin, P. S. (2017). Long-Term, Continuous Stream Discharge Time Series from Measurement Sites in Dry Creek Experimental Watershed, Southwest Idaho. *Dry Creek Experimental Watershed Data*, https://doi.org/10.18122/B2DS3D.

McNamara, J. P., Benner, S. G., Poulos, M. J., Pierce, J. L., Chandler, D. G., Kormos, P. R., et al. (2018). Form and function relationships revealed by long-term research in a semiarid mountain catchment. *Wiley Interdisciplinary Reviews: Water*, *5*(2), e1267.

Miller, C., Routh, P., Brosten, T., & McNamara, J. (2008). Application of time-lapse ERT imaging to watershed characterization. *GEOPHYSICS*, *73*(3), G7–G17. https://doi.org/10.1190/1.2907156

Monteith, J. L. (1981). Evaporation and surface temperature. *Quarterly Journal of the Royal Meteorological Society*, *107*(451), 1–27.

Müller, K.-R., Smola, A., Rätsch, G., Schölkopf, B., Kohlmorgen, J., & Vapnik, V. (1999). Using support vector machines for time series prediction. In B. Schölkopf, C. J. Burges, & A. J. Smola (Eds.), *Advances in kernel methods—support vector learning* (pp. 243–254). Cambridge, MA: MIT Press.

Murari, A., Peluso, E., Gelfusa, M., Garzotti, L., Frigione, D., Lungaroni, M., et al. (2015). Application of transfer entropy to causality detection and synchronization experiments in tokamaks. *Nuclear Fusion*, *56*(2), 026006.

Murari, Andrea, Lungaroni, M., Peluso, E., Gaudio, P., Lerche, E., Garzotti, L., et al. (2018). On the use of transfer entropy to investigate the time horizon of causal influences between signals. *Entropy*, *20*(9), 627.

Newman, A. J., Clark, M. P., Sampson, K., Wood, A., Hay, L. E., Bock, A., et al. (2015). Development of a large-sample watershed-scale hydrometeorological data set for the contiguous USA: data set characteristics and assessment of regional variability in hydrologic model performance. *Hydrology and Earth System Sciences*, *19*(1), 209–223.

Nippgen, F., McGlynn, B. L., Emanuel, R. E., & Vose, J. M. (2016). Watershed memory at the Coweeta Hydrologic Laboratory: The effect of past precipitation and storage on hydrologic response. *Water Resources Research*, *52*(3), 1673–1695. https://doi.org/10.1002/2015WR018196

Packard, N. H., Crutchfield, J. P., Farmer, J. D., & Shaw, R. S. (1980). Geometry from a time series. Physical review letters, 45(9), 712.

Pechlivanidis, I. G., Jackson, B. M., McIntyre, N. R., & Wheater, H. S. (2011). Catchment scale hydrological modelling: a review of model types, calibration approaches and uncertainty analysis methods in the context of recent developments in technology and applications. *Global NEST Journal*, *13*(3), 193–214.

Pechlivanidis, I. G., Jackson, B., McMillan, H., & Gupta, H. (2014). Use of an entropy-based metric in multiobjective calibration to improve model performance. *Water Resources Research*, *50*(10), 8066–8083.

Pedregosa, F., Varoquaux, G., Gramfort, A., Michel, V., Thirion, B., Grisel, O., et al. (2011). Scikit-learn: Machine learning in Python. *Journal of Machine Learning Research*, *12*(Oct), 2825–2830.

Penman, H. L. (1948). Natural evaporation from open water, bare soil and grass. *Proc. R. Soc. Lond. A*, *193*(1032), 120–145.

Priestley, C. H. B., & Taylor, R. J. (1972). On the assessment of surface heat flux and evaporation using large-scale parameters. *Monthly Weather Review*, *100*(2), 81–92.

Rasouli, K., Hsieh, W. W., & Cannon, A. J. (2012). Daily streamflow forecasting by machine learning methods with weather and climate inputs. *Journal of Hydrology*, *414–415*, 284–293. https://doi.org/10.1016/j.jhydrol.2011.10.039

Rhoades, A. M., Jones, A. D., & Ullrich, P. A. (2018). The Changing Character of the California Sierra Nevada as a Natural Reservoir. *Geophysical Research Letters*, *45*(23), 13–008.

Rinderer, M., Ali, G., & Larsen, L. G. (2018). Assessing structural, functional and effective hydrologic connectivity with brain neuroscience methods: State-of-the-art and research directions. *Earth-Science Reviews*, *178*, 29–47. https://doi.org/10.1016/j.earscirev.2018.01.009

Ruddell, B. L., & Kumar, P. (2009a). Ecohydrologic process networks: 1. Identification. *Water Resources Research*, *45*(3).

Ruddell, B. L., & Kumar, P. (2009b). Ecohydrologic process networks: 2. Analysis and characterization. *Water Resources Research*, *45*(3).

Scanlon, B. R., Zhang, Z., Save, H., Sun, A. Y., Schmied, H. M., van Beek, L. P., et al. (2018). Global models underestimate large decadal declining and rising water storage trends relative to GRACE satellite data. *Proceedings of the National Academy of Sciences*, 201704665.

Schreiber, T. (2000). Measuring information transfer. *Physical Review Letters*, *85*(2), 461.

Sendrowski, A., & Passalacqua, P. (2017). Process connectivity in a naturally prograding river delta. *Water Resources Research*, *53*(3), 1841–1863.

Shannon, C. E. (1948). A note on the concept of entropy. *Bell System Tech. J.*, *27*, 379–423.

Sharma, A. (2000). Seasonal to interannual rainfall probabilistic forecasts for improved water supply management: Part 3—A nonparametric probabilistic forecast model. *Journal of Hydrology*, *239*(1–4), 249–258.

Shrestha, R. R., & Nestmann, F. (2009). Physically Based and Data-Driven Models and Propagation of Input Uncertainties in River Flood Prediction. *Journal of Hydrologic Engineering*, *14*(12), 1309–1319. https://doi.org/10.1061/(ASCE)HE.1943-5584.0000123

Singh, V. P. (2011). Hydrologic synthesis using entropy theory. *Journal of Hydrologic Engineering*, *16*(5), 421–433.

Singh, V. P. (2013). *Entropy theory and its application in environmental and water engineering*. John Wiley & Sons.

Skøien, J. O., Blöschl, G., & Western, A. W. (2003). Characteristic space scales and timescales in hydrology. *Water Resources Research*, *39*(10).

Smith, T. J., McNamara, J. P., Flores, A. N., Gribb, M. M., Aishlin, P. S., & Benner, S. G. (2011). Small soil storage capacity limits benefit of winter snowpack to upland vegetation. *Hydrological Processes*, *25*(25), 3858–3865. https://doi.org/10.1002/hyp.8340

Smola, A. J., & Schölkopf, B. (2004). A tutorial on support vector regression. *Statistics and Computing*, *14*(3), 199–222.

Soulsby, C., Birkel, C., & Tetzlaff, D. (2016). Modelling storage-driven connectivity between landscapes and riverscapes: towards a simple framework for long-term ecohydrological assessment. *Hydrological Processes*, *30*(14), 2482–2497. https://doi.org/10.1002/hyp.10862

Stratton, B. T., Sridhar, V., Gribb, M. M., McNamara, J. P., & Narasimhan, B. (2009). Modeling the Spatially Varying Water Balance Processes in a Semiarid Mountainous Watershed of Idaho1. *JAWRA Journal of the American Water Resources Association*, *45*(6), 1390–1408. https://doi.org/10.1111/j.1752-1688.2009.00371.x

Tetzlaff, D., Birkel, C., Dick, J., Geris, J., & Soulsby, C. (2014). Storage dynamics in hydropedological units control hillslope connectivity, runoff generation, and the evolution of catchment transit time distributions. *Water Resources Research*, *50*(2), 969–985. https://doi.org/10.1002/2013WR014147

Tetzlaff, Doerthe, McNamara, J. P., & Carey, S. K. (2011). Measurements and modelling of storage dynamics across scales. *Hydrological Processes*, *25*(25), 3831–3835. https://doi.org/10.1002/hyp.8396

Todini, E. (2007). Hydrological catchment modelling: past, present and future. *Hydrology and Earth System Sciences*, *11*(1), 468–482. https://doi.org/10.5194/hess-11-468-2007

Tokar, A. S., & Johnson, P. A. (1999). Rainfall-runoff modeling using artificial neural networks. *Journal of Hydrologic Engineering*, *4*(3), 232–239.

Tyler, S. W., Burak, S. A., McNamara, J. P., Lamontagne, A., Selker, J. S., & Dozier, J. (2008). Spatially distributed temperatures at the base of two mountain snowpacks measured with fiber-optic sensors. *Journal of Glaciology*, *54*(187), 673–679. https://doi.org/10.3189/002214308786570827

Vapnik, V. (1998). *The nature of statistical learning theory*. New York: Springer Verlag.

Vapnik, V. N., & Chervonenkis, A. J. (1974). Theory of pattern recognition.

de Vos, N. J., & Rientjes, T. H. M. (2005). Constraints of artificial neural networks for rainfall-runoff modelling: trade-offs in hydrological state representation and model evaluation. *Hydrology and Earth System Sciences*, *9*(1/2), 111–126. https://doi.org/10.5194/hess-9-111-2005

Weijs, S. V., Schoups, G. vd, & Giesen, N. (2010). Why hydrological predictions should be evaluated using information theory. *Hydrology and Earth System Sciences*, *14*(12), 2545–2558.

Wibral, M., Pampu, N., Priesemann, V., Siebenhühner, F., Seiwert, H., Lindner, M., et al. (2013). Measuring information-transfer delays. *PloS One*, *8*(2), e55809.

Williams, C. J., McNamara, J. P., & Chandler, D. G. (2009). Controls on the temporal and spatial variability of soil moisture in a mountainous landscape: the signature of snow and complex terrain. *Hydrology and Earth System Sciences*, *13*(7), 1325–1336. https://doi.org/10.5194/hess-13-1325-2009

Xia, Y., Mitchell, K., Ek, M., Sheffield, J., Cosgrove, B., Wood, E., et al. (2012). Continental-scale water and energy flux analysis and validation for the North American Land Data Assimilation System project phase 2 (NLDAS-2): 1. Intercomparison and application of model products. *Journal of Geophysical Research: Atmospheres*, *117*(D3).

Yang, Y., & Burn, D. H. (1994). An entropy approach to data collection network design. *Journal of Hydrology*, *157*(1–4), 307–324.

Yenko, M. K. (2003). *Hydrometric and Geochemical Evidence of Streamflow Sources in the Upper Dry Creek Experimental Watershed, Southwestern Idaho* (PhD Thesis). Boise State University, Boise, ID.

Yu, P.-S., Chen, S.-T., & Chang, I.-F. (2006). Support vector regression for real-time flood stage forecasting. *Journal of Hydrology*, *328*(3–4), 704–716.

Yucel, I., Onen, A., Yilmaz, K. K., & Gochis, D. J. (2015). Calibration and evaluation of a flood forecasting system: Utility of numerical weather prediction model, data assimilation and satellite based rainfall. *Journal of Hydrology*, *523*, 49–66. https://doi.org/10.1016/j.jhydrol.2015.01.042